UNIVERSITÀ
DEGLI STUDI
DI PADOVA

Sede Amministrativa: Università degli Studi di Padova
Dipartimento di Scienze Chimiche

CORSO DI DOTTORATO DI RICERCA IN SCIENZE MOLECOLARI
CURRICOLO: SCIENZE CHIMICHE
CICLO XXIX

COHERENT MULTIDIMENSIONAL ELECTRONIC SPECTROSCOPY: FROM BIOINSPIRED TO BIOLOGICAL SYSTEMS

Tesi redatta con il contributo finanziario di ERC-StG QUENTRHEL

Coordinatore: Ch.mo Prof. Antonino Polimeno

Supervisore: Ch.ma Prof. Elisabetta Collini

Dottorando: Elena Meneghin

Abstract

Could quantum phenomena affect biological processes? This question has always thrilled scientists but, only from the last decade, we have been witnessing determined and rapid strides in refinement of the experimental tools capable to unravel quantum dynamics. The unique property of assessing simultaneously distinct phenomena in the ultrafast time regime makes coherent two-dimensional electronic spectroscopy the leading technique in the novel field of quantum biology.

Artificial antennas, thanks to their lower degree of complexity, represent ideal test systems to clarify the design principles that allow quantum phenomena to survive in their natural counterparts. We studied different multi-chromophoric model systems of light-harvesting complexes by self-assembling pigment-peptide conjugates. Distinct chromophore and protein components were tested to clarify which of these two parts has a crucial role in preserving quantum phenomena.

When dealing with natural light-harvesting systems, one complicating factor in the interpretation of coherent signals is that vibronic coupling gives rise to additional oscillating patterns that might overlap with electronic features. We therefore provided a detailed investigation of the peculiar signatures of isolated pigments, such as chlorophyll *a* and bacteriochlorophyll *a*.

The expertise and the knowledge matured dealing with artificial antennas and isolated chromophores have been put to use in the interpretation of the ultrafast dynamics of a naturally occurring light-harvesting system, peridinin-chlorophyll-protein.

Quantum effects may contribute, not only to the photophysical, but also to photochemical behavior of multichromophores, such as proton transfer capability. H-tunnelling is an exquisitely quantum phenomenon which is very sensitive to distance fluctuations between donor and acceptor. In this work, we exploited again two-dimensional electronic spectroscopy to explore how H-tunnelling is affected by the motions of the surrounding and, therefore, if the coupling with nuclear motion can really fasten the overall kinetics of the reaction.

Abstract (italiano)

Fenomeni di tipo quantistico possono contribuire in modo fondamentale in processi di tipo biologico? Questa domanda ha da sempre entusiasmato gli scienziati ma, solo a partire dall'ultima decade, stiamo assistendo ai passi da giganti fatti nella messa a punto di strumenti sperimentali sempre più efficienti nel rilevare dinamiche di tipo quantistico. La spettroscopia elettronica coerente bidimensionale, grazie alla sua peculiarità di dare accesso all'osservazione simultanea di fenomeni di diversa tipologia nel regime ultraveloce, si presenta come la tecnica principe nel nuovo campo della biologia quantistica.

Le antenne artificiali, grazie al loro minor grado di complessità, sono sistemi modello ideali per delucidare quali siano i principi strutturali che permettono a fenomeni di tipo quantistico di sopravvivere nei loro analoghi naturali. Abbiamo studiato diversi sistemi multi-cromoforici, modello dei complessi antenna naturali, grazie all'auto-assemblaggio di sistemi coniugati pigmento-peptide. Sono state confrontate diverse tipologie di cromoforo e di componente proteica per determinare quale delle due parti costituenti avesse un ruolo cruciale nel preservare i fenomeni quantistici.

Nello studio dei sistemi antenna naturali, un fattore che può complicare ulteriormente l'interpretazione dei segnali coerenti, è l'accoppiamento vibronico, il quale dà origine a componenti oscillanti che potrebbero sovrapporsi a quelle elettroniche. Per tale ragione abbiamo provveduto a condurre un'indagine dettagliata dei contributi peculiari di pigmenti isolati come la clorofilla *a* e la batterioclorofilla *a*.

L'esperienza e la conoscenza maturate nello studio di sistemi antenna artificiali e di cromofori isolati hanno permesso l'interpretazione della dinamica ultraveloce di un complesso antenna naturale, la *peridinin-chlorophyll-protein*.

Effetti di tipo quantistico possono influenzare non solo processi di tipo fotofisico, ma anche reazioni fotochimiche come, ad esempio, il trasferimento di protoni. Il *tunnelling* protonico, infatti, è un fenomeno di natura squisitamente quantistica e che risulta molto sensibile alle fluttuazioni della distanza tra donatore e accettore. In questo lavoro abbiamo utilizzato spettroscopia elettronica coerente bidimensionale

per esplorare come il *tunnelling* protonico possa essere influenzato dai moti dell'intorno e, di conseguenza, come la cinetica globale della reazione possa essere velocizzata dall'accoppiamento con moti nucleari.

Contents

1 Introduction

Every second 10^{17} J of solar energy floods the planet Earth. Most of the photons that reach the surface are collected and readily harnessed by photosynthetic organisms in one hundred billionth of a second. How natural antennas can reach the remarkable efficiency of 95% [1]?

Over the past few years, light-harvesting has emerged as the mile stone of a new research field that bridges the gap between the wonderfully complex but messy biological world and the magnificently orderly world of quantum physics. The novel discipline is quantum biology.

Quantum mechanics describes reality as a world where particles can exist simultaneously in more places at once, where they can tunnel through impenetrable barriers or, moreover, no matter how far apart they are, where they can communicate instantaneously. This formulation may give a complete description of the behaviour of atoms and of their intimate constituents, but can it be extended also to classical objects we are more familiar with, such as cats?

Erwin Schrödinger was intrigued by that puzzling question. In his collection of lectures "What is life?" [2] he suggested that macroscopic order that can be found in life may reflect the order at quantum level. However, the attempts of finding a physical and mathematical description of complex living things found fierce criticism both by physics and biology communities. Fragile quantum effects were expected to be detectable only in experiments close to the absolute zero and in near perfect vacuum. How could quantum effects possibly play a role in warm, wet and noisy biological systems [3]?

Over the past decade a series of experiments has been proposed to demonstrate what in the 20th century was matter of purely theoretical formulations. Recent progresses in technology allowed developing ultrafast spectroscopies capable to follow quantum dynamics in real time. In this context, two-dimensional electronic spectroscopy (2DES) [4] became the leading technique thanks to its capability of resolving quantum signatures up to femtosecond timescale.

One of the first proofs that quantum phenomena may be relevant in biological systems came precisely from the early stages of photosynthesis. In 2007, in the laboratories of Berkley, California, a new energy transfer (ET) scheme was probed by

means of 2DES [5]. Long-lasting superpositions (coherences) of electronic states sited on different molecules were unravelled within light-harvesting protein complexes. Only three years later, the same phenomenon was detected in Toronto [6], but this time, at room temperature. These astonishing evidences opened to a new interpretation of the subtle mechanisms that control energy flow from the antennas to the reaction centre where charge separation occurs and a more stable form of chemical energy is created. Excitation, instead of being localized on a single chromophore and hopping from one site to another, appeared to be delocalized over the entire system for a remarkable long period. Sampling simultaneously all the possible routes towards the reaction centre is therefore possible and thus the quickest path can be followed. The secret of the almost unitary quantum yield of the ET process may have its roots in long-lasting coherences that, exceeding typical dephasing rates, persist in timescale compatible with ET.

The novel challenge scientists are facing nowadays consists of unveiling the subtle mechanisms that hinder coherences dephasing. A deep understanding of such processes may also lead to possible future application to artificial devices.

Several hypotheses to explain how Nature can prevent dephasing have been proposed for the past few years and can be essentially divided into two groups. The first approach looks at the role of the coupling of exciton coherences with intra-chromophore vibrational modes [7–9], while the second invokes a possible interplay of protein fluctuation and coherent excitation [10,11]. Moreover, both the processes could possibly contribute depending on the peculiarities of the system.

Identifying the crucial and underlying mechanisms responsible for long-living exciton coherences can be a hard challenge when dealing with huge protein complexes, since the number of degrees of freedom is enormous. Even if fascinating, the complexity of natural systems drove researchers to design artificial toy systems to reduce variability and to disentangle more easily the key factors that sustain quantum coherences.

Multi-chromophoric aggregates could mimic natural protein complexes: tuneable chromophores, instead of chlorophylls or carotenoids, are arranged within protein scaffolds. Changing selectively the pigment or the peptide components would help identifying whether intimate vibrational or more global structural factors are crucial in quantum transport.

Besides light-harvesting, other biological functions seem to have quantum basis, and they range from olfaction to magnetoreception [12]. Indeed, recent findings pointed out that odorants are recognized not only on the basis of their shape, but apparently their vibrational spectrum play an important role assisting electron tunnelling among the receptor sites [13]. Moreover, birds navigation appears to be related to quantum spin dynamics of transient photoinduced radical pairs initiated in the retina [14].

Another crucial biological process to whose efficiency quantum mechanics could contribute is enzymatic catalysis. It plays a fundamental role in speeding up reactions and making life eventually possible. Proton, hydride and hydrogen transfers are often involved in the rate-determining step of plenty of biochemical reactions. The short De Broglie wavelength of the proton makes H-tunnelling very sensitive to distance fluctuations. Specific dynamics of the protein scaffold in the surroundings of the catalytic site may favour tunnelling of protons, thus speeding up the reaction. The non-zero probability that protons can tunnel determines a quantum correction to the purely classical activation free energy of the reaction itself.

The primary aim of this work was giving a deep insight of the mechanisms that sustain quantum coherences, ranging from bioinspired structures to biologically occurring systems. As mentioned above, 2DES represents the most suitable spectroscopic technique to assess those ultrafast dynamics. A brief overview of theoretical background behind non-linear spectroscopic methodologies is given in Chapter 2. The experimental setup for 2DES implemented in our laboratories, together with several non-trivial strategies we proposed to collect efficiently 2DES signal are described in Chapter 3.

The core of my research activity consists in taking advantage of the remarkable capability of 2DES to assess distinct phenomena at femtosecond timescale to characterize coherent dynamics and other quantum processes, such as H-tunnelling. Chapter 4 shows a comparative study of three different artificial antennas, exquisitely designed to assess how distinct intra-chromophore vibrational properties or different peptide scaffold can affect quantum coherent energy transfer.

2DES data retain several features arising from diverse phenomena. Characteristic signatures resulting from the peculiar intra-chromophore vibrational and electronic structure can overlap to the most interesting collective behaviours resulting from exciton interaction. A crucial aspect in dealing with both artificial and natural large antennas, consists in disentangling the features of the monomers, in the first case, or of the assembled chromophores, in the second. Chapter 5 aims specifically to identify the distinctive signatures of two of the most important harvesters in natural photosynthesis, chlorophyll *a* and bacteriochlorophyll *a*.

The know-how developed in the early characterizations described in Chapter 4 and 5 found its utmost application in the study of ultrafast dynamics of peridinin-chlorophyll-protein, a naturally occurring light-harvesting complex (Chapter 6).

As closure of the research activity here presented, Chapter 7 reports how 2DES can assess not only quantum coherent energy transfer, but can also help to unravel the determining structural factors that allow H-tunnelling in enzymatic catalysis. The inner core of porphycene was chosen as structural model of enzyme active site, as its two isomeric forms interconvert by double hydrogen exchange. The role in promoting H-tunnelling of vibrational modes of the entire ring is therefore investigated.

2 Light-molecules interaction

Life on our planet is profoundly connected to the solar light and several aspects of the living matter are exquisitely tuned on the solar spectrum. Living organisms can accomplish specific biological functions thanks to the interaction of specific molecules with ultraviolet, visible and infra-red electromagnetic radiations, both to harvest solar energy and to protect themselves from solar radiations.
In this Chapter, we will deal with the theoretical aspects of the interaction of electromagnetic fields with matter, the necessary starting point to understand photoinduced phenomena and to design novel experimental methods capable to assess the details of such phenomena.
In spectroscopy, we need to describe light and matter as one complete system. A purely quantum description of light-matter interaction would start from the definition of the Hamiltonian of the system, $\hat{H}$, given by the sum of (i) the Hamiltonian of the molecules, $\hat{H}_M$ (accounting for their electronic and nuclear degrees of freedom), (ii) the Hamiltonian of the light field, $\hat{H}_L$, and finally (iii) the Hamiltonian describing the light-matter interaction, $\hat{H}_{int}$:

$$\hat{H} = \hat{H}_M + \hat{H}_L + \hat{H}_{int} \tag{2-1}$$

Solving the entire problem with a full quantum approach would mean to solve the coupled equations of motion of the quantum electrodynamics, for the light field, and of the quantum dynamics, for the molecular system. It is not a trivial task, even for small systems, but such approach is mandatory in specific cases where the non-classical properties of the light play a fundamental role as, for instance, when entangled photons or quantum photon statistics measurements are considered.

2.1. Semi-classical description of light-matter interaction

In laser spectroscopy applications light can be conveniently described classically. Indeed, the equations describing the absorption and the processes of non-linear signal generation within macroscopic samples are the well-known Maxwell equations described in the electromagnetism theory. However, light interacts with molecules that must be treated from a quantum mechanical point of view.

Therefore, spectroscopy lies in a boundary region where the macroscopic world (with its classical description) meets the microscopic one (described with a quantum approach).

The semi-classical approach can well explain most of the phenomena occurring when dealing with spectroscopic techniques. The detailed derivation of the semi-classical Hamiltonian, where the light electric field is accounted as an external and classical parameter can be found in ref. [15].

Within the semi-classical approach, instead of solving simultaneously the coupled equations of motion for the light and matter variables, we can simplify the mutual light-matter interaction into a 'one-way' interaction. The experiment can be formally divided into two stages.

In the first stage a quantum system interacts with the perturbing incoming field; the field drives the system out of equilibrium, but the matter does not affect the radiation. This assumption is reasonable, since we are interested on the effects that light produces on the molecules. Eq. (2-1) can be thus simplified by neglecting term $\hat{H}_L$:

$$\hat{H} = \hat{H}_M + \hat{H}_{int} \tag{2-2}$$

Within the perturbation theory framework, $\hat{H}_{int}$ is treated as a small perturbation of the of the Hamiltonian of the quantum molecular system, $\hat{H}_M$. While the latter term is time-independent, $\hat{H}_{int}$ shows a temporal dependence since light is an oscillating electromagnetic field.

Once the quantum operators of the radiation observables are replaced with their expectation values, the molecule variables can be separated from field variables within the motion equations. The time-dependent expectation values of physical observables arising from the motion of the charges in the molecule can thus be evaluated by solving the quantum dynamics of the molecular system. Among them we can find the polarization of the molecular system, $P(t)$.

In the second stage the expectation value of the induced polarization becomes a source of the electromagnetic field, $E_{sig}(t)$, which represents the spectroscopic signal. Indeed, using the system quantum dynamics calculated in the first stage, the time-dependent charge density, namely $P(t)$, is used to define the radiated electromagnetic field.

One of the possible approaches capable of describing the time evolution of a quantum system perturbed by pulses of light is the time-dependent perturbation theory, as demonstrated in the next Section.

2.2. Perturbative expansion of the wavefunction

In quantum mechanics, the temporal evolution of a quantum system is described by the time-dependent Schrödinger equation. The system, together with its properties, is suitably represented as a time-dependent wavefunction $|\Psi(t)\rangle$.

$$\frac{d|\Psi(t)\rangle}{dt} = -\frac{i}{\hbar}\hat{H}(t)|\Psi(t)\rangle \tag{2-3}$$

As mentioned before, the Hamiltonian of the quantum molecular system $\hat{H}_M$ is time independent, while the Hamiltonian accounting for light-matter interaction $\hat{H}_{int}$ oscillates in time.
The evolution of the quantum system in absence of light perturbation is given by the analytical solution of Eq. (2-3):

$$|\Psi(t)\rangle = e^{-\frac{i}{\hbar}\hat{H}_M(t-t_0)}|\Psi(t_0)\rangle \tag{2-4}$$

where t and t_0 are the observation and the initial time, respectively.
The operator that describes the time dependence of the system, also called time-evolution operator, $\hat{U}(t,t_0)$, can thus be expressed as:

$$\hat{U}(t,t_0) = e^{-\frac{i}{\hbar}\hat{H}_M(t-t_0)} \tag{2-5}$$

A convenient approach to calculate the evolution of the quantum system perturbed by an electromagnetic field consists in the interaction picture. It is an intermediate representation between the Schrödinger picture and the Heisenberg picture. Whereas in the other two pictures either the wavefunctions or the operators carry time dependence, in the interaction picture both carry part of the time dependence of observables.
A new set of wavefunctions and operators (here labelled with subscript I) can thus be defined, emphasizing the time-evolution due to the difference between $\hat{H}$ and $\hat{H}_M$, namely to the interaction with the external radiation:

$$|\Psi_I(t)\rangle = \hat{U}(t,t_0)|\Psi(t)\rangle \tag{2-6}$$

$$\hat{O}_I = \hat{U}^\dagger(t,t_0)\ \hat{O}\ \hat{U}(t,t_0) \tag{2-7}$$

where $\hat{O}$ is a generic operator.
Time-dependent Schrödinger equation (Eq. (2-3)) can be re-written within the interaction picture as:

$$\frac{d|\Psi_I(t)\rangle}{dt} = -\frac{i}{\hbar}\hat{H}_{int,I}(t)|\Psi_I(t)\rangle \tag{2-8}$$

where $\hat{H}_{int,I}(t)$ is the Hamiltonian of the weak perturbation expressed in the interaction picture as defined in Eq. (2-7):

$$\hat{H}_{int,I} = \hat{U}^{\dagger}(t,t_0)\ \hat{H}_{int}\ \hat{U}(t,t_0) \tag{2-9}$$

We consider the external radiation field as constituted by laser pulses, assumed to be short compared with any time scale of the system but long compared to the oscillation period of the light field, e.g. in the semi-impulsive limit. When the quantum system interacts once with the external field, Eq. (2-8) can be conveniently integrated as follows:

$$|\Psi_I(t)\rangle = |\Psi_I(t_0)\rangle - \frac{i}{\hbar}\int_{t_0}^{t} d\tau_1 \hat{H}_{int,I}(d\tau_1)\,|\Psi_I(\tau_1)\rangle \tag{2-10}$$

In a more general picture, we can consider n interactions with laser pulses and Eq. (2-10) results in the perturbative expansion:

$$\begin{aligned}|\Psi_I(t)\rangle = |\Psi_I(t_0)\rangle + \sum_{n=1}^{\infty}\left(-\frac{i}{\hbar}\right)^n \int_{t_0}^{t} d\tau_n \int_{t_0}^{\tau_n} d\tau_{n-1} \ldots \int_{t_0}^{\tau_2} d\tau_1 \\ \hat{H}_{int,I}(\tau_n)\hat{H}_{int,I}(\tau_{n-1}) \ldots \hat{H}_{int,I}(\tau_1)|\Psi_I(t_0)\rangle\end{aligned} \tag{2-11}$$

where τ_n represents the instant in which the n^{th} light-quantum system interaction occurs. It is worthy to note that Eq. (2-11) is an expansion in powers of the weak perturbation $\hat{H}_{int}(t)$, and not of the full Hamiltonian $\hat{H}(t)$. Going back to the Schrödinger picture we obtain:

$$\begin{aligned}|\Psi(t)\rangle = |\Psi^{(0)}(t_0)\rangle + \sum_{n=1}^{\infty}\left(-\frac{i}{\hbar}\right)^n \int_{t_0}^{t} d\tau_n \int_{t_0}^{\tau_n} d\tau_{n-1} \ldots \int_{t_0}^{\tau_2} d\tau_1 \\ \hat{U}(t,t_0)\hat{H}_{int,I}(\tau_n)\hat{H}_{int,I}(\tau_{n-1}) \ldots \hat{H}_{int,I}(\tau_1)|\Psi(t_0)\rangle\end{aligned} \tag{2-12}$$

In third-order non-linear spectroscopies the terms in Eq. (2-11) and Eq. (2-12) we are interested in are the wavefunctions resulting after three interactions with the external field, namely:

$$\begin{aligned}|\Psi_I^{(3)}(t)\rangle = \left(-\frac{i}{\hbar}\right)^3 \int_{t_0}^{t} d\tau_3 \int_{t_0}^{\tau_3} d\tau_2 \int_{t_0}^{\tau_2} d\tau_1 \\ \hat{H}_{int,I}(\tau_3)\hat{H}_{int,I}(\tau_2)\hat{H}_{int,I}(\tau_1)|\Psi_I(t_0)\rangle\end{aligned} \tag{2-13}$$

$$|\Psi^{(3)}(t)\rangle = \hat{U}(t,t_0)|\Psi_I^{(3)}(t)\rangle =$$

$$= \left(-\frac{i}{\hbar}\right)^3 \int_{t_0}^{t} d\tau_3 \int_{t_0}^{\tau_3} d\tau_2 \int_{t_0}^{\tau_2} d\tau_1 \, \hat{U}(t,\tau_3)\hat{H}_{int}(\tau_3) \tag{2-14}$$

$$\hat{U}(\tau_3,\tau_2)\hat{H}_{int}(\tau_2)\hat{U}(\tau_2,\tau_1)\hat{H}_{int,I}(\tau_1)\hat{U}(\tau_1,t_0)|\Psi(t_0)\rangle$$

Eq. (2-14) has an intuitive physical interpretation: initially the system is only subjected to Hamiltonian $\hat{H}_M$ (i.e. propagates freely) until time τ_1, described by the time evolution operator $\hat{U}(\tau_1,t_0)$. At time τ_1, it interacts with the perturbation $\hat{H}_{int,I}(\tau_1)$ and, subsequently, it again propagates freely until time τ_2, and so on.

2.3. Perturbative expansion of the density matrix

The previous Section has treated the evolution of a "pure" state of the quantum system described by the wavefunction $|\Psi(t)\rangle$ on Hilbert space. This idealized representation cannot characterize a mixed state, namely a statistical ensemble of several quantum states, which often occurs in real systems. When we deal with statistical ensembles and we don't know the exact initial quantum state, the system can be conveniently described by the density operator, $\hat{\rho}$. This operator formalism is a generalization of the pure state quantum mechanics described so far.

When the system is in state $|\Psi_1\rangle$ with the probability P_1, while it is in state $|\Psi_2\rangle$ with probability P_2, it can be described as a statistical mixture of the states $|\Psi_1\rangle$ and $|\Psi_2\rangle$. Generalizing the problem, for a statistical mixture of the states $\{|\Psi_j\rangle\}$ with respective probabilities $\{P_j\}$, the density operator can be defined as:

$$\hat{\rho} = \sum_j P_j \, |\Psi_j\rangle\langle\Psi_j| \tag{2-15}$$

As the Schrödinger equation (Eq. (2-3)) represents the time-evolution of a pure quantum states, the Liouville-von Neumann equation describes the temporal evolution for a mixture of states:

$$\frac{d\hat{\rho}(t)}{dt} = -\frac{i}{\hbar}\left[\hat{H}(t),\hat{\rho}(t)\right] \tag{2-16}$$

Moreover, Eq. (2-16) can be deduced from (2-3), as demonstrated in ref. [16].

Since the time evolution of the wavefunction in the interaction picture, $|\Psi_I(t)\rangle$, is formally equivalent to the Schrödinger equation (Eq. (2-8)), the same is true for the density matrix in the interaction picture, $\hat{\rho}_I(t)$, for which we obtain an equation formally equivalent to the Liouville-von Neumann equation:

$$\frac{d\hat{\rho}_I(t)}{dt} = -\frac{i}{\hbar}\left[\hat{H}_{int,I}(t),\hat{\rho}_I(t)\right] \tag{2-17}$$

The perturbative expansion of the density operator can be determined by solving iteratively Eq. (2-17), as already demonstrated for the wavefunction in Section 2.2:

$$\hat{\rho}_I(t) = \hat{\rho}_I(t_0) + \sum_{n=1}^{\infty} \left(-\frac{i}{\hbar}\right)^n \int_{t_0}^{t} d\tau_n \int_{t_0}^{\tau_n} d\tau_{n-1} \ldots \int_{t_0}^{\tau_2} d\tau_1 \\ \left[\hat{H}_{int,I}(\tau_n), \left[\hat{H}_{int,I}(\tau_{n-1}), \ldots \left[\hat{H}_{int,I}(\tau_1), \hat{\rho}_I(t_0)\right] \ldots\right]\right] \tag{2-18}$$

It follows that the third-order term of the density operator in the perturbative expansion is given by:

$$\hat{\rho}_I{}^{(3)}(t) = \left(-\frac{i}{\hbar}\right)^3 \int_{t_0}^{t} d\tau_3 \int_{t_0}^{\tau_3} d\tau_2 \int_{t_0}^{\tau_2} d\tau_1 \\ \left[\hat{H}_{int,I}(\tau_3), \left[\hat{H}_{int,I}(\tau_2), \left[\hat{H}_{int,I}(\tau_1), \hat{\rho}(t_0)\right]\right]\right] \tag{2-19}$$

where we assume that $\hat{\rho}(t_0) \equiv \hat{\rho}_I(t_0)$, which is the equilibrium density operator.
The third-order term of the density operator can also be expressed in the Schrödinger picture using Eq. (2-7):

$$\hat{\rho}^{(3)}(t) = \hat{U}(t,t_0)\hat{\rho}_I{}^{(3)}(t)\hat{U}^{\dagger}(t,t_0) = \\ = \left(-\frac{i}{\hbar}\right)^3 \int_{t_0}^{t} d\tau_3 \int_{t_0}^{\tau_3} d\tau_2 \int_{t_0}^{\tau_2} d\tau_1 \, \hat{U}(t,\tau_3)\hat{H}_{int}(\tau_3) \\ \hat{U}(t,t_0)\left[\hat{H}_{int,I}(\tau_3), \left[\hat{H}_{int,I}(\tau_2), \left[\hat{H}_{int,I}(\tau_1), \hat{\rho}(t_0)\right]\right]\right]\hat{U}^{\dagger}(t,t_0) \tag{2-20}$$

Eq. (2-20) represents how a statistical mixture evolves in time as a consequence of three interactions with an external field. The derivation of the third-order term of the density operator will be crucial to calculate the third-order nonlinear polarization term and, finally, the response function for experiments that concern three interactions of the quantum molecular system with laser pulses.

2.4. Response function

Most of ultrafast spectroscopies typically measure an induced macroscopic polarization generated in the material as response to an external field perturbation.
For a weak electric field, the polarization depends linearly on the strength of the electric field:

$$P = \varepsilon_0 \chi^{(1)} E \tag{2-21}$$

where $\chi^{(1)}$ is the linear optical susceptibility and ε_0 the vacuum dielectric constant.

Ultrafast spectroscopic techniques rely on very short laser pulses and intense electric fields and, thus, nonlinear effects become non-negligible. It follows that the polarization must be described as a power expansion of the external electric field E [17]:

$$P = \varepsilon_0(\chi^{(1)}E + \chi^{(2)}EE + \chi^{(3)}EEE + \cdots) \tag{2-22}$$

where $\chi^{(n)}$ are the n^{th}-order optical susceptibilities. The electric field is a vector, thus the linear and nonlinear susceptibilities are tensors. In media with inversion symmetry, such as isotropic systems like solutions, even-order susceptibilities vanish due to symmetry. Therefore, for most media the lowest order for nonlinear polarization is the third one. The macroscopic polarization can also be expressed as the expectation value of the product of dipole moment operator, $\hat{\mu}$, and of the density operator, $\hat{\rho}(t)$:

$$P(t) = \mathrm{Tr}[\mu\rho(t)] = \langle\hat{\mu}\hat{\rho}(t)\rangle \tag{2-23}$$

where μ and $\rho(t)$ are the matrix representations of the dipole moment and density operators, respectively.
For example, in a two-level system:

$$\rho = \begin{pmatrix}\rho_{11} & \rho_{12}\\ \rho_{21} & \rho_{22}\end{pmatrix} \qquad \mu = \begin{pmatrix}0 & \mu_{12}\\ \mu_{21} & 0\end{pmatrix} \tag{2-24}$$

and the polarization equals to:

$$P(t) = Tr\left[\begin{pmatrix}0 & \mu_{12}\\ \mu_{21} & 0\end{pmatrix}\begin{pmatrix}\rho_{11} & \rho_{12}\\ \rho_{21} & \rho_{22}\end{pmatrix}\right] = \mu_{12}\rho_{21} + \mu_{21}\rho_{12} \tag{2-25}$$

Eq. (2-25) shows that only off-diagonal elements of the density matrix generate macroscopic polarization and thus can become source of electric field.
At the third order, in the interaction picture:

$$P^{(3)}(t) = \mathrm{Tr}\left[\mu_I(t)\rho_I^{(3)}(t)\right] \tag{2-26}$$

where $\hat{\mu}_I(t)$ represents the dipole moment operator in the interaction picture. It is worthy to note that the dipole moment operator is time-dependent in this representation, while it is time-independent in the Schrödinger picture.
If we describe the light-matter interaction as dipolar interaction between the external electric field and the dipole moment:

$$\hat{H}_{int,I}(t) = -\hat{\mu}_I(t)E(t) \tag{2-27}$$

If we substitute Eq. (2-27) and the expansion of density matrix described in Eq. (2-19) into Eq. (2-26), we can find the relation between the third-order term of the density operator expansion and the third-order nonlinear polarization:

$$P^{(3)}(t) = \left(\frac{i}{\hbar}\right)^3 \int_{t_0}^{t} d\tau_3 \int_{t_0}^{\tau_3} d\tau_2 \int_{t_0}^{\tau_2} d\tau_1 \, E(\tau_3)E(\tau_2)E(\tau_1) \\ Tr[\mu_I(t)[\mu_I(\tau_3),[\mu_I(\tau_2),[\mu_I(\tau_1),\rho(t_0)]]]] \tag{2-28}$$

As anticipated before, we assume that $\rho(t_0)$ is an equilibrium density matrix that does not evolve in time, thus we can set $t_0 \to -\infty$. Furthermore, a different set of variables can be used:

$$\begin{aligned} \tau_1 &= 0 \\ t_1 &= \tau_2 - \tau_1 \\ t_2 &= \tau_3 - \tau_2 \\ t_3 &= t - \tau_3 \end{aligned} \tag{2-29}$$

where τ_n denotes the absolute time points of the electric field-molecule interaction and t_n represents the time interval between these interactions. We can set $\tau_1 = 0$ since the zero-point of the experiment is arbitrary.
The third-order polarization of Eq. (2-28) can thus be transformed as:

$$P^{(3)}(t) = \left(\frac{i}{\hbar}\right)^3 \int_{0}^{\infty} dt_3 \int_{0}^{\infty} dt_2 \int_{0}^{\infty} dt_1 \\ E(t-t_3)E(t-t_3-t_2)E(t-t_3-t_2-t_1) \\ Tr[\mu_I(t_3+t_2+t_1)[\mu_I(t_2+t_1),[\mu_I(t_1),[\mu_I(0),\rho(-\infty)]]]] \tag{2-30}$$

$P^{(3)}(t)$ can also be written as the convolution of three external electric fields with the third order optical response function $S^{(3)}(t_3, t_2, t_1)$:

$$P^{(3)}(t) = \int_{0}^{\infty} dt_3 \int_{0}^{\infty} dt_2 \int_{0}^{\infty} dt_1 \\ E(t-t_3)E(t-t_3-t_2)E(t-t_3-t_2-t_1)S^{(3)}(t_3,t_2,t_1) \tag{2-31}$$

where the response function is defined as:

$$S^{(3)}(t_3,t_2,t_1) = \left(\frac{i}{\hbar}\right)^3 Tr[\mu_I(t_3+t_2+t_1) \\ [\mu_I(t_2+t_1),[\mu_I(t_1),[\mu_I(0),\rho(-\infty)]]]] \tag{2-32}$$

The dipole moment, $\mu_I(t_3 + t_2 + t_1)$, has a different role compared to the others. Interactions at time 0, t_1 and $t_2 + t_1$ generate the non-equilibrium density matrix $\rho^{(3)}$, whose off-diagonal elements emit an electric field at time $t_3 + t_2 + t_1$, which is the spectroscopic signal. Indeed, the first three interactions are part of the commutators, while the last one is not.

2.5. Feynman diagrams

The response function described in Eq. (2-32) includes various contributions resulting from specific sequences of light-molecule interactions, meaning that only certain Liouville space pathways through the states of the system can contribute to the final signal. These pathways connect specific density matrix elements.

A pictorial and intuitive representation of these interactions is provided by the schematic double-sided Feynman diagrams. Time evolution of bra and ket of the density matrix is represented by right and left vertical arrows, respectively (Figure 2.1), where the time is running from the bottom to the top. Interactions with the dipole operator are represented by diagonal arrows pointing in or out the time lines and representing absorption or emission of radiation, respectively. The last arrow is different from the others since it represents the emission of light from the non-equilibrium density matrix. This difference is marked using a dashed line arrow.

In Figure 2.1 some illustrative examples of double sided Feynman diagrams for the first ($n = 1$), second ($n = 2$) and third ($n = 3$) order of perturbation are reported.

Most non-linear spectroscopic applications aim to study the dynamics of excited states, thus the minimum number of interactions with the external field is three: the first two pulses, indeed, act both on bra and ket of the density matrix producing a pure excited state $|e\rangle\langle e|$ (see Figure 2.1(c)); finally, the third interaction is necessary to stimulate the spectroscopic signal.

When we write explicitly the commutator of the third-order response function in Eq. (2-32), we obtain 2^3 terms resulting from three interactions acting either on the left (ket) or the right (bra) of the density matrix [15,18]:

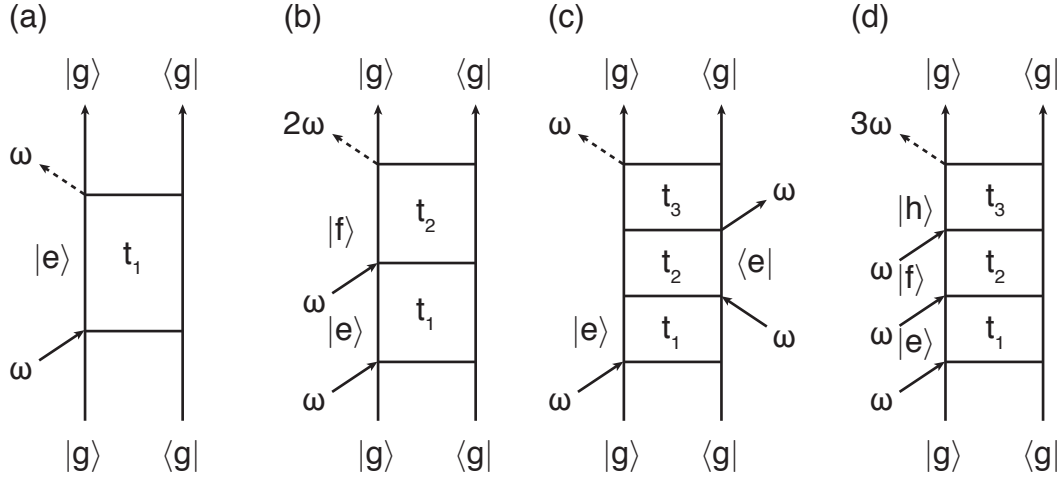

Figure 2.1 Examples of double-sided Feynman diagrams describing different n-order terms of the response function. In panel (a) we represented linear absorption ($n = 1$), in (b) second harmonic generation ($n = 2$), in (c) stimulated emission ($n = 3$) and in (d) third harmonic generation ($n = 3$). Intervals between the interactions with the field with frequency ω are defined as t_n.

$$
\begin{aligned}
&S^{(3)}(t_3,t_2,t_1) = \left(\frac{i}{\hbar}\right)^3 \sum_{i=1}^{4}(R_i - R_i^*) = \\
&= Tr[\mu_I(t_3+t_2+t_1)\mu_I(0)\rho(-\infty)\mu_I(t_1)\mu_I(t_2+t_1)] + && R_1 \\
&\quad -Tr[\mu_I(t_3+t_2+t_1)\mu_I(t_2+t_1)\mu_I(t_1)\rho(-\infty)\mu_I(0)] + && R_1^* \\
&\quad +Tr[\mu_I(t_3+t_2+t_1)\mu_I(t_1)\rho(-\infty)\mu_I(0)\mu_I(t_2+t_1)] + && R_2 \\
&\quad -Tr[\mu_I(t_3+t_2+t_1)\mu_I(t_2+t_1)\mu_I(0)\rho(-\infty)\mu_I(t_1)] + && R_2^* \\
&\quad +Tr[\mu_I(t_3+t_2+t_1)\mu_I(t_2+t_1)\rho(-\infty)\mu_I(0)\mu_I(t_1)] + && R_3 \\
&\quad -Tr[\mu_I(t_3+t_2+t_1)\mu_I(t_1)\mu_I(0)\rho(-\infty)\mu_I(t_2+t_1)] + && R_3^* \\
&\quad +Tr[\mu_I(t_3+t_2+t_1)\mu_I(t_2+t_1)\mu_I(t_1)\mu_I(0)\rho(-\infty)] + && R_4 \\
&\quad -Tr[\mu_I(t_3+t_2+t_1)\rho(-\infty)\mu_I(0)\mu_I(t_1)\mu_I(t_2+t_1)] && R_4^*
\end{aligned}
\tag{2-33}
$$

where R_i^* is the conjugate complex of R_i and, by convention, these terms are written with the last interaction emitted from the ket (on the left).

The 2^3 terms of the non-linear response function are furtherly split by the electric field, as described in Eq. (2-31). Since the total external field is given by three laser pulses, the total third order signal includes 864 terms.

Extracting information from signals with such a great number of contributions could be difficult. However, we can reduce drastically the number of terms imposing suitable experimental conditions, such as (i) time ordering, (ii) phase matching and (iii) rotating wave approximation.

The mathematical demonstration of how these choices can effectively remove some contribution to the spectroscopic signal goes beyond the purposes of this work, however the detailed description can be found in ref. [15].

As mentioned above, in non-linear time-resolved spectroscopies, we describe the external field in the semi-impulsive limit, thus the envelopes of the pulses are approximated by δ-function profiles. It follows that the laser pulses $E_1(t)$, $E_2(t)$ and $E_3(t)$ are shorter than the time separation between them, they do not overlap in time and we can rely on strict time ordering. The n-th laser pulse can be written as:

$$
E_n(t) = \mathcal{E}_n \delta(t-\tau_n)(e^{\pm i\omega_n t \mp \boldsymbol{k}_n \cdot \boldsymbol{r}}) \tag{2-34}
$$

where $\mathcal{E}_n$ is the scalar amplitude of the electric field, ω_n its central frequency and $\boldsymbol{k}_n$its wavevector, bearing its propagation direction.

When rotating wave approximation (RWA) is applied, only terms of Eq. (2-32) containing either $e^{i\omega t}$ or $e^{-i\omega t}$ will contribute to the third-order polarization, but not both. When both RWA and strict time ordering are applied, the number of terms is drastically reduced to four (and the associated complex conjugated terms). The corresponding double sided Feynman diagrams are reported in Figure 2.2.

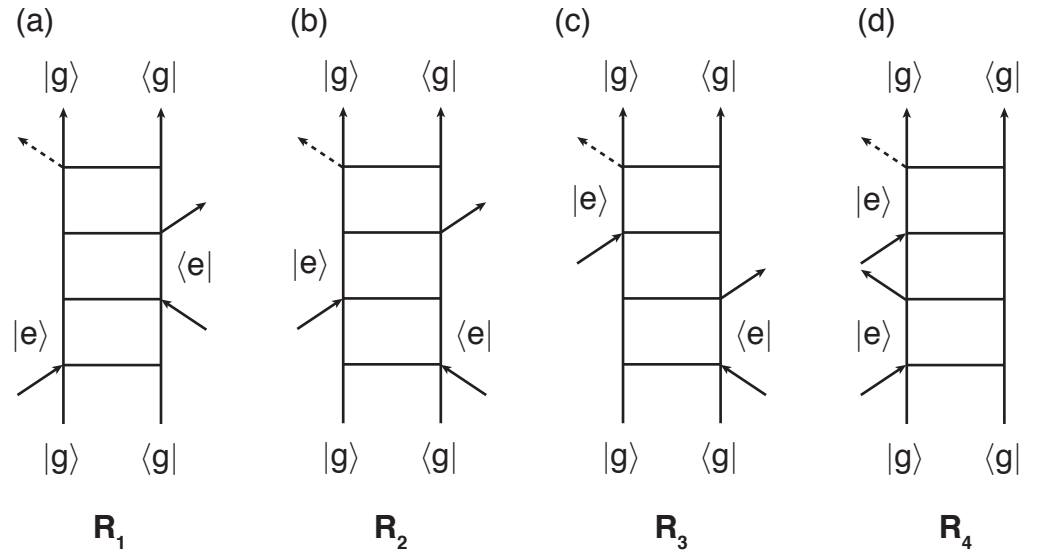

Figure 2.2 Feynman diagrams corresponding to different paths contributing to third order response. (a) and (b) correspond to R_1 and R_2, two stimulated emission paths, while (c) and (d) correspond to R_3 and R_4, ground state bleaching paths. SE and GSB can be distinguished based on the state evolving during t_2: the excited state in the former while the ground state in the latter.

Since the aim of most spectroscopies is studying the excited state dynamics, we are interested in Feynman pathways that generate an excited state population $|e\rangle\langle e|$ after the first two interactions. Afterwards, with the third interaction, the system will emit the third-order signal described by an electric field with frequency lying in the same spectral range of the perturbations. This peculiar process is called stimulated emission (SE) and correspond to R_1 and R_2 Feynman pathways (Figure 2.2).
R_1 and R_2 are ideal terms to study the evolution of the excited state population along t_2, for this reason also called 'population' time. Within the same experimental conditions capable to follow SE pathways, also signals resulting from R_3 and R_4 terms are collected. They describe the ground state bleaching (GSB) process, where we can follow the evolution of the ground state during t_2.
The outcoming fields resulting from specific Feynman pathways can be separated exploiting the different directions along which they are emitted. Thus, a suitable design of the geometry of the experimental setup, allows choosing a specific phase matching direction ($\boldsymbol{k}_s$). Indeed, R_2 and R_3 terms can be collected separately from R_1 and R_4 by tuning the phase matching direction as $\boldsymbol{k}_s = -\boldsymbol{k}_1 + \boldsymbol{k}_2 + \boldsymbol{k}_3$ or $\boldsymbol{k}_s = \boldsymbol{k}_1 - \boldsymbol{k}_2 + \boldsymbol{k}_3$, respectively. The former condition describes rephasing signal, while the latter represents non rephasing signal. 'Rephasing' and 'non rephasing' terminology arises from the different behaviour of the two pathways in t_1 and t_3. In rephasing paths the system evolves with conjugate frequency in the two time intervals generating an echo signal, while, in non rephasing paths it evolves with the same frequency, and the echo is not produced.

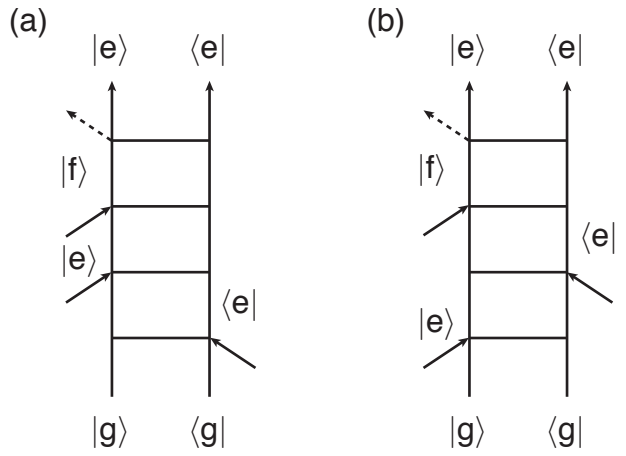

Figure 2.3 Possible additional contributions to the spectroscopic signal: panel (a) and (b) show two Feynman pathways responsible of ESA contribution to rephasing and non rephasing signal, respectively.

However, Feynman pathways described in Figure 2.2 are not the only contributions to the overall signal, since, so far, we have discarded all the terms where the last interaction generates a population of the excited state. Two examples are reported in Figure 2.3. The diagrams show that system is driven into a first excited state by the first two ('pump') pulses, and then the third ('probe') interaction probes a second excited state. This process is defined as excited state absorption (ESA).

2.6. Relaxation process and spectral lineshapes

In the previous Section, we demonstrated that only off diagonal elements of the density matrix contribute to the field of the emitted signal. It follows that the outcoming radiation is generated by a coherent superposition of states, namely a coherence. When an isolated system reaches a coherence after interaction with an external field, it will oscillate continuously between the two states and the radiation that it produces has a frequency matching the energy gap between the states building the coherence.

Spectroscopic experiments usually study statistical ensembles of individual systems in condensed phase. Each molecule is surrounded by slightly different environmental conditions that influence differently its properties. This results in a dynamic distribution of frequencies and phases of their dipole moments and/or in a static distribution of their resonance frequencies. Thus, the overall macroscopic polarization that generates the outcoming signal during the experiment is eventually damped.

We shall illustrate this behaviour for the linear optical response. The absorption spectrum $A(\omega)$ is proportional to the electric field emitted by a sample after one interaction with the perturbing field. The signal is proportional to the first-order polarization induced on the system that, in turn, results from the off diagonal ele-

ments of the density operator. The absorption spectrum is proportional to the Fourier transform (FT) of the time evolution of the correlation function of dipole moments, as demonstrated in ref. [15]:

$$A(\omega) \propto \mathrm{Re} \int_0^\infty dt\ e^{-i\omega t} \mathrm{Tr}[\mu_I(t)\mu_I(0)\rho(-\infty)] = \\ = \mathrm{Re} \int_0^\infty dt\ e^{-i\omega t} \mathrm{Tr}[\mu_{ab}(t)\mu_{ba}(0)\rho_{aa}] \tag{2-35}$$

Eq. (2-35) describes the case in which the frequency of the perturbing radiation is in resonance with the energy gap of states *a* and *b* of the system. In Figure 2.4, some examples of correlation functions of dipole moment and their relative FT spectra are represented.

After the perturbation of the external electric field, some off-diagonal elements of the density matrix are different from zero. If no interaction with the environment influences the molecules of the system, they will oscillate at resonance ω_{ab} frequency *ad infinitum* (green line in Figure 2.4). The absorption spectrum in this peculiar case is described by a δ-function:

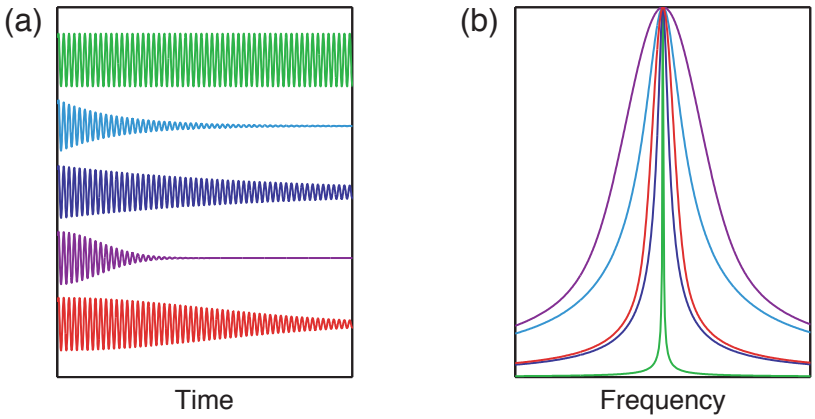

Figure 2.4 Panel (a) shows dipole moment correlation functions characterized by different relaxation conditions while the corresponding Fourier spectrum is shown in panel (b). Green line represents the ideal case when no relaxation process occurs: the corresponding spectrum is a δ-function. Light and dark blue lines represent oscillations subjected to homogeneous relaxation with short and long correlation time, respectively. Their spectra have a Lorentzian shape. Purple and red lines represent the inhomogeneous case with short and long correlation times, respectively, resulting in a Gaussian-shaped spectrum. The longer is the correlation time, the narrower is the corresponding spectrum.

$$A(\omega) \propto \mathrm{Re} \int_0^\infty dt\ e^{-i\omega t} e^{i\omega_{ab} t} = 2\pi\delta(\omega_{ab} - \omega) \tag{2-36}$$

In a real system, each chromophore interacts differently with the surrounding environment, e.g with other chromophores and/or with solvent molecules, leading to the dephasing of coherences. Specifically, for an ensemble of molecules with different environments, the resonance frequencies ω_{ab} are slightly different, resulting in *static* distribution, usually described by a Gaussian function.
Resonance frequency of a single system can also dynamically fluctuate by the various and singular interactions of each molecule. In this description, ω_{ab} is time-dependent and the absorption spectrum can be described as:

$$A(\omega) \propto \mathrm{Re} \int_0^\infty dt\ e^{-i\omega t} e^{i \int_0^t d\tau\ \omega_{ab}(\tau)} \tag{2-37}$$

$\omega_{ab}(t)$ can be conveniently formulated as the sum of the time-independent average frequency $\bar{\omega}_{ab}$ and a time-dependent deviation $\delta\omega_{ab}(t)$, $\omega_{ab}(t) = \bar{\omega}_{ab} + \delta\omega_{ab}(t)$:

$$A(\omega) \propto \mathrm{Re} \int_0^\infty dt\ e^{-i\omega t} e^{i\bar{\omega}_{ab} t} e^{i \int_0^t d\tau\ \delta\omega_{ab}(\tau)} \tag{2-38}$$

Now $\delta\omega_{ab}(\tau)$ can be substituted with a power-series expansion, also called cummulant expansion [15], which is a mathematical tool that helps to solve the integral $e^{i \int_0^t d\tau\ \delta\omega_{ab}(\tau)}$. Finally, after suitable approximations, we can re-write the absorption spectrum as:

$$A(\omega) \propto \mathrm{Re} \int_0^\infty dt\ e^{-i\omega t} e^{i\bar{\omega}_{ab} t} e^{-g(t)} \tag{2-39}$$

where $g(t)$ represents the spectral lineshape which is, by definition, the correlation function of $\delta\omega$:

$$g(t) = \int_0^t \int_0^{\tau'} d\tau' d\tau'' \langle \delta\omega(\tau'')\delta\omega(0) \rangle \tag{2-40}$$

The simplest approach to write explicitly $g(t)$ consists in modelling the correlation function $\langle \delta\omega(t)\delta\omega(0) \rangle$ as an exponential function:

$$\langle \delta\omega(t)\delta\omega(0) \rangle = \Delta^2 e^{-\frac{t}{\tau_c}} \tag{2-41}$$

where Δ is the amplitude of the fluctuations, namely the displacement $\delta\omega$ from $\bar{\omega}_{ab}$, and τ_c is a time constant describing the correlation time. Integrating the correlation function, $g(t)$, twice we obtain Kubo-lineshape function [19,20]:

$$g(t) = \Delta^2 \tau_c^2 \left[e^{-\frac{t}{\tau_c}} + \frac{t}{\tau_c} - 1 \right] \tag{2-42}$$

The function described in Eq. (2-42) is well suited for all the possible broadening mechanisms. For example, a situation where the correlation time τ_c is long with respect to molecular relaxation timescales, describes well the static or inhomogeneous broadening, i.e. when different molecules have different resonance frequency due to their different surroundings but they do not fluctuate. In that case, we get for the lineshape function:

$$g(t) = \frac{\Delta^2 t^2}{2} \tag{2-43}$$

and the resulting absorption spectrum can be written as:

$$A(\omega) \propto \mathrm{Re} \int_0^\infty dt \; e^{-i\omega t} e^{i\bar{\omega}_{ab} t} e^{-\frac{\Delta^2 t^2}{2}} \tag{2-44}$$

which is a Gaussian function centred in $\bar{\omega}_{ab}$ and spectral width equal to Δ. In other words, the absorption spectrum describes the energy distribution of the molecules of the ensemble. This limit is represented by purple and red lines in Figure 2.4.
On the other hand, when the correlation time is short, it follows that fluctuations in frequency and phase are rapid, e.g. a molecule can suddenly change its instantaneous frequency in the entire range Δ. That is the case of dynamic or homogeneous broadening, for which we can write the lineshape function as:

$$g(t) = \Delta^2 \tau_c t = \frac{t}{T_2} = \Gamma t \tag{2-45}$$

where $\Delta^2 \tau_c = \frac{1}{T_2} = \Gamma$ is the decay constant of the exponential function that describes the damping of the oscillation between state *a* and *b*. The resulting absorption spectrum is:

$$A(\omega) \propto \mathrm{Re} \int_0^\infty dt \; e^{-i\omega t} e^{i\bar{\omega}_{ab} t} e^{-\Gamma t} = \frac{2\Gamma}{(\omega - \bar{\omega}_{ab}) + \Gamma^2} \tag{2-46}$$

which is a Lorentzian function centred at frequency $\bar{\omega}_{ab}$. The decay constant Γ includes the contributions of both the decaying constant of the excited state (T_1) and the pure dephasing time ($T_2{}^*$):

$$\Gamma = \frac{1}{T_2} = \frac{1}{2T_1} + \frac{1}{T_2{}^*} \tag{2-47}$$

The first term in Eq. (2-47) accounts for the loss of coherence due to loss of population in the excited state, while the second accounts for to the randomization of the

phases of the oscillations ω_{ab}. This limit is represented by light and dark blue lines in Figure 2.4.
More generally, every system can lie between the two limits described above where, over a sufficiently long time, any molecule will sample all the configurations available. We expect that every molecule has a different instantaneous frequency which evolves in time due to the interactions with the surrounding system. Such process is called spectral diffusion. The fluctuations of ω_{ab} within the range Δ have times typically longer than the oscillation period, but their frequency is not fixed as in the case of inhomogeneous limit. The resulting spectral shape is a Voigt profile which is the convolution of a Lorentz with a Gaussian function.
The treatment outlined above for the description of linear signals can be generalized for higher-order signals and the line shape function $g(t)$ can be used for the calculation of the response function of any order of polarization. As an example, we report the case of R_2 Feynman pathway, which is one of the terms contributing to the total third-order response function.

$$\begin{aligned} R_2(t_1,t_2,t_3) &= \left(\frac{i}{\hbar}\right)^{-3} \mathrm{Tr}[\mu_I(t_3+t_2+t_1)\mu_I(t_1)\rho(-\infty)\mu_I(0)\mu_I(t_2+t_1)] \\ &= \mu_I^4 e^{-i\omega(t_3-t_1)} e^{-g(t_1)+g(t_2)-g(t_3)-g(t_1+t_2)-g(t_2+t_3)+g(t_1+t_2+t_3)} \end{aligned} \tag{2-48}$$

Other theoretical models can describe $g(t)$ in different ways to account, for example, for the temperature dependence of the spectral lineshape. In Brownian oscillator model, the phenomenological amplitude Δ of the fluctuations is replaced by a more meaningful displacement on the nuclear potential surface induced by the temperature. Further models include also spectral density of the solvent or quantum coupling with the vibrational modes.

2.7. Third-order polarization and 2DES signal

As previously suggested, third-order polarization represents the most informative macroscopic observable to study the dynamics of the excited states. As described in Eq. (2-23), there is a direct relation between the macroscopic polarization and the time-dependent density operator. Here we report a pictorial description that follows step-by-step the temporal evolution of the density matrix when the system interacts with three external electric fields in the typical configuration used in 2D electronic spectroscopy (2DES).
Let's consider a three-level system with ground state g, and two excited states e and f that can be both excited by the incoming electric fields Figure 2.5(a). We assume that, in equilibrium conditions, namely before the interaction with the first laser pulse, only state g is populated. It follows that the only non-zero element within the density matrix is: $\rho_{gg} = 1$, as described in Figure 2.5(c).

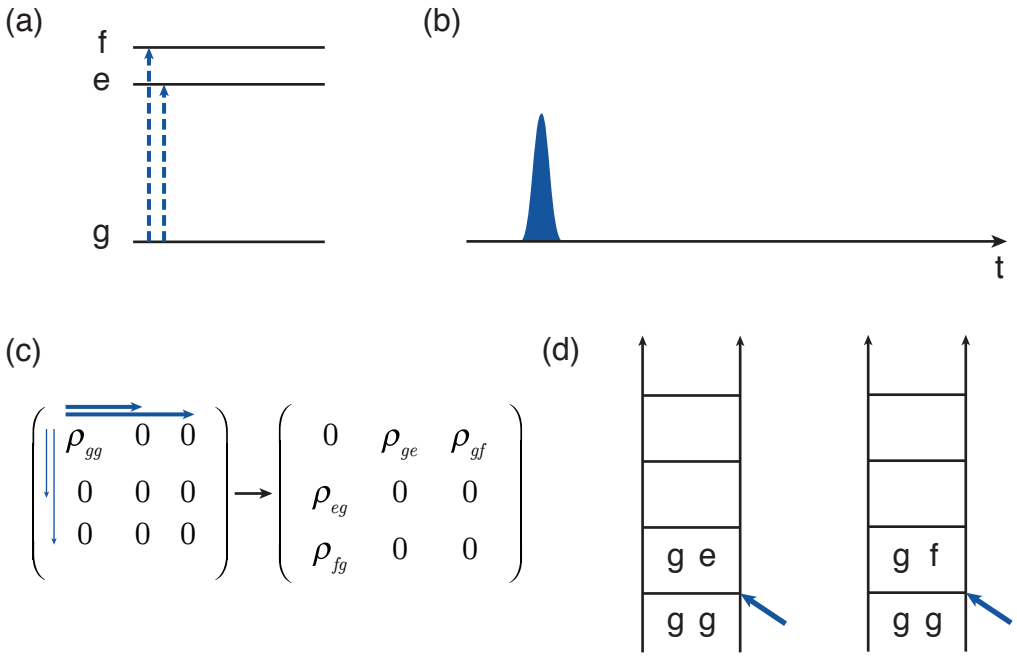

Figure 2.5 (a) Energy level scheme describing the first interaction with the electric field. Dashed lines represent the interaction with the bra of the density operator, i.e. the right arrow in Feynman diagram (d). (b) Time-line of the experiment when only the first pulse has reached the sample. (c) Time evolution of the density matrix after the first interaction, where bold lines represent R_2 pathways.

When the first pulse reaches the sample, it creates coherent superpositions of the ground state with each of the two excited states. In the density matrix picture, it promotes the migration of the population ρ_{gg} towards off-diagonal elements ρ_{ge}, ρ_{gf}, ρ_{eg} and ρ_{fg}. Figure 2.5(c) schematically describes this process, while the corresponding Feynman diagrams are represented in Figure 2.5(d). The interactions of the external field with ket (namely the left side of Feynman diagram) are omitted. In the following Figures, for convenience, we will build Feynman pathways leading to R_2 term of response function, representing the SE pathway of the rephasing signal.

Once $|g\rangle\langle e|$ and $|g\rangle\langle f|$ coherences are generated, they are subjected to dephasing processes during time interval t_1, as described in Section 2.6. Electronic coherences typically dephase quickly at room temperature. Thus, the second laser pulse must reach the sample before the coherences between the ground and one of the excited states has dephased. The second interaction can act either on the bra or on the ket of density matrix, but in the specific case of R_2 pathway, it acts from the left. Let's suppose that in both the pathways that we are following, the second pulse promotes the ket from g to f state (Figure 2.6(a)). In the first Feynman diagram described in Figure 2.6(d), a coherence of two excited state $|e\rangle\langle f|$ is produced. That coherence

represents a contribution to the total signal that retains a damped oscillating behaviour in t_2 with frequency proportional to the energy gap between the two states e and f. In the second Feynman diagram, a pure state $|f\rangle\langle f|$ (also called population) evolves in time interval t_2. In other words, after the second perturbation of the electric field, the system reaches a population or a coherence between the excited states evolving in t_2.

Other Feynman pathways than the two shown in Figure 2.6 are possible. For example, when the dipole operator interacts with the bra, it returns to the ground state and thus the population $|g\rangle\langle g|$ evolves in t_2.

When also the third pulse reaches the sample, a coherence between the ground and the excited states rises again. In the example reported in Figure 2.7, the third pulse brings the bra to the ground state, thus generating coherence in both cases. It will then dephase in time t_3 by emitting an electric field that represents the spectroscopic signal.

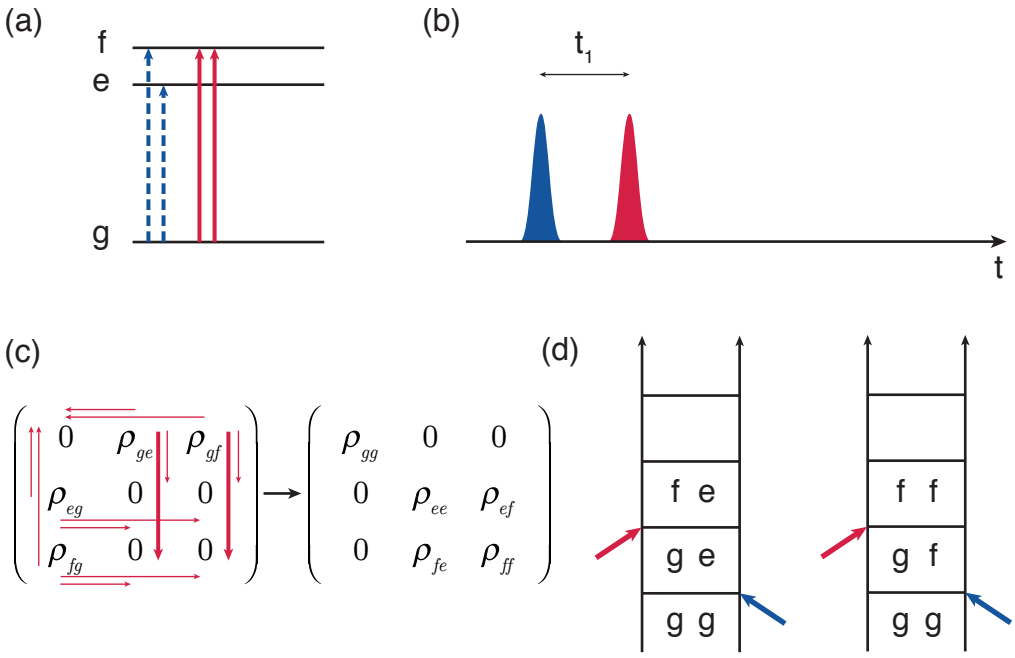

Figure 2.6 (a) Energy level scheme describing the second interaction with the electric field. Solid lines represent the interaction with the ket of the density operator, i.e. the left arrow in Feynman diagram (d). (b) Time-line of the experiment when also the second pulse has reached the sample. (c) Time evolution of the density matrix after the second interaction, where bold lines represent R_2 pathways.

If we postulate the existence of a fourth state of the system, h, having approximately twice the energy of states e and f, the third pulse could produce coherence $|h\rangle\langle e|$ or $|h\rangle\langle f|$ interacting with the ket of the density operator. Such coherences oscillate with frequency close to the energy of the exciting pulses and belong to excited state absorption pathways.

Finally, the component of the overall signal corresponding to R_2 Feynman pathway is emitted in phase matching direction $\boldsymbol{k}_s = -\boldsymbol{k}_1 + \boldsymbol{k}_2 + \boldsymbol{k}_3$ of the rephasing signal. As anticipated in Section 2.5, other Feynman pathways can produce a signal which is emitted in the same phase matching direction, such as GSB (R_3) and ESA pathways.

The overall signal, S_T, is recorded as function of time delays between exciting laser pulses, t_1, t_2 and t_3, but usually it is discussed in terms of 2D frequency maps. The most popular choice to visualize S_T consists, indeed, in taking the Fourier transform of t_1 and t_3 delay times:

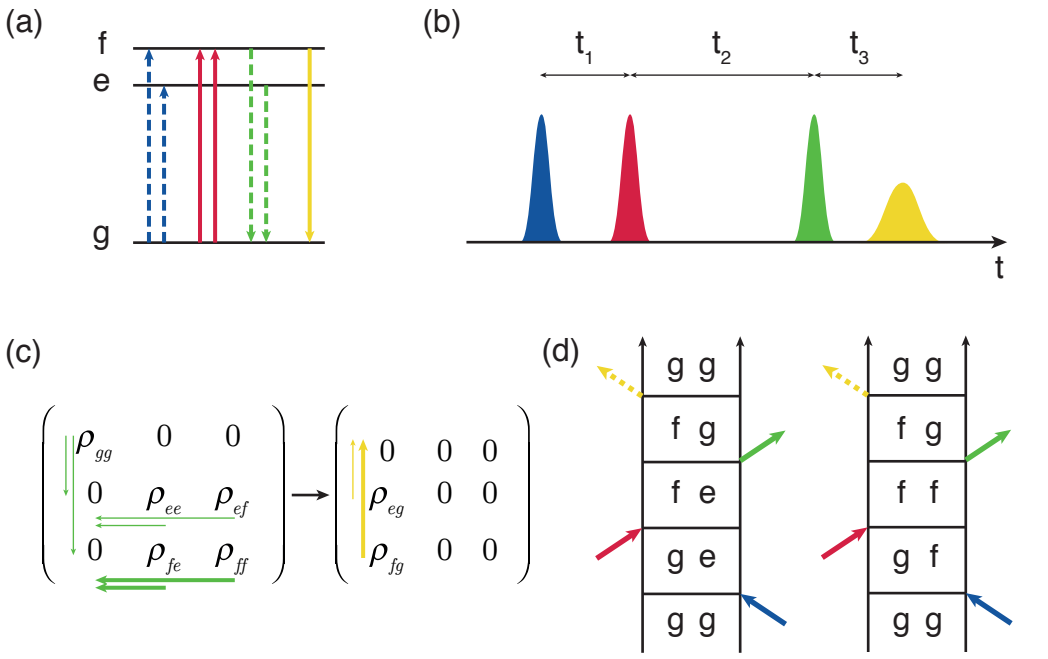

Figure 2.7 (a) Energy level scheme describing the third interaction with the electric field. Solid and dashed lines represent the interaction with the ket and bra of the density operator, i.e. the right and the left arrow in Feynman diagram (d), respectively. (b) Time-line of the experiment when also the third pulse has reached the sample and the signal is emitted. (c) Time evolution of the density matrix after the third interaction, where bold lines represent R_2 pathways.

$$S_T(t_1, t_2, t_3) \rightarrow S_T(\omega_1, t_2, \omega_3) \tag{2-49}$$

where ω_1 and ω_3 are Fourier transform of t_1 and t_3, respectively.
As previously reported, within t_1 and t_3 time intervals the nonzero elements of density matrix represent coherences between the ground and the excited state. The transformation described in Eq. (2-49) correlates the intensity of these oscillating signals with their frequency. It follows that, for a fixed t_2 time value, we can build a two-dimensional intensity map, bearing ω_1 (also called excitation frequency) and ω_3 (emission frequency) as x- and y-axis, respectively.
2D electronic spectra consist in visual maps that correlate the electronic energy before the second field interaction and after the third perturbation, namely before and after delay time t_2, during which dynamics of the excited state occurs. Since the temporal evolution of the system is spread into two dimensions, the spectral resolution is enhanced and, for example, the energy of donor and acceptor counterparts in energy transfer processes are directly revealed by excitation and emission frequency, respectively.
The only time variable we have kept is the so-called population time (t_2), thus we can follow the excited state dynamics looking at the time-evolution of the intensity of the peaks in the 2D maps along t_2.
An example of rephasing 2DES map, related to the system described above, is shown in Figure 2.8. SE and GSB signals appear as positive peaks, while ESA pathways result as negative contributions. In particular, cross-peaks pinpoint coupling between states e and f resulting from SE schemes. The peaks shape gives important information about the inhomogeneous broadening along diagonal, and the homogeneous broadening along the orthogonal direction.
Following the evolution of 2DES map in t_2 we can detect the distinct temporal behaviour of the various components. When, after the first two interactions, the system is placed into a population, ($|e\rangle\langle e|$ or $|f\rangle\langle f|$), the resulting signal will decay in t_2 following the dynamical properties of the excited state e or f. If, on the contrary, the system reaches a coherence state, ($|e\rangle\langle f|$ or $|f\rangle\langle e|$), it will generate damped oscillating signals in t_2 that can be detected at cross-peaks positions at coordinates (ω_e, ω_f) and (ω_f, ω_e) onto the 2DES map. The frequency of these beatings $(\omega_f - \omega_e)$ is proportional to the energy gap between the two excited states, and their damping time, Γ, is related to the pure dephasing time $T_2{}^*$ of the coherence and to the decaying constants of both the excited states e and f ($T_{1,e}$ and $T_{1,f}$, respectively):

$$\Gamma = \frac{1}{T_2} = \frac{1}{2}\left(\frac{1}{T_{1,e}} + \frac{1}{T_{1,f}}\right) + \frac{1}{T_2{}^*} \tag{2-50}$$

An extensive explanation of the importance and behaviour of coherent signals appearing in 2DES datasets is reported in the next Section.

2.7.1. Vibrational vs electronic coherences

Rephasing and non rephasing spectra are capable of resolving quantum correlations that appear as beatings of specific peaks in the 2DES spectrum in t_2 delay time. However, the underlying pathways originating these signals are often ambiguous. In early publications [5,21,22] these beatings were assigned to coherences being responsible for ultrafast and extremely efficient coherent quantum transport. In principle, all the states that can be simultaneously excited by the first two incoming pulses can result in a coherence that produce an oscillating signal. When the exciting laser pulses have spectral bandwidth of thousands of wavenumbers, also superpositions of electronic states can indeed be generated.
In molecules and aggregates, electronic transitions are often coupled to several inter- or intra-molecular vibrational modes, whose energy typically ranges from 100 to 3000 cm^{-1} and, in particular, vibrations around 1400 cm^{-1}, due to C=C stretching, are often strongly coupled to electronic transitions [18].

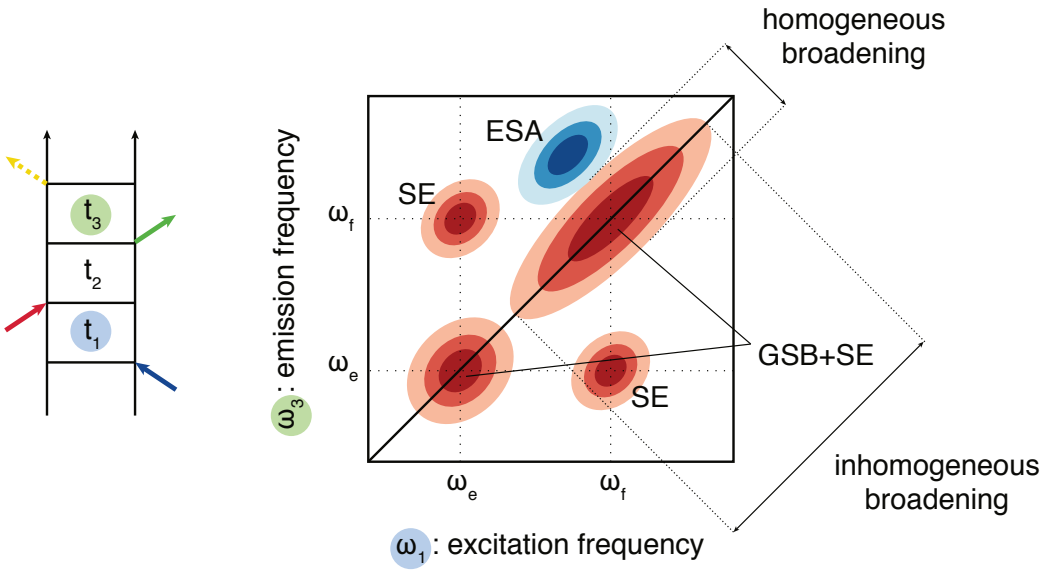

Figure 2.8 Typical structure of 2D frequency/frequency electronic spectrum, where ω_1 and ω_3 are Fourier transform of time intervals t_1 and t_3, respectively. The dependence of the spectroscopic signal on ω_1 and ω_3 is conveniently visualized in the 2D map, where ω_1 and ω_3 are taken as x and y axis, respectively. The signal appears in the map as positive (GSB and SE) or negative (ESA) peaks. Coordinates of peaks are related to the energies of the states involved in Feynman pathways contributing to the overall signal, in this case excited states e and f. The shape of peaks can reveal and distinguish homogeneous and inhomogeneous broadening. Crosspeaks reveal the presence of coupling between states e and f.

Moreover, the magnitude of excitonic coupling, J, in excitonic aggregates usually lies in the same energy range of vibrational modes. It follows that vibronic and excitonic systems have several spectroscopic analogies, that often complicate the interpretation of coherent beating in 2DES.
The possibility of distinguishing vibrational from electronic coherences is crucial within the interpretation of the complex pattern of oscillations belonging to the spectroscopic signal. A careful analysis of the different Feynman pathways contributing in the two distinct cases will help to identify diagnostic pattern of signals for vibronic and excitonic systems.
We consider two distinct model systems, as examples of the two situations described above. The simplest model of a vibronic system is represented by two electronic states, g and e (ground and excited state, respectively), each one coupled to a one-dimensional vibrational nuclear coordinate q with frequency Ω. This model will henceforth be named as displaced harmonic oscillator (DHO). The second model system consists of two-level molecules with same electronic properties and no coupled vibrations that are excitonically interacting with resonance coupling J (homodimer). The resulting system, called exciton dimer (ED), has new eigenstates, α and β, whose energy difference is proportional to $2J$ [23].
For the first model, well described by Turner *et al.* [24], in Figure 2.9 Feynman pathways resulting in an oscillating signal in t_2 are listed, both for rephasing and non-rephasing experiment. In this examples we are accounting only for GSB and SE pathways, discarding ESA contributions, even though they could be relevant if electronic states at higher energy are present. The specific position on the 2DES map where a certain pathway contributes is pinpointed with a coloured dot, recalling the colour of the corresponding Feynman diagram. The distribution of these signals in rephasing spectrum recall the features of a chair and, for this reason, it will be referenced as '*chair* pattern'. In non rephasing spectrum, instead, the distribution is flipped upside-down. Indeed, in rephasing spectrum the signal occurring at coordinates $(\varepsilon + \Omega, \varepsilon - \Omega)$ has oscillating character, while at $(\varepsilon + \Omega, \varepsilon + \Omega)$ it has not. The opposite happens in non rephasing spectrum. Generalizing the model to the case where several vibrational modes are coupled to the electronic transition, many other beatings with frequency Ω_i contribute to the overall signal at specific coordinates determined by $\varepsilon \pm n\Omega_i$ ($n = 0,1,2$). Moreover, this model is not accounting for the case in which the vibrations at the electronic ground state are populated before the first perturbation. For vibrational modes with energy higher than $k_B T$ (~250 cm^{-1} at room temperature this assumption is always valid, however, for low frequency vibrations, further Feynman pathways must be considered. They indeed set as starting point non-zero elements such as $|g_1\rangle\langle g_1|$, giving rise to oscillating signals at the coordinate $\varepsilon - \Omega$ along the excitation frequency.

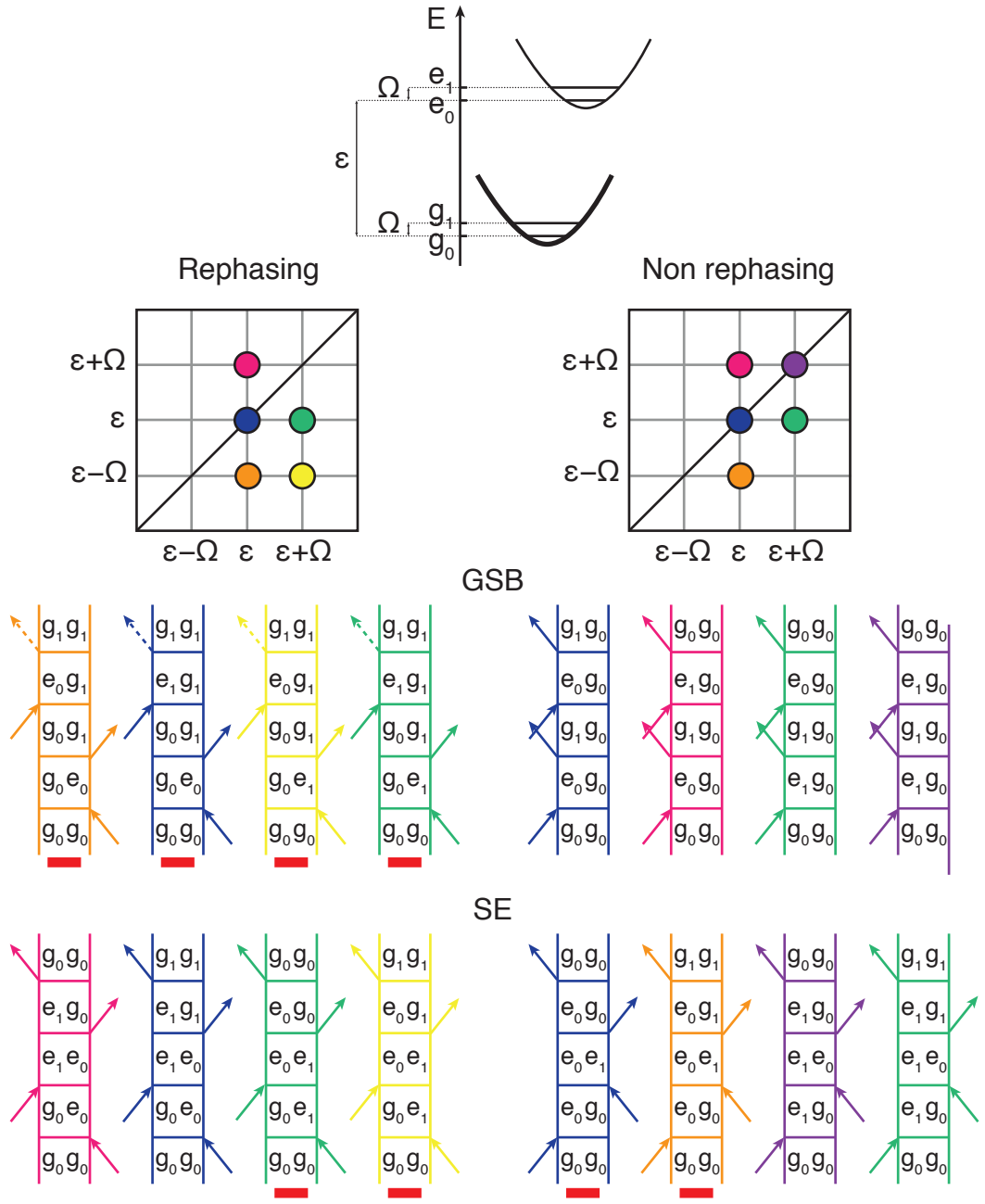

Figure 2.9 The positions in rephasing (left) and non-rephasing (right) maps of the oscillating vibrational coherences represented by the correspondent GSB and SE Feynman paths. The vibration is coupled equally with both the ground and the excited states as shown by the schematic model. Red lines pinpoint Feynman pathways leading to vibrational coherences having positive oscillation frequency.

ED model, instead, describes the behaviour of a homodimer, but it can be applied to any pair of coupled electronic states that can be simultaneously excited by the laser spectrum. Within this model, the oscillating signals are generated by coherent superpositions of excitonic (or electronic) states and the number of possible contributions is drastically reduced if compared to the previous model.
In both rephasing and non rephasing spectra only two Feynman pathways produce signals oscillating with frequency $|\varepsilon_\alpha - \varepsilon_\beta|$, where ε_α and ε_β are, respectively, the frequency of α and β exciton transitions. These beatings appear at cross-peaks $(\varepsilon_\alpha, \varepsilon_\beta)$ and $(\varepsilon_\beta, \varepsilon_\alpha)$ in the rephasing experiment and on the diagonal positions $(\varepsilon_\alpha, \varepsilon_\alpha)$ and $(\varepsilon_\beta, \varepsilon_\beta)$. No further contributions are predicted by the model and, thus, this pattern is considered a fundamental hint to recognize electronic coherences and distinguish them from vibrational ones.
The dephasing time of electronic coherences is strongly dependent on the temperature. At room temperature they typically last for tens of femtoseconds [25,26], depending on the linewidth of the transitions and thus on the coupling with environment and vibrations. On the other hand, vibrational coherences last longer than electronic coherences and they can survive also for several picoseconds. Vibrational wavefunctions and energies are, indeed, much less influenced than the electronic counterpart by inhomogeneity and fluctuations.

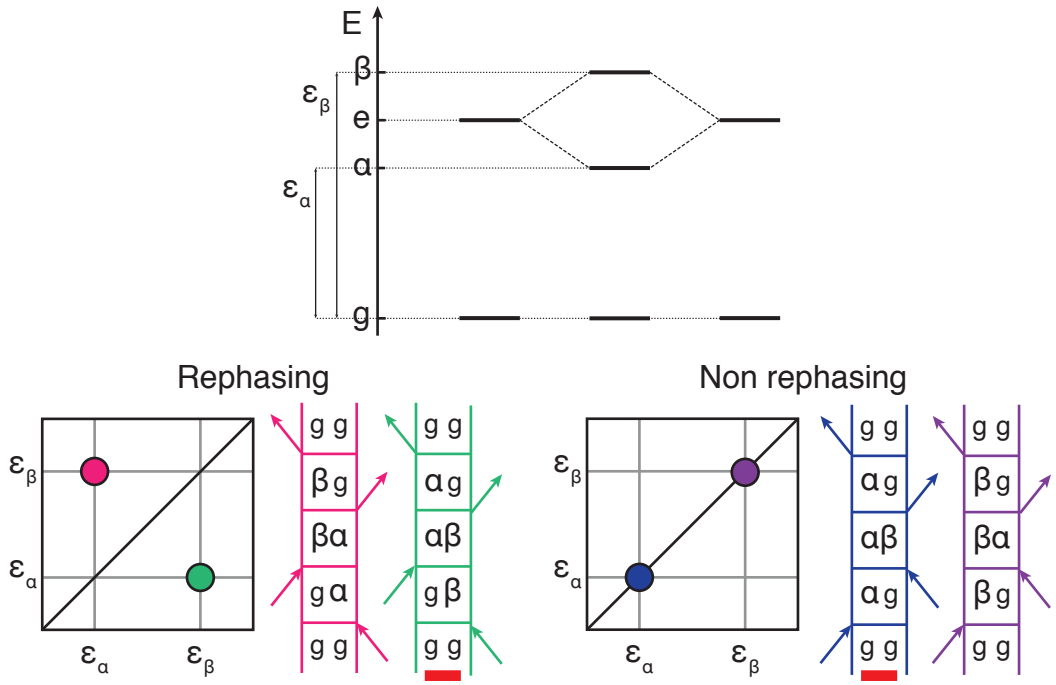

Figure 2.10 The positions in rephasing (left) and non-rephasing (right) maps of the oscillating electronic coherences represented by SE Feynman paths. The model used is a homodymer system (see Section 1.5). Red lines pinpoint Feynman pathways leading to electronic coherences having positive oscillation frequency.

The two models described above are two limit cases, but in real systems we can often deal with intermediate cases, where vibrational and excitonic transitions are coupled. The corresponding Feynman pathways produce oscillating signal resulting in spectral schemes that are intermediate between what described in Figure 2.9 and Figure 2.10. Indeed, recent theoretical models has demonstrated that the coupling between vibrational modes and electronic transitions may explain the outstanding long-living character of peculiar kinds of coherences experimentally detected [11,27–31].

2.8. Chirality

In our analysis of how an electromagnetic radiation field interacts with the molecular system, we have, to this point, considered only the perturbation induced by the oscillating electric field, $E(t)$ on the system dipole operator $\hat{\mu}$. In addition to the optical properties related to the dipole moment treated so far, there are other minor effects that are actually more sensitive to the excited state properties.

For example, coupled interactions involving both the electric $E(t)$ and magnetic $B(t)$ component of the exciting field can cause the dipole strength of a transition to be different for left- and right-circularly polarized light. This is the definition of circular dichroism (CD). This effect is orders of magnitude less intense if compared with the dipole interaction but it can be very informative of the system.

The Hamiltonian operator accounting for light-molecule interaction described in Eq. (2-27) must be re-written to include the time-dependent perturbation induced also by the magnetic field:

$$H_{int}(t) = -\hat{\mu}E(t) - \widehat{m}B(t) \tag{2-51}$$

where $\widehat{m}$ is the magnetic dipole operator, given by:

$$\widehat{m} = \frac{e}{2m_e c}(r \times \hat{p} + g_e S) \tag{2-52}$$

where e and m_e are the electron charge and the electron mass, respectively, c is the speed of light, r is the position of the electron, $\hat{p}$ is the linear momentum operator, g_e is the electronic g-factor (2.00232) and S is the angular momentum associated with the electron spin [18].

CD spectroscopy measures the experimental observable, $\Delta\varepsilon$ (namely the difference between molar extinction coefficients of left- and right- circularly polarized light), which is related to the rotational strength $\mathfrak{R}_{eg}$ of the transition between electronic states e and g:

$$\mathfrak{R}_{eg} \approx \frac{3000 ln(10) hc}{32\pi^3 N_A}\left(\frac{n}{f^2}\right)\int \frac{\Delta\varepsilon(\nu)}{\nu} d\nu \tag{2-53}$$

where h is Planck constant, N_A is Avogadro's number, n the refractive index, f the local field correction, and ν the frequency. For historical reasons, circular dichroism is often described in terms of the molar ellipticity, $[\Theta]$, in the arcane units of '100 degrees centimeters squared per decimole', where the angular units reflect the fact that plane-polarized light passing through an optically active sample emerges with elliptical polarization.

From a theoretical point of view, $\mathfrak{R}_{eg}$ is described by the Rosenfeld equation as [32]:

$$\mathfrak{R}_{eg} = -\mathrm{Im}\langle e|\widehat{m}|g\rangle \cdot \langle e|\hat{\mu}|g\rangle = -\mathrm{Im}(m_{eg} \cdot \mu_{eg}) \tag{2-54}$$

Thus, the rotational strength equals zero when electric and magnetic transition dipole moments are orthogonal, which is the case for non-chiral molecules. For example, in a typical planar molecule the electric dipole moment lays on the molecular plane, while the magnetic dipole moment results orthogonal to the electric one. In this case the molecule is non-chiral, the rotational strength is zero and no difference is recorded after the interaction with left- or right- circularly polarized light. However, if the molecule or the molecular assembly is chiral, this relation is not fulfilled anymore.

A detailed description of the interaction in Eq. (2-54) within molecules bearing intrinsic chirality goes beyond the purposes of this work, however a comprehensive treatment can be found in ref. [33]. Instead, we will focus the attention on how CD signal can arise from interactions between distinct chromophores that do not have intrinsic chirality.

When two or more molecules are in close proximity and their dipole moments are not orthogonal, the optical properties of the whole system cannot be simply described by the sum of the properties of the single units [18]. Let's consider the model of two identical interacting chromophores, namely the excitonic homodimer already cited in previous Sections. It represents the simplest model to describe excitonic interactions, and it is the basis for the treatment of excitation migration within more complex multichromophoric systems, that will be investigated in the experimental Chapters.

The interaction between the two identical two-level molecules generates excitonic states that can be expressed as linear combination of electronic states of the monomers. If each isolated monomer bears electronic states g and e, the resulting dimer will be described by excitonic states α and β generated by the excitonic interaction (Figure 2.11(a)) [18].

For the peculiar case of the exciton homodimer, the rotational strength includes three terms [18]:

$$\mathfrak{R}_{mon} = -\left(\frac{1}{2}\right)\mathrm{Im}(m'_{eg(1)} \cdot \mu_{eg(1)} + m'_{eg(2)} \cdot \mu_{eg(2)}) \tag{2-55}$$

$$\mathfrak{R}_{e-m} = \pm\left(\frac{1}{2}\right)\mathrm{Im}(m'_{eg(1)} \cdot \mu_{eg(2)} + m'_{eg(2)} \cdot \mu_{eg(1)}) \tag{2-56}$$

$$\mathfrak{R}_{ex} = \pm\left(\frac{\pi}{2\lambda_{eg}}\right)(R_2 - R_1) \cdot (\mu_{eg(2)} \times \mu_{eg(1)}) \tag{2-57}$$

where $m'_{eg(n)}$ is an intrinsic property of the monomer n and does not depend on where the molecule is located within the oligomer, λ_{eg} is the wavelength of the optical transition of the monomer and $(R_2 - R_1)$ is the distance between the two interacting molecules.

$\mathfrak{R}_{mon}$ represents the sum of the intrinsic rotational strength of the two isolated monomers, also called *one-electron* contribution. $\mathfrak{R}_{e-m}$ accounts for the coupling of the electric transition dipole moment of one molecule and the magnetic transition dipole moment of the other (*electric-magnetic coupling*).

Finally, the last term, $\mathfrak{R}_{ex}$, also called *coupled-oscillator* term, depends on the two electric dipole moments and on their mutual orientation. This term dominates over $\mathfrak{R}_{mon}$ and $\mathfrak{R}_{e-m}$, since it depends only on the electric transition dipole moments that are, as anticipated, far more intense than the magnetic counterparts. Eq. (2-57) can be rewritten as:

$$\mathfrak{R}_{ex} = \pm\left(\frac{\pi}{2\lambda_{eg}}\right)|R_{21}| \cdot D_{eg} sin\theta cos\varphi \tag{2-58}$$

where $|R_{21}|$ is the distance between centers of the two molecules, D_{eg} is the dipole strength of the monomer, θ the angle between $\mu_{eg(1)}$ and $\mu_{eg(2)}$, and φ the angle between R_{21} and the cross product of the two electric dipole moments. This term generates two bands of opposite sign in the CD spectrum, centred on the energy of the excitonic states. Figure 2.11(b) shows the comparison between the absorption spectrum of the monomer, and the absorption and CD spectrum of the dimer. Excitonic coupling is undoubtedly recognizable in the latter, while the absorption spectrum of the dimer shows only a slight broadening if compared with the monomer.

Eq. (2-58) shows that CD spectrum, not only provides information on the exciton coupling, but also on dipole strength, on the distance between the molecules and, especially, on the mutual orientations of the electric transition dipole moments. All these properties are useful and necessary to determine the geometry and the conformation of the multichromophoric system. In the following Chapters we will make extensive use of CD spectra to identify the energy of the different excitonic transitions involved in the nonlinear response of multichromophoric systems, not always easily identifiable only basing on the absorption spectra.

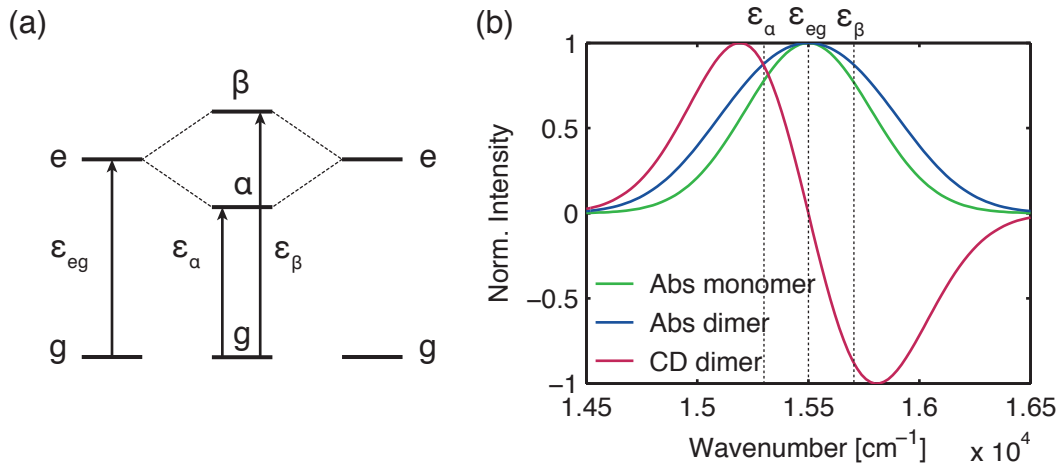

Figure 2.11 (a) Energy level diagram of a homodimer, taken as model for excitonic interaction. (b) Simulated absorption (blue line) and circular dichroism (red line) spectra of the model system compared to the absorption spectrum (green line) of the monomeric unit ($J = 200$ cm^{-1}, $\lambda_{eg} = 645$ nm, FWHM $= 650$ cm^{-1}).

3 Experimental techniques

3.1. Standard spectroscopic methods

As described in the previous Chapter, the aim of spectroscopy is to discover the properties of a selected material or molecule through their response when perturbed by electromagnetic radiation.
The investigation of each optical property requires an appropriate optical setup. Absorption spectroscopy, as well as emission and circular dichroism spectroscopies, are nowadays based on standard and commercial instrumentation. In contrast, advanced ultrafast spectroscopies, such as 2DES, need specific homemade setups.

3.1.1. Linear absorption and emission

The most common and frequently used optical spectroscopy is the steady-state absorption spectroscopy, which is a linear technique that measures the intensity of light absorbed by a sample. It scans a range of wavelengths, selected by a monochromator, providing for each one the absorbance, defined as minus the logarithm of the ratio between the intensity of the light before and after the sample [18]:

$$A(\omega) = -log\left(\frac{I(\omega)}{I_0(\omega)}\right) = \varepsilon(\omega)lC \tag{3-1}$$

where I and I_0 are the intensity of light detected after and before the sample. The absorbance is linearly related to the optical path l and the concentration of the sample C through the molecular extinction coefficient $\varepsilon(\omega)$. Absorption spectroscopy is useful for identifying the nature of the samples, determining at which wavelengths they absorb and to have a control on sample concentration. In our laboratories, linear absorption measurements are performed with a Varian Cary 5 spectrometer.
A second conventional technique is fluorescence spectroscopy that detects the intensity of light emitted by a sample after excitation. Both fluorescence emission and excitation spectra can be measured with the same spectrometer. In the former case, the excitation wavelength is fixed, while wavelengths of the emitted radiation are scanned. In the latter case, instead, the excitation wavelengths are scanned, while

the fluorescence is recorded at fixed emission wavelength. This spectroscopy is useful to study, for example, excited states emission and energy transfer yield. Furthermore, in some cases it can replace absorption spectroscopy when more sensitivity is necessary. The instrument used in the works reported in the following Chapters, FluoroMax 3 spectrometer (Horiba, Jobin Yvon), can also be coupled to a cryostat to perform low-temperature measurements (77 K).

3.1.2. Time-resolved fluorescence

Investigation of electronic excited state may require the measurement of the fluorescence lifetime by following the decay of the fluorescence intensity after the excitation of the sample. The excitation within this experiment is provided by a pulsed light source, such as a laser or a pulsed nanoled, and the intensity of the fluorescence as a function of time is followed with an ultrafast photodiode. One of the most diffuse and informative methods to measure fluorescence lifetimes is based on time-correlated single photon counting technology (TCSPC) [34–37]. In our laboratories, two TCSPC setups are available, with two different time resolutions. The first is an optional configuration of FluoroMax 3, where excitation lamp and detector are replaced by a pulsed nanoled source and a single-photon detector, respectively. This apparatus has a resolution of about 1.5 ns and can measure decays up to milliseconds time range. In the second setup, instead, the sample is excited by a frequency-doubled femtosecond Ti:Sapphire laser (exciting source within the range 370-490 nm) and the detection is performed through an avalanche photodiode. In this case a time resolution of about 150 ps can be achieved but only 12.5 ns after photoexcitation can be investigated.

3.1.3. Circular dichroism

In a circular dichroism (CD) measure, the light of a lamp is alternately prepared to be left- and right- circularly polarized by means of a Pockels cell. This modulation is made at a specific frequency so that a lock-in amplifier coupled to the photomultiplier tube can detect only the differential CD effect. In our laboratories, CD spectra are measured with a Jasco J-710 spectrometer.

3.1.4. Raman spectroscopy

Raman spectra were recorded with a home-built micro-Raman system, based on a Triax-320 ISA spectrograph. Different excitation sources are available to be able of selecting resonant and non resonant excitation conditions for the different samples: Ar^+ laser (488 and 514 nm), He-Ne laser (633 nm) and CW Ti:sapphire laser (785 nm). An Olympus BX 40 optical microscope equipped with a 20× objective is optically coupled to the spectrograph. The measurements were carried out on microcrystalline powder samples typically kept in a cryostat cell at 77K to minimize photo-degradation processes during the measure.

3.2. 2DES spectroscopy

Two-dimensional electronic spectroscopy (2DES) is a third order nonlinear technique which is successfully spreading in the latest years thanks to its capability of unravelling both the electronic and the vibrational couplings and ultrafast dynamics of the systems under investigation.

As already outlined in Chapter 2, 2DES is a four-wave mixing experiment, which involves three exciting electric fields, that stimulate a third-order response, and a strongly attenuated local oscillator (LO) that allows heterodyne detection of the signal radiated after the interaction with them.

In a typical 2DES experiment, the delay time between the first two laser pulses (called coherence time or t_1) and between the last two (called population time or t_2) are both scanned and a simultaneous spectral resolution of the time delay between the third pulse and the signal (called rephasing time or t_3) is performed by a spectrometer and a CCD (charge-coupled device) camera (Figure 3.1).

Unlike other third order techniques, the possibility of 2DES to scan independently all the three time delays allows disentangling overlapped signals and unravelling correlations between different transitions. This flexibility enables investigation of molecular systems with previously unavailable detail; for example, molecular couplings and exact energy transfer pathways can be directly followed on the energy map. Furthermore, important information lies in the time evolution of the signal at off-diagonal positions along t_2. Indeed, the possible presence of beatings in the signal amplitude as a function of t_2 is typically associated with the dynamic evolution of coherent superpositions of states.

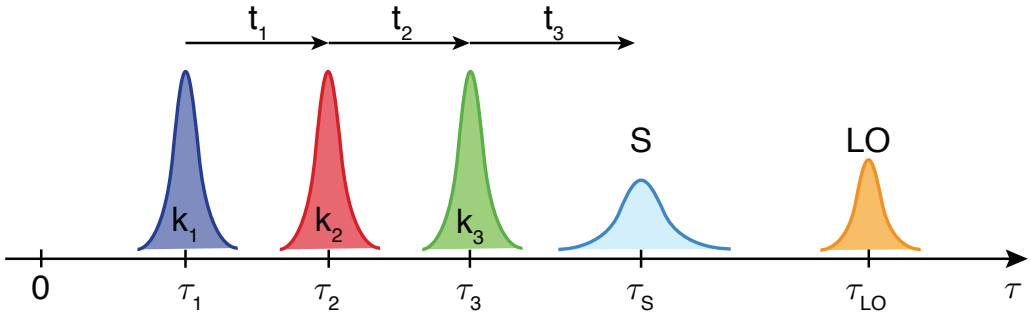

Figure 3.1 Pulse sequence used to obtain a 2DES spectrum. The time period t_1 is usually referred to as the coherence time, the second time period t_2 is known as the population time and the third time period t_3 is usually called rephasing time. The excitation frequency is obtained by Fourier transforming along the t_1 axis, while the emission frequency of 2DES maps is the Fourier transform of t_3 axis. LO is the fourth attenuated pulse used for heterodyne detecting the signal S.

The price to pay for the overwhelming advantages of this technique is the complexity of the optical setup and a few challenges in the implementation of the experiment (like, for example, isolating and detecting the third-order signal despite its weak intensity, gaining phase stability, achieving broad laser bandwidth, and phasing the absorptive spectra to correctly distinguish real and imaginary portion of the signal). The technique is still relatively young and most efforts are still being paid in the development of new technological solutions to overcome the well-known issues and to improve the quality of the data. Among the progresses accomplished so far there are, for example, interferometric 2DES experiments where phase stability is achieved through interference [38]; passive phase stabilization methods based on diffractive optic element (DOE) [39,40] or on beam splitters (BS) [41]; pulse-shaping methods combined to partially collinear beam geometry [42,43] where phase-cycling is used both to separate rephasing and non-rephasing signal and to remove scatter contributions; single-shot approaches that can acquire a 2D spectrum in a single laser shot, using tilted wavefronts to spatially create an array of delay times within the sample (GRadient-Assisted Photon Echo spectroscopy, GRAPE [44]).
Several improvements to the methods listed above have been proposed worldwide. Zigmantas *et al.* [45] built up a DOE-based setup with high signal-to-noise ratio achieved with a double modulation lock-in detection, while Heisler *et al.* [46] suggested the same methodology applied to a BS-based setup.
Cerullo *et al.* [47] proposed a pump-probe geometry setup, Translating-Wedge-Based Identical Pulses eNcoding System (TWINS), that uses couples of birefringent wedges to delay in time the pulses with high precision and great phase stability.
Fuller and co-workers [48] published a hybrid pulse-shaper-DOE method that takes high precision in timing the pulses and the simultaneous recording of rephasing and non rephasing signal from pump-probe geometry and background-free signal from DOE-based part of the setup.
The experimental scheme adopted for 2DES experiments in our laboratory is based on the scheme proposed by Hauer *et al.* [40], to which we applied several improvements both (i) to the optical hardware, to obtain a better phase stability, a more efficient noise cancelation and a more versatile setup, and (ii) to the software for the experiment control and data acquisition and analysis.
With respect to other setups presented in the literature, we could achieve a better long- and short-term phase stability [40], which is a crucial aspect to measure reliable 2DES maps and to perform long lasting experiments.
Moreover, our setup is particularly versatile since it can achieve an independent control on every time delay between pulses, making possible to switch easily from rephasing ($-k_1 + k_2 + k_3$), to non-rephasing ($+k_1 - k_2 + k_3$) to double quantum ($+k_1 + k_2 - k_3$) experiments by simply changing the time ordering of the pulses (see Section 3.2.5).

Experimental data recorded for a methanol solution of phthalocyanine are shown below to elucidate the various steps necessary to generate 2DES spectra.

3.2.1. Optical setup

The experimental setup is illustrated in Figure 3.2.

A Coherent® Libra laser system generates a continuous pulse train centred at 800 nm with a repetition rate of 3 KHz. The outcoming pulses have a bandwidth of about 12 nm and time duration of about 100 fs.

The central wavelength of laser pulses is converted in the visible range using a commercial non-collinear optical parametric amplifier (NOPA) (Light Conversion® TOPAS White).

After a preliminary stage of compression and phase shaping (see Section 3.2.2), the pulse from the NOPA is split into four identical replicas arranged in BOXCARS geometry (see inset in Figure 3.2) focusing the incoming beam into a 2D diffractive optic element (DOE) with the spherical mirror SM3.

The outgoing divergent beams are collimated and parallelized by a donut-shaped spherical mirror (DSM1), with the same focal length of the focusing mirror SM3 (500 mm).

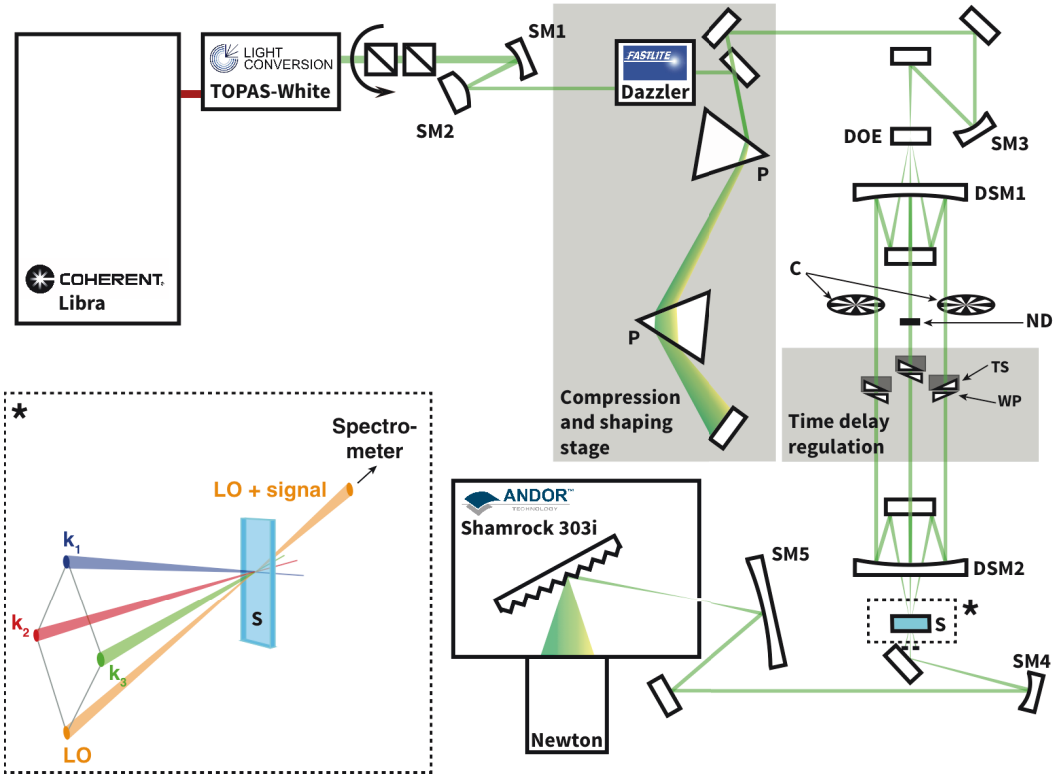

Figure 3.2 Schematic setup for recording 2DES spectra. Abbreviations: (SM) spherical mirror, (P) prism, (DOE) diffractive optical element, (DSM) donut spherical mirror, (C) chopper, (ND) neutral density filter, (WP) wedge pair, (TS) translational stage, (S) sample. Inset: schematic representation of BOXCARS geometry.

Three 4° CaF_2 wedge pairs (WP), mounted on linear stages (Aerotech® Ant 95), introduce variable delays in the excitation pulses. The position of the wedges must be accurately controlled to guarantee repeatability and precision of time delay between pulses. The choice of CaF_2 instead of the more common fused silica, is more suitable since it induces less phase distortions in broadband pulses because of higher Abbe number [49]. The 4° wedges guarantee an accurate control of time delay, with a precision of abut 0.07 fs, in a range of more than 2 ps. The fourth pulse is used as a local oscillator (LO) and its power is conveniently attenuated with a graduated neutral filter in order to maximize the heterodyne signal. The four beams are focused onto the sample by DSM2 with a focal length of 200 mm. The third order signal propagates in the LO direction and the signal-LO interference is delivered to the spectrograph (Andor® Shamrock 303i) equipped with a CCD (Charge-Coupled Device) camera (Andor® Newton).
During the 2DES experiment, the CCD camera collects other spurious contributions besides the signals. A suitable acquisition method and a post-processing procedure (see Section 3.2.7) are thus necessary to remove the unwanted contributions and gain a high signal-to-noise ratio. The signal acquisition routine is based on the double modulation lock-in method proposed by Augulis *et al.* [45] and will be discussed in detail in Section 3.2.6.

3.2.2. Compression and shaping stage

The time resolution of a 2DES experiment is directly related to pulse duration: the shorter the pulse, the better the time resolution [50]. The pulse duration is strongly correlated to its spectral bandwidth. The shortest pulse for a given bandwidth is called transform-limited (TL) pulse. When a broadband pulse passes through a transmissive optic, the different frequency components present in the pulse propagate with different speed in the medium and this lead to a chirped pulse that has longer time duration. This phenomenon occurs because in standard materials like glass or fused silica the refractive index is wavelength-dependent. Therefore, red light travels faster than the blue one when it traverses them. It has been demonstrated that chirped pulses produce artifacts in 2DES experiments [51,52] and, thus, exciting the sample with TL pulses becomes crucial.
A prism compressor and an acousto-optic programmable dispersive filter (AOPDF, Dazzler®) are used to control the phase of all the spectral components in the broadband pulses and obtain TL pulses at the sample position.
The AOPDF corrects the pulse phase distortions setting a phase correction for each frequency component. This procedure can be easily explained by considering the frequency dependence of the phase of the electric field as follows:

$$E(\omega) = S(\omega) \cdot e^{(-i\omega_0 t + \phi(\omega))} \tag{3-2}$$

where $S(\omega)$ is the spectral shape, ω_0 is the central frequency of the pulse and ϕ is the phase function. Usually $\phi(\omega)$ is conveniently described by a Taylor series defined around the value ω_0 and truncated at the forth order:

$$\begin{aligned}\phi(\omega) = \phi(\omega_0) + \left(\frac{d\phi}{d\omega}\right)_{\omega_0}(\omega-\omega_0) + \frac{1}{2}\left(\frac{d^2\phi}{d\omega^2}\right)_{\omega_0}(\omega-\omega_0)^2 \\ + \frac{1}{6}\left(\frac{d^3\phi}{d\omega^3}\right)_{\omega_0}(\omega-\omega_0)^3 + \frac{1}{24}\left(\frac{d^4\phi}{d\omega^4}\right)_{\omega_0}(\omega-\omega_0)^4\end{aligned} \tag{3-3}$$

The different orders in this expression describe different properties of the temporal profile of the pulse. The linear term is related to the arrival time of the pulse, while the second order describes the linear chirp. Higher terms correspond to phase distortions with point (even orders) or axial (odd orders) symmetry with respect to ω_0 [53]. In a TL pulse the phase shows only a linear frequency dependence, and thus terms with higher orders should not be present. The TL pulse can be recovered by estimating the coefficients of the terms in the series and then cancelling them *via* the AOPDF.

In principle, the AOPDF can impose the chosen phase at each frequency component with a resolution of about 1.5 nm. However, the device is based on the acousto-optic interaction within a crystal, which generates itself a huge positive chirp. Thus, the AOPDF is capable to compensate the self-induced chirp only at the cost of managing a narrower bandwidth. Therefore, a further chirp compensation stage is necessary when dealing with broadband pulses. To this purpose, our setup includes also a standard prism compressor [54,55] that consists of a couple of prisms made of SF11, an optical glass with very low Abbe number that guarantees a wider spectral compensation range.

The measurement of the pulse profile is performed with the frequency resolved optical gating (FROG) technique at the sample position [56] that reveals the frequency-resolved auto-correlation of the pulse. In our setup, we can take advantage of the BOXCARS geometry to perform FROG by simply replacing the sample with a non-zero third order material, typically acetone. The use of the same cuvette for the sample solution and acetone guarantees identical operating conditions, and thus pulse properties, in FROG and in 2DES measurements.

The different kinds of distortions that can be encountered in a FROG measurement are shown in Figure 3.3, which illustrates the alteration of the coefficients of the second, third and fourth order terms of the Taylor series in Eq. (3-3). To recover a TL pulse, we iteratively modify the coefficients of the different terms of Eq. (3-3) *via* the AOPDF, checking the pulse temporal length until the best conditions are found.

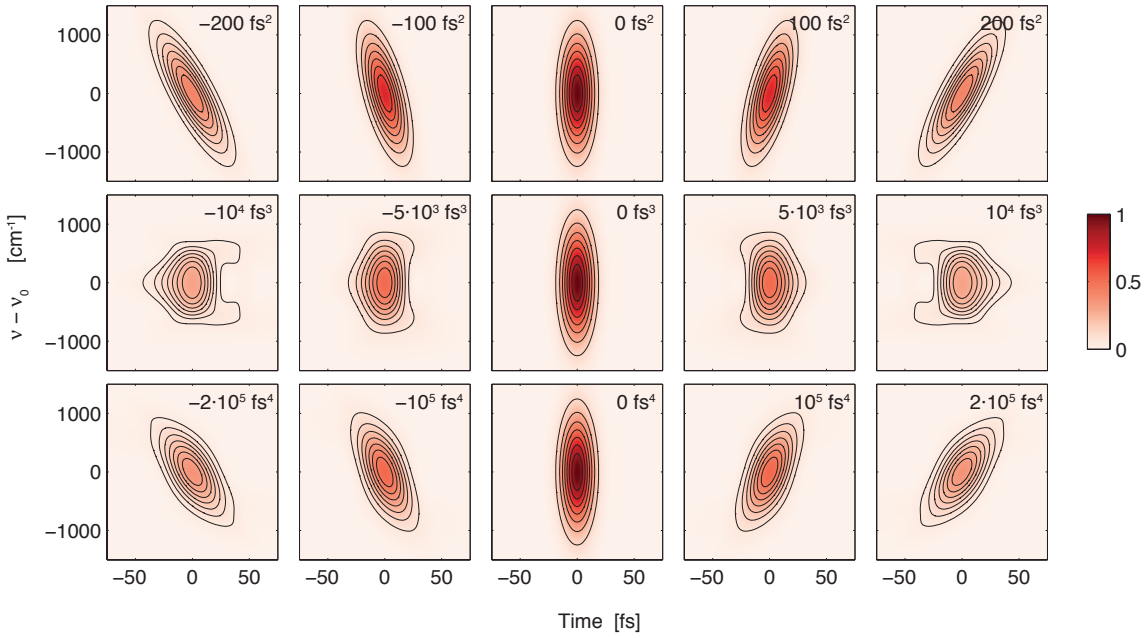

Figure 3.3 Effect of the chirp at different orders on the FROG measure. The first, second and third row show the distortions at the second, third and fourth order, respectively. The displacements from optimal TL parameters are reported in each plot.

3.2.3. Phase matching conservation

Phase matching conditions are crucial for non-collinear 2DES experiments. The propagation of the exciting pulses at three vertices of a square (BOXCARS geometry, see inset in Figure 3.2) is the ideal condition to generate the third order signal along the fourth vertex, corresponding to the LO propagation direction. However, deviations of even a small angle on the propagation direction of one of the beams can produce artefacts in the collected signal [57]. Therefore, the exciting beams must be carefully aligned in order to keep correct relative angles.

A critical factor for phase matching conservation is the alignment of the optical WP used to time delaying the pulses because, even with very high quality wedges, small deviations of the beams were detected. The procedure adopted to correct this deviation consists in checking the pulses geometry with a CCD camera placed at the sample position. Firstly, the setup is perfectly aligned without wedges and the four beams position is set before, after and on the focus point. As shown in Figure 3.4(a), the pulses are well arranged on the vertices of a square. The WP are subsequently placed on the beam paths and the deviations (see Figure 3.4(b)) from the previous position are compensated by slightly rotating the wedges around both the beam propagation axis and the axis orthogonal to the laser table. As shown in Figure 3.4(c), the square geometry of the four beams is eventually restored.

Finally, the optical wedges are moved by the translation stages and the conservation of the beams position is checked *via* the CCD camera. This guarantees that phase-matching condition will be preserved during the whole 2DES experiment.

3.2.4. Time delays calibrations

A crucial step in preparing a 2DES experiment is the calibration of translation stages that regulate the wedges positions and the thickness of CaF_2 that the pulse passes through. A sub fs precision of the time delay within the entire scanned range is necessary to obtain meaningful 2DES map. The problem arises because in a non-collinear 2DES measurement the phase of the signal depends on the phase of each pulse. When the time delay is controlled by a translation stage, its accuracy should be adequate to conserve the phase difference between pulses. This task is far from being trivial because the scanned time range is greater than 2 ps and even an error of 0.5 fs in time delay definition induces a $\pi/2$ phase shift (at 600 nm).
The procedure for time delay calibration that we propose here is inspired by the method suggested by Turner *et al.* to determine the global phase offset [58]. We use the linear relation in Eq. (3-4) that associates the position x_i (in mm) of the i-th stage, and thus the position of the optical wedge, to a time delay τ_i (in fs) of the pulse i-th (Figure 3.1):

$$\tau_i = c_i(x_i - x_{i,0}) \tag{3-4}$$

where c_i is the calibration coefficient $(\mathrm{fs} \cdot \mathrm{mm}^{-1})$ that must be determined. τ_i is defined with respect to the time zero of the experiment, when the linear stages are all in positions $x_{i,0}$ (in mm) that guarantees equal time delay of all the exciting pulses from LO, τ_{LO} (Figure 3.1).

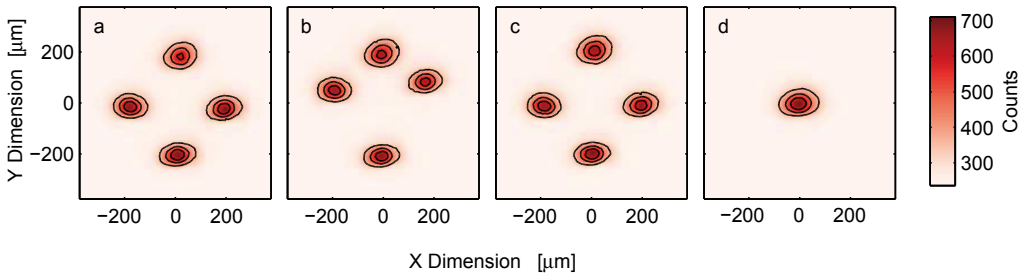

Figure 3.4 2D contour plots of the four beam profiles recorded by the CCD camera at the sample position. (a) The setup is carefully aligned to achieve a perfect square arrangement of the four pulses: no delaying material is present. (b) A WP is placed on the beam path of each exciting pulse. (c) The square arrangement is recovered after a slight rotation of the wedges around both the beam propagation axis and the axis orthogonal to the laser table. (d) In the focus position the four beams are perfectly overlapped.

The calibration procedure consists in two main tasks: (i) determine the time zero of the experiment and therefore the positions $x_{i,0}$ of the three linear stages that satisfy the condition: $\tau_i(x_{i,0}) = 0$ fs; (ii) find the linear coefficients c_i to convert a displacement of the stage in a time delay from the zero of the experiment.
Within the proposed setup, an efficient calibration procedure consists in recording the spectral interference (SI) produced by each exciting pulse with the LO, whose position is fixed in time. A 25 μm pinhole is placed at the sample position where the four beams are spatially overlapping and the SI of the LO with each one of the three exciting pulses is recorded by the spectrometer.
The Fourier transform of the SI is the simplest method to correlate the position of the WP stages with the LO-pulse time delay. However, the time delay can be retrieved directly from the stage position only in a limited time range. In fact, as the LO-pulse delay is increased, the fringes of the resulting SI become narrower. This method works until the CCD camera and the spectrograph can spectrally separate the fringes of the interference and it lacks the necessary precision needed to ensure phase-stability during the whole experiment. Moreover, the evaluation of the position of the Fourier transform peaks lacks the precision needed to ensure phase-locking during the experiments. A more sophisticated time delay calibration routine is therefore necessary.
First, we roughly estimate the positions of the three stages $x_{i,in}$ that set the same time delay from LO for each i-th exciting beam: we usually set a delay of approximately 500 fs. We subsequently scan x_i in a short range (about 20% of the length of the wedge) around $x_{i,in}$, obtaining a matrix F_i of spectral interferograms between the i-th beam and the LO, recorded for different x_i (see Figure 3.5(a)). Each column of the matrix F_i represents an interference spectrum $f_i(\omega)$ recorded when i-th stage is at position x_i. The shape of $f_i(\omega)$ evolves as the delay between the interfering beams changes due to the motion of the linear stage.
At this point we have three matrices F_i ($i = 1,2,3$) that contain all the information about the evolution of the pulse delays with respect to the fixed LO as the stages move.
Then, one of the excitation beams is selected as the reference, for example beam 1. Thus $f_1(\omega)$ recorded for chosen x_1 is subtracted from F_j of the other two beams, where $j = 2,3$. The resulting difference matrix, G_1 (Figure 3.5(b)) is spectrally integrated (black line in Figure 3.5(c)). The computed trace is therefore Hilbert transformed and its absolute value is stored (red line in Figure 3.5(c)).
This procedure is iterated subtracting different $f_1(\omega)$ of the reference beam recorded for distinct x_1 position of the first stage. The columns of data obtained after the integration and Hilbert transform of each G_j are merged in the matrix $H_{1,j}$ shown in Figure 3.5(d). It presents non negligible terms only at the positions of the

linear stages where the reference beam and the *j*-th beam ($j = 2,3$) have the same time delay from LO (e.g. $\tau_1 = \tau_2$ or $\tau_1 = \tau_3$), called respectively $x_{1,0}$ and $x_{j,0}$. A linear function can be used to fit the trend observed in matrix $H_{1,j}$. The function is defined as:

$$x_{j,0} = m_{1,j} x_{1,0} + q_{1,j} \tag{3-5}$$

where $m_{1,j}$ and $q_{1,j}$ are the slope and the intercept of the linear function (black line in Figure 3.5(d)). Each point on the line can be set as actual zero position of the calibration. In other words, with this linear function we can choose an arbitrary position as zero of the reference stage ($x_{1,0}$) and automatically get the zero position for the other stages (namely $x_{2,0}$ and $x_{3,0}$).

In order to practically and reliably obtain the parameters $m_{1,j}$ and $q_{1,j}$ of the linear function we can fit matrix $H_{1,j}$ with a Gaussian surface. The centre of the Gaussian function is modelled with the linear function in Eq. (3-5) obtaining a Gaussian tunnel shape. Once repeated the same procedure for all the pulses, we choose an arbitrary $x_{1,0}$ value, obtaining a tern of zero stage positions ($x_{0,1}, x_{0,2}, x_{0,3}$) in which the three exciting pulses are overlapped in time. This condition is used as the time-zero of the experiment.

The second step of the calibration procedure consists in determining the linear calibration coefficients c_1, c_2 and c_3 for the three pulses (see Eq. (3-4)).

As shown by Figure 3.5(e), F_i can be conveniently multiplied for a function $e^{-i2\pi\omega x_i c_i}$, where c_i is chosen to make the interference pattern perfectly horizontal.

$$I_{i,m,n}(c_i) = F_{i,m,n} e^{-i2\pi\omega_m x_{i,n} c_i} \tag{3-6}$$

The idea at the basis of the proposed procedure is to mathematically compensate for the evolution of the spectral interference coupled to the movement of the wedge. In other words, we want to determine which is the exact delay to be mathematically subtracted in order to achieve an interference pattern perfectly constant along the whole wedge scan. A suitable maximization algorithm is then applied to find the best values of c_i guaranteeing the condition of constant interference pattern that we want achieve:

$$\max_{c_i} \sum_m \left| \sum_n I_{i,m,n}(c_i) \right| \tag{3-7}$$

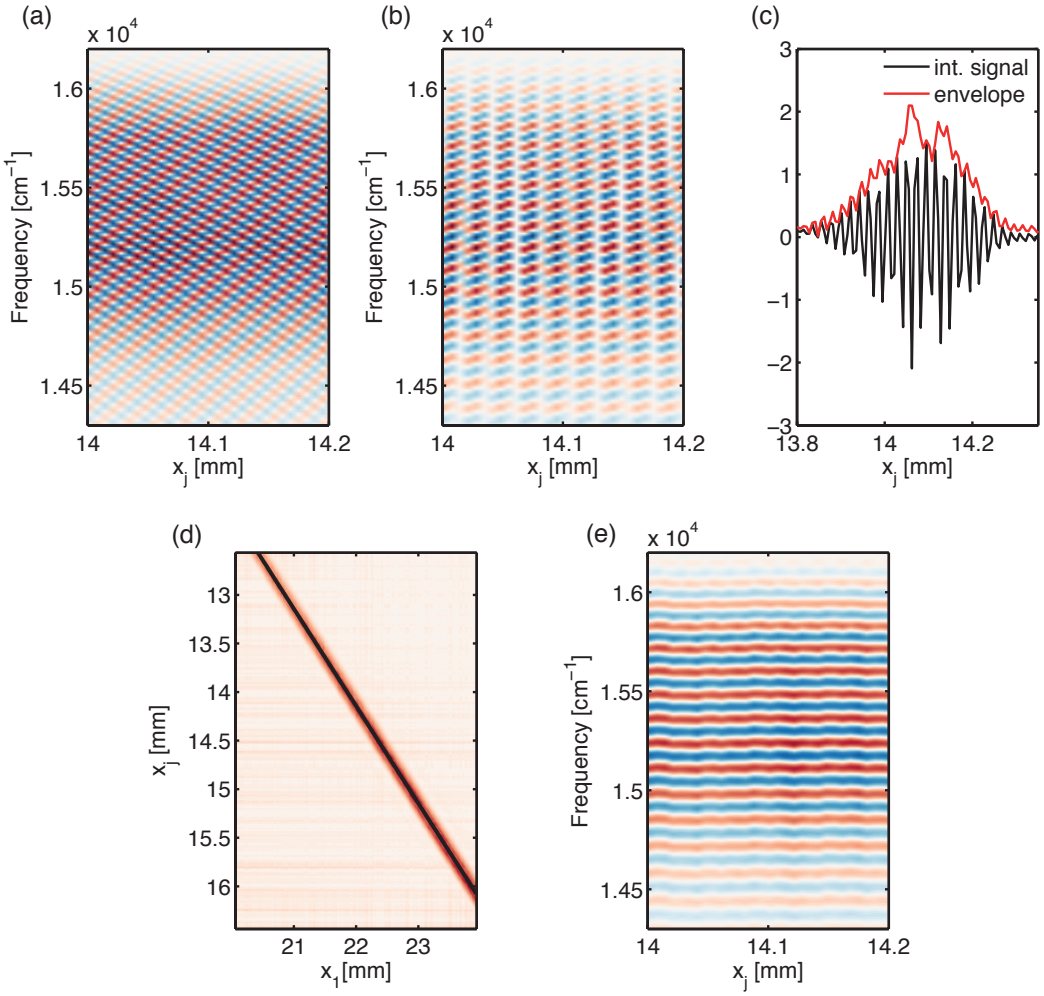

Figure 3.5 Different steps of the time delay calibration procedure: (a) graphical representation of the matrix F_i. Each column is a spectral interferogram $f_i(\omega)$ recorded at a specific x_i. (b) Graphical representation of the matrix G_j obtained subtracting the spectrum $f_1(\omega)$ from F_j, where $f_1(\omega)$ is recorded for a specific position x_1 of the stage that controls beam 1 (reference). (c) Result of the spectral integration of G_j (black line) and the absolute value of its Hilbert transform (red line); (d) matrix $H_{1,j}$ where $x_{1,0}$ vs $x_{j,0}$ is described by a linear fit (black line); (e) result of the minimization problem described in Eq. (3-7).

The linear coefficients c_i are determined in a range that is much smaller than what actually spanned by the stage during the experiment, thus a further refinement of these values is needed. Thanks to the c_i values just calculated (Eq. (3-4)), the time delay of the reference beam, τ_1, is scanned synchronously with τ_j ($j = 2,3$) while their difference is kept constant, typically at 150 fs. While LO and the third exciting beam are blocked. The resulting set of interferograms at different τ_1 are merged to form the matrix $F_{1,j}$. Ideally, the relative phase difference $\phi_{1,j}$ of the two pulses should be constant during the scan, but in effect small phase drifts are detected.

Even small linear drifts of the phase of the interference may lead to phase drift also of the third order signal and therefore they must be corrected.

$$I_{1,j,m,n}(p_{1,j}) = F_{1,j,m,n} e^{-i2\pi\omega_m(p_{1,j}\tau_{1,n})} \tag{3-8}$$

where the correction parameter $\mathrm{p_j}\tau_{1,\mathrm{n}}$ is the small delay correction and $p_{1,j}$ is an adimensional scaling parameter. Solving a maximization problem as before, $p_{1,j}$ can be determined:

$$\max_{p_{1,j}} \sum_m \left| \sum_n I_{1,j,m,n}(p_{1,j}) \right| \tag{3-9}$$

Assuming that c_1 of the reference beam is exact, it can be demonstrated that the corrected coefficients $c_{j,corr}$ for the other two exciting beams can be expressed as:

$$c_{j,corr} = c_j(p_{1,j} + 1) \tag{3-10}$$

Eq. (3-10) can be generalized to the non linear case by adding higher order terms in Eq. (3-4), but the discussion of this topic goes beyond the purposes of this work.
Finally, retrieving the exact value of τ_{LO} is crucial for the analysis of the third order signal, but it cannot be easily determined by the SI generated by the 25 μm pinhole because this configuration does not reproduce the working conditions in a 2DES experiment. We therefore collect the heterodyne non-resonant TR-FROG of the solvent in a cell. This procedure consists in collecting the interference pattern produced by the third order signal generated by the solvent and the LO. During the experiment the three exciting pulses arrive simultaneously while τ_{LO} is scanned. The function $\tau_{\mathrm{LO}}(x_i)$ is estimated with a linear fit so that the exact value of $\tau_{\mathrm{LO}}(x_{i,0})$ is computed.
This calibration method resolves some of the most important issues of non-collinear 2DES setups [50]. The accuracy achieved in finding the reciprocal time delays between the exciting pulses and $\tau_{\mathrm{LO}}(x_{i,0})$ is crucial to obtain high quality 2DES data.

3.2.5. Time scan definition

The described 2DES experimental setup enables to scan independently all the different time delays of the three exciting beams. However, there are schemes more convenient than others to acquire rephasing and non rephasing portion of the signal with improved phase stability. In 2DES experiments, the phase of the heterodyne detected signal is function of the individual phases of each pulse (see Eq. (3-11)):

$$\begin{aligned} \phi_{s,reph} &= -\phi_1 + \phi_2 + \phi_3 - \phi_{LO} \\ \phi_{s,nonreph} &= +\phi_1 - \phi_2 + \phi_3 - \phi_{LO} \end{aligned} \tag{3-11}$$

We found that the most suitable configuration consists in fixing the delay of beam 3 with respect to LO and moving simultaneously only the first and the second beam. In other words, we are defining a new origin of the temporal axis of the experiment at $\tau_3 = 0$. This choice does not allow exploiting the advantages of the full rotating frame but the spectra gain phase stability. Indeed, the phase of third order signal is function only of the phase difference between beam 1 and 2 since $\phi_3 - \phi_{\mathrm{LO}}$ becomes constant during the scan. Moreover, full rotating frame advantages can be achieved in the post processing procedure as explained in Section 3.2.7.

3.2.6. Signal acquisition

The signal acquisition routine is based on the double modulation lock-in method proposed by Augulis *et al.* [45]: the signal is modulated at a certain frequency and thus it can be isolated from all the other spurious contributions. In our setup, the CCD camera collects series of spectra with a repetition rate of $\omega_{\mathrm{CCD}} = 500$ Hz, while the second and the third exciting pulses are modulated respectively at $\omega_{f_1} = 200$ Hz and $\omega_{f_2} = 40$ Hz with optical choppers. Hence the signal is extracted at $\omega_s = \omega_{f_1} - \omega_{f_2} = 160$ Hz, which is the difference of the two modulating frequencies.

The laser pulse train, the CCD camera and the optical choppers are suitably synchronized and phase-locked. The modulation frequencies must be selected accurately. First, it is necessary to extract the signal at a frequency lower than Nyquist frequency ($\omega_{\mathrm{CCD}}/2 = 250$ Hz). Second, to achieve a phase-locked signal on the CCD, one of the modulation frequency must be a multiple of the other. This condition guarantees that the CCD collection is always synchronized with both the chopper cycles. We typically choose a $\omega_{f_2} = \frac{\omega_{f_1}}{2n+1}$ so that ω_{CCD} is always different from $(2n+1) \cdot \omega_{f_2}$ to assure that the collected signal is not affected by other modulation contributions.

With this method, most of the scattering contributions are removed, since they reach the CCD camera with the frequency of modulation of a single chopper or they are not modulated at all. However, the acquired signal still contains some unwanted contributions, as reported in Table 3.1.

Table 3.1 All the possible signal contributions acquired by a quadratic detector. Only the real part of these contributions can be recorded. The double lock-in method allows removing most of the spurious contributions. The contributions highlighted in red are kept and processed in order to retrieve the final signal.

$\times$	$\boldsymbol{E_1^*}$	$\boldsymbol{E_2^*}$	$\boldsymbol{E_3^*}$	$\boldsymbol{E_{LO}^*}$	$\boldsymbol{E_S^*}$
E_1	$\lvert E_1\rvert^2$	$E_1E_2^*$	$E_1E_3^*$	$E_1E_{LO}^*$	$E_1E_S^*$
E_2	$E_2E_1^*$	$\lvert E_2\rvert^2$	$E_2E_3^*$	$E_2E_{LO}^*$	$E_2E_S^*$
E_3	$E_3E_1^*$	$E_3E_2^*$	$\lvert E_3\rvert^2$	$E_3E_{LO}^*$	$E_3E_S^*$
E_{LO}	$E_{LO}E_1^*$	$E_{LO}E_2^*$	$E_{LO}E_3^*$	$\lvert E_{LO}\rvert^2$	$E_{LO}E_S^*$
E_S	$E_SE_1^*$	$E_SE_2^*$	$E_SE_3^*$	$E_SE_{LO}^*$	$\lvert E_S\rvert^2$

3.2.7. Data processing

The raw signal acquired by the CCD in the double lock-in detection configuration is expressed as:

$$S_a = |E_S|^2 + 2\Re\{E_S E_{LO}^*\} + 2\Re\{E_S E_1^*\} + 2\Re\{E_3 E_2^*\} \tag{3-12}$$

An example of raw rephasing data collected at a fixed population time is reported in Figure 3.7(a). The emission wavelength axis is immediately interpolated in order to achieve an energy axis evenly spaced; this assure a correct output of the fast Fourier transform algorithm when acting on this axis. Our aim is to isolate the pure signal E_S from the contribution $E_S E_{\mathrm{LO}}^*$. In order to do so we need to operate on the complex data. We must recognize that E_S is generated after the interaction of the pulse k_3 with the sample. This causality property must be imposed to the signal: the inverse Fourier transform is performed along ω_3 axis and the positive part of the resulting temporal axis is removed. This mathematical trick corresponds to impose a negative time delay to the interference between LO and the third order signal. Then, the resultant data is Fourier transformed and ω_3 axis is retrieved (Figure 3.6).

After this set of operations the signal S_a become complex valued $\hat{S}_a$: the real part is equal to the data recorded by the CCD and the imaginary part is a copy of the original data with a phase shift of $-\pi/2$. The rotating frame formalism (RF) is applied to axis t_1, the optical frequency of the signal is detuned adding or subtracting a reference frequency ω_{ref}, which is usually taken as the central frequency of the spectral window:

$$S_{b,\mathrm{reph}} = \hat{S}_{a,\mathrm{reph}} e^{i2\pi\omega_{\mathrm{ref}}t_1} \tag{3-13}$$

$$S_{b,\mathrm{nonreph}} = \hat{S}_{a,\mathrm{nonreph}} e^{-i2\pi\omega_{\mathrm{ref}}t_1} \tag{3-14}$$

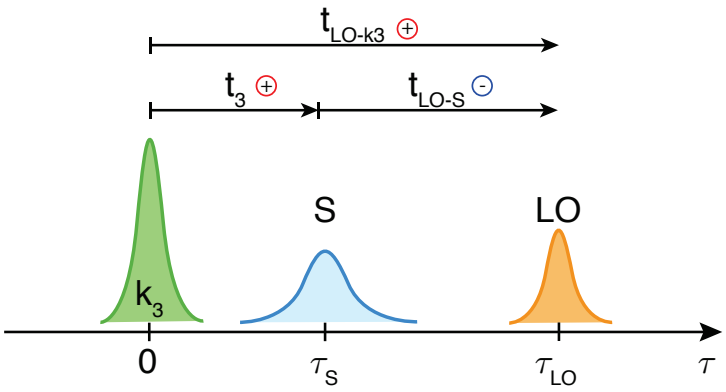

Figure 3.6 Scheme elucidating the enforcement of the causality property. In our time scan, k_3 is kept fixed during the measurement (Section 3.2.5). Also $t_{\mathrm{LO}-k3}$ is set fixed and positive. The experimentally accessible time delay which is then Fourier transformed is $t_{\mathrm{LO}-\mathrm{S}}$, which has to be defined negative in order to obtain a positive t_3, in agreement with causality conditions.

This operation allows to greatly reduce the sampling frequency of the signal along the t_1 axis. The maximum frequency observed in the RF signal is decided by the bandwidth of the experiment which is in the order of few thousands of wavenumbers.

An example of rephasing data S_b is shown in Figure 3.7(b). Finally, the delay between LO and the time zero of the experiment must be accounted for (Figure 3.7(c)):

$$S_c = S_b e^{i2\pi\omega_3\tau_{LO}} \tag{3-15}$$

The delay between the zero of the experiment ($\tau_3 = 0$) and LO is measured exploiting the heterodyne detection of the non-resonant TR-FROG signal of a pure solvent. The inverse Fourier transform of the interference pattern when all the pulses are set at the zero position gives a peak at τ_{LO}. The distance of LO from the zero of the experiment controls how dense are the fringes of the interference pattern in the collected spectra; it is usually set in the interval 300-500 fs.

In order to remove the other additional spurious contributions from the signal, inverse Fourier transform is performed on ω_3 axis and a time-filter along the resulting t_3 dimension is applied (Figure 3.7(d)). The filter is tuned to keep only the portion of the t_3 axis between zero and 80-100 fs, where the signal is supposed to be present. This operation allows removing most of the remaining spurious contribution in Eq. (3-12). The initial transient of the signal can be slightly affected by $E_S E_1^*$ and $E_3 E_2^*$ when the delay between signal and k_1 pulse and the delay between k_3 pulse and k_2 pulse, respectively, are within the filter window. This condition however is verified only for short population times.

As last step of data processing, the final excitation/emission frequency maps as in Figure 3.7(e) is retrieved: a Fourier transform along the t_1 axis is performed and the excitation frequency is shifted again by ω_{ref} to account for the RF.

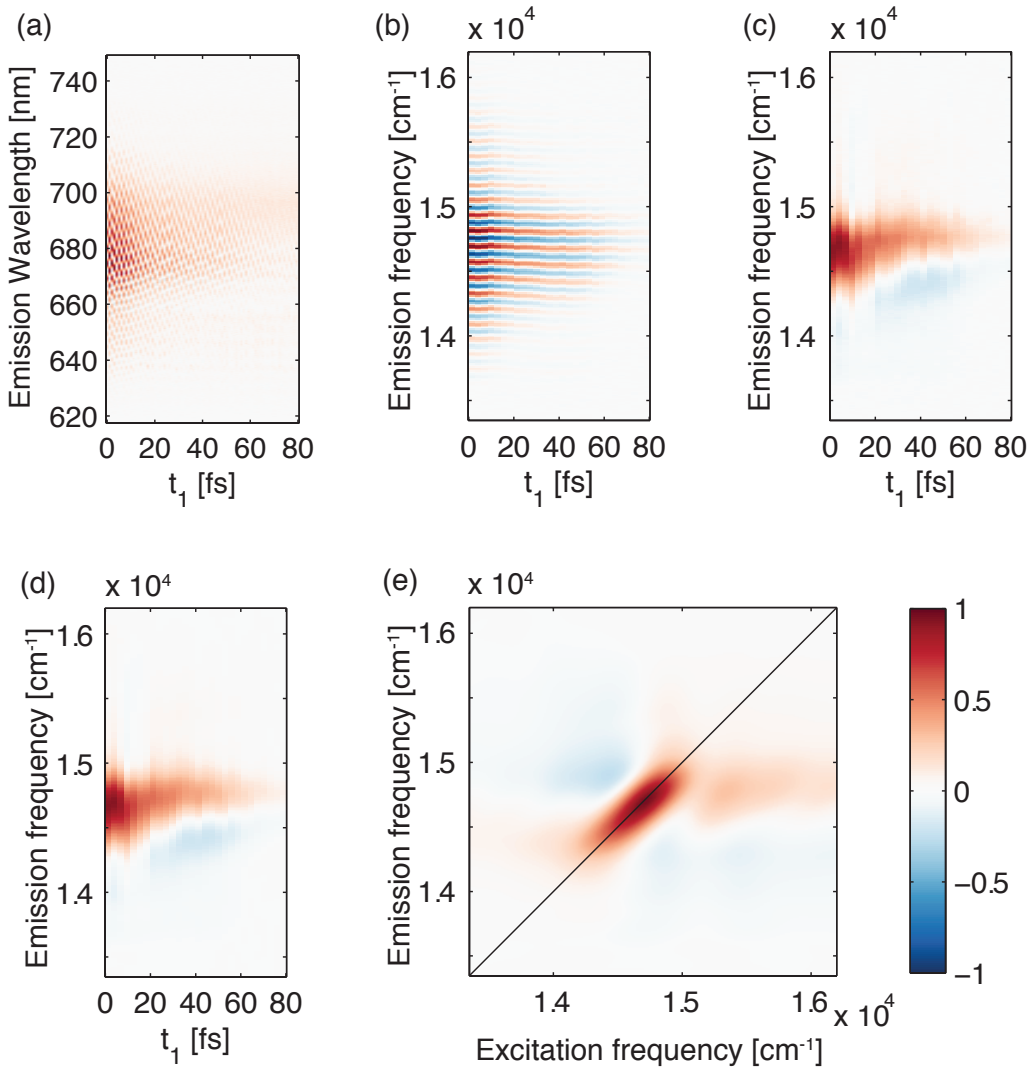

Figure 3.7 Scheme of data processing. (a) Raw interferogram acquired scanning t_1, while t_2 is kept constant. (b) RF is applied to t_1. (c) Delay between LO and the time zero of the experiment is removed. (d) Result of time filtering in the t_3 dimension. (e) Final map resulting after Fourier transforming the t_1 axis.

3.2.8. 2DES maps analysis

Once applied the data processing procedure described above, we obtain a 3D matrix of the third order signal as a function of ω_1, t_2 and ω_3. The evolution of the 2D maps along t_2 provides lot of information about the relaxation dynamics of the systems, the possible presence of transfer processes and the energy of the states involved

in the transfer. Moreover, the ultrafast time resolution allows following the evolution of both vibrational and electronic coherence at early times after photoexcitation.

All the phenomena listed above contribute to the overall third-order signal and can be classified in two groups depending on the evolution of the signal in t_2. The first group includes non-oscillating pathways, represented by Feynman diagrams where the system reaches a pure state after the first two interactions. The second group consists of oscillating contributions described by Feynman diagrams where, after the first two interactions, the system is in a coherent superposition of states [16].

Our group developed several methods to analyse 2DES signals as function of t_2 [59]. The rich choice offered allows adopting from time to time the most suitable approach depending on the kind of system under investigation. The proposed methodologies can be divided into two main approaches: the first consists in extracting firstly the population dynamics through global target analysis, and, afterwards, isolating and characterizing the oscillating signals (Section 3.2.8.1); the second approach consists instead in analysing simultaneously non-oscillating and oscillating components, without any preliminary subtraction operation (Section 3.2.8.2).

3.2.8.1. Separate analysis of coherence and population dynamics

The decay of the signal in t_2 provides information about the time constants regulating the relaxation dynamics of the system. The analysis of decays in 2DES signals is very similar to that of pump probe. The only difference consists in having 2D decaying spectrum in the former case, rather than a 1D spectrum in the latter. Several works have reported examples of global target analysis also on 2DES maps [60,61] identifying the contribution to the map coming from different species or states.

A possible approach to isolate oscillations due to coherences from the decaying signal consists in removing the non-oscillating part of the signal. It can be achieved by fitting the decay trace of each point of the 2DES map with a multi-exponential function and, afterwards, subtracting it from the experimental data.

However, a global fit of the decay of the map is more rigorous since it can identify common decaying behaviours within the spectral window of the 2DES map, avoiding punctual aberrations. Thus, even though a subsampling in ω_1 and ω_3 direction is performed, the dynamic behaviour of the whole map is equally captured. For the global fitting procedure of the non-oscillating part of the signal, we exploit the approach proposed by Van Stokkum, called variable projection algorithm [62,63].

Once the fitting function is subtracted from the experimental data, the resulting 3D matrix of oscillating residuals can be analysed with different methods to unravel frequencies and time properties of the associated coherences.

3.2.8.1.1. Fourier transform maps

The most common methodology used to determine the frequencies of the oscillations in t_2 consists in performing Fourier transform (FT) of the residuals extracted as described above. A particularly convenient way of visualising the results of the FT is the so-called 'Fourier map' or FT map [64]. They are obtained by Fourier transforming the 3D matrix of the residuals along the t_2 axis. Thus, a 3D spectrum as a function of ω_1, ω_2 and ω_3 can be built.

A convenient way to display the content of the 3D FT matrix consists in plotting 2D slices selected for fixed values of ω_2 and as a function of ω_1 and ω_3. In these 2D maps the amplitude and phase distributions of beatings with selected frequency are visualized as function of ω_1 (excitation) and ω_3 (emission) axis. This method is extensively used by many groups [7,9,65–67]. However, since the intensity of the signal in the map is dependent on the laser shape, FT maps can appear distorted and degraded by artefacts. When it happens, a second analysis procedure can be adopted, as described in the following Section.

3.2.8.1.2. Time-frequency representation

Time-frequency representations (TFR) retain information in both frequency and time domain. Thus, it is possible to follow in time the intensity of the oscillations with a specific frequency. Several kinds of TFR have been proposed so far. The first application of TFR in the analysis of the evolution of 2D spectra was the Wavelet transform [68]. This method and other linear and bilinear (BTFR) approaches have been recently analysed and compared in our research group [69]. Several combinations of TFR were tested, and the best performing tool for 2DES data was selected: it is the combination of a bilinear transform, the smoothed pseudo Wigner-Ville (SPWV), with a linear transform, the short-time Fourier transform (STFT).

This peculiar representation, that, for simplicity, we will call BTFR from now on, will be exploited in the data analysis presented in this thesis as follows. The residuals as function of population time, resulting after subtraction of the non-oscillating signal, are extracted for a point (ω_1, ω_3) of interest of the 2D map. Thus, the BTFR map is generated applying the transform to these residuals. The resulting plot shows the signal as function of the frequency of the oscillating components (y-axis) and of population time (x-axis). Absolute maps show only the intensity of the beatings, whereas real maps can highlight also the relative phases. Summarizing, thanks to BTFR maps, it is possible to distinguish efficiently oscillations at different frequencies and comparing their relative amplitude and phase. Moreover, it is possible to follow their dependence on population time and thus determine the corresponding dephasing times.

An example of the exhaustive analysis that we usually perform on 2D data is shown in Figure 3.8. On the residuals of the multi-exponential fitting, we first perform the

conventional FT and the linear prediction z-transform (LPZ), a transform that enhances the resolution of FT when applied to decaying oscillating signals [69]. The absolute and real amplitude of the BTFR plots are subsequently shown.

3.2.8.2. Global analysis of coherence and population dynamics

To overcome some of the limitations characterizing the methods described in the previous Sections, a novel procedure has been proposed by my research group [59]. It allows extracting all information from a complete 2DES dataset, analysing simultaneously non-oscillating and oscillating components, without any preliminary subtraction operation.

Using the most general approach, both oscillating and non-oscillating decay contributions can be described with a complex exponential function: in the former case, the imaginary part of the complex function is zero and the real part carries all the information on the decay constants. In the latter case, real and imaginary part are nonzero and the function accounts for amplitude, dephasing rate, frequency and phase of the oscillation.

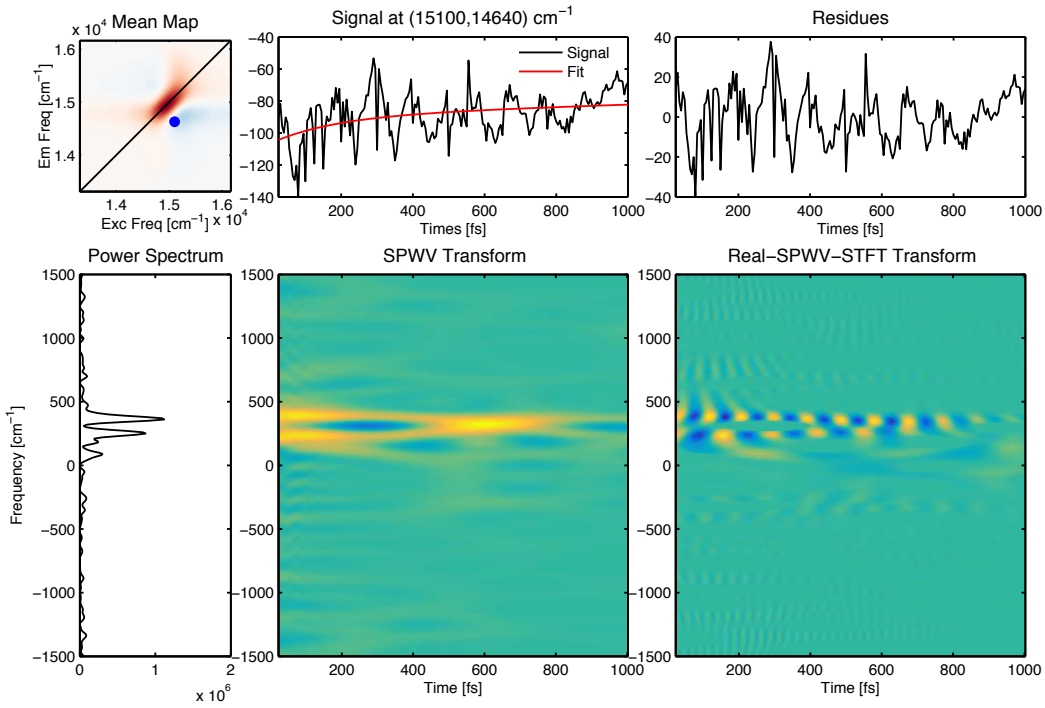

Figure 3.8 An example of the analysis performed on a single point of the 2D map. (a) A point is selected in the map and the time trace at that coordinates is extracted. (c) Multi-exponential fitting is performed on the time trace. (b) The fitting function is subtracted to the experimental trace to remove all non oscillating contributions. (d) Fourier transform and LPZ transform are applied on oscillating residuals. (e) and (f) are absolute and real BTFR maps, respectively. Absolute BTFR map highlights the intensity changes of the oscillation. Real map allows assessing also the realtive phase of the oscillations.

First of all, the number n of complex exponential functions for the fit has to be chosen. The core of the fitting procedure consists in the solution of a minimization process through the variable projection algorithm, as described in detail by Volpato *et al.* [59]. Briefly, the outputs of the procedure are (i) the amplitude, (ii) the time constant and (iii) the frequency value for each of the n exponential components, as described by the scheme in Figure 3.9. In particular, amplitude maps can be divided into two groups: the firsts are associated to real exponentials and population dynamics and the seconds to complex exponentials and coherent dynamics. The formers are called decay-associated spectra (DAS), in analogy with the definition previously proposed in similar methods [61,70], whereas maps associated to the coherence-set are called coherence-associated spectra (CAS), see Figure 3.9.
The power of this global fitting procedure consists in being capable of simultaneously retrieving coherence and population dynamics from a full (real and imaginary, rephasing and non-rephasing) 2DES dataset. Unlike previous methods, this methodology allows a quantitative analysis of the decaying time of all the components. Thus, it will be extensively exploited in the 2DES data analysis to assess the temporal behaviour of coherent patterns, since it is a crucial aspect in our research field.

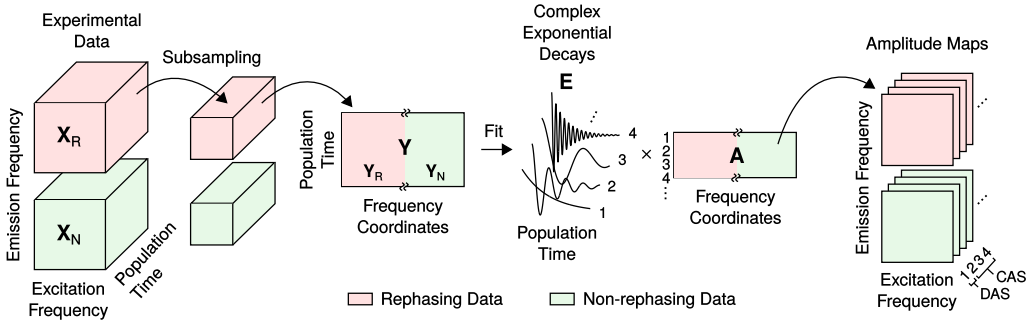

Figure 3.9 Schematic illustration of the fitting method. Rephasing and non-rephasing data ($\mathbf{X_R}$ and $\mathbf{X_N}$) are subsampled and reshaped into the matrix $\mathbf{Y}$, to which the global fitting procedure is applied. Decay constants, frequencies and matrix $\mathbf{A}$ are then recovered. Rephasing and non-rephasing amplitude maps are obtained from matrix $\mathbf{A}$ for each complex exponential decay component. Two types of maps can be identified: decay-associated spectra (DAS) and coherence-associated spectra (CAS).

4 Artificial light harvesters

Natural light harvesting antennas are fascinating machines that evolution process has finely tuned leading to extremely efficient solar light capture. In such pigment-protein complexes structures, dynamics and functionalities are strictly related.
The subtle reason of their efficiency lies in the high level of organization of antennas, where pigments are geometrically arranged in precise positions, in close proximity and embedded in a protein scaffold. The well-defined configuration brings to specific interactions among the chromophores and thus to a peculiar framework of the electronic states.
Recent discoveries seem to suggest that the efficiency of natural systems may be related to long-lasting electronic coherences but the subtle mechanism that hinders the coherence dephasing are still not fully understood. The various hypotheses proposed to explain the phenomenon can be divided into two main approaches: the first invokes the interaction of the delocalized exciton states with intra-chromophore vibrational modes [8,29,71,72] while the second suggests that vibrations of the protein scaffold may help to sustain those oscillations [10,11].
Artificial antennas represent ideal test systems thanks to their lower degree of complexity and may help to clarify the actual mechanism that sustains exciton beatings, if any. The artificial systems designed in our laboratory take inspiration from natural antennas and are based on pigments which are synthetic analogous of the natural ones.

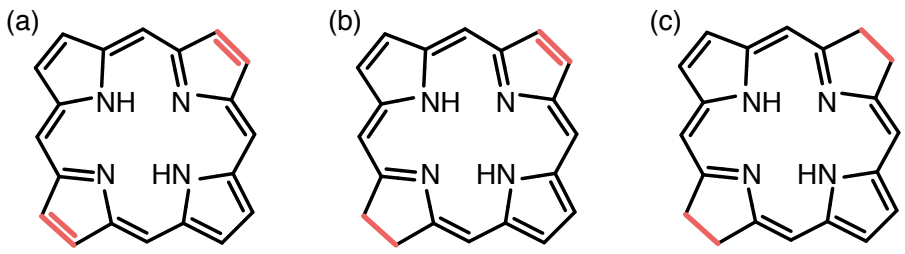

Figure 4.1 Comparison of chemical structure of porphyrin (a), chlorin (b) and bacteriochlorin (c).

Chlorophyll *a* and bacteriochlorophyll *a* represent the major light-harvesters of natural antennas. Chemically, they both are tetrapirrole compounds, a chlorin and a bacteriochlorin, respectively. Porphyrins are considered valid artificial analogues of the photosynthetic pigments, since they share the tetrapyrrolic backbone (Figure 4.1). The proposed artificial harvester systems contain either a carboxy derivative of free base tetraphenylporphyrin (H_2TPP), 5-(4'-carboxyphenyl)-10,15,20-triphenylporphyrin, or a free-base derivative of chlorophyll *a*, methyl pyropheophorbide *a* (PPH).
In this Chapter, we explore the distinct behaviour of three artificial antennas characterized by different chromophores and peptide constituents with the specific aim of assessing whether the intra-chromophore vibrational framework or the coupling with the protein scaffold play any role in sustaining electronic long-living coherences. First, System I, constituted by H_2TPP and a natural peptide, was investigated (Section 4.2). In System II, instead, an artificial peptide replaced the natural one, while conserving the chromophore component (Section 4.3). Finally, System III retained the same peptide constituent of System II, but PPH was chosen as pigment (Section 4.4).

4.1. Self-assembling strategy

The architecture of the studied artificial antennas is realized exploiting the self-assembling properties of peptide-chromophore conjugates.
Each monomer consists in a functional chromophore covalently linked to a synthetic peptide. Like in natural light-harvesting systems, the pigments are responsible for light absorption, while the aminoacid sequence has a structural function.
As shown in Figure 4.2, the two components have different hydrophilicity: the chromophore has a prevalent apolar character, while the peptide is amphiphilic. We took advantage of these properties to induce self-assembling of the supramolecular system tuning the polarity of the solvent. The monomers are stable in methanol (MeOH) and, when the polarity of the solvent is increased by adding water, the aggregation is induced. The pigments are thus segregated in a central core protected from the polar solvent by the peptide component.
The close proximity induces exciton interactions among the chromophores, manifested as specific spectral changes in the absorption and circular dichroism (CD) spectra. The variation of the coupling as response of the change of the polarity of the solvent is studied with steady-state absorption spectroscopy and CD spectroscopy. The solvent conditions that favour the higher interaction among the pigments can thus be selected.

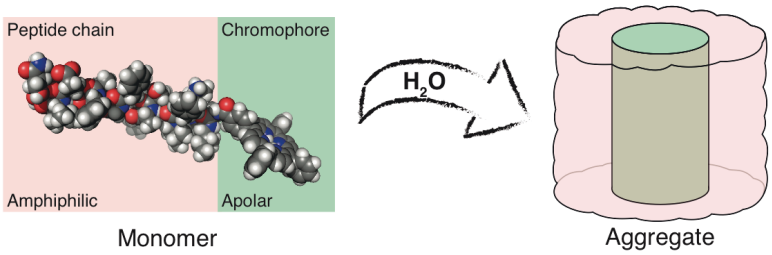

Figure 4.2 Scheme of the self-assembling strategy: the increase of the solvent polarity induces the interaction among the apolar pigments while the peptide component shields the chromophoric core from the solvent.

4.2. System I

4.2.1. Monomer properties

The properly functionalized free base H_2TPP is covalently linked to the N-terminus of a naturally occurring peptide, called magainin as shown in Figure 4.3. The monomer was synthetized in the laboratories of prof. M. Gobbo following the experimental procedure reported in a previous work [73].
[Leu^{21}]magainin 2 is a 23 aminoacid cationic peptide (CAMP), that shows a powerful antimicrobial activity against Gram-positive and Gram-negative bacteria perturbing the bacterial membrane and forming pores. Its H_2TPP-conjugate was originally designed for antimicrobial photodynamic therapy (PDT) for eukaryotic cells, because this CAMP does not express hemolytic activity nor toxicity towards mammalian cells. Therefore, the initial therapeutic application of this conjugate exploits the selectivity of the peptide for bacterial membrane and, at the same time, the cytotoxic activity of the photosensitizer, that is the H_2TPP. After photoexcitation there is a finite probability that a fraction of molecules of the chromophore crosses over into the triplet state. It triggers the oxygen excitation to singlet state, which is highly reactive and can damage a variety of cellular components.
Magainin is an amphiphilic peptide that assumes a random coil conformation in water solution. However, it was observed that the conjugation of a H_2TPP moiety induces a helicoid form as shown in Figure 4.3(d): two populations are present, the first with helicoidal and the second in random coil conformation [73].
The electronic properties of H_2TPP-magainin sample do not show significant differences with respect to the free chromophore, as pointed out by the comparison of their steady-state absorption spectra in Figure 4.3(b), meaning that the link to the peptide chain does not affect sensibly the electronic structure of the tetrapyrrole.

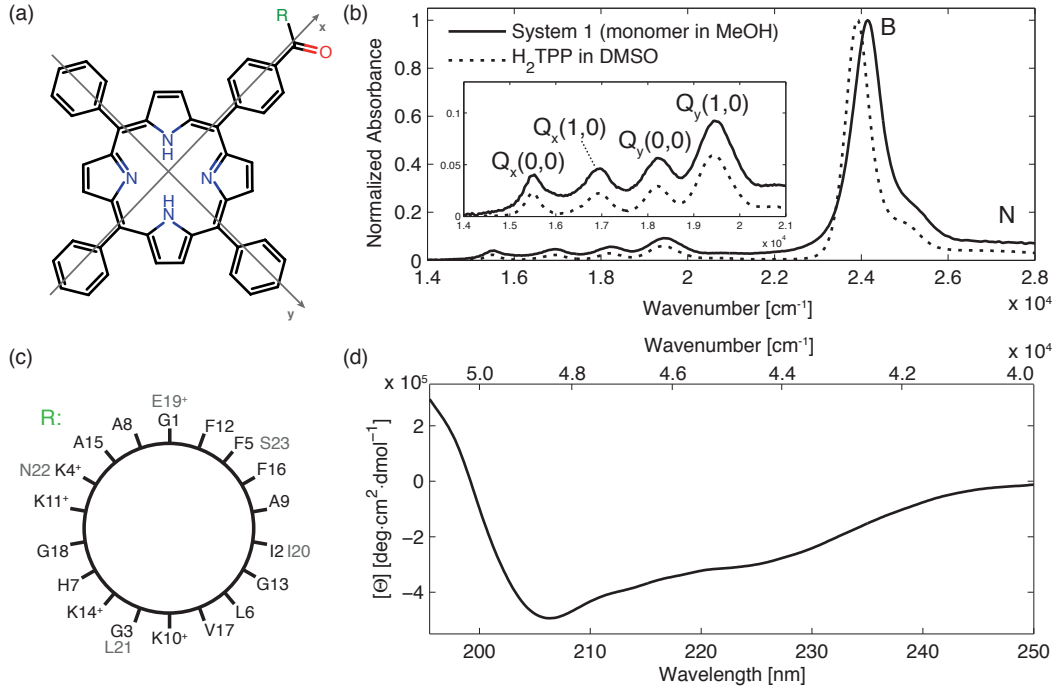

Figure 4.3 (a) Molecular structure of the functionalized H_2TPP. (b) Steady-state absorption spectra of the monomer of System I in MeOH (solid line) and of H_2TPP in DMSO (dashed line). The intensities are normalized to 1 on the maximum of the B band. (c) Helical wheel representation of the bioinspired peptide conjugated to the chromophore in (a). (d) Circular dichroism spectrum of a solution $2{\cdot}10^{-5}$M of the monomer of System I in MeOH (quartz cuvette, pathlength 1 mm).

The porphyrin absorption spectrum presents signals in three main spectral regions. The so-called Q bands are responsible for the red-purple colour. They consist of two separate relatively weak electronic transitions in the visible region between $1.5{\cdot}10^4$ and $2{\cdot}10^4$ cm^{-1} . The intense Soret or B band occurs in the near-UV region and is centred at $2.42{\cdot}10^4$ cm^{-1}. Other transitions are present in the UV region, but are usually quite weak, like N bands, appearing at higher energy with respect to the B band.

Since H_2TPP is a 22 π-electron conjugated system, Gouterman four-electron- four-orbital model [74] gives a picture, although oversimplified, that well reproduce the main features of its steady-state absorption spectrum. Within this model the two highest occupied π orbitals and two lowest π* orbitals are involved in the transition giving rise to the observed absorption bands. The Q and B bands arise from a linear combination of the one-electron symmetry-allowed transitions among the molecular orbitals. For the lower energy Q bands, the transition dipoles nearly cancel out, resulting in weak absorptions. For the higher energy B bands, the transition dipoles reinforce, giving the intense absorption in the near-UV region.

The effective directions of the electronic transition moments are represented in Figure 4.3(a) [75,76]. According to Gouterman interpretation [74], the presence of four Q bands is the consequence of the molecular symmetry, because the presence

of two hydrogens in the centre of the tetrapyrrole results in a D_{2h} symmetry. The bands at $1.55 \cdot 10^4$ cm^{-1} and $1.83 \cdot 10^4$ cm^{-1} are associated to $Q_x(0,0)$ and $Q_y(0,0)$ transitions respectively, while the bands at $1.70 \cdot 10^4$ cm^{-1} and $1.95 \cdot 10^4$ cm^{-1} are their vibronic sidebands $Q_x(1,0)$ and $Q_y(1,0)$ respectively.

4.2.2. Aggregate preparation

As anticipated in the previous Section, the polarity of the solvent determines the self-assembling properties of System I. We followed the changes of the steady-state absorption spectrum and of the CD spectrum as the polarity of the solvent is increased. We prepared five solutions with the same concentration of the monomer ($2 \cdot 10^{-5}$ M), but with different ratios (v/v) of MeOH and H_2O.

If the electronic coupling J has approximately the same magnitude of the coupling with the environment, as it is the case, aggregation results in spectral line broadening [77]. Indeed, as the polarity is increased, the B band in the absorption spectra gets broader, proving that aggregation occurs in polar environment (Figure 4.4(a)). The Q bands, however, are far less affected by the solvent change and undergo only a slight red-shift due to the change of solvent polarity. The transition dipole moments of the Q bands are indeed very weak, thus it is not surprising that dipole-dipole interaction does not affect markedly Q bands spectral region.

Higher ratios of H_2O in the solvent composition also increase the amount of peptides in a random coil conformation, as shown in Figure 4.4(b). CD spectra pointed out that in polar environment a weak exciton signal arises (Figure 4.4(c)) in the B band spectral region, manifested as a positive Cotton effect. The absence of CD signal in the Q bands spectral region confirms what already found in steady-state absorption measurements, since CD depends in a complex manner on the mutual orientations and positions of transition dipole moments of the interacting monomers (see Section 2.8). Based on these results, we selected the solvent mixture that ensures the stronger circular dichroism signal, in other words we chose the environmental conditions that mostly promote excitonic interactions among pigments. The most polar mixture MeOH:$H_2$0/10:90 has thus been selected.

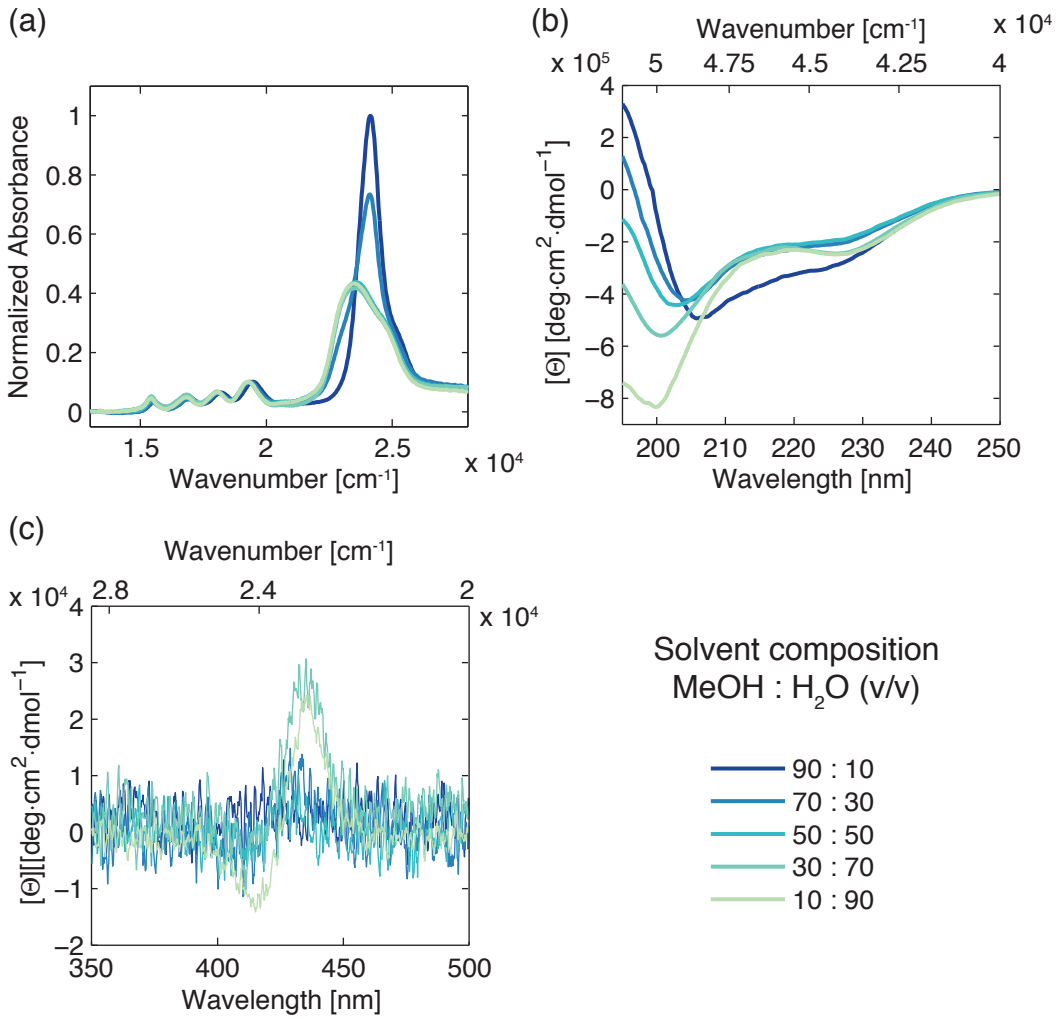

Figure 4.4 (a) Steady-state absorption spectra of solutions of H_2TPP-magainin at different solvent composition (conc. $2 \cdot 10^{-5}$ M, pathlength 1mm). (b) Circular dichroism spectra of the solutions in the peptide region. (c) Circular dichroism spectra of the solutions in the B band spectral region.

4.2.3. Preliminary optical characterization

Electronic and vibrational properties of both the monomer and the aggregate have been preliminarily characterized through conventional optical spectroscopic techniques to ease the subsequent ultrafast investigation.

As anticipated in the previous Section, the process of aggregation is followed by spectral changes both in the steady-state absorption and in the CD spectrum, especially in the B band spectral region. A global multi-Gaussian fitting of both the absorption and CD band helped to identify four main features under the congested B-band of the aggregate, as shown in Figure 4.5(a) and in Table 4.1.

The least number of exciton transitions that can be expected in the B-band region for the simplest porphyrin oligomer, namely a dimer, is four. Indeed, we have demonstrated in Section 2.8 that a homodimer originating from two-level monomers, results in two exciton states that can be represented as linear combinations of the monomers excited states. Within B-band spectral region of the monomer, two nearly overlapping electronic transitions are detected. Thus, for a dimer, four exciton states are foreseen. This is a somewhat oversimplified approach, but it represents now the only option available to provide a meaningful, although preliminary, interpretation of the spectroscopic properties of these signals. A great modelling effort by our collaborators is currently underway but satisfactory results have not been achieved so far. The assumption that the optical properties are due to excitations delocalized over not more than two monomeric units is however supported by preliminary theoretical results and by the comparison with other aggregated systems [78,79].

Excitonic interactions are known to open additional non-radiative relaxation pathways, as demonstrated by the noticeable decreasing in fluorescence quantum yield (FQY) of the aggregate, $(11.4 \pm 0.4)\%$, with respect to FQY of the monomer, $(1.6 \pm 0.2)\%$. This trend is evident in the fluorescence emission spectra shown in Figure 4.5(b) and is confirmed by the fluorescence lifetimes (Table 4.2) obtained from TCSPC measurements performed on the two systems (Figure 4.5(c)).

Since understanding if there is any interplay in the ultrafast regime between electronic and vibrational coherences is our main challenge in the study of artificial light-harvesting systems, a fundamental step consists in depicting a clear picture of the vibrational modes of the chromophore. Raman spectra of both the free chromophore H_2TPP and of H_2TPP-magainin conjugate are reported in Figure 4.5(d,e) for two different excitation frequencies ($1.95 \cdot 10^4$ cm^{-1} and $2.05 \cdot 10^4$ cm^{-1}). As the Figure points out, the conjugation to the peptide chain does not affect significantly the vibrational properties of the porphyrin-peptide conjugate with respect to the free chromophore, especially in the low frequency modes region. A direct comparison with the aggregate system is lacking since it was not possible to reach the concentration needed to perform a Raman experiment.

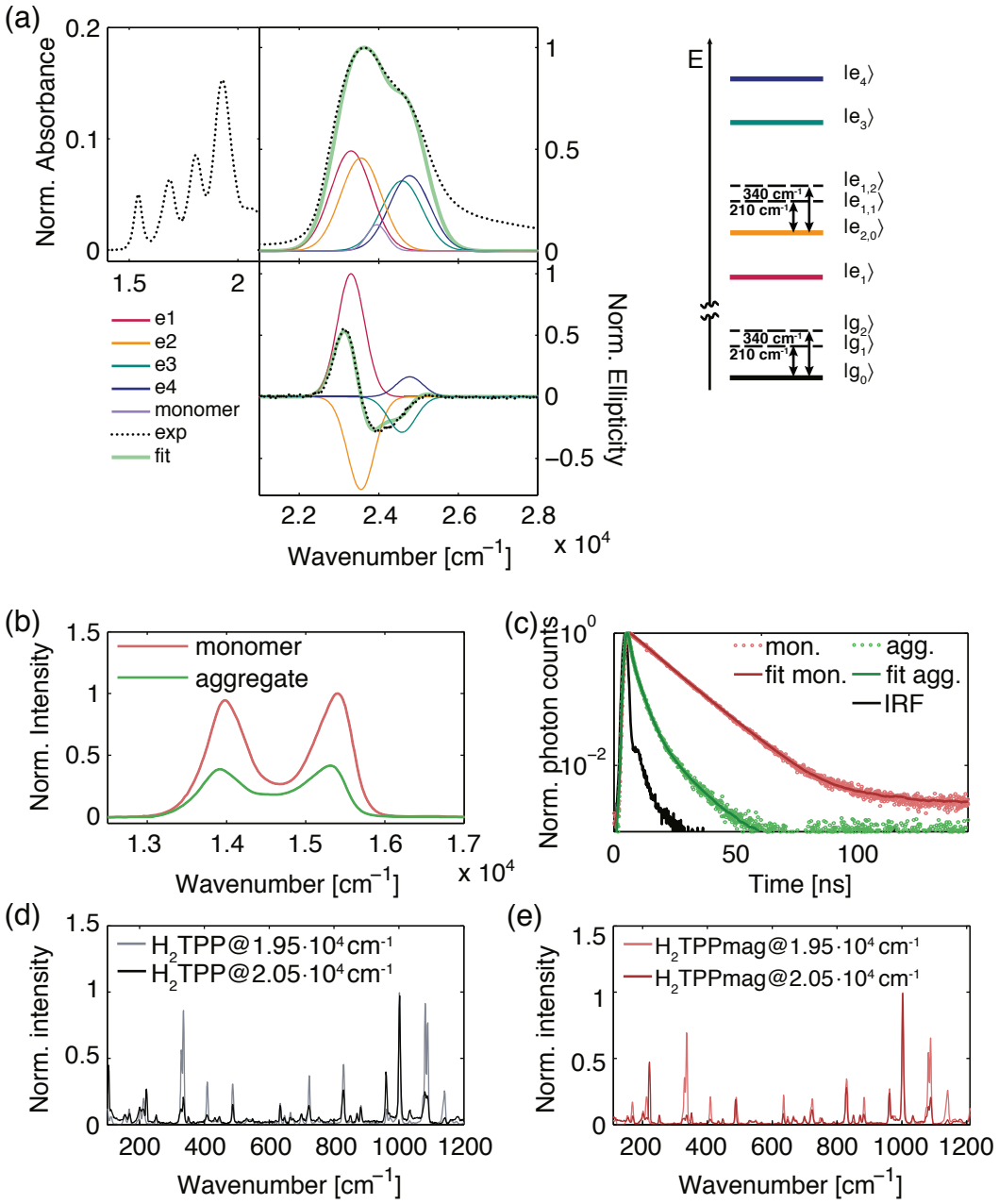

Figure 4.5 (a) Multi-Gaussian global fit of the B-band in the steady-state absorption and CD spectra and energy level diagram of the aggregate. (b) Steady-state fluorescence emission spectra (monomer exc. at $2.42{\cdot}10^4$ cm^{-1}; aggregate exc. at $1.95{\cdot}10^4$ cm^{-1}). (c) Experimental fluorescence decay traces of the monomer (pink) and of the aggregate (green) obtained by TCSPC technique (nanoled exc. source centred at $2.56{\cdot}10^4$ cm^{-1}) and multi-exponential fitting traces. (d) Raman spectra of H_2TPP powder with $1.95{\cdot}10^4$ cm^{-1} and $2.05{\cdot}10^4$ cm^{-1} excitation (T = 77 K). (e) Raman spectra of H_2TPP-magainin powder with $1.95{\cdot}10^4$ cm^{-1} and $2.05{\cdot}10^4$ cm^{-1} excitation (T = 77 K).

Table 4.1 Energy of the exciton states resulting from global fitting procedure performed on the B-band of the steady-state absorption spectrum and of the CD spectrum (Figure 4.5(a)).

State	Energy [cm^{-1}]
e_1	23300
e_2	23550
e_3	24580
e_4	24775

Table 4.2 Parameters of multi-exponential fitting of TCSPC measurements reported in Figure 4.5(c).

Monomer			Aggregate		
Component	Amplitude [%]	Time [ns]	Component	Amplitude [%]	Time [ns]
1	92	11.8	1	51	2.8
2	8	5.3	2	35	0.8
			3	14	9.3

4.2.4. 2DES characterization

A comparative study of the ultrafast dynamics of both the monomer and the aggregate of System I has been performed by mean of 2DES spectroscopy. The comparison with the monomer is particularly useful to identify the vibrational signatures of H_2TPP-magainin itself and to recognize which of the observed dynamics are unique to the self-assembled excitonic system.

To perform 2DES measures, the NOPA was tuned to give 60 fs pulses, centred at $2.38 \cdot 10^4$ cm^{-1} (Figure 4.6 (a) and Figure 4.7 a)) and with energy equal to 15 nJ at the sample position. These pulse conditions are far from being optimal, but the analysed B-bands fall into a spectral region very difficult to be obtained with our NOPA, making the measurements very challenging. Only another work performing 2DES on the Soret band has been published so far [80].

Thus, we accurately selected a spectral range guarantees the excitation of a superposition of the two exciton states $|e_2\rangle$ and $|e_3\rangle$ (as reported in the energy level diagram of Figure 4.5(a)) of the aggregate system.

4.2.4.1. Monomer

Rephasing spectra were acquired for population times ranging from 0 to 600 fs in 5 fs increments, with each experiment repeated two times to ensure reproducibility. The absolute and real parts of 2DES signal of the monomer present a very similar evolution along the population time, as shown in Figure 4.6(b). Since the investigated time window is very short, no significant 2D line-shape modifications are detected.

The global analysis method described in Section 3.2.8.2 revealed a bi-exponential decaying behaviour of the monomer (Figure 4.6(c)). It shows a fast (300 fs) and a longer time component ($\gg$ 1ps). The oscillating part of the rephasing signal reveals two main beating components (Figure 4.6(d)) whose frequency matches two Raman modes, at 230 cm^{-1} and 340 cm^{-1}, that are associated to a wagging vibrational mode of the phenyl rings and an in-plane deformation of H_2TPP, respectively [81]. Thus, the beatings detected in 2DES dataset of the monomer can be easily attributed to vibrational coherences of the chromophore.

4.2.4.2. Aggregate

The evolution along population time of the absolute and real parts of 2DES signal of the aggregate reveals similar features (Figure 4.7(b)). At early times the signal is elongated along the diagonal. As the population time increases, together with a decrease of the overall signal intensity, the global shape of the map becomes rounder and the signal relaxes from higher to lower detection frequencies.

The real part of the signal shows a main positive feature close to the diagonal and a negative contribution below the diagonal, probably due to an excited state absorption.

The global analysis method revealed three main exponential decaying components, two in the ultrafast timescale, 110 fs and 370 fs, and a longer contribution, ($\gg$ 1ps). The second and the third components match quite well the decaying contributions detected in the monomer, while the first represents an additional relaxation pathway found only after aggregation. The 2D-DAS (see Section 3.2.8.2) associated to the first component accounts for an ultrafast energy transfer from the higher exciton state to the lower one.

Figure 4.7(c), confirms the qualitative observation reported above. The region above the diagonal clearly decays as function of t_2, as denoted by the red area, corresponding to positive amplitudes. Despite the general decaying trend, the region below diagonal shows a clear increasing amplitude (in blue, negative amplitudes). As a consequence of the limited spectral width of the exciting laser pulses, the dynamics of the B band exciton states appears as alterations of a unique bi-dimensional feature, rather than separated contributions.

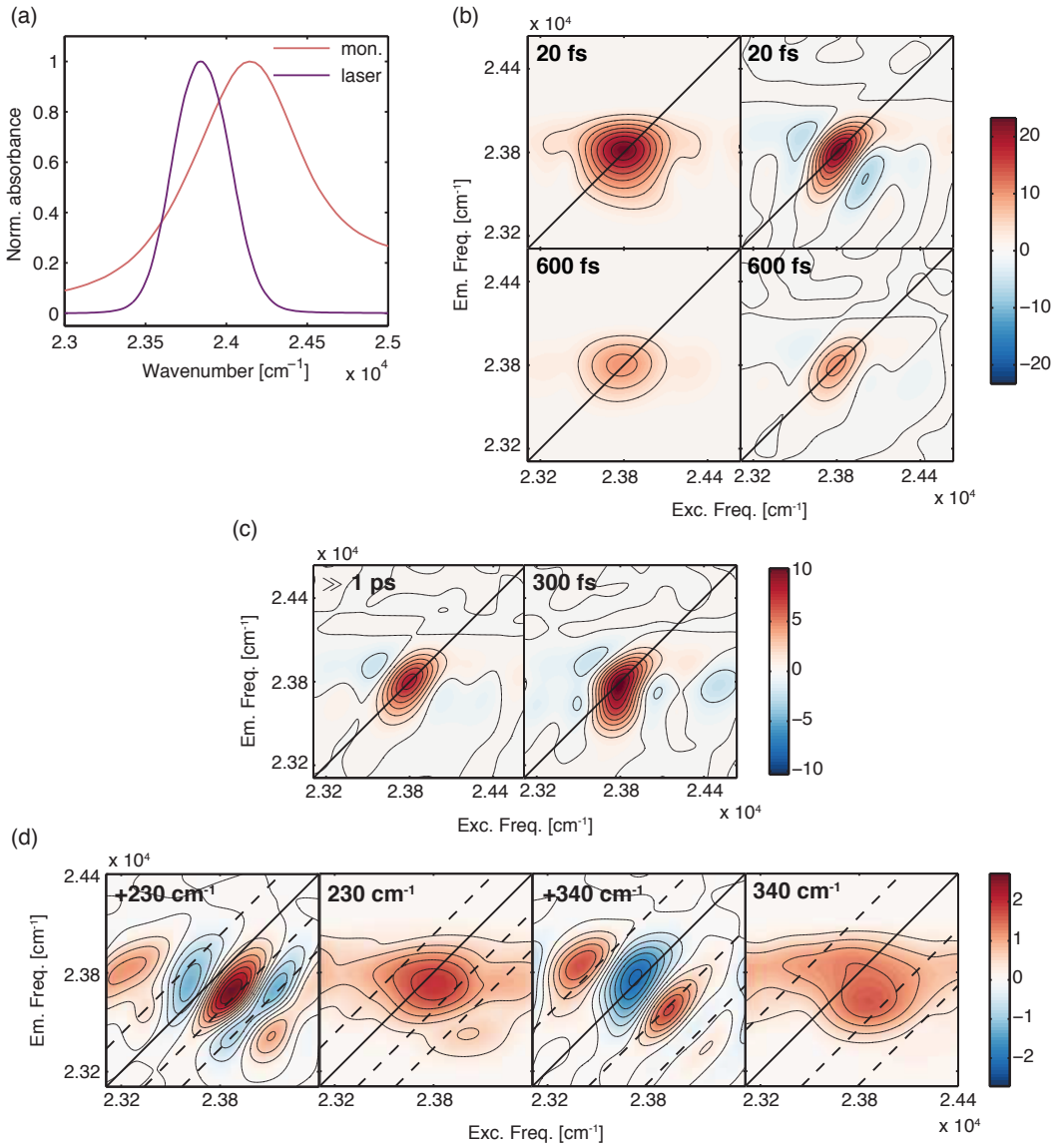

Figure 4.6 (a) Steady-state absorption spectrum of the monomer (pink line) and excitation laser spectrum in the 2DES experiment (violet line). (b) Absolute (left column) and real part (right column) of 2DES rephasing signal of the monomer. Results of the global fit of the monomer dataset: (c) real part of 2D-DAS of the two non-oscillating components for the rephasing signal; (d) real part (left) and modulus (right) of 2D-CAS related to the oscillating components.

The oscillating part of the signal reveals two main contributions with frequency equal to 210 cm^{-1} and 340 cm^{-1} (Figure 4.7(d)) and dephasing time much longer than the investigated time window ($\gg$ 1ps). As in the case of the monomer, the two oscillating signals are interpreted as vibrational coherences. Their amplitude distribution over the 2D map is compatible with what predicted by the DHO model (Section 2.7.1) and, moreover, their frequency matches well the frequency of the vibrational coherences detected also in the monomer dataset and in Raman spectra. However, the singular value decomposition (SVD) analysis performed on the residual matrix pointed out that the previous model was not capturing all the beatings present in the dataset since the first eigenvector shows additional oscillating components with frequency ranging from 500 cm^{-1} to 600 cm^{-1} [63]. The fitting procedure was not able to reproduce those features because they are located in a very narrow region at the edge of the 2D map and their amplitude is weak.

A more qualitative approach is therefore necessary and BTFR (see Section 3.2.8.1.2) resulted to be very helpful in revealing the positions where the high frequency beatings appear. After exploring the whole 2D map, short-living oscillations with frequency close to 600 cm^{-1} were detected at cross peaks positions between the two exciton states, above and below the diagonal, as shown in Figure 4.7(e).

Within the investigated spectral range, 600 cm^{-1} corresponds to the energy gap of the two exciton states that are coherently excited during the experiment. The qualitative analysis performed with BTFR suggested that those coherences lives more than 100 fs, which is quite a long dephasing time for purely electronic coherences at room temperature. Raman spectrum of the monomer reveals a vibrational mode at 630 cm^{-1} that is associated to an out of plane deformation of the porphyrin ring. In agreement with recently proposed models [8,9], this vibration may prevent the rapid loss of coherence among the two exciton states. The absence of such a signal in the 2DES dataset of the monomer is consistent with our hypothesis. Still, more proofs to sustain our interpretations are needed.

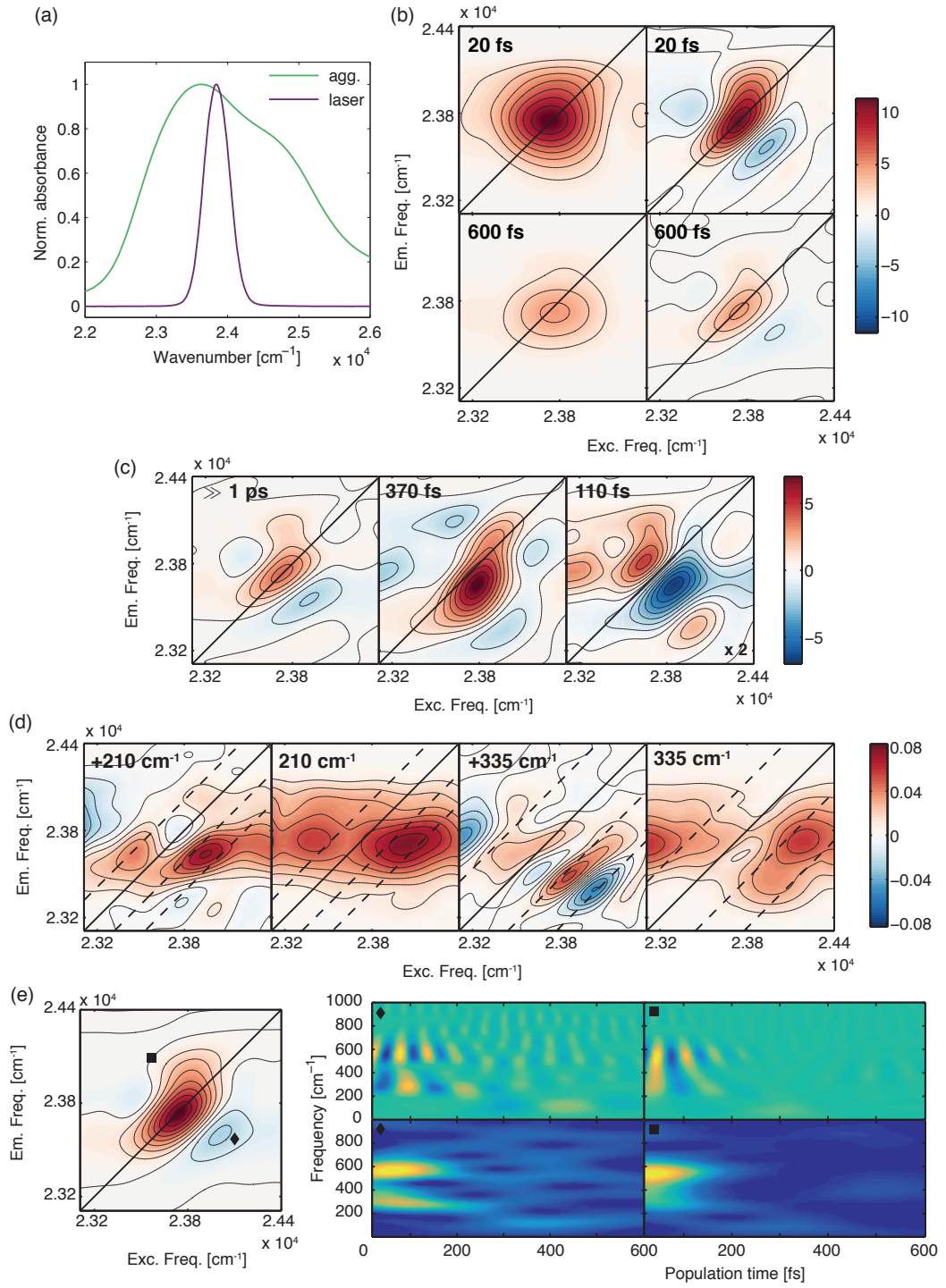

Figure 4.7 (a) Steady-state absorption spectrum of the aggregate (green line) and excitation laser spectrum in 2DES experiments (violet line). (b) Absolute (left column) and real part (right column) of 2DES rephasing signal of the aggregate at selected population times. Results of the global fit of the aggregate dataset: (c) real part of 2D-DAS of the two non-oscillating components for the rephasing signal; (d) real part (left) and modulus (right) of 2D-CAS related to the oscillating components. (e) BTFR analysis of the two cross-peaks (square and diamond) between the exciton states e_1 and e_2. The real part (first row) and the modulus (second row) of the BTFR map are shown.

4.3. System II

4.3.1. Monomer properties

The monomer of System II carries the same chromophore of System I, free base H_2TPP, which is covalently linked to the N-terminus of an artificially designed peptide, shown in Figure 4.8(a,b). The compound, that from now on will be called H_2TPP-*ap* (artificial peptide) was synthetized by E. Zurlo in the laboratories of prof. M. Gobbo, following the procedure reported in a previous work [82]. The 15–residues peptide (*ap*, H-(Ala-Aib)$_7$-Ala-OH) consists of an alternating sequence of L-alanine (Ala) and α-aminoisobutyric acid (Aib) that promotes α-helix secondary structure, as demonstrated by CD spectrum in Figure 4.8(d). The artificial peptide conjugate was studied in parallel with the natural magainin conjugate, System I described in Section 4.2, to highlight similarities in their optical and electronic properties and verify the possibility of using the peptide *ap*, easier and faster to synthetize, in artificial light harvesting applications.

The electronic structure of H_2TPP-*ap*, analogously to H_2TPP-magainin, doesn't show significant differences if compared to the free chromophore H_2TPP (Figure 4.8(b)). For a detailed description of the electronic properties of H_2TPP we refer to Section 4.2.1.

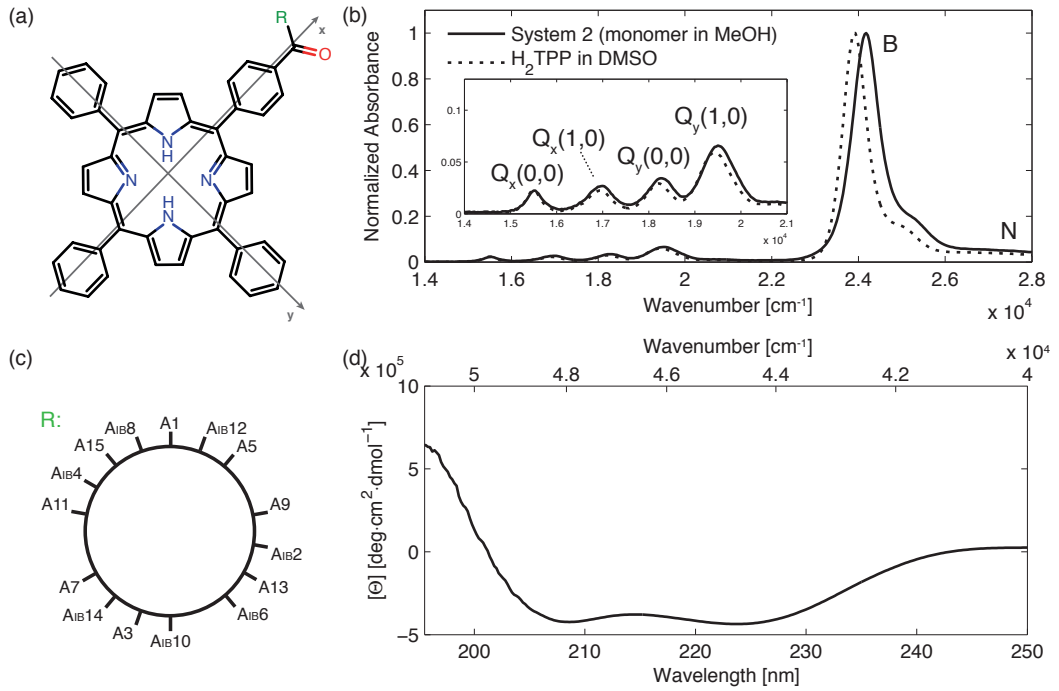

Figure 4.8 (a) Molecular structure of the functionalized H_2TPP. (b) Steady-state absorption spectra of the monomer of System II in MeOH (solid line) and of H_2TPP in DMSO (dashed line). The intensities are normalized to 1 on maximum of B band. (c) Helical wheel representation of the artificial peptide conjugated to the chromophore in (a). (d) Circular dichroism spectrum of a solution $5{\cdot}10^{-5}$M of the monomer of System II in MeOH (quartz cuvette, pathlength 1 mm).

4.3.2. Aggregate preparation

The optimal mixture of MeOH and H_2O to obtain self-assembling, and thus exciton interaction of H_2TPP-*ap*, was chosen following the same procedure as for System I. During the tests a concentration $5 \cdot 10^{-5}$ M of the monomer was used.
In the specific case of *ap*, the α-helix secondary structure of the peptide is not affected by the chromophores self-assembling process, as demonstrated by the CD spectra recorded in the near UV-region and reported in Figure 4.9(b). The same measurements were repeated in the B band spectral region (Figure 4.9(c)), revealing intense exciton interaction only for MeOH/H_2O ratios smaller than 50:50 (v/v). Also in this case, we selected the solvent mixture that ensures the stronger CD signal and the stronger coupling *J*, e.g. 30:70. Moreover, as for System I, no CD signal was detected in the Q bands spectral region, confirming the steady-state absorption measurements.

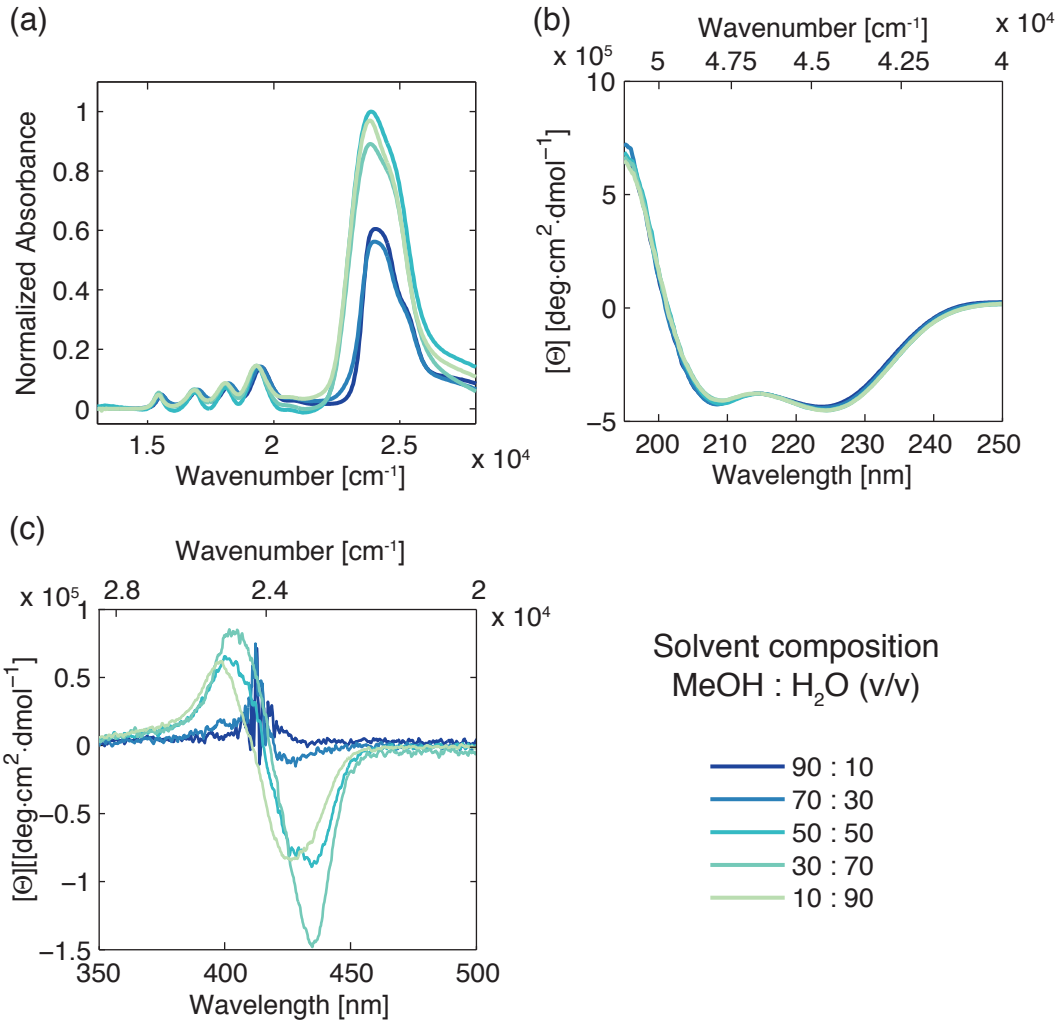

Figure 4.9 (a) Steady-state absorption spectra of solutions of the H_2TPP-*ap* with different composition of the solvent (conc. $5 \cdot 10^{-5}$ M, pathlength 1mm). (b) Circular dichroism spectra of the solutions in the peptide region. (c) Circular dichroism spectra of the solutions in the B band spectral region.

4.3.3. Preliminary optical characterization

A preliminary step of conventional characterization of the electronic properties of the monomer and of the aggregate was necessary to ease the subsequent ultrafast investigation.

A global multi-Gaussian fitting of both the steady-state absorption and CD bands helped to identify four main features under the congested B-band of the aggregate (Table 4.3), as shown in Figure 4.9(a), that are interpreted as the transitions to exciton states of the aggregate. Lacking the supramolecular structure, the same remarks reported for System I can be made.

A noticeable decreasing of the intensity of the fluorescence emission spectrum after aggregation is detected, as reported in Figure 4.9(b). The results obtained with steady-state fluorescence spectroscopy are further confirmed by the fluorescence lifetimes (Table 4.4) obtained from TCSPC measurements performed both on the monomer and on the aggregate (Figure 4.10(c,d)). This behaviour was detected also in System I and is ascribable to the presence of non-radiative relaxation pathways in the aggregate, that are absent in the monomer.

The study of System I pointed out that the vibrational structure of the free chromophore is conserved within the conjugated compound, especially for the low frequency modes. Moreover, we know from steady-state absorption and CD characterization, that the exciton is delocalized on the chromophoric part of the conjugated species. For those reasons, we took the Raman spectrum of free H_2TPP as reference for the subsequent interpretation of the ultrafast datasets.

Table 4.3 Energy of the exciton states resulting from global fitting procedure performed on the B-band of the steady-state absorption spectrum and of the CD spectrum (Figure 4.10(a)).

State	Energy [cm^{-1}]
e_1	23420
e_2	23995
e_3	24950
e_4	25740

Table 4.4 Parameters of multi-exponential fitting of TCSPC measurements reported in Figure 4.10(c,d).

Monomer			Aggregate		
Component	Amplitude [%]	Time [ns]	Component	Amplitude [%]	Time [ns]
1	97	12.0	1	28	5.1
2	3	5.5	2	72	1.6

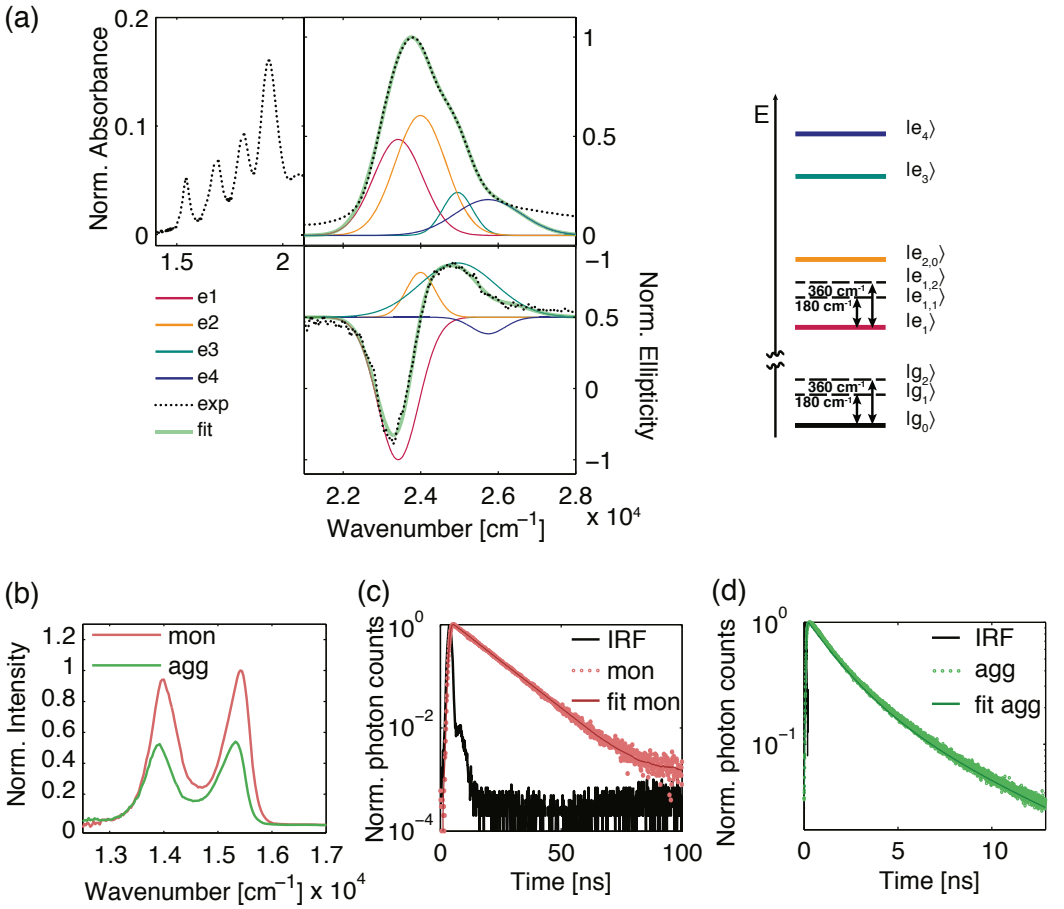

Figure 4.10 (a) Multi-Gaussian global fit of the B-band of steady-state absorption and CD spectrum and energy level diagram of the aggregate. (b) Steady-state fluorescence emission spectra (monomer exc. at $2.42 \cdot 10^4$ cm^{-1}; aggregate exc. at $1.95 \cdot 10^4$ cm^{-1}). (c) Experimental fluorescence decay trace of the monomer obtained by TCSPC technique (nanoled exc. source centred at $2.70 \cdot 10^4$ cm^{-1}) and bi-exponential fitting trace. (c) Experimental fluorescence decay trace of the aggregate obtained by TCSPC technique (the sample is excited by femtosecond Ti-Sapphire laser centred at $2.70 \cdot 10^4$ cm^{-1}) and bi-exponential fitting trace.

4.3.4. 2DES characterization

The 2DES measures have been carried out in the same experimental conditions applied to System I. This time we selected a spectral range that guarantees the excitation of a superposition of the two exciton states $|e_1\rangle$ and $|e_2\rangle$ (as reported in the energy level diagram of Figure 4.10(a)) of the aggregate system.

4.3.4.1. Monomer

The evolution of the absolute and real parts of 2DES signal of the monomer, are shown in Figure 4.11(b). In both case, at early times the signal is elongated along the diagonal, while, for higher values of population time, the signal relaxes to the lower part of the 2D map.
The global analysis revealed a bi-exponential decaying behaviour, consisting of a longer component ($\gg 1$ ps) and an ultrafast one (300 fs) (Figure 4.11(c)). The oscillating fingerprints of the monomer can be identified as four vibrational coherences having frequency (i) 170 cm^{-1}, (ii) 250 cm^{-1}, (iii) 330 cm^{-1} and 420 cm^{-1} (Figure 4.11d)). Components (i) and (ii) are related to a skeletal breathing mode and a wagging mode of the phenyl rings, respectively, while components (iii) and (iv) are two different in-plane deformation of H_2TPP [81].

4.3.4.2. Aggregate

The ultrafast behaviour of the aggregate of System II is similar to that of the monomer, since also in this case a bi-exponential decay is detected: the two time constants are respectively $\gg 1$ ps and 330 fs (Figure 4.12(c)). The coherent part of the signal revealed two main components with frequency equal to 180 cm^{-1} and 360 cm^{-1} (Figure 4.12(d)). They can both be ascribed to vibrational coherences already detected in the monomer. The global analysis reveals a third oscillating component with very short dephasing time (70 fs) and a frequency of 550 cm^{-1} (see Figure 4.12(e)) that doesn't match with any vibrational mode previously detected in H_2TPP-*ap*. Within the investigated spectral region, 550 cm^{-1} is compatible with the energy gap between the exciton states excited in a coherent superposition during the 2DES experiment. Moreover, the fast dephasing time is compatible with the expected damping time of an electronic coherence at room temperature. The absence of a vibrational mode with energy close to the energy gap between the exciton states of the aggregate may be the reason that explains why no long-lasting electronic coherence is detected. Moreover, the comparison with System I suggests that the flexibility of the peptide might have a non-negligible role in preventing the dephasing of the coherence.

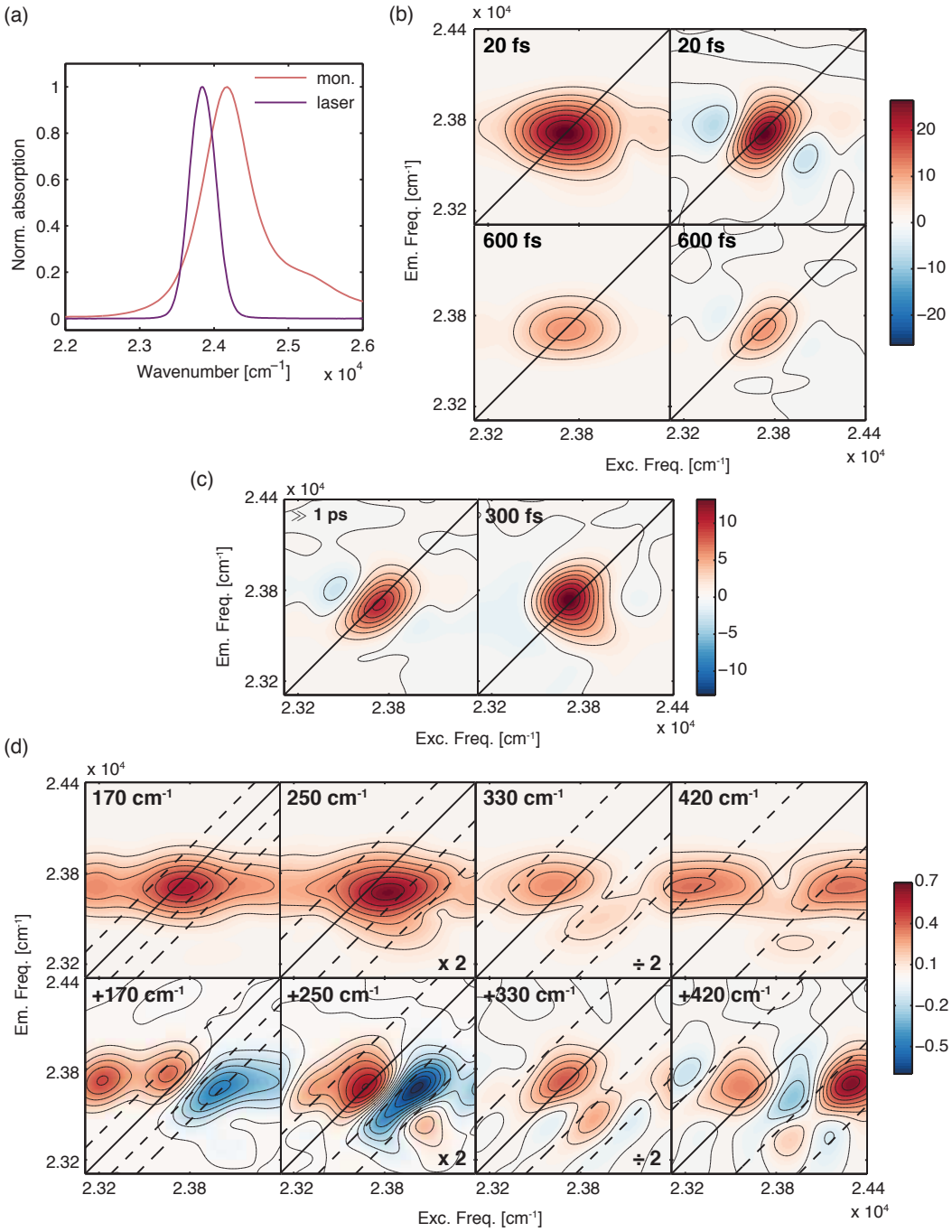

Figure 4.11 (a) Steady-state absorption spectrum of the monomer (pink line) and excitation laser spectrum of 2DES experiment (violet line). (b) Absolute (left column) and real part (right column) of 2DES rephasing signal of the monomer. Results of the global fit of the monomer dataset: (c) real part of 2D-DAS of the two non-oscillating components for the rephasing signal; (d) modulus (first row) and real part (second row) of 2D-CAS related to the oscillating components.

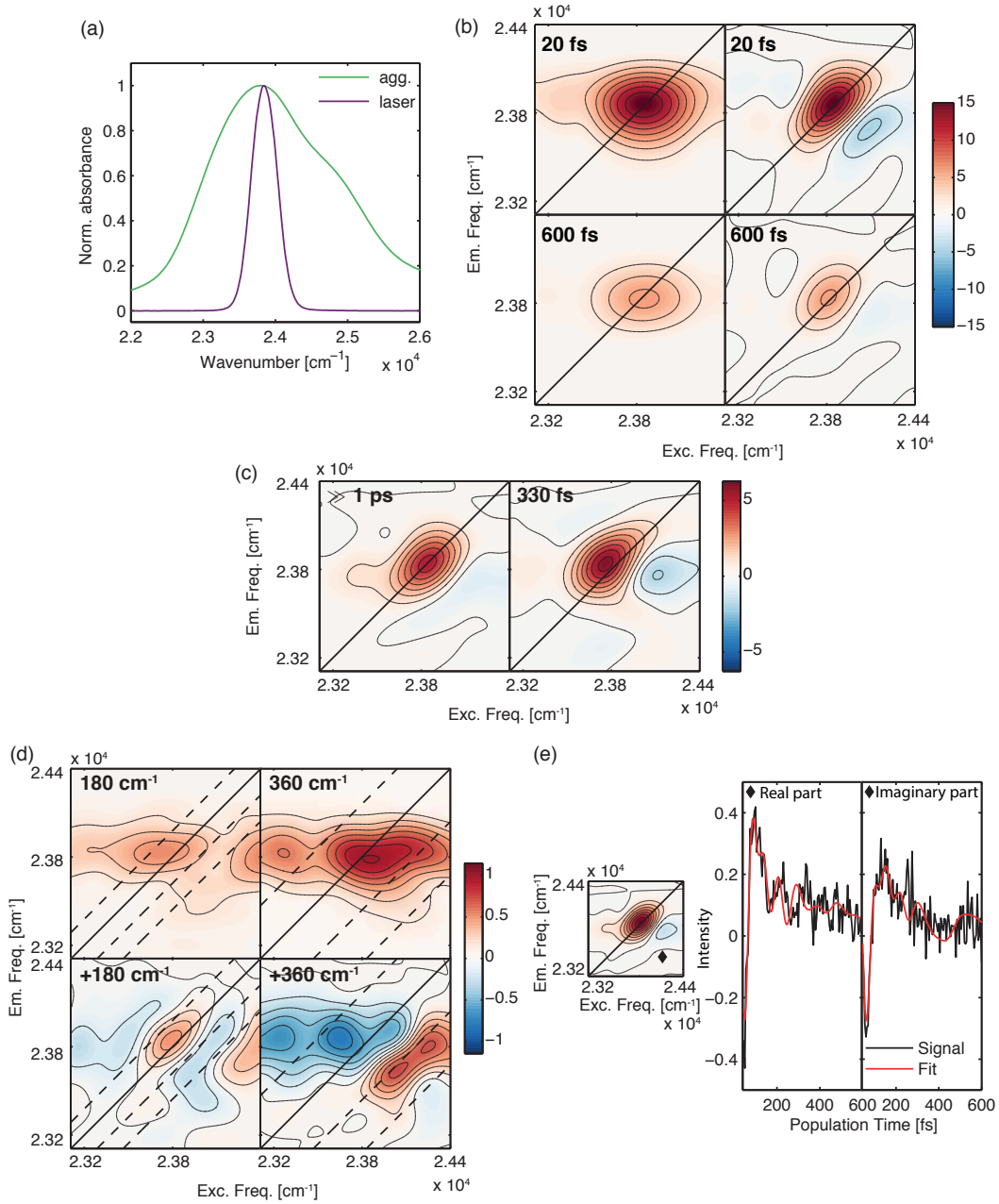

Figure 4.12 (a) Steady-state absorption spectrum of the aggregate (green line) and excitation laser spectrum of 2DES experiment (violet line). (b) Absolute (left column) and real part (right column) of 2DES rephasing signal of the aggregate. Results of the global fit of the aggregate dataset: (c) real part of 2D-DAS of the two non-oscillating components for the rephasing signal; (d) modulus (first row) and real part (second row) of 2D-CAS related to the oscillating components. (e) Real and imaginary part of the rephasing signal extracted for the cross-peak (diamond) below the diagonal. The fit (red line) reveals an overdamped oscillation with frequency close to 550 cm^{-1}.

4.4. System III

In System III we designed a monomer composed by a peptide part folded in helicoidal secondary structure, as the monomer of System II. However, the porphyrinic chromophore was replaced by a chlorin (Figure 4.1), characterized by a stronger Q_y transition dipole moment. This will allow moving the excitation bandwidth in 2D experiments from the B the Q band region, where the laser performances are considerably less prohibitive.

4.4.1. Monomer properties

The monomer was synthetized by F. Biscaglia in the laboratories prof. M. Gobbo following the procedure described in ref. [73]. The chromophore part consists in pyropheophorbide *a* methyl ester (PPH), shown in Figure 4.13(a), obtained from the natural occurring photosynthetic pigment, pheophorbide *a*. Its steady-state absorption spectrum (Figure 4.13(c)) is mainly determined by the delocalized π-electron system of the macrocycle conjugated ring, as for H_2TPP in 4.2.1.

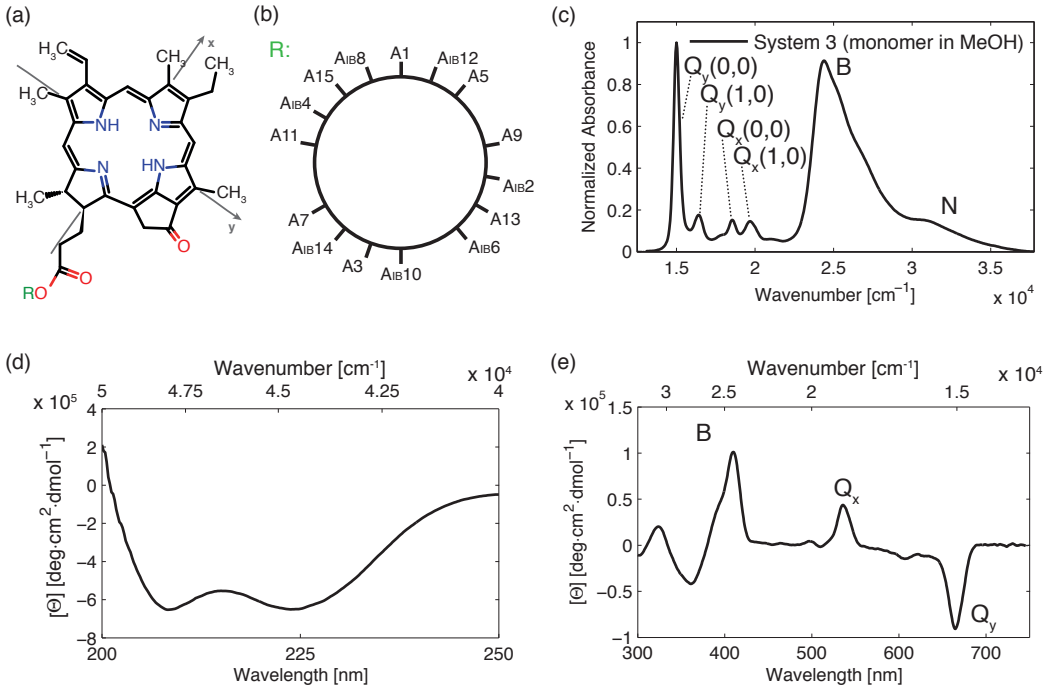

Figure 4.13 (a) Molecular structure of the functionalized PPH. (b) Steady-state absorption spectra of the monomer of System III in MeOH (solid line). The intensity is normalized to 1 on maximum of $Q_y(0,0)$ band. (c) Helical wheel representation of the artificial peptide conjugated to the chromophore in (a). (d) Circular dichroism spectrum of a solution $4.5{\cdot}10^{-5}$M of the monomer of System III in MeOH (quartz cuvette, pathlength 1 mm).

A typical chlorin spectrum shows four well-resolved Q bands at lower energy and a stronger allowed overlapping Soret (B) band system at higher energy. Both these bands are associated with electronic displacement along two orthogonal axes x and y. Following the notation used in the literature [83], x-axis is chosen perpendicular to the reduced double bond of the fourth pyrrole ring, while y-axis is directed approximately along the NH-NH axis (Figure 4.13(a)). The transition dipole moment related to the band of lower energy is y-polarized.

Many absorption components are observed in the Q region since the electronic transitions are followed by vibronic sidebands. $Q_y(0,0)$ and $Q_x(0,0)$ bands appear respectively at $1.50 \cdot 10^4$ cm^{-1} and $1.86 \cdot 10^4$ cm^{-1}. The vibronic progression for both the electronic transitions is well defined: the band at $1.64 \cdot 10^4$ cm^{-1} and the shoulder at $1.79 \cdot 10^4$ cm^{-1} are related respectively to $Q_y(1,0)$ and to $Q_y(2,0)$ transitions, while $Q_x(1,0)$ and $Q_x(2,0)$ bands appear at $1.97 \cdot 10^4$ cm^{-1} and at $2.10 \cdot 10^4$ cm^{-1}, respectively (Figure 4.13(c)) [84].

PPH also manifests dichroic properties, as shown in Figure 4.13(d). Opposite Cotton effect have been detected for $Q_y(0,0)$ and $Q_x(0,0)$ transitions that appear respectively as a negative and positive CD peaks. The CD signal in the Soret region has a reverse behaviour: a positive Cotton effect is detected for the transitions with lower energy within the B band, while a negative CD signal is associated to the transitions with higher energy (Figure 4.13(e)).

In the monomer of System III, PPH is conjugated to the 15–residues artificial peptide (*ap*) used also in System II. The alternating sequence of Ala and Aib, as seen for System II and demonstrated by CD spectrum recorded in the peptide range (Figure 4.13(d)), promotes α-helix secondary structure.

4.4.2. Aggregate preparation

The aggregate was prepared following the same procedure used for System I and II and using a constant concentration of monomer of $4.5 \cdot 10^{-5}$ M. In contrast with what noticed for H_2TPP, in this case also the Q bands result strongly affected by the coupling interaction since for PPH the associated transition dipole moments are more intense.

The peptide retains a predominantly α-helix conformation at all the $MeOH/H_2O$ ratios, as demonstrated by the CD spectra recorded in the near UV-region and reported in Figure 4.14(b). More extended alterations are detected in the CD spectra recorded in the visible region (Figure 4.14(c)), since both B and Q bands are involved in the exciton interaction and they reveal strong exciton couplings for ratios (v/v) smaller than 30:70. The increase of the polarity of the solvent results in the rising of a positive CD signal in the Q_y region accompanied by a global red shift of the band due to the change of the polarity of the environment. Since Q_x band is associated to a weak transition dipole moment, it suffers only a red shift, as observed

for Q bands in H_2TPP. Conversely, B band is strongly affected by exciton coupling upon aggregation, as demonstrated by the rising of a dispersive signal in the spectral region where we detected a positive Cotton effect in the monomer.
We selected the solvent mixture (e.g. 10:90) that induces the most marked changes listed above and thus guarantees higher exciton coupling.

4.4.3. Preliminary optical characterization

A clear picture of the photophysical properties of the monomer and of the aggregate is necessary to understand the behaviour of the artificial antenna.
As previously proposed, the components of the exciton band revealed in Q region were disentangled by a global multi-Gaussian fitting of both the steady-state absorption and CD band of the aggregate, as shown in Figure 4.15(a) and Table 4.5.
The mirror symmetry rule is observed in the steady-state fluorescence emission spectrum of the monomer, as shown in Figure 4.15(c). We can therefore conclude that the vibrational structure is essentially conserved in the electronic ground state and in the first excited state.
The intensity of the steady-state fluorescence emission spectrum of the aggregate is notably weaker, as found in the artificial antennas studied in the previous Sections. This experimental evidence is confirmed by the great difference between the FQY of the monomer, $(41.3 \pm 4.2)\%$, and the FQY of the aggregate, $(6.4 \pm 0.4)\%$. The profile of the fluorescence spectrum of the aggregate (Figure 4.15(c)) is peculiar, since it shows two maxima at $1.39 \cdot 10^4$ cm^{-1} and at $1.42 \cdot 10^4$ cm^{-1} with equal intensity.
The maximum of emission at higher energy is likely due to the fluorescence of residual monomers in solutions. Given the difference in the FQYs of the two species, even small quantities of monomeric species can give rise to a non-negligible fluorescence signal.
Fluorescence lifetime measurements (Figure 4.15(d)) were performed with a $1.64 \cdot 10^4$ cm^{-1} emitting nanoled. The time evolution of the monomer fluorescence emission decays can be described as a mono-exponential function, with a time constant of 7.1 ns. The aggregate trace, on the other hand, can be fitted only with a bi-exponential decay function. The first decay time is very short (1.7 ns), just a little longer than the exciting pulse, while the second is close to the decay time detected for the monomer (6.3 ns).
The excitation frequency corresponds, incidentally, to the maximum of the absorption $Q_Y(1,0)$ band of the monomer. Since FQY of the monomer is very high, the component with longer decay detected in the TCSPC measurement (Table 4.6) can be attributed to the fluorescence emission of traces of monomer still present in solution. The different value of the monomer lifetimes obtained from the two measurements is related to the different mixture of solvent that was used.
The shorter lifetime of the aggregate is compatible with its low value of FQY.

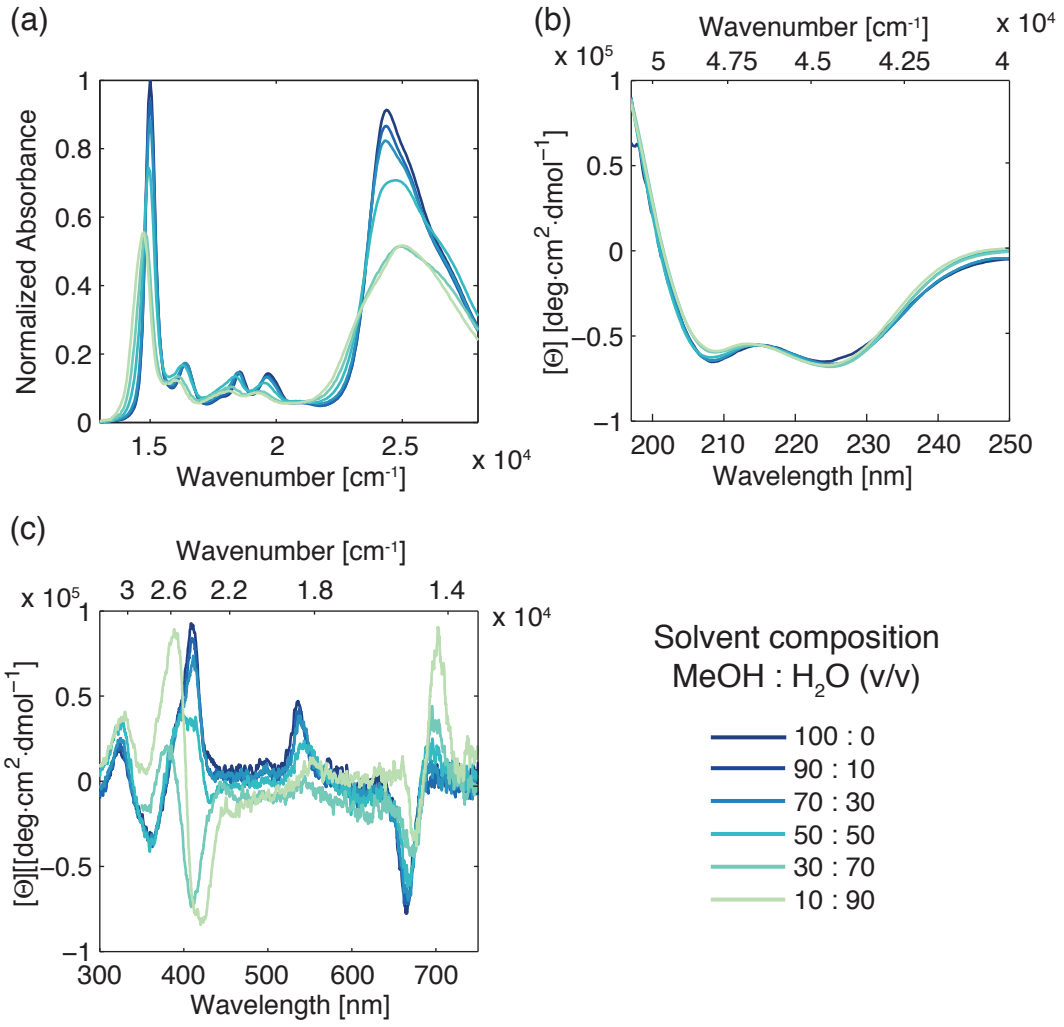

Figure 4.14 (a) Steady-state absorption spectra of solutions of the PPH-*ap* with different composition of the solvent (conc. $4.5 \cdot 10^{-5}$ M, pathlength 1mm). (b) Circular dichroism spectra of the solutions in the peptide region. (c) Circular dichroism spectra of the solutions in the visible spectral region.

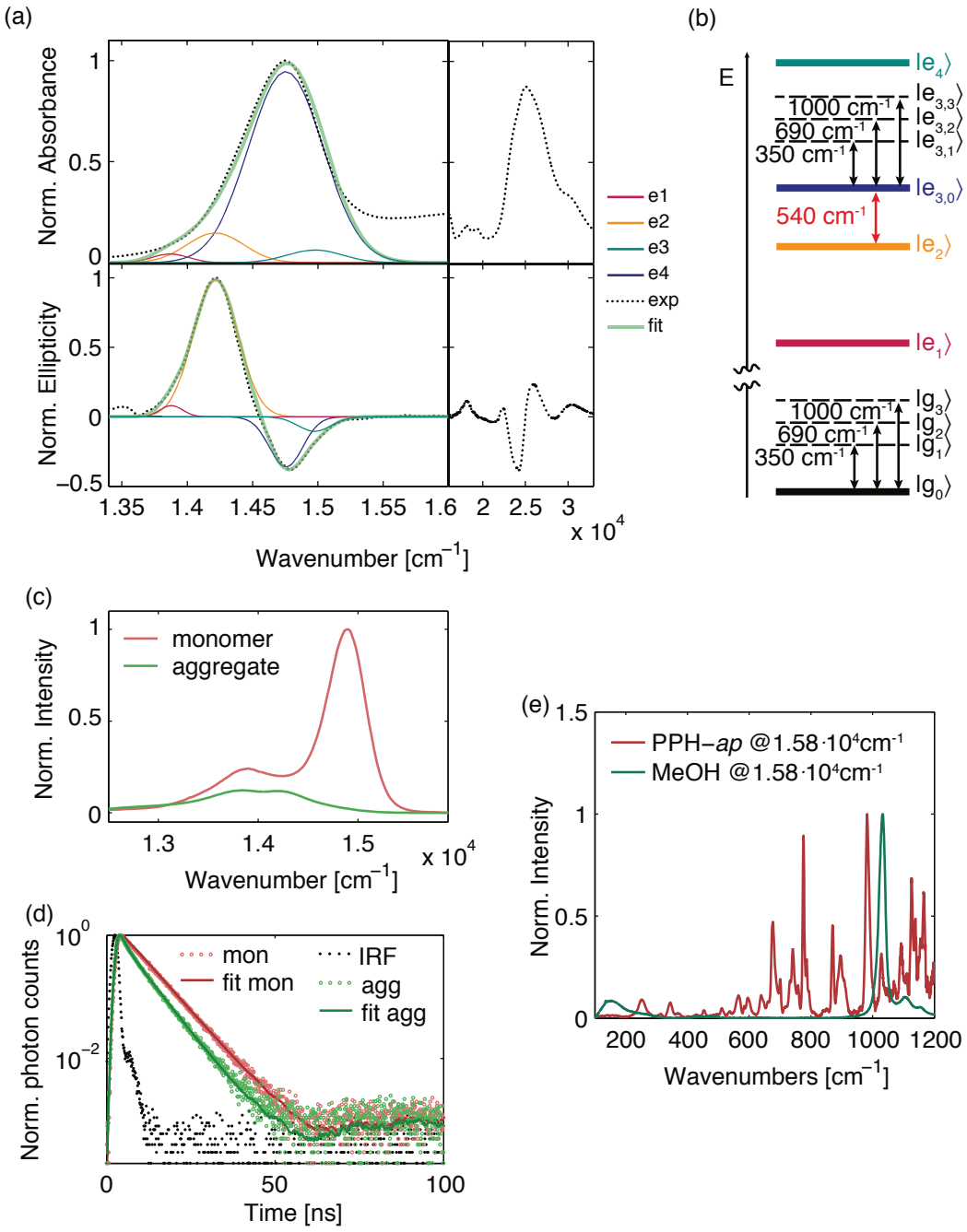

Figure 4.15 (a) Multi-Gaussian global fit of the Q_y-band of steady-state absorption and CD spectrum and (b) energy level diagram of the aggregate. (c) Steady-state fluorescence emission spectra (exc. at $1.64 \cdot 10^4$ cm^{-1}). (d) Experimental fluorescence decay traces obtained by TCSPC technique (nanoled exc. source centred at $1.64 \cdot 10^4$ cm^{-1}) and multi-exponential fitting traces. (e) Raman spectra of PPH-*ap* powder (pink line) and MeOH (blue-green line) with $1.58 \cdot 10^4$ cm^{-1} excitation (T = 77 K).

Table 4.5 Energy of the exciton states resulting from global fitting procedure performed on the Q_y-band of the steady-state absorption spectrum and of the CD spectrum (Figure 4.15(a)).

State	Energy [cm^{-1}]
e_1	13880
e_2	14220
e_3	14760
e_4	14980

Table 4.6 Parameters of multi-exponential fitting of TCSPC measurements reported in Figure 4.15(d).

Monomer			Aggregate		
Component	Amplitude [%]	Time [ns]	Component	Amplitude [%]	Time [ns]
1	100	7.1	1	82	6.3
			2	18	1.7

4.4.4. 2DES characterization

A comparative study of the ultrafast dynamics of the monomer and of the aggregate of PPH-*ap* has been performed with 2DES experiments (Figure 4.16 and Figure 4.17). The spectrum of the exciting pulses was tuned in order to cover both the $Q_y(0,0)$ band of the monomer and to create a superposition of the exciton states of the aggregate labelled as $|e_2\rangle$ and $|e_3\rangle$ in Figure 4.15(a). Within System III, the transition dipole moments of Q bands are more intense than what detected for both System I and II. Thanks to this property, rather than B-bands, we chose to study Q-bands since in their spectral region our setup can gain a broader laser bandwidth. It follows that the maximum beating frequency detectable within the experiment is higher.

Both rephasing and non rephasing spectra were acquired for population times ranging from 0 to 1 ps in 5 fs increments to catch the ultrafast coherent behaviour of the system, and from 1 to 2 ps in 20 fs increments to reveal longer non coherent dynamics. Each experiment was repeated two times to ensure reproducibility.

4.4.4.1. Monomer

The shape of the 2DES map of the monomer does not change significantly as function of the population time, since the investigated window is quite short. The flattening of the positive signal elongated on the diagonal slightly increases and an ultrafast decay of the intensity of the 2DES signal is recorded.
This observation is confirmed by the global fitting procedure that disentangled a bi-exponential decaying behaviour for the monomer. Both rephasing and non rephasing experiments show an ultrafast component (70 fs) ascribable to the spectral diffusion and a decay with a time constant longer than the investigated time window ($t \gg 2$ ps). The slower component was expected since we are investigating the dynamics of the lower excited state that has a lifetime of few nanoseconds.
The 2D-DAS associated to the two components are reported in Figure 4.16(c).
The coherent part of the rephasing signal revealed several oscillating components ascribable to vibrational coherences of both the ground and first excited state (Q_y) of the monomer. As reported in Figure 4.17(e), the spectral distribution of the frequency of the beatings reproduces quite well the main features of the Raman spectrum recorded for the powder of PPH-*ap*. Moreover, 2D-CAS revealed that the oscillating signals are arranged in a "chair-pattern" as expected for vibrational coherences in the DHO model [24] (Figure 4.16(d)). In the rephasing measures, the features are mainly localized below the diagonal as shown by the 2D-CAS associated to positive oscillation frequency and shown in Figure 4.16(d). The phase trend observed in the real maps further confirms the assignment. For vibrational coherences, the amplitude of the oscillating signal is expected to change sign for displacement from the diagonal equal to a vibrational quantum [85]. As examples, in Figure 4.16(d) the 2D-CAS only for the three main beatings are shown, while the complete list of the detected oscillating components is reported in Table 4.7.

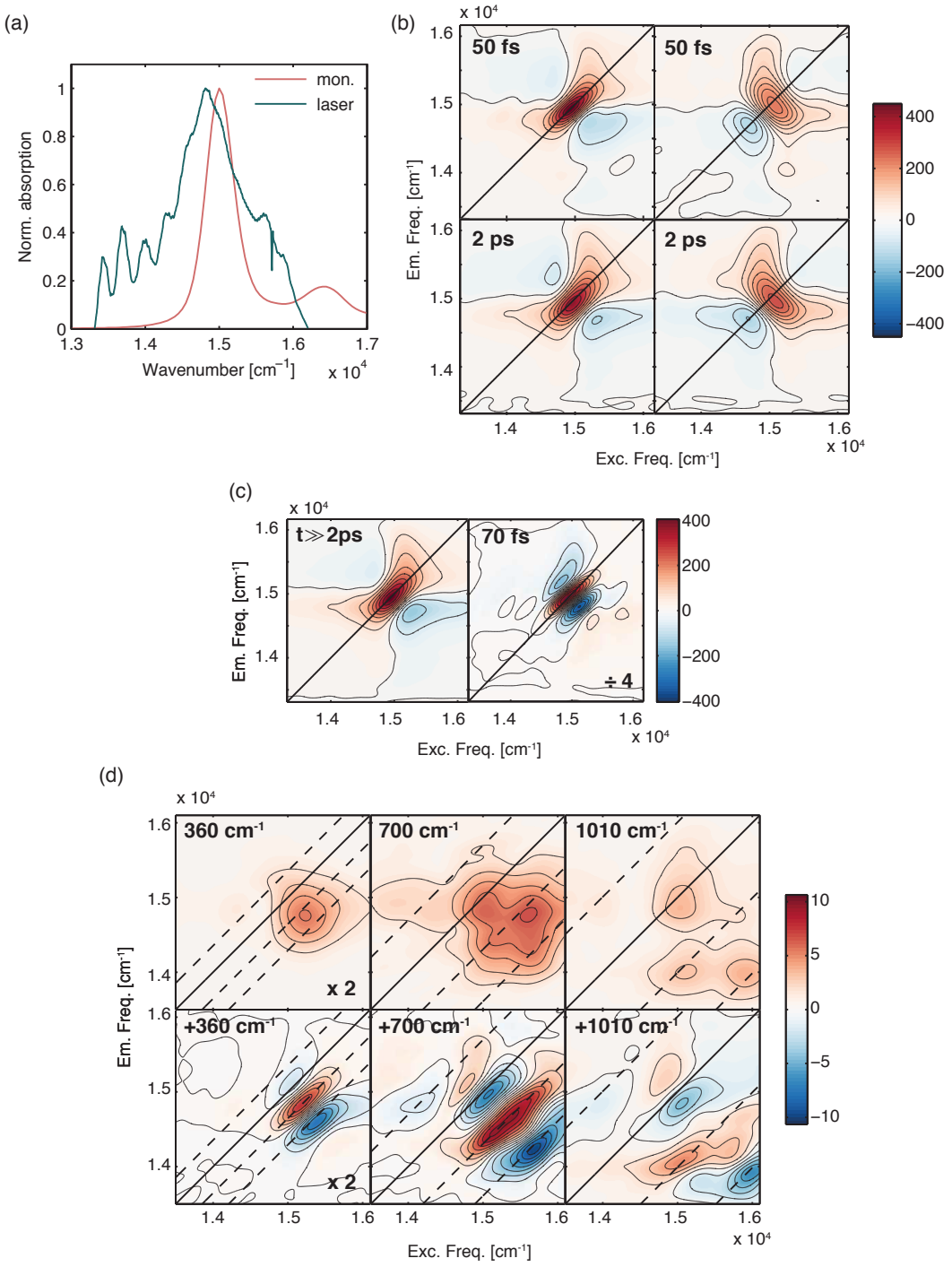

Figure 4.16 (a) Steady-state absorption spectrum of the monomer (pink line) and excitation laser spectrum of 2DES experiment (blue-green line). (b) Rephasing (left column) and non-rephasing (right column) maps of the monomer for different population times. Results of the global fit of the monomer dataset: (c) real part of 2D-DAS of the two non-oscillating components for the rephasing signal; (d) modulus (first row) and real part (second row) of 2D-CAS related to the main oscillating components.

4.4.4.2. Aggregate

The evolution of 2DES map of the aggregate reveals interesting features. For short population time delays the real rephasing signal is elongated along the diagonal, as in the monomer, but the detected signal presents a broader linewidth along the diagonal, in agreement with the steady-state absorption band. Secondly, non rephasing map is anti-diagonal, since inhomogeneous dephasing in non-rephasing signals (free induction decays) results in round peaks with significantly broader antidiagonal linewidths [15]. At longer delay times, a cross-peak clearly rises below the diagonal both in the rephasing and in the non rephasing maps. The signal is localized at $(1.476,1.421)\cdot 10^4$ cm^{-1} coordinates that correspond to the cross-peak between two exciton states, respectively $|e_3\rangle$ and $|e_2\rangle$.

The non-coherent part of the rephasing signal reveals a bi-exponential decaying behaviour. A sub-100 fs component was detected and assigned to spectral diffusion. As expected [86], this phenomenon is slower (80 fs) in the aggregate than in the monomer. The second decaying component is much faster (3.4 ps) than in the monomer ($\gg$ 2 ps). This is not surprising because excitonic interactions can give rise to additional non-radiative relaxation pathways.

The oscillating pattern in the 2D spectra of the aggregate is very similar to that of monomer. The spectral distribution of the beatings, as shown in Figure 4.17(e), matches very well the monomer signatures, even if the aggregate peaks are more broadened, indicating a wider distribution of the energy of the coherences than in the monomer. It is worthy to remember that in agreement with time-frequency indetermination principle, a larger bandwidth corresponds to a shorter time.

Moreover, the 2D-CAS associated to the main oscillating components of the aggregate dataset and reported in Figure 4.17(d) show a good matching with the corresponding 2D-CAS of the monomer. The similarities with the monomer dataset, together with the typical chair-pattern distribution of oscillating signals, endorse the interpretation of those beatings in terms of purely vibrational coherences both of the ground and excited state of the aggregate.

A careful comparison of the Fourier transform spectra of monomer and aggregate revealed a discrepancy in the spectral region of the beatings between 500 and 600 cm^{-1}, where a possible beating related to the coherence between $|e_2\rangle$ and $|e_3\rangle$ should be found (red square in Figure 4.17(e)). The aggregate shows a peak broadened towards higher energies and this contribution comes from the overdamped beating signal reported in Figure 4.17(f). It was detected at coordinates $(1.476,1.421)\cdot 10^4$ cm^{-1} that we attributed to the cross-peak below diagonal between the two exciton states $|e_2\rangle$ and $|e_3\rangle$ of the aggregate. In other words, we detected an oscillating signal whose frequency matches the energy gap between the two identified exciton states.

Raman spectrum in Figure 4.17(e) reveals that PPH-*ap* has a vibrational mode with frequency close to the energy difference between $|e_2\rangle$ and $|e_3\rangle$. Despite the energy requirement necessary to sustain a long living electronic coherence was satisfied, no beating component with long dephasing time could be detected. Instead, we found an overdamped oscillation with the typical behaviour expected for an electronic coherence at room temperature, but that cannot be considered relevant for quantum energy transport.

In conclusion, our study on System III clearly pointed out that matching the energy gap between two exciton states and the energy of a vibration mode of the system is necessary but not sufficient condition to create a long lasting electronic coherence among the chromophores.

Moreover, the results obtained for System III are in good agreement with the ultrafast dynamics detected in the excitonic framework of System II, while in System I we found a possible long lasting vibronic coherence. Indeed, in both System II and System III the peptide constituent is rigidly stuck in a helicoid conformation, while in System I self-assembling takes the peptide to lose its secondary structure.

Table 4.7 Complete set of output parameters of the global fitting procedure for 2DES datasets of the monomer (upper part) and of the aggregate (lower part).

Monomer						
Component	1	2	3	4	5	6
Frequency [cm^{-1}]	0	0	±260	±350	±640	±700
Time constant [ps]	$\gg 2$	0.07	0.34	0.76	0.16	0.36
Component	7	8	9	10	11	12
Frequency [cm^{-1}]	±750	±870	±1010	±1070	±1120	±1160
Time constant [ps]	$\gg 2$	0.19	0.84	0.42	0.26	0.42
Aggregate						
Component	1	2	3	4	5	6
Frequency [cm^{-1}]	0	0	±250	±350	±690	±750
Time constant [ps]	3.6	0.08	0.24	0.40	0.74	0.24
Component	7	8	9			
Frequency [cm^{-1}]	±870	±1000	±1230			
Time constant [ps]	0.34	$\gg 2$	$\gg 2$			

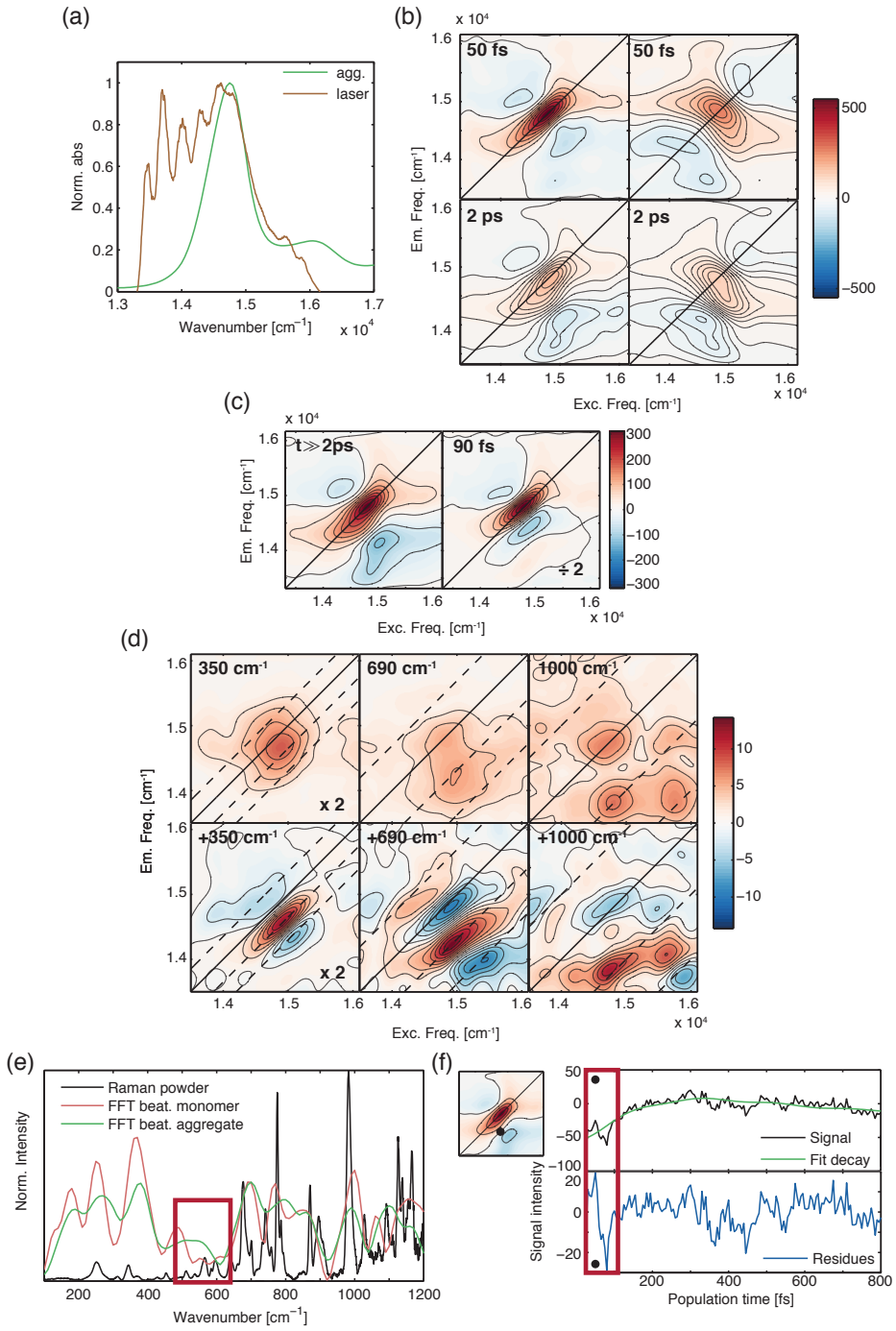

Figure 4.17 (a) Steady-state absorption spectrum of the aggregate (green line) and excitation laser spectrum of 2DES experiment (brown line). (b) Rephasing (left column) and non-rephasing (right column) maps of the monomer for different population times. Results of the global fit of the aggregate dataset: (c) real part of 2D-DAS of the two non-oscillating components for the rephasing signal; (d) modulus (first row) and real part (second row) of 2D-CAS related to the main oscillating components. (e) Fourier transform of the coherent part of the 2DES datasets of the monomer (pink line) and of the aggregate (green line). Raman spectrum of the powder of PPH-*ap* (black line) is also reported. (f) Real part of the rephasing signal extracted for the cross-peak (circle) $(1.476,1.421)\cdot10^4$ cm^{-1}. The residuals (blue line, lower box) of the fit (green line, upper box) reveal an overdamped oscillation with frequency close to 550 cm^{-1} (red square).

4.5. Final remarks

The compared analysis of the three different artificial antennas proposed in this Chapter revealed non-trivial aspects possibly involved in preventing the dephasing of electronic coherences.

The study pointed out that the presence of an intra-molecular vibrational mode matching the energy gap between two exciton states is not a sufficient condition to gain a long-lasting exciton coherence, as it was instead suggested by recently proposed theoretical models [29].

Besides, we found evidences suggesting that the presence of a flexible peptide chain may play a key role in preventing the coherence dephasing. Indeed, *ap*, constituent of System II and III, retains its α-helix secondary structure in all solvent conditions, even in the polar mixture that favours the aggregation process. In both these antennas no long-lasting beating ascribable to an electronic superposition was detected.

By contrast, magainin, the peptide component of System I, loses its secondary structure in polar solvents (see Figure 4.4(b)). In this system, an exciton coherence with a longer dephasing time was recorded. A possible explanation of the phenomenon is that the pigments within the aggregate are subject to fluctuations of the protein environment that influences intensely the energy of the sites and sustain the exciton superposition itself. Still, a more targeted investigation on the effects of the protein scaffold and of the solvent must be pursued.

5 Photosynthetic chromophores

2DES found its success and its primary application in studying the ultrafast excited state dynamics of light-harvesting systems to disentangle the principles of their remarkable efficiency.

One complicating factor in the interpretation of 2DES datasets is that both vibrational and electronic coherences may contribute to the oscillating part of the spectroscopic signal, since ultrafast pulses may create coherent superposition of electronic as well as vibrational states. Vibronic coupling, as described in Section 2.7.1, gives rise to oscillating coherences of ground-state and excited-state vibrational wave packets that might overlap with electronic features [16]. Several efforts have been paid in the attempt of disentangling vibrational and electronic coherences but there is still no agreement on the methodology to distinguish between them in measurements [9,24,87]. Therefore, to assess the real origin of quantum beats in 2DES measurements on antenna complexes and ascertain the role of electronic coherence in the energy transport during light harvesting, the study of the beating behavior of isolated pigments can be particularly helpful. In isolated pigments, only vibrational and/or vibronic contributions are indeed expected to contribute to the beating pattern.

The work presented in this Chapter aims at investigating the peculiar spectroscopic signatures of the most abundant photosynthetic pigments, chlorophyll *a* (Chl*a*) and bacteriochlorophyll *a* (Bchl*a*). A clear picture of their dynamical behavior is the first step to understand the mechanisms that support the extremely efficient photosynthetic process in more complex antenna systems and, furthermore, to apply the acquired knowledge in developing biomimetic devices for energy conversion.

5.1. Chlorophyll a

Chl*a* is the most abundant photosynthetic light harvester, widespread in cyanobacteria, green algae and terrestrial plants [88–90]. It serves a dual role, as light absorber and as redox participant in electronic excitation trapping and electron transporting events towards the reaction centres. Chl*a* appears to be ubiquitous in oxygenic photosynthesis and its role is determined by its unique photochemical properties. For this reason, these pigments have been widely studied, not only to assess their role in biological functions, but also with the aim of developing molecular models for bio-inspired artificial systems.

Previous investigations on femtosecond dynamics of the first excited state of Chl*a* were aimed at identifying the vibrational modes more strongly coupled to the electronic transition and at distinguishing ground state and excited state modes with high resolution together with the role of solvent and spectral diffusion [91–93]. So far, spectroscopic investigations were mainly focused on Chl*a* photophysical behavior following first excited state excitation. Previous ultrafast coherent spectroscopic characterization studied the intramolecular vibrational modes contributing to the oscillatory part of the 2DES signal. The beating with frequency ~740 cm^{-1} was analyzed in detail since it is related to a vibrational mode specifically coupled to the electronic transition to the first excited state. Frequencies and dephasing times of ground and excited state vibrational coherences were indeed determined [91]. Moreover, the high time resolution of 2DES was exploited to assess the early spectral time evolution that highlighted significant solvent dependence in the extent of inhomogeneous broadening and in the dynamics of spectral diffusion, assigned to specific solute-solvent interactions [93].

In this work the attention was mainly focused, instead, on the relaxation and decoherence dynamics among the vibronic states of the first excited states. Our study aims, more generally, to give a more detailed insight into the internal conversion process within the first excited state of Chl*a*. The capability of 2DES to follow dynamics on femtoseconds time-scale was exploited to unravel downward excitation energy pathways of the most abundant natural harvester. This process is particularly relevant since it contributes to the rate of the primary charge separation in reaction center in oxygenic photosynthesis. The coherent vibrational motions involved in internal conversion process and determining its mechanism were disentangled. Our approach is based on the combined analysis of 2DES datasets, recorded using different laser exciting spectra, with resonant and off-resonant Raman spectra.

5.1.1. Experimental methods

2DES experiments were performed tuning the commercial NOPA to give exciting pulses in two different spectral ranges as shown in Figure 5.2(a) and Figure 5.3(a), centered at $1.54 \cdot 10^4$ cm^{-1} (set I) and $1.56 \cdot 10^4$ cm^{-1} (set II), respectively. The temporal profile of the excitation pulses at the sample position was characterized by FROG measurements. The pulse duration and the spectral bandwidth are 18 fs and 820 cm^{-1} (FWHM) in the first set of measures; 24 fs and 610 cm^{-1} in the second set. The energy of the exciting pulses was 7 nJ at the sample position. The optical layout used for 2DES measurements is described in detail in Chapter 3.

Rephasing spectra were acquired for population times ranging from 0 to 800 fs in 5 fs increments, with each experiment repeated three times to ensure reproducibility for both the spectral windows.

The samples were prepared dissolving Chl*a* (Sigma Aldrich) in MeOH and diluting until the optical density was 0.3 with a pathlength of 1 mm. The resulting concentration was $5 \cdot 10^{-5}$M. In this conditions Chl*a* is not expected to form aggregates and, indeed, we verified that, lowering the concentration down to two orders of magnitude, the steady-state absorption spectrum resulted to be stable [93–95]. Steady-state absorption spectra were acquired before and after each scan to control that no degradation of the sample was occurred during the 2DES measurements.

Steady-state and time-resolved fluorescence emission characterization of MeOH solutions of Chl*a* were also performed to assess the photophysical properties of the lowest energy excited states.

Resonance and off-resonance Raman spectra were recorded on Chl*a* powders with a home-built micro-Raman system, based on a Triax-320 ISA spectrograph with excitation sources at $1.58 \cdot 10^4$ and $1.95 \cdot 10^4$ cm^{-1}, respectively.

5.1.2. Results

5.1.2.1. Preliminary characterization of chlorophyll a

Steady-state absorption, steady-state fluorescence emission and fluorescence lifetime characterizations were performed on Chl*a* in methanol solution (Figure 5.1(b,c)). Resonance and off-resonance Raman spectra were recorded on Chl*a* powder instead (Figure 5.1(d)).

The Gouterman's four orbital model [74] predicts the Q-band of Chl*a* spectrum as consisting in two (possibly overlapping) independent electronic transitions called Q_x (S_2) and Q_y (S_1). The names of the bands come from the polarization directions within the macrocycle plane as shown in Figure 5.1(a).

The bands related to those transitions in Chl*a* steady-state absorption spectrum are broadened by inhomogeneous effects and by the activation of low-frequency molecular vibrations. However, the higher energy vibronic transitions appear as separated sidebands.

While the lower energy band (at $1.50 \cdot 10^4$ cm^{-1}) is assigned to $Q_y(0,0)$ transition, the assignments of the other transitions is not straightforward. Historically, two different interpretations of the Q bands were proposed. The first, proposed in the '60s [96], identifies the Q_x component with the signal at $1.74 \cdot 10^4$ cm^{-1}, while the second, from the '80s [94], assigns that transition to the feature at $1.70 \cdot 10^4$ cm^{-1}. This last attribution has been driven by the observation that the energy gap ΔE between Q_x and Q_y transitions is significantly solvent dependent, since solvent molecules can coordinate to the central Mg atom[94,95]. Thus, energy distribution of electronic states is strongly affected by the coordination geometry of the central Mg atom. Alcohols induce 6-fold coordination resulting in an energy distribution of the electronic states as depicted by the '80s assignment.

More recent interpretations state that Q_x and Q_y transitions, far from being independent transitions, are strongly mixed. Since Q_x is nearly resonant with the vibronically active mode of Q_y at 1500 cm^{-1}, the *x*-polarized intensity is split nearly equally into two components and thus is distributed over the entire Q-band system [97,98].

To further support the *x* character of the band at $1.70 \cdot 10^4$ cm^{-1}, we reported the steady-state emission fluorescence spectrum in Figure 5.1(b). Mirror symmetry rule between absorption and emission spectra is clearly violated. The absorption spectrum is much more intense in the spectral region of the Q_y sideband, suggesting indeed a contribution of a second electronic transition, which from now on will be simply identified as Q_x [99].

Then we characterize the fluorescence lifetime (Figure 5.1(c)) of Chl*a* in MeOH, revealing a bi-exponential behavior with time constants t_1=5.7 ns (94%) and t_2=10.4 ns (6%), which is the first evidence of complex relaxation dynamics within Q bands.

Comparing the experimental Resonance and off-resonance Raman spectra, we can infer that almost the same vibrational modes are active in the ground and in the first exited state. This is in good agreement with the small Huang-Rhys factors reported in previous works [100] due to the rigidity of the molecular structure. Moreover, the comparison of the two spectra shows that the mode at 740 cm^{-1} (due to in-plane deformation of pyrrole rings [101]) is noticeably enhanced in resonance conditions.

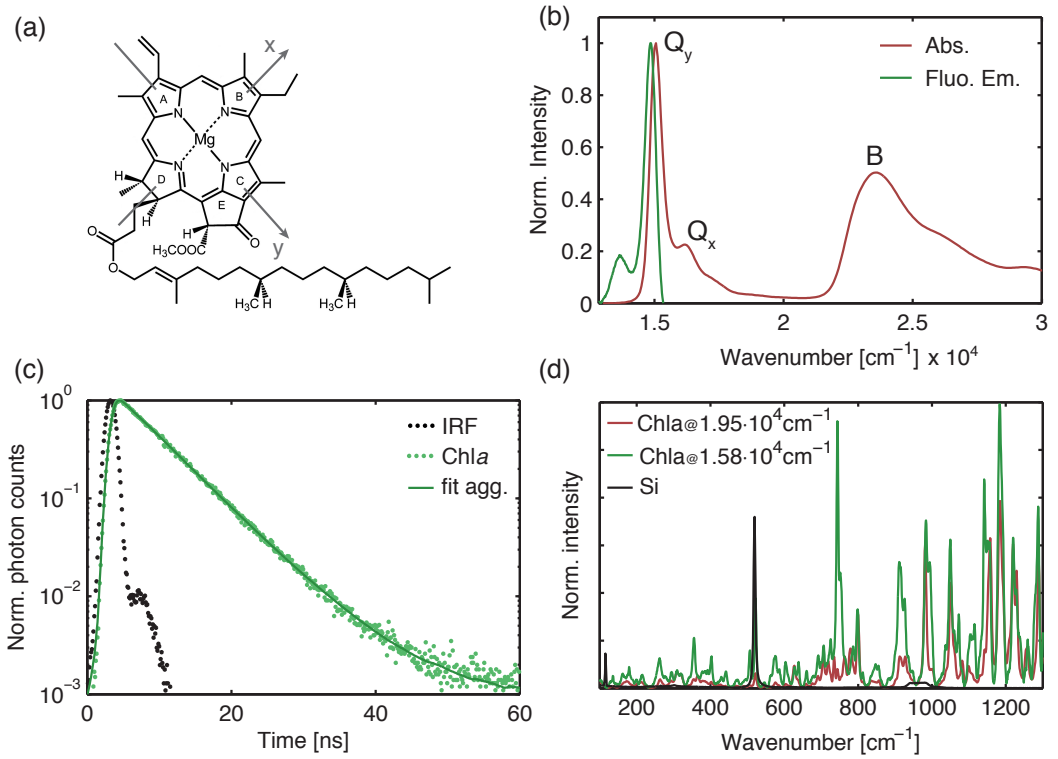

Figure 5.1 (a) Molecular structure of the Chl*a*. The directions of dipole moments polarization are also reported. (b) Steady-state absorption spectrum of the monomer of Chl*a* (red line) and steady-state fluorescence emission spectrum (green line). The intensities are normalized to 1 on the maximum of Q_y band. (c) Experimental fluorescence decay trace of Chl*a* (green dots) obtained by TCSPC technique (nanoled exc. source centred at $2.56 \cdot 10^4$ cm^{-1}, instrumental response in black) and multi-exponential fitting trace (green line). (d) Off-resonance (red) and Resonance (green) Raman spectra of Chl*a* powder (T = 77 K). The reference Silicon signal is also reported (black).

5.1.2.2. 2DES characterization

2DES is a powerful tool to unveil both populations and coherences dynamics in the ultrafast timescale. Unlike Raman spectroscopy that gives information only on the energy of the vibrational modes, 2DES can distinguish between ground or excited state vibrational modes, providing also the dephasing times of vibrational coherences. Since we are dealing with an isolated pigment, the coherent part of 2DES signal is expected to be consistent with Raman measurement results.

Within the first set of measurements, the identification of the vibrational modes more strongly coupled with the Q_y transition has been performed, following the dynamics of the first 800 fs after photoexcitation. According to the prediction of DHO model (Section 2.7.1), the signatures arising from vibrational coherences of the ground and of the excited state occurs in distinguishable positions in 2DES map, and thus both their energy and dephasing times can be characterized separately.

In set I, the exciting laser spectrum was tuned so to cover mainly the $Q_y(0,0)$ band, with a bandwidth of 800 cm^{-1} (green-blue line in Figure 5.2(a)).

The rephasing maps shows the typical features expected for isolated Chl*a* molecules [91,93] (Figure 5.2(b)): at early population times the positive signal is elongated on the diagonal, with negative features on both sides. Significant 2D line-shape modifications are not detected within the investigated time window.
The global fitting analysis revealed two non-oscillating components: (i) a slower decay (3.6 ps) describing the relaxation of the whole map and (ii) a faster contribution (150 fs) associated to spectral diffusion dynamics that confirms previous observations reported in literature [93,102]. 2D-DAS of set I are reported in Figure 5.2(d).
The analysis of the coherent part of the 2DES signal revealed several components. If we model the system as a DHO featuring a single vibrational state with frequency $\omega_2 = \Omega$ both in the ground and in the excited state, it is demonstrated that the signals arising from vibronic coherences and contributing to the rephasing signal form a characteristic chair-pattern of five contributions [24]. The cross-peaks at coordinates $(\varepsilon, \varepsilon \pm \Omega)$, where ε is the energy of the electronic transition, are crucial to disentangle and characterize the dynamics of the excited and ground state vibrational coherences. From the careful analysis of the signals occurring in those two positions, the main vibrational modes of the ground and of the excited state were detected and reported in Table 5.1. The results are compared with the Raman signatures detected in the preliminary characterization and with the results of previous studies. The intensity of the 740 cm^{-1} mode clearly rises in the region where vibrational coherences of the excited state are expected (Figure 5.2(c)). This observation perfectly agrees with the intensity enhancement of the same vibrational mode in the resonant Raman spectrum.

Table 5.1 Frequency of vibrational coherences revealed in 2DES measurements (set I) and vibrational Raman modes. As comparison, the vibrational modes detected in previous works are also reported. The most intense oscillations are identified with asterisks.

Ground state [cm^{-1}]	Excited state [cm^{-1}]	Raman modes [cm^{-1}]	Vibr. coherence[a] [cm^{-1}] [92]	Vibr. coherence[b] [cm^{-1}] [92,100]
260*	260*	262	259	259
400	400*	403	345	407
480*	450	442	456	--
540*	520	506	518	519
660	650	660	--	667
740	745	744	740	744
760*	790*	780	789	799

[a] Measures performed in acetone.

[b] Measures performed in petroleum ether/2-propanol.

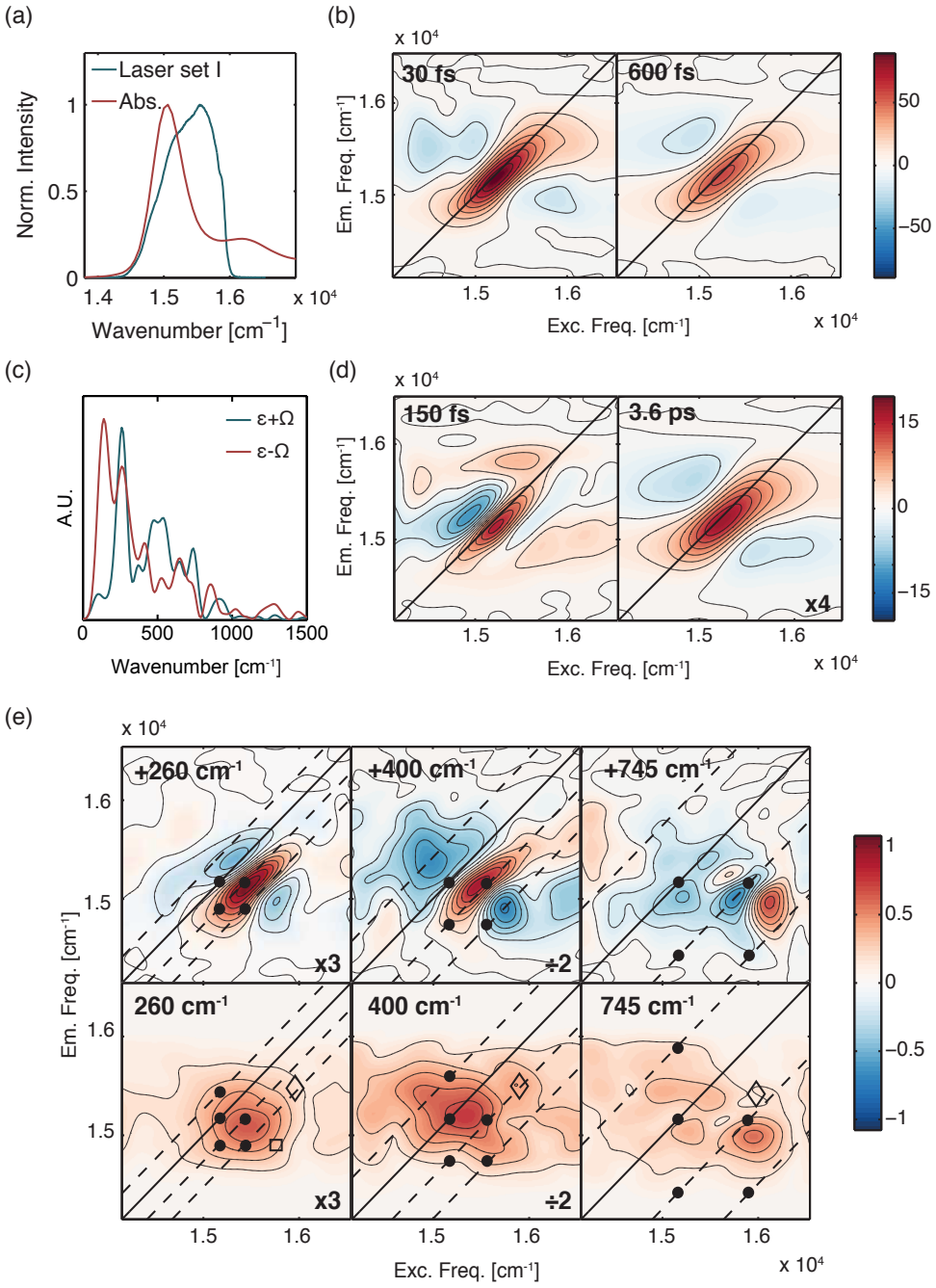

Figure 5.2 (a) Steady-state absorption spectrum of Chl*a* (red line) and excitation laser spectrum of 2DES experiment in Set I (blue-green line). (b) Real part of 2DES rephasing signal at two different population times. (c) Fourier Transform of coherent signals found for coordinates $(\varepsilon, \varepsilon + \Omega)$ and $(\varepsilon, \varepsilon - \Omega)$, where vibrational coherences of excited (blue line) and ground (red line) state are expected, respectively. (d) 2D-DAS of the two non-oscillating components for the rephasing signal computed by global fit analysis. (e) Real part (upper row) and modulus (lower row) of 2D-CAS related to the oscillating components. Black dots pinpoint the positions of vibrational coherences predicted by the DHO model, while diamonds and squares show further contributions not predicted by the model.

In agreement with previous works, the vibrational modes with frequency 260 cm^{-1}, 400 cm^{-1} and 760 cm^{-1} cm^{-1} are particularly relevant, thus the related 2D-CAS are reported in Figure 5.2(e). If inhomogeneous broadening at room temperature is taken into account, the positions where the oscillating signals are detected in the 2D map and the positions predicted by the DHO model (black circles) are in good agreement.

The few discrepancies between the predicted and experimental patterns can be explained invoking processes not accounted in the DHO model. For example, the signal in the 2D-CAS of the 260 cm^{-1} oscillation, pinpointed with the empty square, can be easily attributed to a coherence most likely involving hot vibrational states of the electronic ground state, which can be thermally populated at room temperature (at room temperature k_BT is indeed estimated to be the 250 cm^{-1}).

All the 2D-CAS reported in Figure 5.2(e) show a feature in the high-energy portion of the maps (diamonds), not fully explainable with previous considerations. To further characterise the nature of those coherences and have an insight of the relaxation dynamics within the electronic states of the Q bands, a second set of measurements was performed. The exciting laser spectrum was tuned to cover both the $Q_y(0,0)$ band and its sideband with mainly Q_x character (Figure 5.3(a)).

Figure 5.3(b) shows the evolution of the 2DES map over population time. For early times, two different diagonal features can be distinguished: (i) a signal elongated along the diagonal and centred at $1.54 \cdot 10^4$ cm^{-1} that corresponds to the blue tail of the Q_y state, whose dynamics has been investigated in set I; (ii) a second diagonal contribution appearing around $1.64 \cdot 10^4$ cm^{-1}. The position of this signal is compatible with the red part of the sideband with Q_y- Q_x mixed character. This peak is characterized by an ultrafast dynamics since its amplitude halves in 100 fs. In addition, 2DES maps are characterized by the presence of a strong cross peak between the recognised diagonal contributions, featuring a lively dynamics in the first hundred femtoseconds after photoexcitation. Moreover, a negative feature is clearly recognisable above the diagonal, resulting from ESA pathways opened by shifting the exciting spectrum towards higher energies.

The positions and the dynamic evolution of the main peaks characterizing the 2DES maps, reported in Figure 5.3(b), suggest the presence of an ultrafast relaxation dynamics from Q_x state to lower energy states, i.e. vibronic states within the Q_y band.

The global fitting analysis disentangled the non-oscillating and the oscillating signatures of the 2DES signals of Chl*a*. Within the first group, three main components were detected with decaying constants of (i) $\gg$2 ps, (ii) 2 ps and (iii) 110 fs and the resulting 2D-DAS are reported in Figure 5.4(a,c).

The time constant determined for component (i) is consistent with the lifetime of Q_y electronic state reported in the preliminary characterization, while component (ii) is compatible with the value of the slower decay detected in set I. Indeed, 2D-DAS

of the two components show positive signals along the diagonal in the spectral region assigned to Q_y state.
Component (iii) revealed a negative feature elongated on the diagonal in the spectral region attributed to Q_y band. It clearly accounts for a rising of the population of the electronic state Q_y in the ultrafast timescale. Furthermore, the higher energy portion of the diagonal reveals a weak positive signal which is associates to a decaying feature. It is located at energy compatible with the Q_x state. We can therefore attribute this ultrafast time component to the relaxation of population from Q_x to Q_y state within the Q bands.
2D-DAS of component (iii) revealed also a complex pattern for excitation frequency $1.64 \cdot 10^4$ cm^{-1}: the signal amplitude along this x coordinate shows, indeed, several sign changes (Figure 5.4(a)). This evidence suggests the presence of complex relaxation dynamics between Q_x and Q_y state, involving several intermediate states. Thus the overall process is not characterized by a unique decaying component, but, more likely, by a distribution of components with different time constants. Within the exploited approach we are only capable to capture the *effective* 110 fs exponential evolution.
The dynamics of the population of the states, together with the results of the global fit, are extracted at relevant positions in the diagonal region of the 2DES maps and plotted in Figure 5.4(b). The real rephasing signal as function of the population time confirms the presence of a 110 fs dynamics removing population from the highest energy state Q_x towards the lowest energy states Q_y. 2DES signal of the cross-peak below diagonal is also shown, denoting the non-oscillating behavior of the transfer in this timescale.

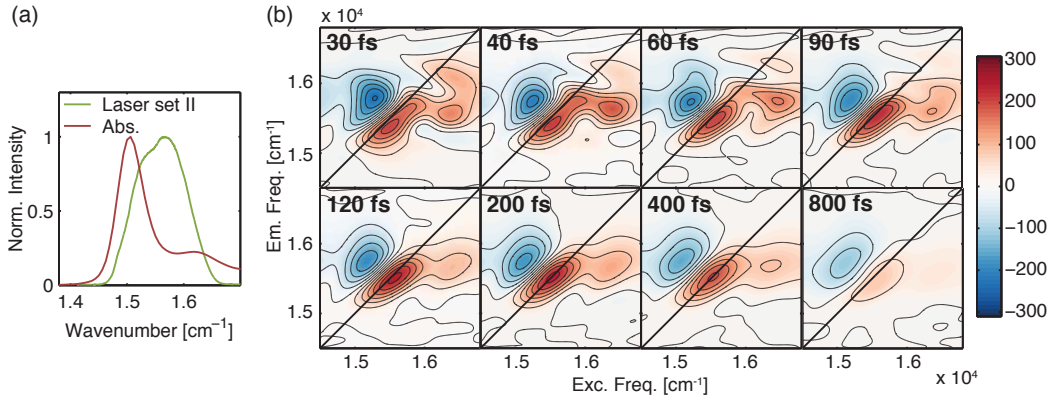

Figure 5.3 (a) Steady-state absorption spectrum of Chl*a* (red line) and excitation laser spectrum of 2DES experiment in Set II (green line). (b) Real part of 2DES rephasing signal at different population times.

The main oscillating component revealed by the global fit consists of an overdamped coherence with frequency centred at 700 cm^{-1} and dephasing time of 45 fs (Figure 5.4(d)). As expected [103], 2D-CAS obtained for the oscillating components with positive frequency shows an intense pattern below diagonal, while the oscillating component with negative frequency appears above. The two signals appear at cross-peak positions located between the electronic states Q_y and Q_x.
As explained in Section 2.7.1, the signal arising from electronic coherences appear as a double feature above and below diagonal at positions $(\varepsilon_1, \varepsilon_2)$ and $(\varepsilon_2, \varepsilon_1)$, where ε_1 and ε_2 are the energy values of the two electronic states.
The coherent behaviour of the regions out of the diagonal is quite complex: the distribution in frequency of the beatings is quite wide and characterized by ultrafast damping times. Thus, the global fitting analysis has some limitations in disentangling all the oscillating components that are present in the 2DES signal.
In this peculiar case a Fourier analysis was considered more adequate. Thus, once the non-coherent part of the signal was determined by the global analysis, it was subtracted from the 2DES signal and the resulting residuals, containing the purely oscillating signals, are Fourier transformed.
This analysis confirms the presence of the vibrational coherences already emerged in set I, mainly contributing in positions compatible with the chair-pattern predicted by the DHO model.

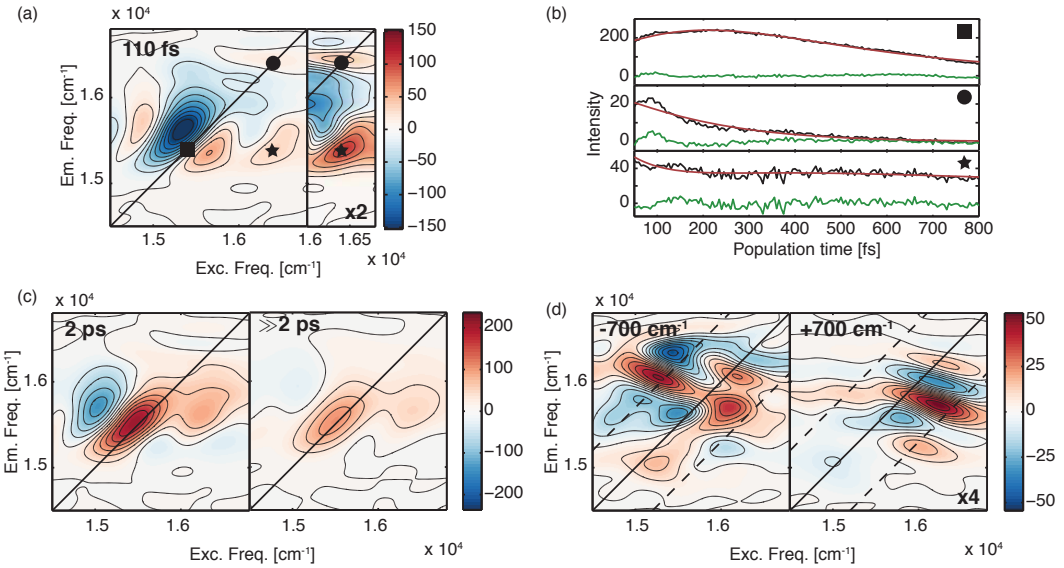

Figure 5.4 Results of global fit analysis. (a) 2D-DAS of component with 110 fs time constant. The higher excitation frequency region is zoomed and shown in the right panel. Symbols represents the coordinates of 2D map where the traces of 2DES signal (black lines) reported in panel (b) have been extracted. The output of fitting procedure (red line) and the residuals (green line) are also shown. (c) 2D-DAS of the other two non-oscillating components. (d) 2D-CAS of the overdamped oscillating component with central frequency equal to 700 cm^{-1}. The amplitude distribution of oscillations with positive and negative frequency are shown.

Nevertheless, oscillating components with different frequency were found at the main cross-peak position and not fully corresponding to Raman frequencies. The main components detected in this spectral region are: (i) 470 cm^{-1}, (ii) 560 cm^{-1}, (iii) 690 cm^{-1} and (iv) 760 cm^{-1}, as highlighted in the FT power spectrum reported in Figure 5.5(a). The associated Fourier maps, e.g. the 2D maps where the amplitude of oscillations with a selected frequency is plotted as function of excitation and emission energy, are shown in Figure 5.4(d). In all the maps two features are present above and below diagonal, whose distance from the diagonal itself corresponds exactly to the analysed frequency. Signals contributing in these positions can be explained only invoking relaxation pathways that involve coherences between Q_x state and vibronic states $Q_{y,n}$ of the first excited state. The steady-state absorption spectrum (Figure 5.1(b)) revealed that the transition dipole moment to Q_x state, which contributes to the response function of these signals, is relatively large. It is not surprising that the features arising from those coherences are very intense within the investigated spectral window. Indeed, the amplitude of the signals related to the vibrational chair-pattern and centred at Q_y energy is dampened by the smaller overlap with the laser spectrum.

We will refer to such coherent superpositions of Q_x and $Q_{y,n}$ states as *electronic/vibronic coherences* (EVC) to distinguish their different origin from the vibrational coherences observed in set I and described in Section 2.7.1.

The Feynman diagrams associated to these signals (Figure 5.4(b)) explain why the frequency of the oscillations contributing at the cross peaks can be identified as the energy gaps between the lower vibronic states $Q_{y,n}$ and the electronic state Q_x, where $Q_{y,n}$ states were identified both by the Raman analysis and by set I analysis (Figure 5.1(c) and Figure 5.2(e)).

The dynamic behaviour of EVC supports our assignment. Vibrational coherences of set I have indeed damping times in the order of hundreds of femtoseconds, whereas EVCs have damping times faster than 60 fs, as demonstrated by Figure 5.6. Their overdamped behaviour also explains the high indeterminacy in the frequency domain and thus the broadening of the corresponding FT spectra (Figure 5.5(a)).

Short-time Fourier transform (STFT) of the EVC signals was performed to estimate their dephasing times. STFT results in a 2D time-frequency plot (Figure 5.6(a)) where the evolution in population time of the beatings with distinct frequency can be followed. In order to quantify the damping time of specific beatings, we cut horizontal slices of the 2D STFT 2D plot at fixed frequencies.

The resulting traces are then fitted with a the convolution of an exponential function and a Gaussian window that accounts for the boundary effect of STFT [69] (Figure 5.6(a)). This procedure revealed EVC dephasing times of about 45 fs, as shown in Table 5.2.

Finally, the peculiar properties of the coherence with frequency equal to 760 cm^{-1} deserve a more detailed analysis. Since the resolution in frequency domain of the coherent beatings does not help to disentangle the contribution of vibrational coherences of ground and Q_y states from EVC, a time domain analysis can provide more useful information. Indeed, STFT analysis revealed the presence of 760 cm^{-1} oscillating component in two different temporal regimes (Figure 5.6(b)): (i) a long-living component was detected in the lower part of the 2DES map (dephasing time ~700 fs), while (ii) an overdamped component (~50 fs) appeared at higher emission energy. Signal (i) is therefore associated to a vibrational coherence, while signal (ii) to EVC.

Table 5.2 Fitted dephasing times of STFT of EVC signals detected in set II.

Component	1	2	3	4
Frequency [cm^{-1}]	470	560	690	760
Dephasing time [fs]	45	43	46	51

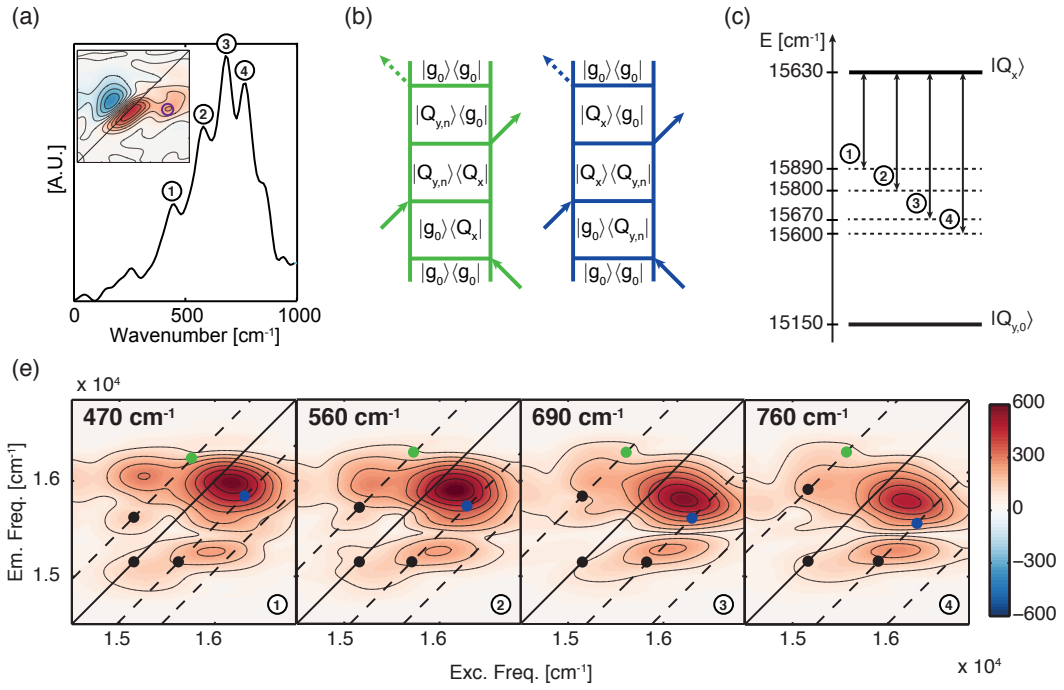

Figure 5.5 (a) FT power spectrum of the beating contributing at the cross peak position pinpointed in the map of the inset (violet circle). (b) Feynman diagrams associated to EVC pinpointed in panel (e) with circles with the same colour code. (c) Energy level diagram schematizing the vibronic states of Q_y band involved in coherent superpositions with Q_x state within the internal conversion process. The energy of the each vibronic state is consistent with Raman analysis and with the results obtained in Set I. The energy of the coherences corresponds to peaks found in panel (a): (1) 470 cm^{-1}, (2) 560 cm^{-1}, (3) 690 cm^{-1} and (4) 760 cm^{-1}. (e) Fourier maps related to those beatings. Black dots indicate the coordinates where vibrational signatures are expected, while green and blue dots show the positions where EVC contribute.

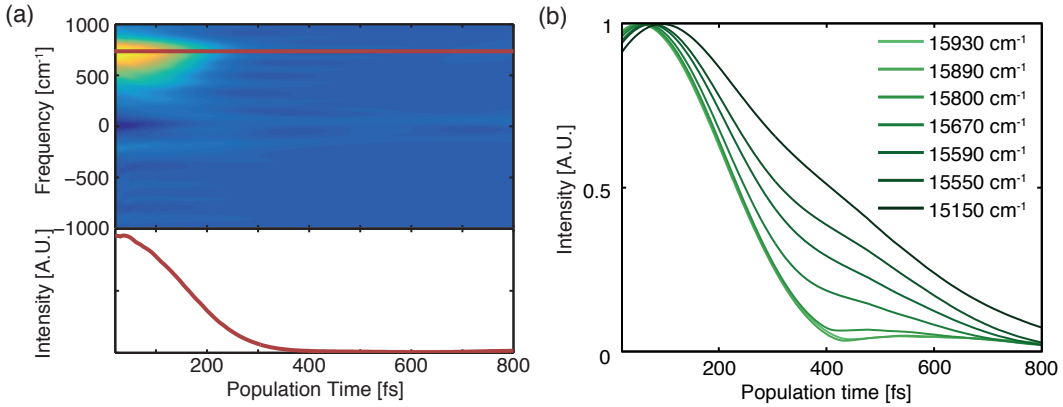

Figure 5.6 Scheme of the procedure to estimate the dephasing time of EVC. (a) A slice of the absolute value of STFS 2D plot (upper panel) is extracted for the frequency of the beating under analysis at 760 cm^{-1} (lower panel). The STFS 2D plot has been obtained applying STFT to risidues extracted at coordinates $(1.64, 1.59) \cdot 10^4$ cm^{-1}. (b) Slices extracted at 760 cm^{-1} beating frequency from STFS 2D plots obtained analysing the residues extracted at fixed excitation frequency ($1.64 \cdot 10^4$ cm^{-1}) and decreasing emission frequencies (see legend).

5.1.3. Discussion

The characterization of the coherent dynamics of Chl*a* in MeOH proposed in this work aimed, firstly, to determine the vibrational framework of both the Q_y and ground states by the analysis of the coherent contributions of the 2DES signal of set I. The typical pattern of the beatings detected in set I identified the oscillating signals as vibrational coherences. Moreover, global analysis determined long dephasing times (hundreds of femtoseconds) that are consistent with our assignment. The first set of measurements enabled to map the peculiar signatures of Chl*a* arising from vibrational coherences of both the ground and first excited state.

However, 2D-CAS obtained in set I revealed unexpected oscillating signals at positions not predicted by the DHO model, but appearing close to the higher energy edge of the 2D map. Therefore, in set II we used a blue-shifted exciting bandwidth to move the spectral window and further study the nature of those contributions. This new set of 2D maps captured a complex and ultrafast dynamics involving both the first and the second excited states, respectively Q_y and Q_x.

The process of intra-chromophore energy transfer involved distinct mechanisms that evolve in different timescales. The slower process (110 fs) is a non-coherent relaxation from the higher state Q_x to the lower Q_y and demonstrated both by the 2D-DAS in Figure 5.4(a) and by rephasing signal traces (Figure 5.4(b)). They revealed non-oscillating signatures that clearly decay with 110 fs time constant on the upper part of the diagonal where the contribution of the population of state Q_x is confirmed by previous works [94,98,99]. Similarly, the cross-peak $(\varepsilon_2, \varepsilon_1)$ below diagonal revealed a 110 fs exponential decaying behaviour, while the cross-peak $(\varepsilon_1, \varepsilon_2)$ above does not follow the same dynamics, thus confirming the non-coherent character of the energy transfer (where ε_1 and ε_2 are respectively the energy of

electronic states Q_y and Q_x). This behaviour is not detectable in the set I since Q_x state is only marginally populated.

The ultrafast (45 fs) mechanism of energy transfer is clearly coherent (Figure 5.4(d)) and involves superpositions of Q_x state and Q_y vibronic states. Since those oscillating signatures appear at cross-peaks both above and below diagonal and they have dephasing times of 45 fs, we cannot interpret these beatings as vibrational coherences.

Moreover, the distinct origin of the two kinds of beatings and the different positions where they are expected to appear are immediately clear comparing the Feynman diagrams [24,87] describing the vibrational coherences detected in set I with the diagrams (Figure 5.5(b)) describing the EVC found in set II. EVCs contribute at positions $(\varepsilon_2, \varepsilon_{1,n})$ and $(\varepsilon_{1,n}, \varepsilon_2)$ (where $\varepsilon_{1,n}$ is the energy of Q_y vibronic state involved in the superposition) and beat with frequency equal to $\Delta E = \varepsilon_2 - \varepsilon_{1,n}$. As discussed above, the Fourier maps in set II include both a contribution of the chair-pattern expected for vibrational coherences with frequency ΔE and the further EVC contributions at $(\varepsilon_2, \varepsilon_{1,n})$ and $(\varepsilon_{1,n}, \varepsilon_2)$ positions. Luckily, the distinct origin of the oscillating signals could be distinguished by damping times analysis, since the former signal show dephasing times of hundreds of femtoseconds, while the latter lives for less than 45 fs.

Specifically, set II unveiled the presence of 760 cm^{-1} beating contributing both as a vibrational coherence and as EVC that are disentangled due to their distinct dephasing times: longer (hundreds of femtoseconds) for the former on the chair pattern and much faster (51 fs) for the latter. Different authors have recently discussed the presence of a mode with frequency close to 750 cm^{-1} with various spectroscopic analysis: resonance Raman [99,104–106], fluorescence line-narrowing [105], pump-probe [100], 2DES [91,93,102] and T-RACS [91] experiments. All these studies confirmed that the mode is particularly important in the description of the photophysical behaviour of Chl*a*; moreover, comparing Resonant and off-resonant Raman spectra we can infer that this mode is strongly coupled with the Q_y transition. However, our study pointed out the important role of a coherent beating with such a frequency within internal conversion of Q bands.

5.1.4. Final remarks

2DES characterization of Chl*a* discussed in this work gives a new and detailed insight on the relaxation and dephasing dynamics of internal conversion process within the Q-bands of the most widespread chromophore in photosynthetic apparatuses.

Set I revealed the presence of coherent signals with purely vibrational origin and whose positions in the 2DES map fulfil the predictions of DHO model. A new kind of vibronic coherences were then unveiled when the investigated spectral region was blue-shifted, and whose occurrence was not predictable on the base of the model commonly used. The importance of *hot vibronic coherences* is dual: (i) they represent a previously unknown coherent pathway of internal conversion from Q_x to Q_y state of Chl*a* and (ii) they point out how, within an isolated chromophore, a new kind of coherent patterns not previously predicted can contributes to the 2DES signal.

As mentioned above, Q bands of Chl*a* are intimately involved in light harvesting process as much as in energy and electron transfer within the photosynthetic apparatus. A detailed description of the ultrafast dynamics of the first excited states of the chromophore is therefore crucial within the study of the highly efficient mechanisms that regulate photosynthetic energy transport.

Lacking a fully global and satisfying methodology for disentangling vibronic from electronic coherences, the interpretation of 2DES datasets is always a critical step. Long-living coherences are typically attributed to electronic-vibrational couplings, which give rise to vibronic coherences appearing in peculiar positions of the 2DES map that were predicted by the DHO model [9,87]. On the other hand, fast dephasing oscillations in 2DES signal, are commonly related to purely electronic coherences and expected at specific coordinates predicted by the excitonic dimer (ED) model [87] (see Section 2.7.1). Our study pointed out how a straightforward interpretation, purely based on the dephasing time and on the positions over the 2DES map of the oscillating signals, is not possible and can be misleading. A complete model of the vibrational and electronic states of the system is therefore needed for a correct attribution of the 2DES signals.

We can thus infer that the identification of *electroinc/vibronic coherences* overcomes the limits of the over-simplified DHO and ED models, highlighting how the most interesting features arise from the complex nature of the system under analysis.

5.2. Bacteriochlorophyll a

While Chl*a* is the major light-harvester in plants and algae, Bchl-*a* is the main pigment in bacterial photosynthesis. Differently from Chl*a*, whose ultrafast dynamic properties have been characterized by several groups through different 2D techniques in different spectral regions [91,93], few and not fully exhaustive are the papers devoted to the investigation of BChl*a* [107]. This is because the red-shifted absorption spectrum of the BChl*a* is at the limit of the available spectral bandwidth of the most common laser systems.

5.2.1. Experimental methods

2DES experiments were performed tuning the output of the commercial NOPA to cover as much as possible the spectral region of the lowest energy electronic transition, as shown in Figure 5.7(b). It was not possible to tune the exciting bandwidth further to the red because of instrumental limitations. The pulse duration of 20 fs was determined at the sample position by FROG measurements giving a spectral bandwidth of 750 cm^{-1}. Moreover, the energy of the exciting pulses in the same position was 7 nJ.

Both rephasing and non rephasing spectra were acquired for population times ranging from 0 to 800 fs in 5 fs increments, with each experiment repeated four times to ensure reproducibility for both the spectral windows.

The samples were prepared dissolving Bchl*a* (Livchem Logistics GmbH, purity >95%) in MeOH and diluting until the optical density was 0.3 with a pathlength of 1 mm. The resulting concentration was $3 \cdot 10^{-5}$M. Since Bchl*a* is extremely sensible to the presence of oxygen in solution, several freeze-pump-thaw cycles were performed on MeOH solution within the cell. It was sealed immediately after the degassing procedure to avoid possible production of oxidized byproducts during the measurements. Moreover, steady-state absorption spectra acquired before and after each scan confirmed that no degradation of the sample occurred during the 2DES experiments.

5.2.1. Results and discussion

5.2.1.1. Preliminary characterization of bacteriochlorophyll a

Steady-state absorption, steady-state fluorescence emission and fluorescence lifetime characterizations were performed on Bchl*a* in methanol solution (Figure 5.7(b,c)). Resonance and off-resonance Raman spectra were recorded on Bchl*a* powder instead (Figure 5.7 (d)) exciting the sample at $1.58 \cdot 10^4$ and $1.95 \cdot 10^4$ cm^{-1}, respectively.

Unlike Chl*a*, in steady-state absorption spectrum of Bchl*a*, the two lowest-energy states, Q_y and Q_x, are well separated (~3500 cm^{-1}) from each other, allowing an unambiguous distinction of the absorption bands resulting from the two corresponding transitions. Neither solvent nor temperature changes can determine inversion of the energy ordering the two states [97,108]. As shown in Figure 5.7(b) *y*-polarized transition moment determines the band at $1.30 \cdot 10^4$ cm^{-1} and its vibronic shoulder. Q_x band, instead, occurs at $1.64 \cdot 10^4$ cm^{-1} and is clearly separated from the orthogonal transition.

As a further support to this interpretation, we report the steady-state emission fluorescence spectrum in Figure 5.7(b). Mirror symmetry rule is fulfilled [109], since fluorescence emission occurs only from Q_y state, which is well separated in energy from Q_x state.

We then characterize the fluorescence lifetime (Figure 5.7 (c)) of Bchl*a* in MeOH, revealing a bi-exponential behavior with time constants t_1=2.0 ns (96%) and t_2=10.0 ns (4%). The slower component is close to the value detected in Chl*a*. The other one, instead, is much shorter and it could be correlated to the smaller energy gap between Q_y and the ground state in the bacterial pigment.

Comparing the experimental Resonance and off-resonance Raman spectra, we can deduce that almost the same vibrational modes are active in the ground and in the first exited state. This is in good agreement with the small Huang-Rhys factors reported in previous works [108] due to the rigidity of the molecular structure. The intensity of Raman signal related to the vibrational mode with frequency 755 cm^{-1} is noticeably enhanced in resonance conditions, as predicted by its Huang-Rhys factor [108]. Also the intensity of the Raman signal at 830 cm^{-1} is significantly increased in resonance conditions, despite experiments of fluorescence line narrowing (ΔFLN) in ref. [108] reported a small electron-phonon coupling for this vibrational mode. In effects, ΔFLN measurements were performed in resonance with Q_y electronic transition, while excitation energy in our Raman experiment was $1.58 \cdot 10^4$ cm^{-1}, closer to Q_x electronic transition. We can therefore conclude that the enhancement of the 830 cm^{-1} Raman signal suggest a stronger coupling of this mode to Q_x electronic transition rather than to Q_y in Bchl*a*.

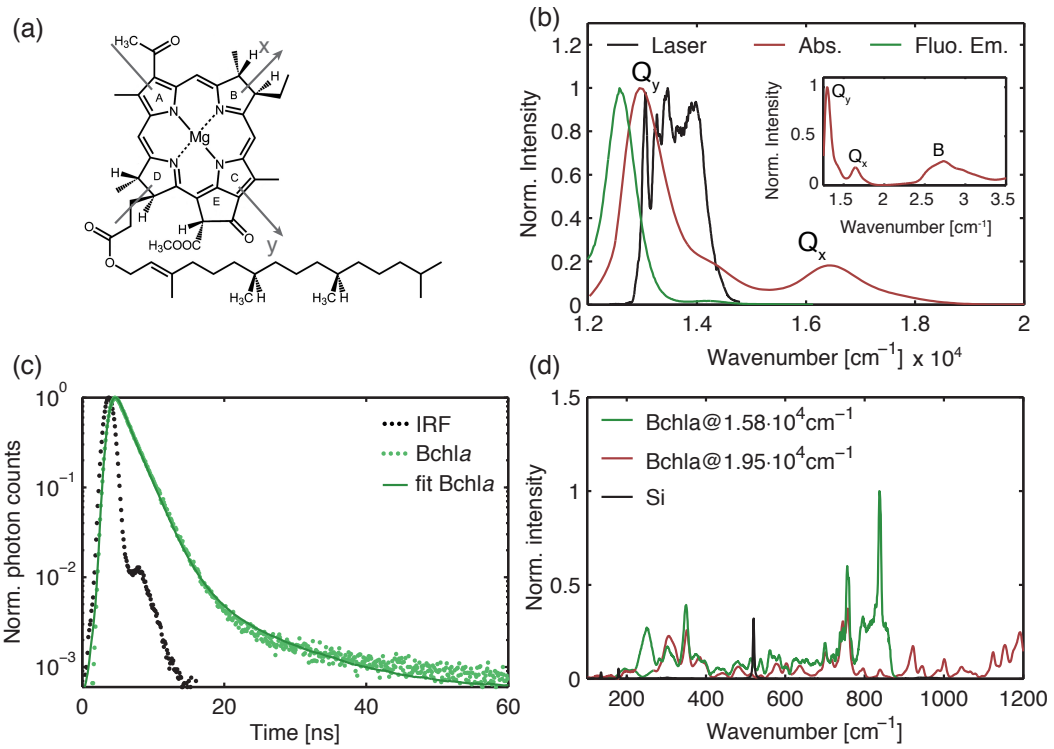

Figure 5.7 (a) Molecular structure of the Bchl*a*. The directions of polarization dipole moments are also reported. (b) Steady-state absorption spectrum of Bchl*a* in MeOH in the region of the Q bands (red line), steady-state fluorescence emission spectrum (green line) and laser spectrum (black line) used for the 2DES experiment. The inset shows the full steady-state absorption spectrum covering also the B bands region. The intensities are normalized to 1 on the maximum of Q_y band. (c) Experimental fluorescence decay trace of Bchl*a* (green dots) obtained by TCSPC technique (nanoled exc. source centred at $2.56 \cdot 10^4$ cm^{-1}, instrumental response in black) and multi-exponential fitting trace (green line). (d) Off-resonance (red) and Resonance (green) Raman spectra of Bchl*a* powder (T = 77 K). The response of Si platelet used as reference is also reported (black).

5.2.1.2. 2DES characterization

The population and coherent dynamics of the first excited state (S_1) of Bchl*a* are characterized *via* 2DES. The investigated spectral region, as shown in Figure 5.7(b), covers both the Q_y transition and its vibronic transition. As already anticipated, experimental limitations allow investigating only the blue side of the $Q_y(0,0)$ band, since our commercial NOPA could not be tuned further towards the red frequency range.

In Figure 5.8(a) two significant 2DES maps (rephasing, non-rephasing) recorded for different population time delays are reported. The rephasing signal shows a main positive feature elongated on the diagonal and a negative component above the diagonal, due to an excited state absorption (ESA) contribution. Within the population time window here investigated, the only detectable significant evolution of the shape is a slight broadening of the central feature towards lower energies. The non rephasing signal, instead, is almost anti-diagonal, as expected when a unique electronic transition is investigated.

The novel global analysis based on a complex multi-exponential fit developed by our research group is used to disentangle also in this case the different oscillating and non oscillating components that contribute to the 2DES signal [59].

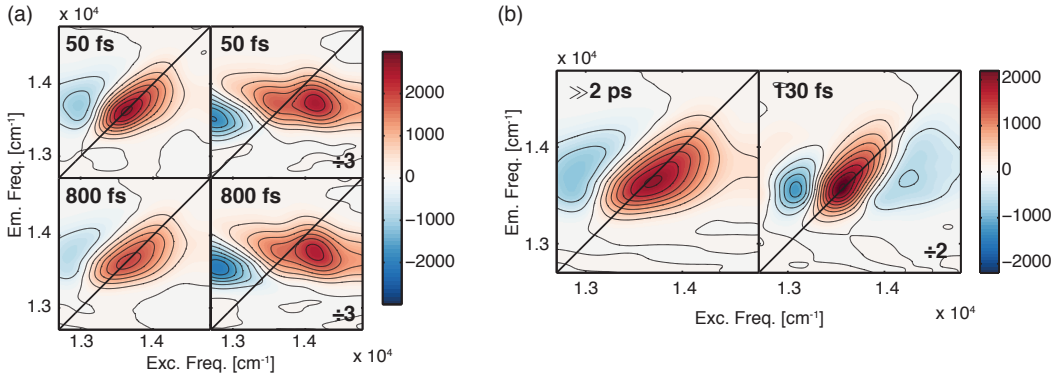

Figure 5.8 (a) Rephasing (left column) and non-rephasing (right column) maps of 2DES dataset of Bchl*a* for different population times. (b) Real part of 2D-DAS of the two non-oscillating time components for the rephasing signal determined by global fitting analysis.

As reported in Figure 5.8 (b), the non-oscillating component of the rephasing signal shows a bi-exponential decaying behaviour. The main component has a decaying constant much longer than the investigated time window and its 2D decay associated spectrum (2D-DAS) has the same features of the rephasing maps recorded for t_2 higher than 200 fs. In agreement with time-resolved fluorescence measurements (Figure 5.7(c)), where 2 ns lifetime was determined for Q_y state, this time constant can be easily attributed to the population decay of the Q_y band. The second exponentially decaying component has a very short time constant, close to 130 fs, and it can be related to the spectral diffusion. The 2D-DAS shows indeed an exponentially decaying behaviour along the diagonal and two exponentially increasing features above and below the diagonal. Spectral diffusion time constant of Bchl*a* is also consistent with the one we observed in previous 2DES measurements on Chl*a*.
Dealing with an isolated chromophore and since the exciting laser spectrum was tuned to cover a specific electronic transition (Q_y), the oscillating part of signal unveils the vibrational coherences more strongly coupled with the resonant transition. As anticipated above and described in Section 2.7.1, those quantum beatings contribute to 2DES signal at specific positions on the 2D map [24,87].
Taking into account the inhomogeneous broadening, the energy of the $Q_y(0,0)$ transition corresponds to the lower edge of both excitation and emission axes. Thus, only a part of the oscillating contributions predicted by the DHO model can be detected within the investigated spectral region. Indeed, two out of the five expected peaks have emission energy that lies outside the investigated spectral window (white circles in Figure 5.9(a)). Moreover, within the collected datasets two out of the three detectable peaks had very low intensity (yellow circles). Thus only a cross peak located below the diagonal was clearly visible (orange circle). Similar issues were encountered by Fransted *et al.* [107] exploring 2DES spectra of Bchl*a* in solution (methylene chloride and chloroform).
Quantum beatings expected at this position consist in vibrational coherences of both ground and excited state and result from Feynman pathways described by diagrams reported in (Figure 5.9(b)).
A detailed analysis of the oscillating contributions was performed in the selected spectral region, both in frequency and in time domain. Global fit analysis revealed the presence of six main beating components, as reported in Table 5.3. All these frequencies correspond to vibrational modes identified also in the Raman spectra; they can be classified in two different groups depending on their dephasing times: close to or higher than 1 ps (componenets 3, 4 and 5) and hundreds of femtoseconds (components 1, 2 and 6), respectively.
The long living components 3, 4 and 5 present the highest amplitudes and contribute more to the overall beating behaviour of the 2D maps. For example, components 4 and 5, close in frequency, generates the interference clearly visible in the signals reported both in upper and lower panel of Figure 5.9(d). These long-living

components (3 and 5 in particular) have been already captured also in the 2DES characterization of Bchl*a* monomer previously proposed by Fransted *et al.* [107].
More interesting is the behaviour of the quickly damped components 1, 2 and 6. All these modes have a very low intensity in the Raman spectra, which is consistent with the fast dephasing time detected by the global analysis. The contribution of component 2 is mainly detectable in the real rephasing signal (upper panel, Figure 5.9(d)) at the coordinates pinpointed by the green dot in Figure 5.9(c). The linear prediction Z-transform (LPZ) [110] reported in Figure 5.9(e) furtherly confirmed the result of the global fit and the effective presence of these components.
In particular for component 6, the Raman characterization shows the presence of a vibrational mode at the same frequency that is enhanced in resonance conditions. This evidence, together with the short damping time and the particular position where this mode contributes more, seems to suggest that this component is attributable to a vibrational mode in the excited state.
The analysis of the Raman spectra highlighted also the presence of a strong enhancement of the bands between 800 and 900 cm^{-1} in resonance conditions. Despite that, we couldn't detect any beating component in this range in the in 2D spectra, thus confirming the conclusion reported above that 830 cm^{-1} vibrational mode is coupled more strongly to the Q_x electronic transition than to Q_y.
The Raman spectra show several modes in the spectral region below 300 cm^{-1}. A full comparison with oscillations in 2D spectra in this low frequency region is not fully possible since these modes appear in the 2D maps very close to diagonal, where the dynamics of populations prevail hiding all other oscillating contributions.
As a final observation, we made sure that Raman-active modes of MeOH (higher than 1000 cm^{-1}) are not contributing to the oscillating dynamics. The possibility of finding non-resonant response contributions due to vibrational modes of the solvent has been already documented in the literature [107].

Table 5.3 Fitting parameters for the oscillating components in 2DES rephasing signal of Bchl*a*.

Component	1	2	3	4	5	6
Frequency [cm^{-1}]	330	410	580	670	735	750
Dephasing time [fs]	250	150	800	$\gg 2000$	1860	140

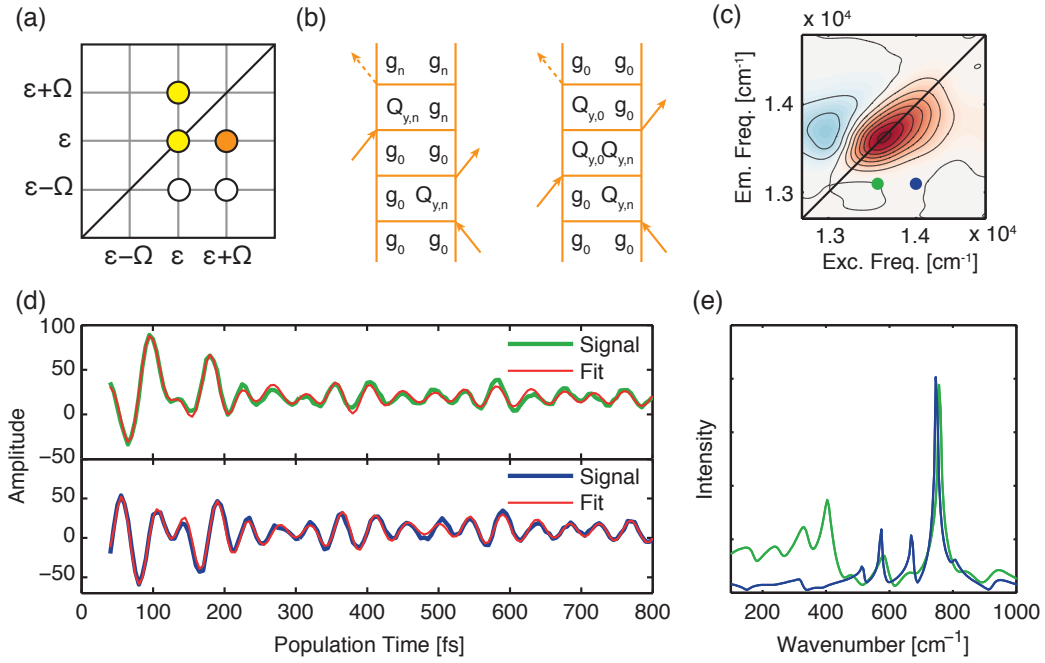

Figure 5.9 (a) Chair pattern of oscillating signals predicted for a vibrational coherence with frequency Ω by the DHO model. ε is the energy of Q_y electronic transition. Yellow and orange circles pinpoint the positions of the detectable beatings within the investigated spectral region. The orange dot shows the coordinates on 2D map where coherent signals in Bchl*a* dataset are clearly discernible. (b) Feynman diagrams representing the vibrational coherences of ground (left) and excited (right) contributing in the orange position. (c) Meaningful coordinates (green and blue dots) where the real rephasing signal is extracted. The traces extracted at these positions (respectively green and blue lines) are plotted in panel (d) together with the fitting function (red lines) resulting from global analysis. (e) LPZ-transform of the 2DES signal (colour code is conserved in panels (c,d,e)).

5.2.2. Final remarks

2DES measurements of Bchl*a* monomer in MeOH solution described in this work reveal the presence of six distinct vibrational coherent beatings. A novel and detailed characterization of those oscillating patterns is here proposed, offering a complete time and frequency domain description that had never been reported before in literature. A previous 2DES characterization of the Bchl*a* monomer [107] was indeed strongly affected by an overlapping non resonant response of the solvent, making the disentanglement of chromophore signatures a hard issue. The choice of MeOH as solvent, thanks to its low polarizability, overcomes these problems.

Particularly interesting is the identification of at least three quickly damped components characterized by very short dephasing time. One of these components, with frequency about 750 cm^{-1}, has been tentatively attributed to a vibrational mode of the Q_y excited state.

The peculiar temporal behaviour of these coherences could be misleading when studying the ultrafast dynamics of a complex light harvesting apparatus. Quantum

beatings having fast dephasing time could indeed be erroneously interpreted as long-lasting electronic coherences. However, the ultrafast characterization of Bch*a*, here proposed, pointed out how, even purely vibrational coherence, can have very short damping times.
This work therefore provides a set of preliminary information that are crucial for possible future studies of biological complexes.

6 Peridinin chlorophyll *a* protein

Photosynthetic organisms rely on their light-harvesting apparatus to absorb light and transfer energy to the reaction centres where it is converted into electrochemical potential. Depending on their habitat, these organisms developed specific strategies to enhance their light-harvesting capacity and therefore the variability of antenna complexes detected in Nature is very large.

Photosynthetic dinoflagellates, unicellular algae forming the major component of sea plankton, contain several membrane-bound light-harvesting complexes, similar to those in higher plants and green algae. These organisms contain also water-soluble external light-harvesting proteins, such as Peridinin-Chlorophyll *a*-Protein (PCP) Figure 6.1(a).

Within most of the antenna systems, the main pigment responsible for solar energy absorption is either chlorophyll *a* (Chl*a*) (Figure 6.1(d)) or bacteriochlorophyll *a* (Bchl*a*). In contrast, PCP reveals a unique light-harvesting strategy because it largely relies on the carotenoid peridinin (Per) as the major light-harvesting pigment (Figure 6.1(b)). The organism is therefore capable of collecting the solar radiation also in the 470-550 nm visible spectral region, where chlorophylls do not absorb. This light-harvesting strategy is exquisitely adapted to the environmental light conditions of the habitat occupied by the dinoflagellates, as shown in Figure 6.1(c).

Besides the unique pigments composition, also the carotenoid nature is peculiar. Per belong to a family of carotenoids having a conjugated carbonyl group (Figure 6.1(d)) that alters dramatically their excited state properties, since the lowest excited state gains a significant charge transfer (CT) character.

After the pioneering works of Song and co-workers [111,112], during the last two decades PCP has aroused a great deal of interest in the biophysical community, especially after the publication of its high-resolution X-ray structure. Not only for its biological relevance, but also for its peculiar biophysical behaviour, PCP and, specifically, its energy transfer (ET) process, has been widely studied with several distinct electronic spectroscopies ranging from steady state [113,114] to time-resolved transient optical techniques [114–121]. Moreover, several theoretical models based both on experimental [122] and computational data [123–126] have been proposed. Despite these great efforts, many details concerning the exact nature of

all the channels of energy flow and the precise energy of the excited states of the pigments involved in the process are still not fully clarified. 2DES appears as a good candidate to disentangle the ultrafast steps of the processes and to identify the electronic states directly involved in the ET.

6.1. Protein structure and carotenoid properties

The structure of PCP from the dinoflagellate *Amphidinium carterae* was resolved to 2.0 Å [127], revealing a trimer of protein subunits (Figure 6.1(a)) where the pigments are densely packed into the protein scaffold and do not interact with the solvent. Every subunit counts eight Pers and two Chl*a* (Figure 6.1(b)). Moreover, each monomer is arranged into two domains with pseudo-C_2 symmetry where four Pers are clustered around a molecule of Chl*a*. Distances between Pers within a single domain are 4-11 Å and the conjugated regions of Pers are in van der Waals contact with the tetrapyrrole of the Chl*a* molecules (3.3-3.8 Å). The distance between Mg atoms of the two Chl*a* belonging to different domains is 17.4 Å. Such a tightly packed cluster of pigments creates an ideal medium for efficient ET.

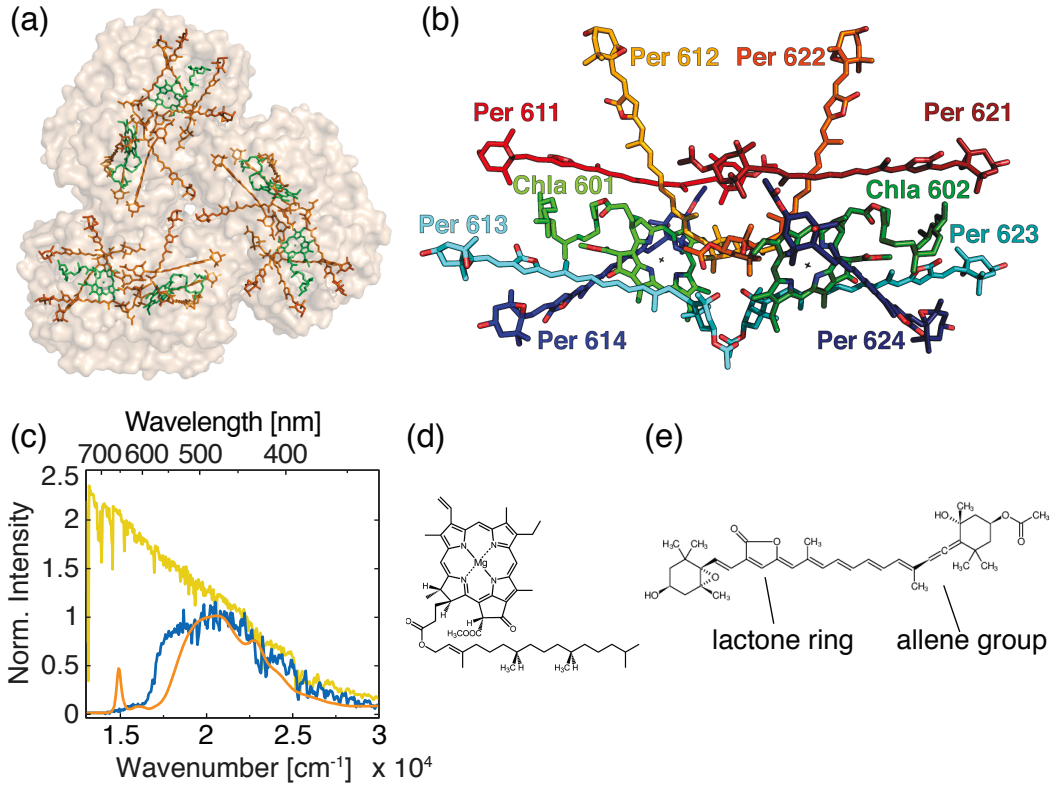

Figure 6.1 (a) The trimeric PCP light-harvesting complex where the pigments, Chl*a* in green and Per in orange, are densely packed. (b) Chromophores belonging to the two pseudo-symmetric domains of the monomers having a stoichiometry of eight Pers and two Chl*a* (labels according to the notation used by Damjanović *et al.* [123]). (c) Absorption spectrum (orange) of PCP, solar irradiance at sea surface (yellow) and 10 m below the surface (blue). The molecular structures of Chl*a* and Per are reported respectively in (d) and (e).

One of the crucial aspects in the study of the mechanism of energy transport among pigments is the characterization of the excited states actually involved in the process. Precisely for this reason, Per has been widely investigated in the past years. Pump-probe measurements [114] revealed that the lowest Per excited state has a lifetime of 3.1 ps in PCP, while the lifetime detected for Per in methanol solution is markedly longer (13.4 ps). Moreover, fluorescence emission from Chl*a* is detected upon excitation on the absorption region of Per [114]. These are proofs that, within the protein complex, an ET channel from Per to Chl*a* must be present.

The optical properties of a typical carotenoid are defined by the π-conjugated electronic system extended along the polyene backbone. The earliest interpretations of the spectroscopic signatures of carotenoids in the UV-visible region were based on a three-level model including a ground state S_0, and two low-lying singlet excited states S_1 and S_2. Since linear polyenes belong to the C_{2h} symmetry group, the three electronic states are denoted as $1A_g^-$ (S_0), $2A_g^-$ (S_1) and $1B_u^+$ (S_2). It follows that $S_0 \rightarrow S_1$ transition is symmetry forbidden, while $S_0 \rightarrow S_2$ transition is optically allowed. S_2 state is associated to a strong transition dipole moment, while $S_0 \rightarrow S_1$ is dark in the linear absorption spectrum.

In addition, Per belongs to a class of carotenoids that owes its peculiar spectroscopic properties to the functional groups attached to the polyene chain, in particular to the conjugated carbonyl group (Figure 6.1(e)). Mimuro *et al.* [128] demonstrated that the carbonyl group, and not the whole lactone ring nor one of other substituents, strongly affects the photophysical properties of Per. Indeed, he compared the fluorescence emission of Per with other three carotenoids: neoxanthin, fucoxanthin and all-trans-β-apo-8'-carotenal. While the first carotenoid lacks the lactone ring, but it is structurally very similar to Per, the other two pigments have a carbonyl functional group conjugated to the polyene chain. These two carotenoids emit predominantly from S_1 state like Per, even if their structural analogies with Per are less extended than in neoxanthin that, instead, fluoresces mainly from S_2 state. This demonstrates how the carbonyl group strongly affect the electronic structure of the carotenoid.

Moreover, the presence of such substituent, together with the electron donor effect of the allene moiety, promotes the formation of intramolecular charge transfer (ICT) state. The actual role and properties of this peculiar state have been widely investigated for the past two decades leading to four main hypothesis: (i) S_1 and ICT are distinct states [116,129–132]; (ii) S_1/ICT states are coherently mixed [115,118,129,133–136]; (iii) S_1(ICT) is a unique state [137]; (iv) ICT is formed by mixing S_2 and S_1 excited states [138].

Within model (i) (Figure 6.2(a)), ICT state involves a structural rearrangement of Per if compared with the ground state. Moreover, in polar solvents ICT state is energetically lower than S_1 state which is consistent with the strong dependence of

fluorescence lifetime on the solvent polarity: it ranges from 172 ps in cyclohexane and benzene to 7 ps in trifluoroethanol [139].
The pronounced dependence of the excited state lifetime on the solvent environment led Frank *et al.* [129] and Zigmantas [115,133,134] to formulate hypothesis (ii) (Figure 6.2(b)), where the ICT and S_1 states are strongly mixed: ICT state represents a second local minimum on the distorted potential surface of S_1 excited state. The higher is the polarity of the solvent, the lower is the second minimum of the potential surface and lower is the barrier between the two minima (Figure 6.2(b)). Moreover, Ghosh *et al.* [136] discovered that, prior to nonradiative decay to the S_1 state, a transition structure between the planar and the twisted form is reached along the potential surface of S_2. Subsequently, the relaxation along the torsional coordinate promotes the population of ICT state.
In hypothesis (iii) ICT state is not separated from S_1 state since ICT is simply a S_1 state with a large intrinsic dipole moment (Figure 6.2(c)).
Finally Wagner *et al.* [138] formulated a further hypothesis (iv) where ICT is an electronic state of peridinin resulting after bond-order reversal in the excited state manifold and mixing of the two lowest singlet excited states, S_1 and S_2 Figure 6.2(d). Moreover, ICT state is characterized by an enhanced dipole moment which is stabilized by polar solvents.

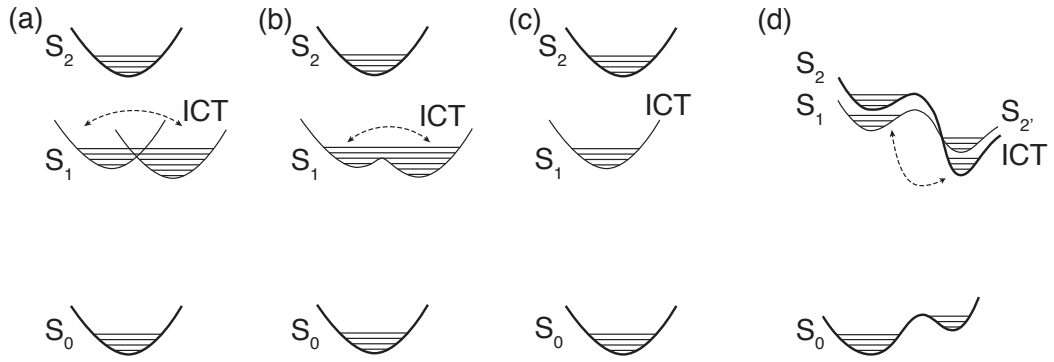

Figure 6.2 Schematic diagrams of the various literature models of the ICT state. The thickness of the potential surface reflects the oscillator strength of the electronic transition from the ground state. Scheme (a) represents model (i) where S_1 and ICT are distinct states; scheme (b) depicts model (ii), which describes S_1 and ICT as strongly mixed; model (iii), where S_1 and ICT are a unique state, is depicted by diagram (c); hypothesis (iv), represented in (d), describes ICT as resulting from the mixing of S_1 and S_2 states after structural rearrangement.

6.2. Energy transfer pathways in PCP

Besides the characterization of peridinin, also the ET pathways within PCP have been widely investigated but still a complete agreement on that topic is lacking. However, several key aspects in the ET process were confirmed by different works [116,117,120,122,123,132]. Steady-state measurements revealed that the overall efficiency of ET from Per to Chl*a* is approximately 88% [114].

Ultrafast transient absorption spectroscopy revealed that, after photoexcitation of the S_2 state of Per, a rapid internal conversion occurs in the order of tens-hundreds of femtoseconds [116,117,120,132].

Several works [116,117] confirmed also that the excitation flow from Per to Chl*a* occurs *via* two channels. The first involves S_2 state of Per as donor and Q states of Chl*a* as acceptors, with an efficiency of about 25-50%. Since, as stated before, internal conversion towards lower singlet states of Per is very fast, ET from S_2 towards Chl*a* has to be very fast to compete with the relaxation process from S_2 to S_1.

The remaining 75-50% of S_2 population relaxes towards S_1/ICT state, possibly involving an intermediate hot S_1 state of Per [117,120,132]. The second and dominant route of ET occurs from S_1/ICT state of Per to Q_y state of Chl*a* in ~3 ps [117,140] with 84% yield.

It was demonstrated that Pers are not perfectly equivalent donors in ET towards Chl*a*. Indeed, in high salt concentration the protein complex releases Per 612/622 but the overall efficiency is not affected. It means that ET from Per 612/622 is too slow to be relevant in the overall process of ET [135]. Finally, the extra 16% of the S_1/ICT population undergoes relaxation towards S_0. The second route of ET from S_1/ICT state is well characterized, since the process is slower and, thus, it does not require femtoseconds resolution to be detected. The first route of ET from S_2, on the contrary, is much faster and has been only marginally investigated. Moreover, it was not fully clarified whether state Q_x or state Q_y of Chl*a* is the main acceptor in ET from the S_2 of Per.

An additional complication is that in PCP, S_2 states of different carotenoids are strongly coupled, especially within the same domain. Carbonera *et al.* [113] calculated the exciton coupling among Pers that ranges from 137 to 334 cm^{-1}. Calculations of S_2 exciton densities pointed out that Per 611/621 has the lowest site energy and therefore the highest exciton density, while Per 612/622 has the highest site energy and thus the lowest exciton density [123]. It follows that internal conversion occurs only in Pers with higher exciton density, such as Per 611/621, Per 613/623 and Per 614/624. S_1 states of Pers, on the contrary, are only weakly coupled among each other.

Several works proposed models including S_2-mediated ET to explain a ground-state bleaching signal of Chl*a* recorded in transient-absorption spectra at 500 fs after photoexcitation and to account for the 88% efficiency [116,117,132,135,141,142]. Most of the works assumed a $S_2 \rightarrow Q_x$ ET between Pers and Chl*a*, since the energy gap among these electronic states is smaller and thus the ET rate should be faster. Other works do not even distinguish among Q states [116,132] of Chl*a*.
Recently Bricker *et al.* [126] calculated the ET from S_2 excitons in PCP, predicting how $S_2 \rightarrow Q_y$ pathway from Pers to Chl*a* is faster (about 200 fs) than $S_2 \rightarrow Q_x$ process (up to 4.83 ps). Moreover, Ghosh *et.al* [143] have very recently performed transient grating measurements on PCP characterizing the ET process. They detected two main transfer routes: the first occurs from S_2 state within 30 fs and is consistent with a quantum coherent transport that involves delocalized Per-Chl*a* exciton states; the second is a 2.5 ps incoherent process initiated by dynamic exciton localization, following the formation of an intermediate Per species which is conformationally distorted. Nevertheless, until now, the literature doesn't propose direct experimental proofs of a coherent $S_2 \rightarrow Q_y$ ET.

6.3. Spectroscopic characterization

6.3.1. Linear characterization

As shown in Figure 6.3, the absorption and CD spectra of PCP are dominated by the S_2 symmetry-allowed electronic transitions of Pers, an inhomogeneous broadened band ranging from $1.7 \cdot 10^4$ to $2.7 \cdot 10^4$ cm^{-1} (from 600 to 370 nm) that overlaps with the Soret band of Chl*a* peaking at $2.27 \cdot 10^4$ cm^{-1} (440 nm). The lack of vibrational structure of S_2 state of Per is similar to what observed for Per in polar solvents [114,115,129], suggesting that PCP complex produces a polar environment around the carotenoids. The structureless band peaks at $2.08 \cdot 10^4$ cm^{-1} (480 nm) that corresponds to the (0,1) vibronic transition, while the shoulder of the band at about $1.90 \cdot 10^4$ cm^{-1} (525 nm) is produced by the (0,0) vibronic transition. These assignments are based on the comparison with the absorption spectrum of Per measured at 77 K in ethanol [112].
The weak band located between $1.55 \cdot 10^4$ and $1.67 \cdot 10^4$ cm^{-1} (645 – 600 nm) is given by the (0,1) Q_y vibronic transition and/or by Q_x transition of Chl*a* [117,140]. Finally, (0,0) Q_y transition of Chl*a* is pinpointed at $1.49 \cdot 10^4$ cm^{-1} (490 nm).
The CD spectrum shows a large positive band at higher energies that well reproduces the features of the absorption spectrum, while at lower energies, within the spectral region of the transitions to Per S_2 state, a strong negative signal appears. These bands with opposite signs point out the presence of exciton coupling among S_2 states of the carotenoids belonging to the same monomer [113].

The spectral region, where the Soret absorption band appears, is characterized by a hole in the CD spectra, meaning that Chl*a* shows a band with negative rotational strength due to its intrinsic chirality. Also Q_x and Q_y electronic transitions of Chl*a* show negative CD signals with same energy of the corresponding absorption signals.

6.3.2. 2DES characterization

One of the most powerful advantages of 2DES is its capability of disentangling contributions of different species that overlap in one-dimensional techniques. The 3D Fourier spectra obtained scanning three different time delays between the exciting pulses opens to the possibility of separating electronic transitions and recognising their nature. In other words, the signals generated by different species can be split in the 2D excitation/emission map. Moreover, the oscillations detected as function of the population time are crucial to identify the chromophore because they carry the information on their vibrational modes and can be used as a fingerprint to discern between the pigments.

The spectral region between $1.5 \cdot 10^4$ and $1.8 \cdot 10^4$ cm^{-1} is particularly interesting if we want to characterize the ET mechanism in PCP antenna complex, from the first bright excited state S_2 of Per to the final acceptor, Q_y state of Chl*a*. Within this range, the steady-state absorption spectrum shows a weak band which is not unambiguously assigned in literature and previous works [134,144] identified the energy of S_1/ICT state of Per and Q_x state of Chl*a* within this spectral window. As mentioned above, these electronic states are strictly involved in the dynamics of energy migration towards the reaction centre of the photosynthetic complex.

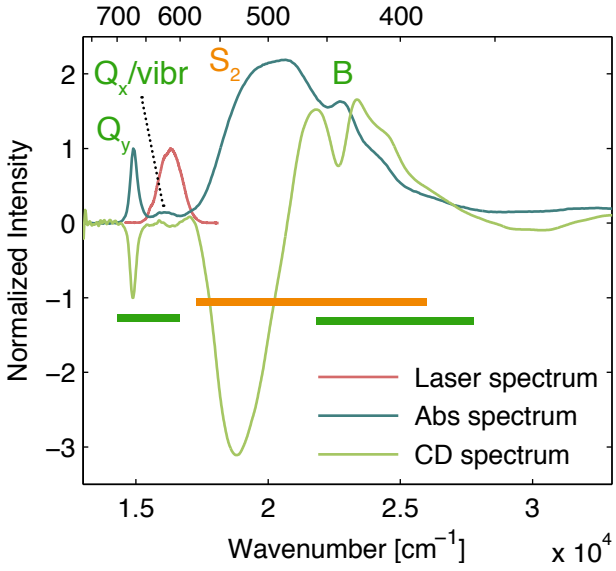

Figure 6.3 Steady-state absorption (blue) and CD (green) spectra of PCP normalized on Q_y transition of Chl*a*. The laser spectrum used in 2DES measurements is reported in pink. The horizontal thick green and orange lines indicate the absorption spectral region of Chl*a* and Per, respectively.

6.3.2.1. Experimental methods

The spectral output of the NOPA was tuned to probe simultaneously S_2 state of Per and both Q_x and Q_y of Chl*a*, as demonstrated by Figure 6.3. The outcoming pulses are thus centred at $1.63 \cdot 10^4$ cm^{-1} (20 fs), with energy equal to 7 nJ at the sample position. We followed the same strategy suggested by Ostroumov *et al.* [70] and the excitation spectrum was tuned at the very edge of the S_2 absorption in order to minimize the signals arising from S_2 excitation, such as GSB and SE, that could hinder other possible weaker signals.

Both rephasing and non rephasing spectra were recorded for population times ranging from 0 to 2 ps in 7.5 fs increments, with each experiment repeated eight times to ensure reproducibility.

PCP antenna complex was extracted and purified by prof. R. G. Hiller from *Amphidinium carterae*, according to the method previously published [145], and kindly provided by prof. D. Carbonera. For 2DES experiments the sample was diluted in sodium phosphate buffer (pH 7.5) until the optical density was about 0.1 with a pathlength of 1 mm within the investigated spectral window. Several freeze-pump-thaw cycles were performed to remove the oxygen from the solution and the cell was sealed immediately after the degassing procedure to avoid the formation of oxidized species during 2DES measurements. The steady-state absorption spectrum of the sample was recorded after each scan to ascertain that the sample was not degraded during the measure.

6.3.2.2. Results

Within the investigated spectral window, the evolution along population time of rephasing and non rephasing signals hardly reveal distinguishable features, since several species simultaneously contributes to the overall signal, as demonstrated by the pure absorptive maps reported in Figure 6.4.

In order to elucidate the origin of the signals overlapping on the diagonal, and to determine whether they are due to Per or to Chl*a*, we performed Fourier analysis of the data as function of the population time. The time traces taken at coordinates along the diagonal of the 2D spectrum of PCP reveal a noticeable oscillating behaviour that carries the information about which vibrational modes are more strongly coupled to the resonant electronic transition. The Fourier spectrum of these time traces significantly differ from point to the point, as shown in Figure 6.5.

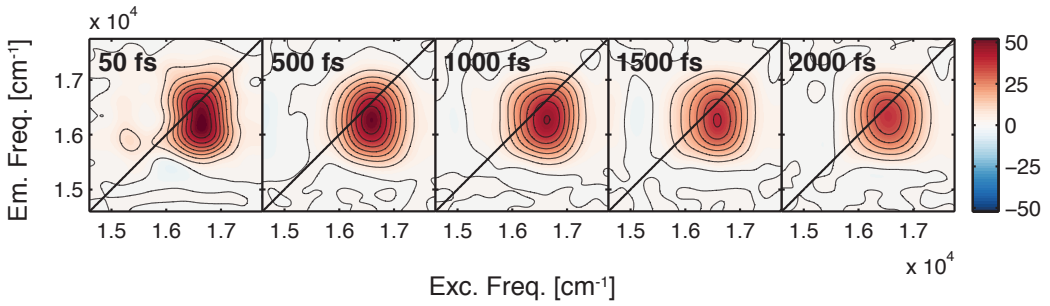

Figure 6.4 Evolution of the real part of the pure absorptive signal along population time of PCP.

Time traces extracted at positions $1.75 \cdot 10^4$ and $1.60 \cdot 10^4$ cm^{-1} (Figure 6.5(c,d)) clearly revealed three high frequency modes, 1180, 1220 and 1560 cm^{-1}. The corresponding Fourier spectra well match the main features of the Resonant Raman spectrum of Per recorded in acetonitrile by Kish *et al.* [146] (Figure 6.5(b)). These three modes are typical of carotenoids [147]: 1180 and 1220 cm^{-1} peaks with their shoulder at lower frequency are peculiar for Per and are attributed the C-C stretching modes strongly mixed with C-H in plane bending modes [148]; the band at 1560 cm^{-1} is related to the stretching modes of the C=C double bonds [149]. The peaks in the Fourier spectra are slightly blue shifted compared with the literature spectrum due to the different environment of the two measurements.

In contrast, the signals extracted at positions $1.75 \cdot 10^4$ and $1.60 \cdot 10^4$ cm^{-1} (Figure 6.5(f,g)) show a completely different pattern. A diagnostic signal can be recognized: it is due to a characteristic vibrational mode of Chl*a* with frequency equal to 750 cm^{-1} (dotted line) [91,93] arising from in-plane deformation of pyrrole rings [101] and already discussed in Section 5.1.2. To give a comparison, Resonant Raman spectrum of Chl*a* in MeOH is reported in Figure 6.5(e).

Furthermore, the global analysis method described in Section 3.2.8.2 is a unique tool capable to disentangle the excited states dynamics in PCP within 2 ps after photoexcitation. The global analysis of both rephasing and non rephasing signals revealed three non oscillating decaying components. Figure 6.6 reports the corresponding 2D-DAS, e.g. the 2D maps where the amplitude related to a specific decaying component is plotted. The associated decay time constants are (i) 60 fs, (ii) 2.8 ps and (iii) a third component which is almost constant within the investigated time window and that can be roughly estimated as $\gg$ 5 ps.

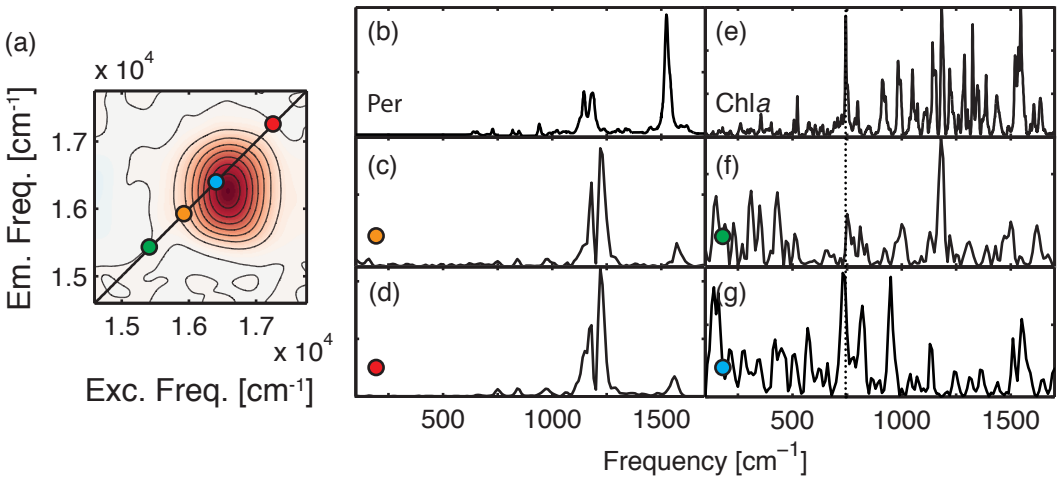

Figure 6.5 Fourier spectra of time traces extracted at positions in the 2D spectrum pinpointed by the coloured circles in (a). Traces (c) (orange circle) and (d) (red circle) reveal beatings related to vibrational modes of Per, as demonstrated by the comparison with its Resonant Raman spectrum (b) in acetonitrile (exc. $1.95 \cdot 10^4$ cm^{-1}, [147]). The diagnostic peak at 750 cm^{-1} typical of Chl*a*, as revealed by the Resonant Raman spectrum in MeOH (exc. $1.58 \cdot 10^4$ cm^{-1}) reported in panel (e), is found in Fourier spectra (f) and (g) of traces extracted at positions shown respectively by the green and the cyan circle.

2D-DAS (i) (Figure 6.6(a)) reveals a complex pattern of signals where the main features are the following: a negative region above and on the diagonal with exciting frequency of about $1.60 \cdot 10^4$ cm^{-1}; a positive region below and on the diagonal with exciting frequency of about $1.65 \cdot 10^4$ cm^{-1}. Positive and negative amplitudes in 2D-DAS indicate respectively an exponential decaying and rising behavior. 2D-DAS (ii) in Figure 6.6(b) shows the strongest decaying component at high values of excitation frequencies, spanning from the diagonal to the lower part of the 2D map, while the region on the diagonal at lower energy shows a weak rising. Finally, 2D-DAS (iii) indicates a slower decay that involves the entire spectral region here investigated.

The global analysis revealed also the presence of several oscillating components which will be crucial to recognize the different species involved in the ET process in PCP. Frequency and dephasing time of the detected oscillating signals are listed in Table 6.1. The 2D maps showing the amplitude associated to a specific oscillating component, 2D-CAS, are reported in Figure 6.7 for the four main components: (i) 750 cm^{-1}; (ii) 1180 cm^{-1}; (iii) 1210 cm^{-1}; (iv) 1565 cm^{-1}.

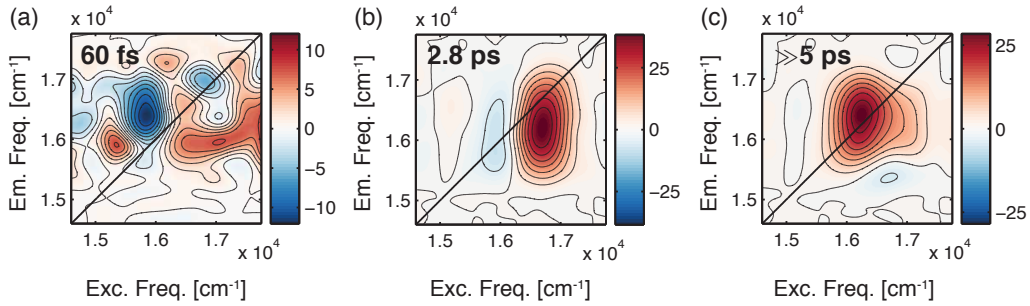

Figure 6.6 2D-DAS resulting from global fit analysis of the pure absorptive signal. The non oscillating components has three distinct decay time constants: (a) 60 fs; (b) 2.8 ps; (c) time constant much longer than the investigated time window.

The signals with frequency (i) appear both in the rephasing and in non rephasing 2D map with a peculiar pattern and have a long dephasing time, 1700 fs. This is the first hint that brings us to assign the signal to a vibrational coherence. Moreover, the peculiar amplitude distribution of 2D-CAS (Figure 6.7(a)) both in rephasing and in non rephasing datasets perfectly reproduce the amplitude distribution predicted within the displaced harmonic oscillator (DHO) model, as described in Section 2.7.1. Five circles (both in rephasing and non rephasing 2D maps) pinpoint the positions where the signal arising from vibrational coherences of ground and excited state are expected in agreement with the DHO model. The centre of the patterns is highlighted by cyan colour and indicates the energy of the electronic transition, $\omega_{e''g} = 1.65 \cdot 10^4$ cm^{-1}, that lies in the spectral region where we demonstrated that Chl*a* contributes.

Coherences (ii) and (iii) have long dephasing time as well, respectively 1200 and 700 fs. We suggest that also those signals arise from vibrational coherences. Differently to what detected for component (i), 2D-CAS (Figure 6.7(b,c)) of rephasing dataset reveals only three (black circles) out of the five signals expected for a two-level system coupled to a nuclear coordinate, as stated before. Accordingly, also 2D-CAS (Figure 6.7(b,c)) of non rephasing dataset display four (black circles) out of the five predicted signals. The discrepancy between experimental data and the prediction is due to the limited laser spectrum. Indeed, the missing signals should have emission frequency equal to $\omega_{e'g} - \nu$, where e' is the excited state involved in the electronic transition and ν is the frequency of the vibrational mode coupled to this transition, namely 1180 and 1210 cm^{-1}. These energies outrange the investigated spectrum, leading to a partial detection of the complete pattern of five peaks. For both components (ii) and (iii) $\omega_{e'g} = 1.60 \cdot 10^4$ cm^{-1}, as shown by the orange circles in Figure 6.7(b,c). 2D-CAS of (ii) and (iii) display further contributions, pinpointed by diamonds, that can be explained as vibrational coherences resulting from vibrational

modes coupled to a second electronic transition that lies at the edge of the studied spectral window, as furtherly discussed below.

Finally, component (iv) has the most peculiar behaviour, since its dephasing time is very fast, 100 fs. Furthermore, rephasing 2D-CAS clearly show a cross-peak $(\omega_\alpha, \omega_\beta)$ and non rephasing 2D-CAS has two diagonal peaks $(\omega_\alpha, \omega_\alpha)$ and $(\omega_\beta, \omega_\beta)$, where $\omega_\alpha = 1.55 \cdot 10^4$ cm^{-1} and $\omega_\beta = 1.71 \cdot 10^4$ cm^{-1}. The positions of these signals are compatible with those predicted by the exciton dimer (ED) model, as described in Section 2.7.1. The detected damping time of component (iv), together with the revealing positions of the beatings of the corresponding 2D-CAS, suggest that coherence (iv) has an electronic character.

Table 6.1 Fitting parameters resulting from the global fitting analysis of the oscillating components in 2DES rephasing and non rephasing signals of PCP.

Component	1	2	3	4
Frequency [cm^{-1}]	750	840	965	1150
Dephasing time [fs]	1700	960	1245	550
Component	5	6	7	
Frequency [cm^{-1}]	1180	1210	1220	1565
Dephasing time [fs]	1200	700	1600	100

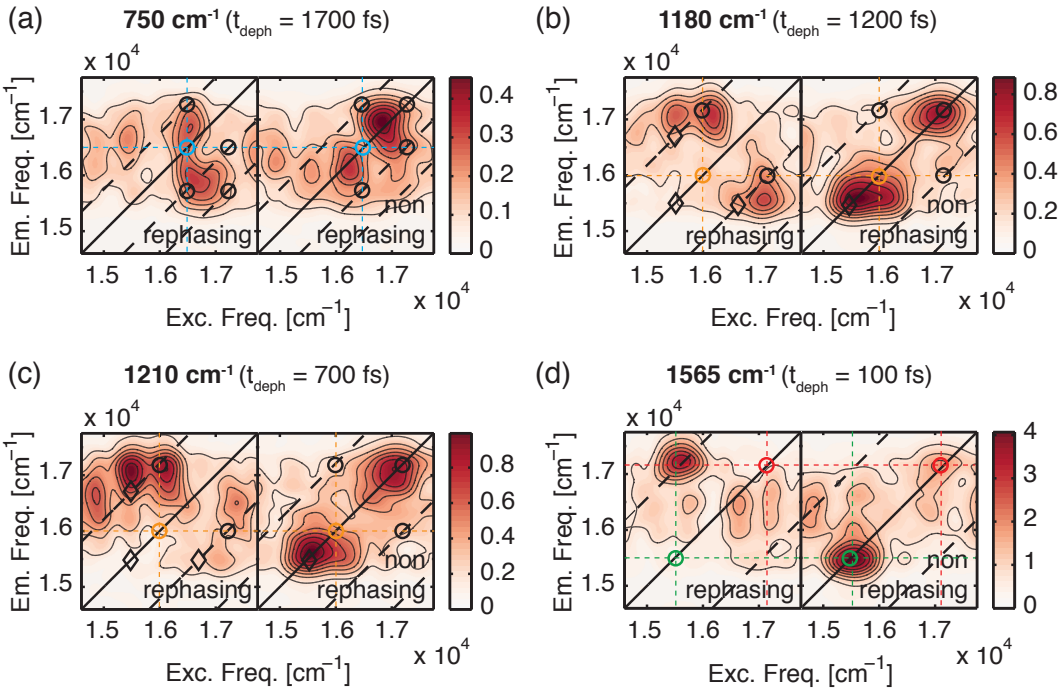

Figure 6.7 2D-CAS of rephasing and non rephasing datasets resulting from global fit. Panels (a), (b), (c) and (d) show respectively 2D-CAS of components (i), (ii), (iii) and (iv). Coloured circles pinpoint the positions of electronic transitions, following the same colour code used in Figure 6.5. Black circles and diamonds indicate the predicted position of signals arising from vibrational coherences.

6.3.2.3. Discussion

The combined interpretation of (i) the steady-state absorption spectrum, (ii) the CD spectrum, (iii) the Fourier analysis of the coherence beatings and, finally, (iv) the global analysis, helped in disentangling the positions of the electronic states of the two species involved in the ET mechanism in PCP.

The Fourier analysis distinguished four distinct regions on the diagonal of the 2DES map thanks to comparison of the frequency of the detected beatings and the Raman spectra of Per and Chl*a*.

Electronic states assignment

As anticipated before, oscillations with frequency equal to the typical vibrational modes of Per, 1180 cm^{-1}, 1220 cm^{-1} and 1560 cm^{-1}, were detected in the spectral regions around $1.60 \cdot 10^4$ cm^{-1} (orange dot in Figure 6.5(a)) and around $1.75 \cdot 10^4$ cm^{-1} (red dot in Figure 6.5(a)). The singlet states of Per possibly lying within the investigated spectral region are S_1, ICT state and S_2 state. About S_1 and ICT states, in all the models depicted in Figure 6.2, their energy gap would be so small that the 2DES experiment performed at room temperature wouldn't be capable to differentiate them in any case. Thus, in the present discussion, Per electronic states between the ground and S_2 states will be considered as a unique state which henceforth will be abbreviated as S_1/ICT.

Looking at the steady-state absorption and CD spectra (Figure 6.3), it is reasonable to attribute the 2D signals in the region around $1.75 \cdot 10^4$ cm^{-1} to the red edge of the S_2 band of Per. Schulte and coworkers [142], performing site-directed mutagenesis of the amino acid residue coordinating a specific carotenoid, assigned the most-red absorption signature of S_2 band to Per 614/624. It follows that, in our experimental conditions, Per 614/624 should be preferentially excited.

2D-CAS of components (ii) and (iii) (Figure 6.7(b,c)) revealed the presence of an electronic transition centered at $\omega_{e'g} = 1.60 \cdot 10^4$ cm^{-1} that perfectly matches the second region where contribution of Per was detected. It follows that e'electronic state can be attributed to S_1/ICT state. The energy estimated in the present work is fully consistent with the value reported by Zigmantas *et al.* [134].

Oscillations with frequency equal to 750 cm^{-1} are detected in two different regions of the 2D map, namely at $1.55 \cdot 10^4$ cm^{-1} (green dot in Figure 6.5(a)) and at $1.65 \cdot 10^4$ cm^{-1} (cyan dot in Figure 6.5(a)). This mode is well known to be a typical strong vibrational signature of Chl*a* and it can thus be used as benchmark.

Absorption and CD spectra demonstrate that the area of the 2D map surrounding the green circle (Figure 6.5(a)) present also signatures compatible with the excitation of the blue edge of the Q_y electronic transition, hereafter named as $Q_{y,1}$. Indeed, 2D-CAS of component (ii) and (iii) reveal further contributions besides the vibrational coherences of Per species. As anticipated before, diamonds in Figure 6.7(b,c)

show oscillating components arising from vibrational modes coupled to an electronic transition lying at the very edge of the laser spectral range, most likely Q_y transition. Indeed, as demonstrated by Chl*a* Raman spectrum (Figure 6.5(e)) and confirmed by Fourier transform of the 2DES signal at the green circle (Figure 6.5(f)), also Chl*a* has a vibrational mode close to 1200 cm^{-1} thus contributing to the overall 2D-CAS in PCP.

2D-CAS of component (i) (Figure 6.7(a)), instead, reveals a second, higher-energy, electronic transition belonging to Chl*a* that is centred at $\omega_{e''g} = 1.65 \cdot 10^4$ cm^{-1}. That observation is perfectly consistent with the Fourier analysis reported in Figure 6.5(g) and the energy of this electronic transition is compatible with the Q_x state of Chl*a*, as reported in previous studies [120,122,133,135].

In summary, we pinpointed the main electronic transitions of Per and of Chl*a* involved in the mechanism of ET. In our experiment we are exciting, in ascending order, the blue edge of Q_y state of Chl*a*, S_1/ICT state of Per ($\omega_{e'g} = 1.60 \cdot 10^4$ cm^{-1}), Q_x state of Chl*a* ($\omega_{e''g} = 1.65 \cdot 10^4$ cm^{-1}) and, finally, the red edge of S_2 state of Per, most likely Per 614/624.

Population dynamics

Given these considerations, a qualitative interpretation of the non oscillating part of the signal can be pursued. Three distinct non coherent phenomena are detected: (i) an ultrafast (~100 fs); (ii) an intermediate (2.8 ps) and (iii) a very long ($\gg$ 5 ps) process.

2D-DAS of component (i) (Figure 6.6(a)) clearly shows a decaying signature at cross-peak below diagonal and a rising signal on the diagonal at $1.60 \cdot 10^4$ cm^{-1}. The data and the decaying time constant are consistent with internal conversion process from S_2 state of Per to S_1/ICT state, as detected in other experimental studies [122,139,140].

2D-DAS of component (ii) (Figure 6.6(b)) accounts for a slower non coherent process. The positive region (decaying 2DES signal) is elongated from the central/high-energy part of the diagonal to the lower edge of the map. A weak negative component (rising signal) is also detected on the low-energy part of the diagonal. Considering the position of these signals and taking into account previous pump-probe [117,120,132,135,139] and transient grating measurements [143], we interpreted the 2.8 ps time constant component as non coherent ET process from Per to Q_y of Chl*a* that is mediated by a Förster mechanism.

Finally, component (iii) represents a very long decay process, involving the low-energy spectral region and probably accounting for internal conversion or radiative decay towards Chl*a* ground state or inter-system-crossing to Chl*a* triplet state.

Coherent ET dynamics

The most interesting and novel finding of the present work is the fast dephasing coherence (1565 cm^{-1}, 100 fs). All the characteristics of this oscillation emerging from the different analyses suggest its attribution to a quantum coherent ET between Per and Chl*a*, $S_2 \rightarrow Q_{y,1}$. 2D-CAS of component (iv) are shown in Figure 6.7(d): rephasing signal shows high-amplitude oscillating signals out of diagonal, while non rephasing signal on the diagonal. This is the typical pattern expected in a ED for electronic coherences and described by the Feynman diagrams reported in Figure 6.8. In this case, in agreement with the assignment made in the previous sub-section, the electronic states interacting to give the delocalized exciton state are a low-energy S_2 state of Per, possibly Per 614/624, and a state on the blue tail of Q_y band, $Q_{y,1}$ of Chl*a*, e.g. a (0,1) vibronic transition. Several studies have indeed suggested that Per 614 has the strongest electronic interaction with Chl*a* [113,123,142]. The detected damping time is slightly longer than what expected for a purely electronic coherence (~50 fs) at room temperature. It is possible that the characteristic vibrational mode of Per at 1560 cm^{-1} may play a role in preventing the dephasing of the coherent superposition of Per and Chl*a* states.

Most of the papers published during the first decade of this century describe the secondary channel of ET between Per and Chl*a* as involving S_2 state as donor and Q_x state as acceptor. The pump-probe data identified a Chl*a* ground state bleaching in the fast timescale, thus Q_x and Q_y populations are indistinguishable [116]. Q_x state was often considered as acceptor state without specific experimental confirmation, but only based on the consideration that the $S_2 - Q_x$ energy gap is lower than $S_2 - Q_y$.

As anticipated in Section 6.2, calculations performed by Bricker *et al.* [126] predicted that the $S_2 \rightarrow Q_y$ ET pathway is the dominant energy transfer pathway in PCP in the sub-picosecond range. Among all the computed ET times, the fastest process involves Per 614 and Chl*a* 601. On the other hand, $S_2 \rightarrow Q_x$ ET pathway is estimated to be extremely inefficient since they determine 4.83 ps time constant for the process, too slow to compete with ultrafast $S_2 \rightarrow S_1$ internal conversion. Moreover, they suggest that the $S_2 \rightarrow Q_y$ ET pathway, rather than the previously suggested $S_2 \rightarrow Q_x$, may be responsible for the reported Chl*a* bleaching signature seen in pump-probe experiments at around 200 fs. Finally, they also propose a possible coherent character of the $S_2 \rightarrow Q_y$ ET pathway.

Our results seem not only to support these theoretical predictions, but they also confirm the conclusions of Ghosh and co-workers [143] that, on the basis of transient grating measurements on S_2 band, distinguish two distinct time regimes for the ET process in PCP: an ultrafast and a slower pathway. Their hypothesis states that

the first is consistent with a coherent mechanism involving an exciton state delocalized over Per and Chl*a*. Thus, the interaction initially lies in the intermediate to strong coupling regime, in which the electronic coupling strength is larger than the system-bath reorganization energy. Afterwards, the coupling rapidly drops as S_2 mixes with dark state S_1 and as system-bath interaction increases owing to the rising ICT character of Per. This concomitant processes result in excitation localization onto single chromophores and in a transition from strong/intermediate to weak coupling regime. Ghosh *et al.* [143] suggested that this condition initiates the ensuing slower pathway mediated by a Förster mechanism.

In this context, our work not only confirms the previous findings of Ghosh and coworkers concerning the two distinct time regimes, as shown in Figure 6.9, but it clearly and directly shows the oscillations arising from the coherent pathway. Moreover, nor coherent, nor non coherent signatures of an ET pathway from S_2 state of Per to Q_x of Chl*a* were detected in our 2DES dataset.

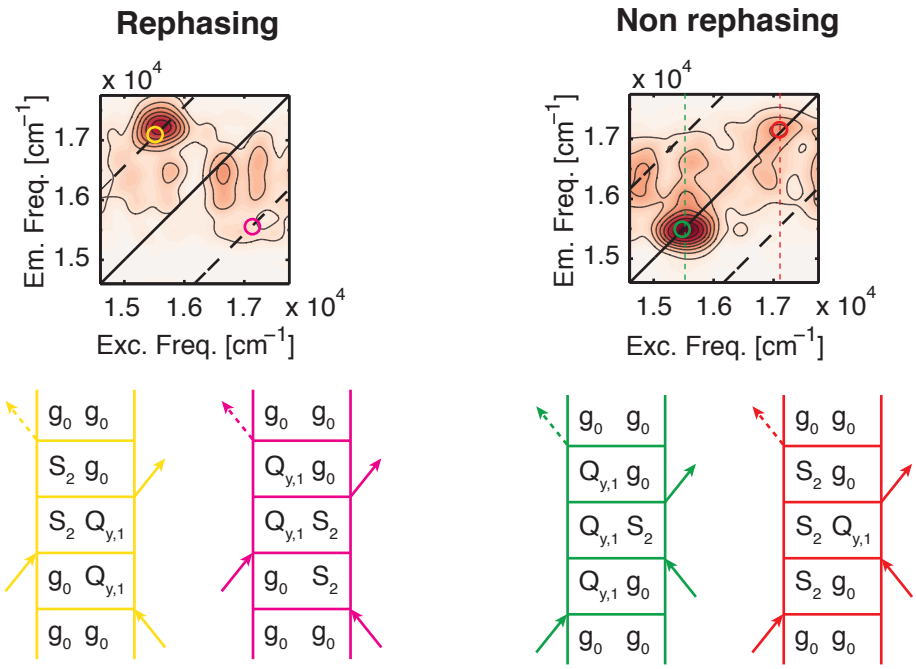

Figure 6.8 Set of double-sided Feynman diagrams representing electronic coherences in rephasing and non rephasing maps.

6.3.2.4. Final remarks and further developments

The present results give a preliminary but, at the same time novel, interpretation of the ultrafast dynamics following photoexcitation in peridinin-chlorophyll *a*-protein. The multidimensionality of 2DES has been a unique and necessary tool capable to disentangle the spectral regions where the electronic transitions of the distinct species appear. The characterization of the coherent beatings of 2DES signal, together with a careful analysis of Resonance Raman spectra of the isolated chromophores, pinpointed four distinct contributions.

Within the investigated spectral region, we detected at $1.60 \cdot 10^4$ cm^{-1} and at $1.65 \cdot 10^4$ cm^{-1}, respectively, S_1/ICT and Q_x electronic transitions (Figure 6.9). In our experimental conditions we could not detect any distinct behavior of S_1 and ICT states, as previously suggested by target analysis performed by van Stokkum *et al.* [122], and therefore we considered them as tightly connected (S_1/ICT). Thus, no further development on the knowledge of the nature of these states has been achieved. Moreover, the red and blue edges of the experimental spectral window revealed the contributions, respectively, of Q_y state and of S_2 state (Figure 6.9). It is likely that, tuning the laser spectrum on the low-energy region of S_2 band, we are selectively exciting one of the Per of the monomer, namely Per 614.

The global analysis revealed the downward pathways of energy in PCP as schematized in Figure 6.9. The process of ET occurs *via* two distinct pathways: an initial sub-picosecond and coherent process is followed by a slower and non coherent pathway. This changing in time-regime was previously detected by Ghosh *et al.* [143], but only 2DES measurements have given the first direct proof that a coherent mechanism is strictly involved in ET process. Moreover, 2DES data also confirm that ET pathway from S_2 state of Per has Q_y, and not Q_x, as acceptor state in Chl*a*.

To find even stronger support to our conclusions, further measurements are scheduled. Indeed, other forms of PCP are available: the light harvesting complex has been reconstituted with bacteriochlorophyll *a* and with chlorophyll *b* that have, respectively, lower- and higher-energy Q_y bands than Chl*a*. Tuning the energy gap between S_2 donor state and Q_y acceptor state could be useful to further confirm the presence of the quantum coherent ET mechanism in the early stages of the overall ET process.

Moreover, we will implement a kinetic model within the global analysis accounting for a more realistic description of the energy pathways. The global fitting methodology used to extract the excited state dynamics assumes indeed a parallel kinetic model [59] and therefore it currently does not fully account for the presence of competitive relaxation pathways. Therefore, the time constants assigned to the different pathways should be considered as 'effective' time constants describing the overall decay of the states. Nevertheless, the qualitative aspect of the excitation energy flow is entirely captured.

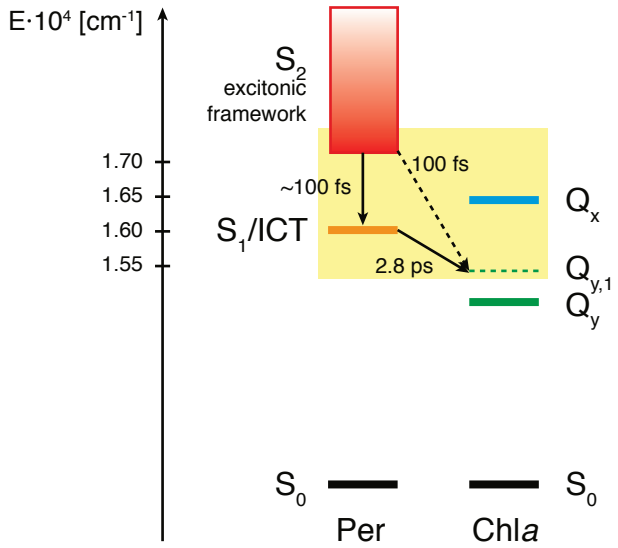

Figure 6.9 Energy level diagram of Per and Chl*a* electronic states in PCP from *Amphidinium carterae*. The Per states are labelled as S_0 (ground state), S_1/ICT (first excited state, orange), and S_2 exciton manifold (second excited state, orange). Chla states are labelled, accordingly, as S_0, Q_y (green) and Q_x (cyan). Yellow area marks the laser spectral range. Non coherent and coherent energy pathways are pinpointed with straight and dashed arrows respectively.

7 Proton tunnelling

2DES, as extensively discussed in the previous Chapters, has well-established applications to the study of photophysical phenomena and, in particular, to the study of natural and artificial multichromophoric light-harvesting systems, given its capability of disclosing exciton dynamics and electronic couplings. The power of unveiling the connection between the initially excited electronic states and the subsequently probed behaviour has also possible applications in photochemistry.

To date, chemical non-equilibrium systems have been widely studied by transient two-dimensional infrared (2DIR) spectroscopy, by introducing an optical perturbation before or during the 2DIR measurement. Various processes have been analysed so far, such as photo-switchable peptides [150], disulfide bond breaking [151], metal-to-ligand charge transfer [152], photoreactivity of metal coordination complexes [153] and protein unfolding dynamics [154].

The capability of directly relating the excitation dependence of a systems to its spectral response in the same measurement can be transferred from vibrational to electronic 2D spectroscopy, as demonstrated by Kullmann *et al.* [155]. The application of 2DES to the analysis of photochemical reactions is still an unexplored field but, at the same time, very promising. Indeed, 2DES intuitively visualize the spectral correlations in photoactive chromophores on ultrafast time-scale and couplings between different species appear as cross-peaks connecting the excitation frequency (absorbing species) with the emission frequency (emitting species). Moreover, 2DES can provide useful information about the reaction mechanism, namely the ultrafast dynamics on the reactive potential energy surface.

Hydrogen or proton transfer is a basic chemical reaction that determines the behaviour of DNA, proteins, enzymes, and many drugs. A purely classical approach is often not sufficient when dealing with this topic, since a proper description of the system cannot avoid to consider the quantum nature of the proton. The *transfer* can be described as the delocalization of the proton wavefunction over the energy minima of the reactant and of the product, fulfilling the conditions for a proton tunnelling mechanism [156]. A proton has a light mass but it is larger than the electron's, thus it results to be more localized and its wavefunction decays faster than the electronic one. It has been demonstrated [157] that the coupling between the reactant

and the product is very sensitive to the donor-acceptor distance and therefore to vibrational modes that affect it.
In this work, we followed the tautomerization process of porphycene, as case study of the basic chemical reaction of the proton/hydrogen transfer mechanism and the possible coupling with vibrations. The task was not trivial since it required ultrafast time resolution and sensitivity to vibrational modes, but 2DES fulfilled both requirements.

7.1. Porphycene, structural properties and tautomerism

Since the first synthesis in 1986 [158], porphycene has attracted the attention of researchers both for its photophysical properties and, due to the intense absorption in the red-light spectroscopic region and the good yields of singlet-oxygen generation, for the potential applications of the unsubstituted molecule and its derivatives as promising photodynamic therapy photosensitizers [159–161].
Free-base porphycene is a structural isomer of free-base porphyrins and retains their central features, namely the cavity formed by four pyrrole rings and two exchangeable protons. However, porphycene and porphyrin differ in the cavity shape, in their symmetry, in NH $\cdots$N distances and, moreover, in the strength of dipole transition moments.
Owing the short distance between the inner nitrogen atoms and therefore the strong NH $\cdots$N hydrogen bonds, porphycene represents a good model system for studying intramolecular hydrogen transfer dynamics without interferences from the environment, since the well-defined inner cavity is isolated from the environment.
As mentioned before, the cavity carries four protonable sites, nitrogen atoms, but only two of them can be protonated simultaneously. This leads to six possible tautomeric forms, two *trans* and four *cis*. In symmetric porphycenes only three out of the six tautomers need to be considered for symmetry reasons.
The tautomerization in non-functionalized porphycene is schematized in Figure 7.1, showing the proton transfer pathway between the four lower stationary points on the potential energy surface of the ground state. Several computational studies [162–167] have pointed out that C_{2h} *trans* structure is the most stable tautomer, while C_{2v} *cis* structure has slightly higher energy and, thus, it is the intermediate configuration in the potential energy surface.
The transfer of two hydrogen atoms in the inner cavity created by the four pyrrole rings has been extensively investigated in the porphyrins and their derivatives [168,169]. The reaction mechanism involves an inter-conversion between two *trans* tautomers that are chemically equivalent and where the protons are bonded on opposite pyrrole rings. In porphyrins, tautomerization occurs *via* a step-wise mechanism that involves thermally activated tunnelling of a single hydrogen atom [170]. The process leads to a *cis* tautomer, where the protons are bounded to adjacent pyrrole rings. From this structure, the molecule can either return to the initial *trans*

configuration or can be converted into the second *trans* tautomer by transferring a second proton (Figure 7.2(a)).

Tautomerization in porphycenes occurs with much faster rates than in porphyrins [171], possibly because of the increased strength of the intramolecular hydrogen bonds, and thus a concerted double-proton transfer has been suggested [172] (Figure 7.2(b)). Different experimental approaches have been followed to investigate this mechanisms in porphycenes [156,173–177], ranging from laser-induced fluorescence, hole burning and dispersed fluorescence spectroscopy in supersonic jets, to transient absorption and fluorescence anisotropy.

Sepioł *et al.* [173] detected in fluorescence excitation spectra a splitting into doublets of the peaks that disappears if one or both the protons were replaced by deuterium, as well as upon complexation with alcohol. This observation was interpreted as evidence for a double hydrogen tunnelling between the symmetric minima of the potential energy surface. This hypothesis was subsequently confirmed by several other works [156,176,178,179] which could not detect any evidence for the formation of intermediate *cis* species. Moreover, Waluk [178] demonstrated that, differently from porphyrins, in porphycenes the tautomerization process is fast also in the lowest excited state. Still the barrier of the potential energy surface of the excited state is higher or wider than in the ground state. The rates of tautomerization in the excited state vary significantly between differently functionalized porphycenes (from 10^9 to 10^{13} s^{-1}) as function of NH $\cdots$N distance [156]. Indeed, in species where the separation between the N atoms is smaller, the tautomerization rate is much shorter than the excited state lifetime. In contrast, in species where that distance is higher, the process is significantly slowed down, so much that it becomes non-competitive with the relaxation of the excited state. This distance dependence is taken as proof that tunnelling happens [180].

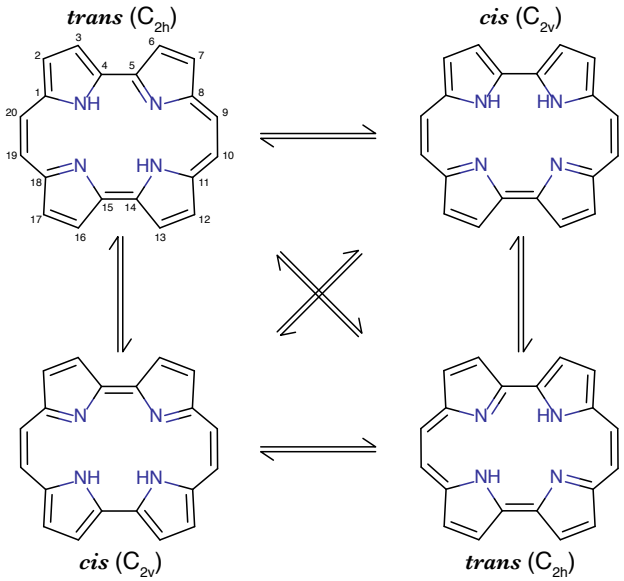

Figure 7.1 *Trans* and *cis* tautomeric forms of symmetric non-functionalized porphycene.

Moreover, several studies pointed out that specific low-frequency vibrational modes, not necessarily involving displacement of inner hydrogens, could favour or hinder tunnelling process by either decreasing or increasing the distance between donor and acceptor nitrogen atoms [156,176–178]. These works reported a totally symmetric $2A_g$ vibration (180 cm^{-1}) as *gating* mode responsible for the enhancement of tunnelling rate. It corresponds to an in-plane deformation of the macrocycle that brings two adjacent nitrogen atoms closer and a hydrogen atom in an intermediate position between them, as shown in Figure 7.2(c). This mode enhances the H-bond strength and lowers the tautomerization barrier. It follows that the energy necessary for enhancing the tunnelling is lower than what required to populate the *cis* species and, thus, a stepwise mechanism is far less favoured.

In this study we examined an asymmetrical 2,7,12,17-tetraphenylporphycene (TPPC) conjugated to a proline-rich antimicrobial peptide, apidaecin 1b, which is bounded in the C9 (*meso*) position (Figure 7.3, C numbering reported in Figure 7.1). Henceforth the compound will be abbreviated as TPPC-*ap*. The functionalization in *meso* position induces asymmetry in the system and consequently the two resulting *trans* tautomers are spectrally discernible.

Planas *et al.* [181] studied different C9-substituted porphycenes discovering that the energy of the first excited state (S_1) strongly depends on the electronic nature of the substituent: the stronger is the electron-donating character of the C9-group, the lower is the energy of S_1 state. They also found that the *trans-1* species (see Figure 7.3) is the most stable species in state S_1.

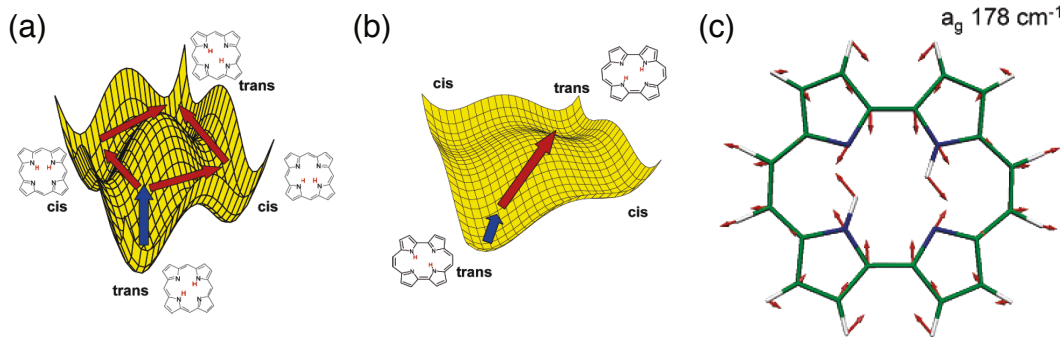

Figure 7.2 adapted from [156]. Tautomerization pathway in porphyrin (a) and in porphycene (b). Blue arrows indicate thermal activation, while red arrows pinpoint tunnelling. (c) Nuclear motion in the *gating* vibrational mode.

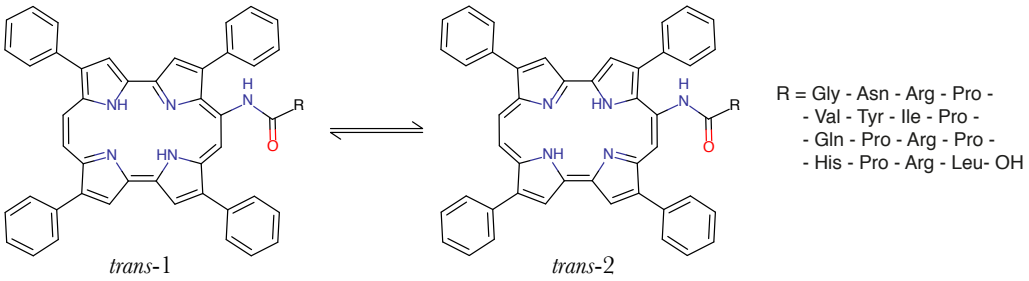

trans-1 *trans*-2

Figure 7.3 *Trans* tautomeric forms of TPPC-*ap* conjugate. On the right, the primary sequence of the bounded peptide apidaecin 1b is reported.

7.2. Electronic States Model

A deep understanding of the tautomerism process cannot avoid a clear knowledge of the electronic transition energies of the tautomers. There are six tautomeric forms in TPPC-*ap*, but within our model, for simplicity, we consider only the contribution of the *trans* species because they are more stable than the four possible *cis* forms, which are unlikely populated (Figure 7.3) both in the ground and in the excited states.

7.2.1. Experimental methods

TPPC-*ap* was kindly donated by prof. M. Gobbo that synthetized the compound following the procedure described in [73]. The linear photophysical properties of the system were measured by steady-state absorption spectroscopy, performed at 295 K, and fluorescence emission/excitation spectroscopy, performed at 295 K and at 77 K. The samples were prepared diluting the chromophore in MeOH to $5 \cdot 10^{-5}$ M for absorption measurements and to $5 \cdot 10^{-6}$ M for fluorescence characterization.

7.2.2. Results and discussion

The steady-state absorption spectrum of TPPC-*ap* (Figure 7.4) is characterized by two distinct regions, namely B-bands and Q-bands regions, in analogy to what previously described for other tetrapyrroles, such as porphyrins, chlorins and bacteriochlorins.

B-band is an asymmetric peak accounting for two distinct electronic transitions, $S_0 \rightarrow S_3$ and $S_0 \rightarrow S_4$, giving rise to the red shoulder at about $2.51 \cdot 10^4$ cm^{-1} and to the maximum at about $2.64 \cdot 10^4$ cm^{-1}, respectively.

Q-bands region is characterized by a multi-component absorption band to which contributes both $S_0 \rightarrow S_1$ and $S_0 \rightarrow S_2$ electronic transitions, lying respectively at around $1.53 \cdot 10^4$ cm^{-1} and $1.59 \cdot 10^4$ cm^{-1}, while the band centered at $1.71 \cdot 10^4$ cm^{-1} is due to higher vibronic transitions. The assignment suggested here is in agreement with computational results of Planas *et al.* [181] and magnetic circular dichroism spectra recorded by Gil *et al.* [182].

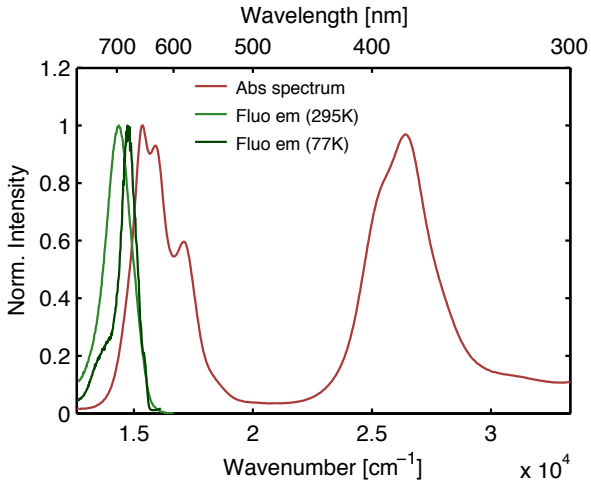

Figure 7.4 Absorption (red line) and fluorescence emission (green lines) spectra of TPPC-*ap* in MeOH. Fluorescence emission was recorded both at 295 K (exc. at $2.5 \cdot 10^4$ cm^{-1}, light green) and at 77 K (exc. at $1.6 \cdot 10^4$ cm^{-1}, dark green).

The absorption spectrum of TPPC-*ap* is significantly different from the spectrum of the symmetrical TPPC [183]. In general, C9 substituents induce B band splitting and the rising of further red-shifted bands in the Q-bands region, revealing the effect of the electron-donating property of the substituent [181], as mentioned before. TPPC-*ap* confirms this behaviour that is mostly detectable from the broadening of the absorption bands towards the red.

The distinct contribution of the two *trans* tautomers of TPPC-*ap* are not fully discernible in a room temperature measurement. The electronic transitions of the two species are indeed overlapped in the same spectral region.

A better insight can been obtained comparing the fluorescence emission and excitation spectra at 295 and 77 K. Planas *et al.* [181] indeed demonstrated that when the temperature is increased from 77 K to 295 K, the fluorescence quantum yield of both tautomers decrease significantly, but the two species behave differently. The high-energy species (*trans-2*) is clearly more quenched than the other one (*trans-1*) by the increase of the temperature. This suggests that at room temperature the excited state population is driven from *trans-2* to *trans-1*. This peculiar behaviour has been exploited to distinguish the contribution of the two tautomers in the spectroscopic signals. The emission spectra shown in Figure 7.4 confirm this behaviour.

Fluorescence emission spectra of TPPC-*ap* recorded at 77 K revealed an interesting shift in energy of the emission bands as a function of the excitation wavelength (Figure 7.5(c)). We performed a systematic study of fluorescence emission as a function of the excitation wavelength and the 2D excitation/emission fluorescence spectrum reported in Figure 7.5(a,b) was recorded. In the zoomed panel, Figure 7.5(b), we clearly recognize a shift of the bands in the excitation fluorescence spectra towards higher energies as function of emission frequency.

The fluorescence excitation spectra of the single tautomers can be extracted from 2D fluorescence data with a Single Value Decomposition (SVD) procedure (see Figure 7.5(d)) [184] that is briefly described in Section 7.2.2.1. These spectra are a powerful tool to extract a clear picture of the energies of the electronic transitions of the two species.

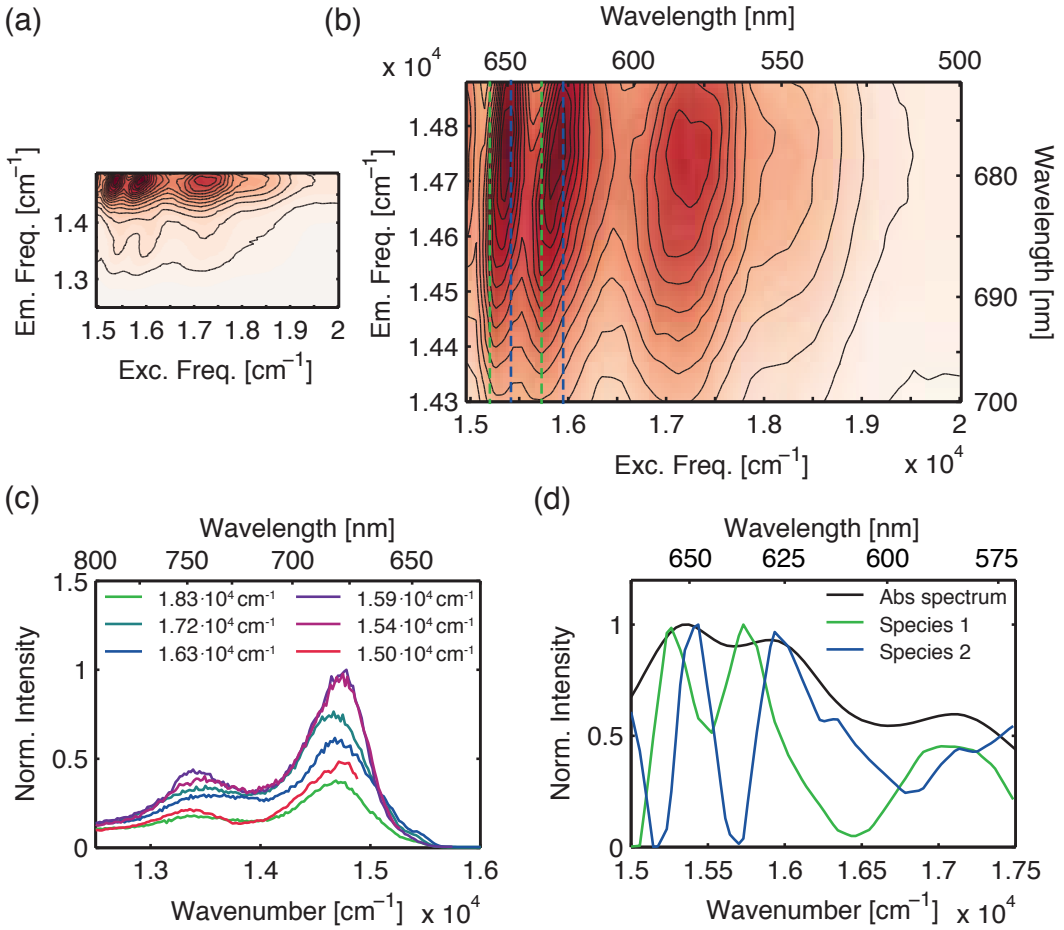

Figure 7.5 (a) 2D excitation-emission fluorescence spectrum of TPPC-*ap* at 77K in MeOH. (b) Zoomed 2D excitation-emission fluorescence spectrum. Dashed green and blue lines pinpoint the distinct contributions of the two species. (c) Fluorescence emission spectra of TPPC-*ap* in MeOH at 77K recorded with different excitation frequency. (d) Fluorescence excitation profiles of the two species were computed with the SVD procedure (*trans*-1: green line; *trans*-2: blue line) and compared to the absorption spectrum (black line).

7.2.2.1. Tautomers disentanglement via SVD procedure

Single value decomposition (SVD) is a well-known procedure capable of sorting the information contained in rectangular data matrixes. Indeed, the 2D excitation/emission spectrum could be represented as a $(m \times n)$ matrix X, having rank r and where m and n are the length of excitation and emission axis, respectively.
The absorption profiles of the two tautomers can be disentangled by solving the problem described in Eq. (7-1).

$$X = S\ D^T \tag{7-1}$$

Where D is a $(n \times r)$ matrix that contains the set of r fluorescence emission spectra of the r individual tautomers and D^T is the corresponding transposed matrix. Matrix S, instead, consists of a set of r column vectors, each one corresponding to the independent excitation profile of the r-th species. The features exhibited by these spectra provide a clear picture of the energies of the electronic transitions of the two species. As discussed before, for the investigated system the two *trans* species are dominant and the possible presence of *cis* tautomers can be neglected: it follows that in our case $r = 2$.
The matrix X can be directly obtained from the measurement shown in Figure 7.5(a,b). Matrix D can be built from the fluorescence emission spectra: it is indeed possible to recover the contribution to the emission of each *trans* tautomer applying a multi-Gaussian fitting procedure to the 77 K emission spectra recorded with excitation frequency equal to $1.83 \cdot 10^4$ cm^{-1} and $1.54 \cdot 10^4$ cm^{-1}.
Since matrix D^T has linearly independent rows (namely the normalized fluorescence emission profiles of the independent species), its right pseudo-inverse matrix $(D^T)^+$ can be computed and, finally, matrix **S** can be evaluated as:

$$S = X\ (D^T)^+ \tag{7-2}$$

S matrix includes also the information on the concentrations of the tautomers and their fluorescence quantum yields. The calculated fluorescence excitation profiles of the independent species are shown in Figure 7.5(d). They allow distinguishing the energy of the $S_0 \rightarrow S_1$ and $S_0 \rightarrow S_2$ electronic transitions for the two *trans* tautomers.
Using the energy of electronic transitions of the two distinct tautomers estimated with the SVD procedure, the steady-state absorption spectrum in the Q-bands region was reconstructed by a multi-Gaussian fit (Figure 7.6(a)) and a scheme the electronic energy levels was then built (Figure 7.6(b)).

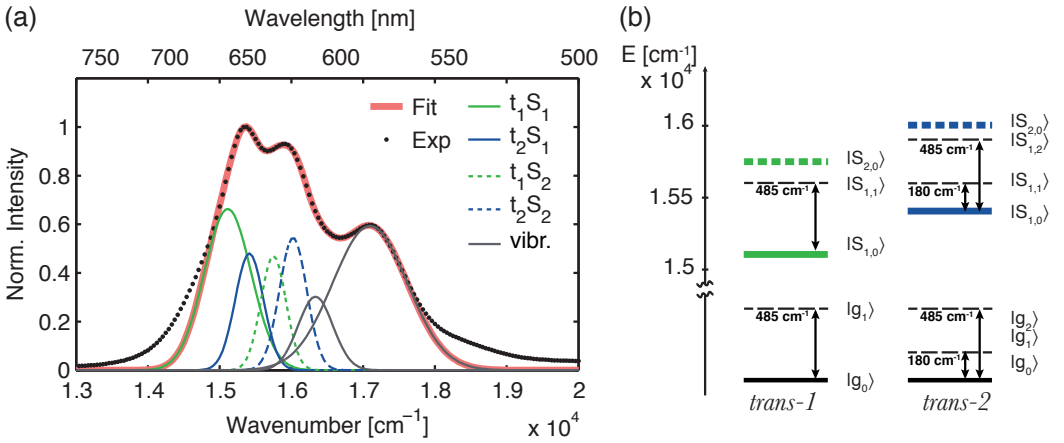

Figure 7.6 (a) Multi-Gaussian reconstruction (red line) of the experimental absorption spectrum (black dots) of TPPC-*ap*. Four components have been estimated by SVD analysis of the fluorescence spectra: S_1 and S_2 transitions of tautomer *trans*-1 in green (solid and dashed lines, respectively); S_1 and S_2 transitions of tautomer *trans*-2 in blue (solid and dashed lines, respectively). Gauss functions plotted in grey account for higher vibronic transitions not captured by the SVD analysis. (b) Putative model of the electronic and vibrational states for the two tautomers built on the basis of the spectroscopic data (2D excitation-emission fluorescence and 2DES) reported in this Chapter.

Table 7.1 Parameters of Multi-Gaussian fitting of the absorption spectrum reported in Figure 7.6(a).

Component	*trans-1* – S_1	*trans-1* – S_2	*trans-2* – S_1	*trans-2* – S_2
Amplitude	0.72	0.50	0.49	0.57
Centre [cm^{-1}]	15112	15750	15414	16024
FWHM [cm^{-1}]	385	232	205	224

7.3. 2DES characterization

7.3.1. Experimental methods

In order to perform 2D spectroscopy on the studied species, the spectral output of the NOPA was tuned to probe simultaneously both S_1 and S_2 electronic transitions of *trans-1* and *trans-2* tautomers of TPPC-*ap*, as demonstrated by Figure 7.7(a). The exciting pulses are thus centred at $1.65 \cdot 10^4$ cm^{-1} (25 fs), with energy equal to 9 nJ at the sample position.

Rephasing spectra were recorded for population times ranging from 0 to 550 fs in 5 fs increments, with each experiment repeated four times to ensure reproducibility. TPPC-*ap* was diluted in MeOH until the sample reached the optical density of 0.3, within the Q-bands spectral region, in a cell with a pathlength of 1mm.

The reproducibility of the steady-state absorption spectrum of the sample was checked after each scan to ascertain that the sample was not degraded during the measure.

7.3.2. Results and discussion

The 2DES spectra of TPPC-*ap* (Figure 7.7(c)) are characterized by a main central peak, elongated along the diagonal as result of the populations of electronic states S_1 and S_2 of both *trans*-1 and *trans*-2 tautomers. For clarity, from now on we will identify with $t_iS_{j,z}$ the *j*-th electronic state ($j = 0,1,2$) of the t_i tautomer ($i = 1,2$ as defined in Figure 7.3) in the *z*-th vibronic state (see energy level scheme in Figure 7.6(b)). As it can be ascertained following the evolution of diagonal signal along the population time (Figure 7.7(b)), the populations of both t_iS_2 states strongly decay, while t_iS_1 states have lifetimes far longer than the time-window.

As shown in Figure 7.7(c) a cross-peak is clearly visible below diagonal, showing a strongly oscillating character that persists during the entire population time window investigated. The cross peak appears in the region of the 2DES map with emission energy close to $t_2S_{1,0}$ electronic transition, at about $1.54 \cdot 10^4$ cm^{-1}. Moreover, also the region above diagonal with excitation energy close to the same electronic transition has a striking beating character.

These evidences represent the first hints that 2DES signal retains several contributions arising from vibrational coherences of both ground and first excited state of the species *trans-2*.

A careful investigation on the beatings of the 2DES dataset is crucial to study whether coherent tunnelling is modulated by the *gating* vibrational mode. To this aim, the global fit analysis described in Section 3.2.8.2 has been applied to analyse the dynamics of both the coherent and the non coherent part of the signal.

The non coherent dynamics is dominated by three main components with distinct time constants as shown in Figure 7.8, which reports the corresponding 2D-decay associated spectra (2D-DAS): (i) ~2 ps; (ii) 570 fs; (iii) 60 fs.

2D-DAS of component (i) revealed that the whole 2D map is decaying with a time constant much longer than the investigated time window. The populations of t_1S_1 and t_2S_1 electronic states are decaying with time constants (ii) and (iii) towards the ground state. Finally, 2D-DAS of component (iii) reveals that the internal conversion from t_iS_2 towards t_iS_1 is extremely rapid and occurs in less than 100 fs.

The study of the coherent part of 2DES signal is more meaningful and revealing for the purposes of our investigation. Global analysis revealed, indeed, the presence of several oscillating components listed in Table 7.2 whose 2D-coherence associated spectra (2D-CAS) are shown in Figure 7.9(b).

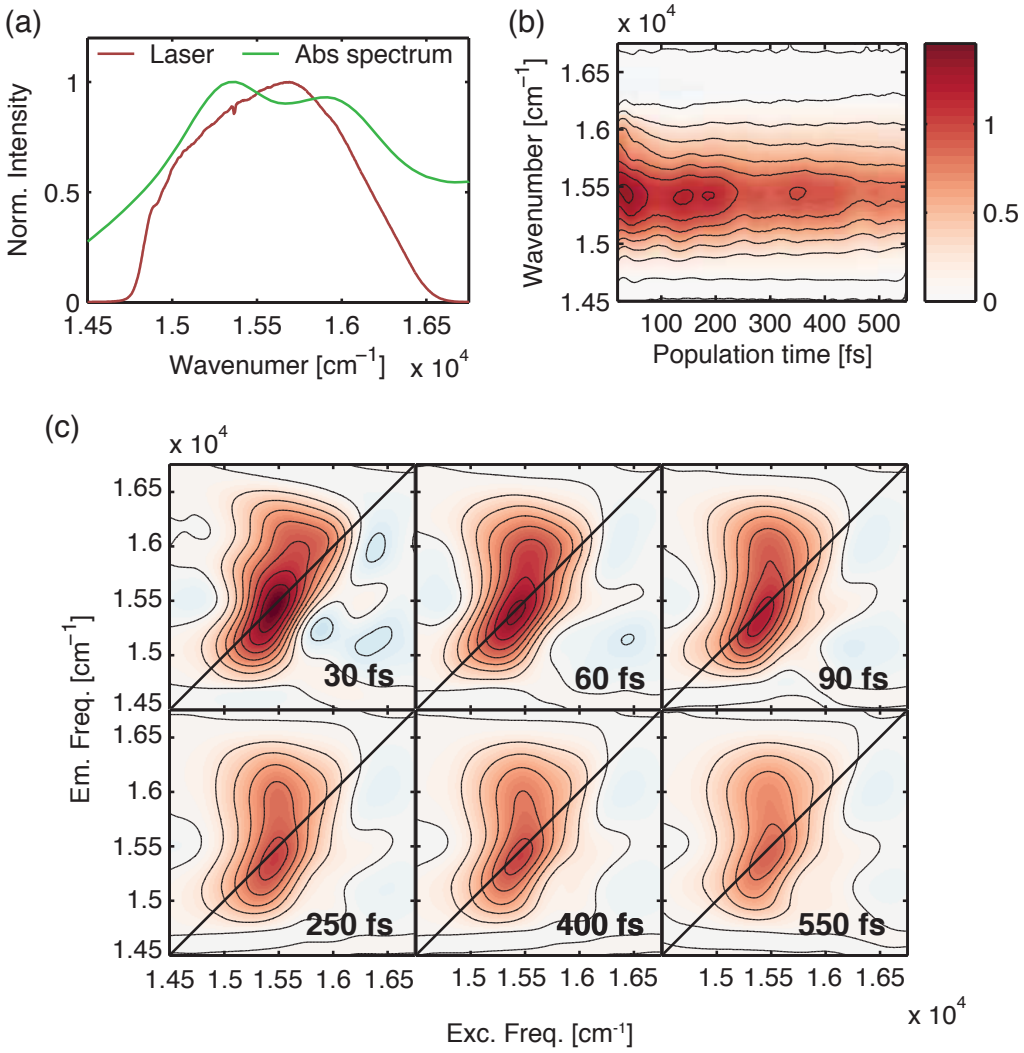

Figure 7.7 (a) Steady-state absorption spectrum of TPPC-*ap* compared to the laser spectrum used in the 2DES experiment. (b) Evolution of the diagonal 2DES signal as function of population time. (c) Real rephasing signal of TPPC-*ap* for significant population times

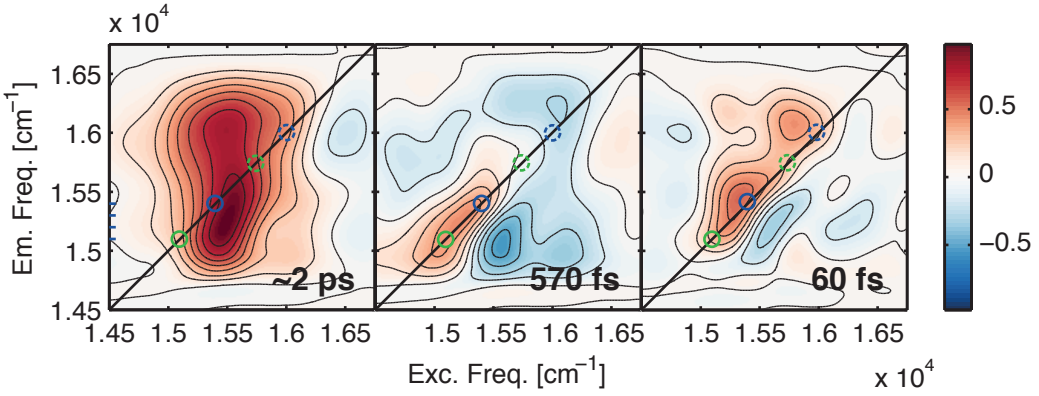

Figure 7.8 Global fit analysis revealed the presence of three distinct decaying components in the non oscillating part of the 2DES signal. Green and blue circles pinpoint the electronic states of the species *trans-1* and *trans-2*, respectively (frequency corresponding to the assignment reported in Table 7.1). Full and dashed line contours indicate the first and the second electronic excited state of the two species, respectively.

All these signals are possibly attributable to vibrational coherences of both ground and t_iS_1 states. Several experimental evidences support this assignment. In the first place, the comparison of the frequency of the beatings with resonant and non-resonant Raman spectra of TPPC-*ap* powder Figure 7.9(a) shows a perfect match in the low-frequency region, especially for the modes at about 480 cm^{-1} and 180 cm^{-1}. Beatings at frequency higher than 500 cm^{-1} present a very weak amplitude and are not fully discernible in the FFT power spectrum of Figure 7.9(a). The global fit instead identified several oscillating signals whose frequency matches the Raman modes. Figure 7.9(b) reports the corresponding 2D-CAS.

Both the position on excitation/emission map and the computed dephasing time of the coherent signals are compatible with the vibrational nature of the oscillations detected in TPPC-*ap* dataset. The positions where DHO model (see Section 2.7.1) predicts the presence of vibrational beatings are pinpointed by the coloured circles in Figure 7.9(b). Most of the beating signals are associated to vibrational coherences of *trans-2* tautomer since the typical chair pattern (blue circles) of the oscillations, or a portion of it, is centred at $1.54 \cdot 10^4$ cm^{-1}, namely the energy of the electronic transition $t_2S_0 \rightarrow t_2S_1$. Distinct contributions of vibrational coherences arising from tautomer *trans-1* are clearly detectable only for high frequency modes, as shown by green circles in Figure 7.9(b). The possible presence of vibrational beatings arising from *trans-1* species in low-frequency 2D-CAS cannot be ruled out, but, since the region of these 2D spectra are very congested of signals, a definitive answer cannot be given.

Raman spectra show that the 480 cm^{-1} mode is selectively enhanced in resonance conditions. The analysis of 2DES signal revealed the presence of two distinct vibrational coherences with frequency close to what detected in Raman experiments,

namely component 4 and 5 (Table 5.3). The two beatings can be reliably distinguished in the global fit analysis because they have significantly different dephasing times, respectively $\gg$ 2 ps and 340 fs. We tentatively attribute the long-lasting vibrational coherence to a ground-state vibrational mode, while the fast-dephasing term to an excited-state vibrational coherence.

The most interesting oscillating signal is component 1, namely 180 cm^{-1} vibrational mode, that several previous works [156,176,185] described as *gating* mode assisting the concerted double-hydrogen transfer. A detailed inspection of the 2D-CAS of component 1 resulting from global analysis has been performed. The behaviour of positive- and negative- frequency beatings has been studied separately, as reported in Figure 7.10(c,d).

As described in Section 2.7.1, within the chair pattern of signals arising from purely vibrational coherences, the sign of the frequency of the oscillating signals is determined by the specific Feynman pathway that describes their origin. As a consequence, signals above and below diagonal have frequency with opposite signs (namely positive frequency below diagonal and negative frequency above diagonal). 2D-CAS in Figure 7.10(d), which displays only the contribution of beatings with negative frequency, clearly shows the presence of oscillating signals below diagonal. A simple interpretation of this signal as vibrational coherence in the DHO framework is not sufficient to explain this signature. A different phenomenon must be present to account for the peculiar amplitude distribution of this beating mode.

If we suppose that the tautomerism reaction could occur during population time, new coherent signals can be predicted. Among them, we can indeed find signals oscillating with negative frequency below the diagonal.

Table 7.2 Output of fitting parameters for oscillating components in 2DES rephasing signal of TPPC-*ap*.

Component	1	2	3	4	5	6
Frequency [cm^{-1}]	180	256	323	476	485	645
Dephasing time [fs]	280	220	170	$\gg$ 2000	340	240
Component	7	8	9	10	11	12
Frequency [cm^{-1}]	670	835	1000	1150	1265	1330
Dephasing time [fs]	2000	$\gg$ 2000	260	$\gg$ 2000	240	150

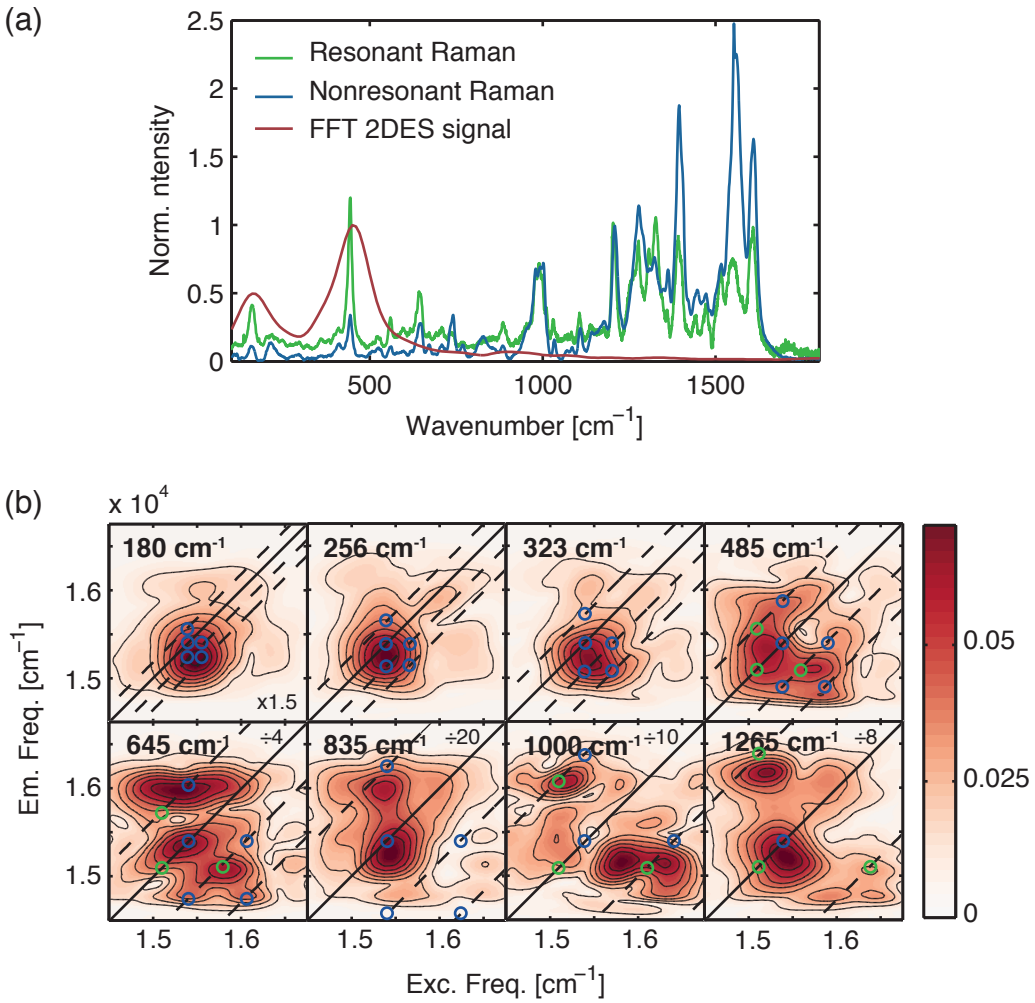

Figure 7.9 (a) Comparison between the beatings detected in the coherent signals of 2DES dataset (red line) with resonant (green line, excitation at $1.58 \cdot 10^4$ cm^{-1}) and non-resonant (blue line, excitation at $1.95 \cdot 10^4$ cm^{-1}) Raman spectra recorded for TPPC-*ap* powder at 77 K. (b) 2D-CAS of the main oscillating components resulting from global fit analysis. The circles pinpoint the predicted patterns for vibrational coherences. Green and blue circles are associated to *trans-1* and *trans-2* species respectively.

We listed all the possible Feynman pathways (Figure 7.10(a,b)) accounting for tautomerism reaction and that oscillates at the 180 cm^{-1} *gating* frequency. Previous works [178] demonstrated that tautomerism of porphycene in the lowest excited state is quite fast because it is assisted by the *gating* vibrational mode. Thus, we considered only stimulated emission pathways having a superposition of S_1 states during population time.

Moreover, we examined both $t_2S_1 \rightarrow t_1S_1$ and $t_1S_1 \rightarrow t_2S_1$ processes. The former represents a downward energy pathway, highlighted with a red line in Figure 7.10(a,b), while the latter occurs upwards in energy. In this discussion, the tautom-

erization happening in S_2 states was neglected since 2D-DAS (Figure 7.8) confirmed that the populations rapidly relaxes towards the low-lying electronic states with a sub-100 fs process.

In these conditions, only four Feynman pathways are possible and the positions of the signals that they predict are reported in 2D-CAS of Figure 7.10(c,d). Yellow and orange dots pinpoint the beatings with positive and negative frequency, respectively. Red contour indicates the downward energy pathways.

Figure 7.10(c,d) shows how the signal at red-contour positions is far more intense than the signal where upward processes are expected. It could suggest that $t_2S_1 \rightarrow t_1S_1$ tautomerization process is more likely to occur than $t_1S_1 \rightarrow t_2S_1$ double-proton transfer.

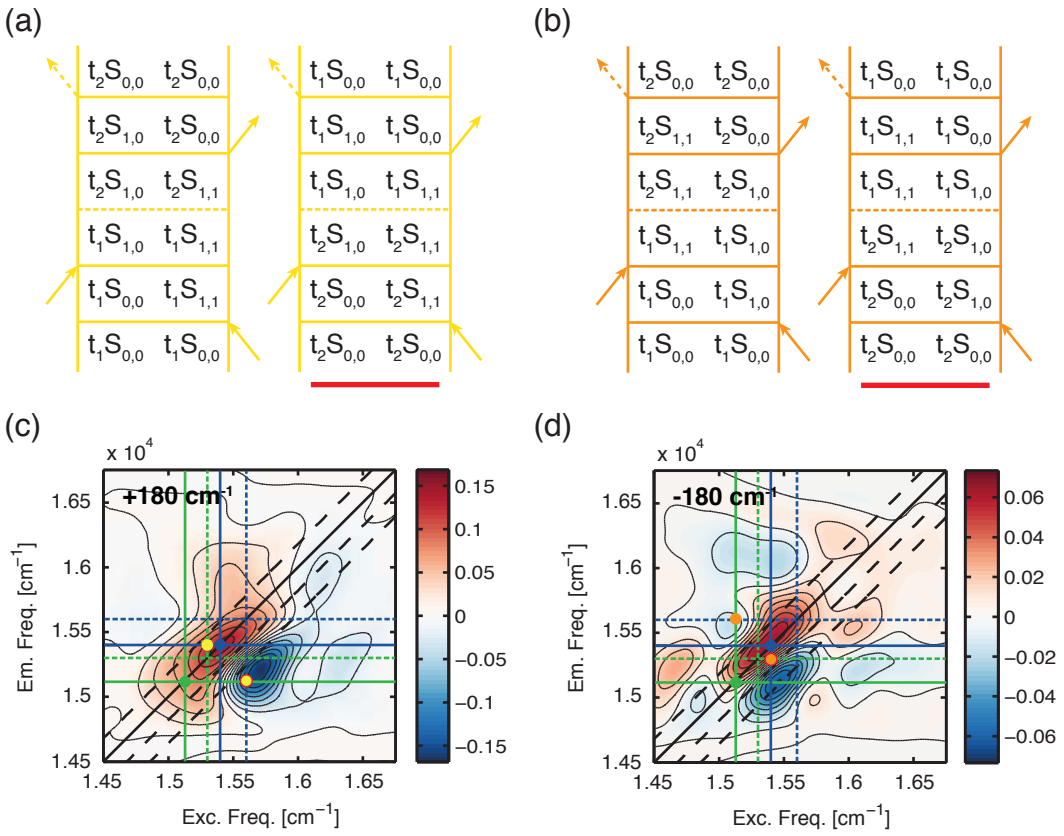

Figure 7.10 Feynman diagrams describing tautomerization reaction between t_1S_1 and t_2S_1 species resulting in positive (a) and negative (b) frequency coherent signals. Downward energy pathways are highlighted with red lines. (c,d) 2D-CAS of the *gating* coherence mode obtained with the global fit analysis. t_1S_1 and t_2S_1 states positions are pinpointed on the diagonal with green and blue dots, respectively. The energy of the electronic and vibronic transitions are shown by full and dashed lines, respectively (the colour code is consistent with the dots). Yellow and orange dots represent positive and negative frequency beatings, respectively. Red contours indicate downwards energy pathways.

7.4. Final remarks

In this work, we explored the possibility to exploit 2DES to investigate a photochemical, rather than a photophysical process. Similar femtochemistry applications are indeed exquisitely rare in the visible range and still not fully exploited despite its huge potential [155]. We have studied double proton transfer process occurring in the well-protected porphycene inner-cavity as enzymatic reaction model.

We develop a methodology capable to disentangle the electronic states of two distinct *trans* tautomers of TPPC-*ap*, based on the SVD analysis of 2D emission/excitation fluoresce spectrum, crucial for the ensuing interpretation of 2DES signals. Despite the still preliminary nature of our data, we think we detected reasonable evidences for a coherent double-proton tunnelling in the first excited state favoured by a *gating* mode at 180 cm^{-1}. The signatures detected in 2D-CAS of this mode, indeed, cannot be associated only to vibrational coherent oscillations due to their peculiar position on the excitation/emission map. Moreover, the peculiar distribution of the amplitude of the signal seems to suggest that the downward process from tautomer *trans-2* to *trans-1* is favoured.

Additional investigations will be performed to confirm these findings. Cryogenic 2DES measurements are scheduled to furtherly confirm the relevance of tunnelling mechanism. Moreover, different samples bearing other substituents will be considered, such as a porphycene with an electron-donating substituent in *meso* position, in order to obtain a better separation of the spectral features of the two relevant tautomers.

8 Conclusions

The research activity described within this thesis was devoted to study coherent dynamics in biomimetic and in biological systems. How Nature could harness quantum mechanisms and take advantage from them is a hot topic in the fringe discipline of quantum biology.
The non-trivial role of quantum phenomena is, nowadays, widely studied in distinct aspects of life. Among them, enzymatic catalysis, the intimate core of every biological process, seems indeed to exploit H-tunnelling in speeding up reaction rates. Not only. Photosynthetic organisms evolved strategies to capture energy from sunlight that are astonishing for their efficiency. Experimental evidences proved that excitation energy flow towards the reaction centre in light-harvesting protein complexes is assisted by a quantum coherent transport.
The intrinsic issue of those phenomena is their extremely fast behaviour. An experimental method capable to give a detailed insight into the excited state dynamics up to femtoseconds timescale is therefore necessary. The leading technique in this field is two-dimensional electronic spectroscopy (2DES), thanks to its capability of following coherent superposition of electronic states. To this aim we made a great effort to build in our laboratory an efficient spectroscopic setup. Non-trivial issues were overcome to guarantee good data quality and reproducibility. Crucial aspects consisted in gaining very accurate exciting pulse timing thanks to a new calibration procedure and exquisitely high control in pulses time duration.
No less important was the expertise matured in data interpretation of complex data. We must not forget that the amount of information enclosed in a complete 2DES dataset is enormous. Extracting the important features is crucial, but the methodology capable to disentangle them is not unique. The deck of analysis tools developed in collaboration with other members of my research group is rich and guarantees freedom of exploring different approaches. Thus the most proper strategy can be chosen, according to the features of the system under investigation.
Different multi-chromophore self-assembling systems were firstly studied, as artificial analogues of natural antennas. They mimic large protein complexes since they are constituted by chromophores embedded in a peptide scaffold. These toy models represent the perfect playground to disentangle the key features responsible for

quantum coherent transport. Synthetic systems can be suitably designed by changing selectively the crucial components. Distinct harvesters were explored, thus changing the intra-chromophore vibrational framework interacting with the exciton superpositions. Also the effects of tuning the spatial arrangement of the peptide scaffold were tested, revealing interesting behaviours. The results suggested that the higher flexibility of the peptide chain might have a non-negligible role in preserving of the exciton coherence, possibly protecting the chromophores from solvent fluctuations with higher efficacy. This remarkable result represents, on one side, a further step towards the understanding of natural systems, and, on the other, a promising starting point for future applications in artificial devices.

As mentioned above, dealing with large light-harvesting protein complexes is not an easy task, since they retain several constituents all contributing to the overall experimental signal. 2DES is a young spectroscopic technique, whose outstanding success derived from detection of coherence patterns in natural multi-chromophoric complexes. Only recently, we are witnessing an upstream trend addressed to obtain a clear-headed understanding of the 2DES signatures of isolated pigments. Our investigation of the two most important harvesters in photosynthetic organisms worked precisely in this direction.

First, we studied clorophyll *a*, ubiquitous in plants and algae. We detected the presence of *electronic/vibronic coherences*, giving rise to a new kind of coherent pattern never observed before. They consist of superpositions of states within Q bands of clorophyll *a* that are expected intimately involved also in excitation energy flow within light-harvesting complexes.

Secondly, a detailed characterization of the oscillating patterns of bacteriochlorophyll *a* is proposed, offering a complete time and frequency domain description never reported before in the literature. Surprisingly, some of the vibrational coherences detected in 2DES dataset have damping time of few hundreds of femtoseconds. Quantum beatings having such a dephasing time could be erroneously interpreted as long-lasting electronic coherences; quite the opposite. Our characterization pointed out that such a temporal behaviour could be related also to purely vibrational coherences.

Finally, 2DES characterization of a natural light-harvesting protein complex, *peridinin-chlorophyll-protein*, was performed. Energy transfer (ET) process within the external antenna of *Amphidinium carterae* involves two distinct pigments, as the name of the protein itself says: chlorophyll *a* and peridinin, a peculiar carotenoid. The unique properties of the multidimensional spectroscopic tool allow disentangling the distinct contributions of the two pigments involved in ET. Moreover, we determined the energy of the electronic states directly involved in the process. The results have great relevance, since the topic is still highly debated in literature. Moreover, signatures of a possible coherent energy transfer between the optically allowed ex-

cited state of the carotenoid and the lowest excited state of chlorophyll were detected. Still, the mechanism is not fully clarified and further 2DES measurements are scheduled.

Proofs of quantum mechanisms were detected also in other biological processes, not only in light-harvesting. H-tunnelling in enzymatic catalysis is one of them. We chose a model system of a catalytic reaction centre, tetraphenylporphycene, to study intramolecular hydrogen transfer dynamics without interferences from the environment. We collected reasonable evidences to state that a *gating* mode of the macrocycle sustains double hydrogen tunnelling. Thus, to further investigate the role of H-tunnelling in enzymatic catalysis, we suggest to move to porphycenes with different substituents in *meso* position and to perform measurements at low temperature where the H-tunnelling mechanism should be favoured.

The general trend emerging from all the results collected and described in this thesis is that certainly Nature performs its functions in a very sophisticate and complex way, and we are still far from fully understand and dominate such mechanisms. Nevertheless, the development of new technological tools, like 2DES, and their application to simplified model artificial systems is assuming increasing relevance towards this aim.

Bibliography

[1] G.D. Scholes, Quantum-coherent electronic energy transfer: did nature think of it first?, J. Phys. Chem. Lett., 1 (2010) 2–8.

[2] E. Schrödinger, What is life?, Cambridge University Press, Cambridge, 1944.

[3] S.F. Huelga, M.B. Plenio, Vibrations, Quanta and Biology, Contemp. Phys., 54 (2013) 181–207.

[4] D.M. Jonas, Two-dimensional femtosecond spectroscopy, Annu. Rev. Phys. Chem., 54 (2003) 425–463.

[5] G. Engel, T. Calhoun, E. Read, T. Ahn, Evidence for wavelike energy transfer through quantum coherence in photosynthetic systems, Nature, 446 (2007) 782–786.

[6] E. Collini, C.Y. Wong, K.E. Wilk, P.M.G. Curmi, P. Brumer, G.D. Scholes, Coherently wired light-harvesting in photosynthetic marine algae at ambient temperature, Nature, 463 (2010) 644–647.

[7] F.D. Fuller, J. Pan, A. Gelzinis, V. Butkus, S.S. Senlik, D.E. Wilcox, C.F. Yocum, L. Valkunas, D. Abramavicius, J.P. Ogilvie, Vibronic coherence in oxygenic photosynthesis, Nat. Chem., 6 (2014) 706–711.

[8] A.W. Chin, J. Prior, R. Rosenbach, F. Caycedo-Soler, S.F. Huelga, M.B. Plenio, The role of non-equilibrium vibrational structures in electronic coherence and recoherence in pigment–protein complexes, Nat. Phys., 9 (2013) 113–118.

[9] J. Lim, D. Paleček, F. Caycedo-Soler, C.N. Lincoln, J. Prior, H. Von Berlepsch, S.F. Huelga, M.B. Plenio, D. Zigmantas, J. Hauer, Vibronic origin of long-lived coherence in an artificial molecular light harvester, Nat. Commun., 6 (2015) 1–22.

[10] H. Lee, Y.-C. Cheng, G.R. Fleming, Coherence dynamics in photosynthesis: protein protection of excitonic coherence, Science, 316 (2007) 1462–1465.

[11] A. Ishizaki, T.R. Calhoun, G.S. Schlau-Cohen, G.R. Fleming, Quantum coherence and its interplay with protein environments in photosynthetic electronic energy transfer, Phys. Chem. Chem. Phys., 12 (2010) 7319–7337.

[12] P. Ball, Physics of life: the dawn of quantum biology, Nature, 474 (2011) 272–274.

[13] J.C. Brookes, F. Hartoutsiou, A.P. Horsfield, A.M. Stoneham, Could humans recognize odor by phonon assisted tunneling?, Phys. Rev. Lett., 98 (2007) 1–4.

[14] C.T. Rodgers, P.J. Hore, Chemical magnetoreception in birds: the radical

pair mechanism, Proc. Natl. Acad. Sci. U. S. A., 106 (2009) 353–360.
[15] S. Mukamel, Principles of nonlinear optical spectroscopy, Oxford University, Oxford, 1995.
[16] L. Valkunas, D. Abramavicius, T. Mančal, Molecular excitation dynamics and relaxation Quantum theory and spectroscopy, Wiley-VCH, Weinheim, 2013.
[17] R.W. Boyd, Nonlinear optics, Academic Press, Inc., San Diego, 1992.
[18] W.W. Parson, Modern optical spectroscopy: with examples from biophysics, Springer, New York, 2009.
[19] M. Blume, Stochastic theory of line shape: generalization of the Kubo-Anderson model, Phys. Rev., 174 (1968) 351–358.
[20] R. Kubo, Advances in Chemical Physics, John Wiley & Sons, Inc., Hoboken, 1969.
[21] F. Caruso, A.W. Chin, A. Datta, S.F. Huelga, M.B. Plenio, Highly efficient energy excitation transfer in light-harvesting complexes: the fundamental role of noise-assisted transport, J. Chem. Phys., 131 (2009) 105106.
[22] P. Rebentrost, M. Mohseni, A. Aspuru-Guzik, Role of quantum coherence in chromophoric energy transport, J. Phys. Chem. B, 113 (2009) 9942–9947.
[23] M. Kasha, H.R. Rawls, M. Ashraf El-Bayoumi, The exciton model in molecular spectroscopy, Pure Appl. Chem., 11 (1965) 371–392.
[24] D.B. Turner, R. Dinshaw, K.-K. Lee, M.S. Belsley, K.E. Wilk, P.M.G. Curmi, G.D. Scholes, Quantitative investigations of quantum coherence for a light-harvesting protein at conditions simulating photosynthesis, Phys. Chem. Chem. Phys., 14 (2012) 4857–4874.
[25] O. V Prezhdo, P.J. Rossky, Relationship between quantum decoherence times and solvation dynamics in condensed phase chemical systems, Phys. Rev. Lett., 81 (1998) 5294–5297.
[26] E. Collini, G.D. Scholes, Electronic and vibrational coherences in resonance energy transfer along MEH-PPV chains at room temperature, J. Phys. Chem. A, 113 (2009) 4223–4241.
[27] A.W. Chin, S.F. Huelga, M.B. Plenio, Coherence and decoherence in biological systems: principles of noise-assisted transport and the origin of long-lived coherences, Philos. Trans. R. Soc. A Math. Phys. Eng. Sci., 370 (2012) 3638–3657.
[28] M. Del Rey, A.W. Chin, S.F. Huelga, M.B. Plenio, Exploiting structured environments for efficient energy transfer: the phonon antenna mechanism, J. Phys. Chem. Lett., 4 (2013) 903–907.
[29] M.B. Plenio, J. Almeida, S.F. Huelga, Origin of long-lived oscillations in 2D-spectra of a quantum vibronic model: electronic versus vibrational coherence, J. Chem. Phys., 139 (2013) 235102.
[30] D. Hayes, G.B. Griffin, G.S. Engel, Engineering coherence among excited states in synthetic heterodimer systems, Science, 340 (2013) 1431–1434.
[31] J.C. Dean, T. Mirkovic, Z.S.D. Toa, D.G. Oblinsky, G.D. Scholes, Vibronic enhancement of algae light harvesting, Chem, 1 (2016) 858–872.
[32] L. Rosenfeld, Quantum-mechanical theory of the natural optical activity of liquids and gases, Zeitschrift Fuer Phys., 52 (1928) 161–174.
[33] K. Nakanishi, N. Berova, R.W. Woody, Circular dichroism: principles and

applications, VCH Publishers, Inc., New York, 1994.
[34] W. Becker, The bh TCSPC Handbook, 6th Edition, Becker & Hickl, Berlin, 2015.
[35] W. Becker, A. Bergmann, Timing stability of TCSPC experiments, in: Proc. SPIE Int. Soc. Opt. Eng., 2006: p. 637209.
[36] D. Phillips, R.C. Drake, D. V O'Connor, R.L. Christensen, Time Correlated Single-Photon Counting (Tcspc) Using Laser Excitation, Instrum. Sci. Technol., 14 (1985) 267–292.
[37] W. Becker, A. Bergmann, C. Biskup, Multispectral fluorescence lifetime imaging by TCSPC, Microsc. Res. Tech., 70 (2007) 403–409.
[38] A.D. Bristow, D. Karaiskaj, X. Dai, T. Zhang, C. Carlsson, K.R. Hagen, R. Jimenez, S.T. Cundiff, A versatile ultrastable platform for optical multidimensional Fourier-transform spectroscopy, Rev. Sci. Instrum., 80 (2009) 73108.
[39] M.L. Cowan, J.P. Ogilvie, R.J.D. Miller, Two-dimensional spectroscopy using diffractive optics based phased-locked photon echoes, Chem. Phys. Lett., 386 (2004) 184–189.
[40] A. Nemeth, J. Sperling, J. Hauer, H.F. Kauffmann, F. Milota, Compact phase-stable design for single-and double-quantum two-dimensional electronic spectroscopy, Opt. Lett., 34 (2009) 3301–3303.
[41] U. Selig, F. Langhojer, F. Dimler, T. Löhrig, C. Schwarz, B. Gieseking, T. Brixner, Inherently phase-stable coherent two-dimensional spectroscopy using only conventional optics, Opt. Lett., 33 (2008) 2851–2853.
[42] S.-H. Shim, M.T. Zanni, How to turn your pump–probe instrument into a multidimensional spectrometer: 2D IR and Vis spectroscopies via pulse shaping, Phys. Chem. Chem. Phys., 11 (2008) 748–761.
[43] J.A. Myers, K.L.M. Lewis, P.F. Tekavec, J.P. Ogilvie, Two-color two-dimensional Fourier transform electronic spectroscopy with a pulse-shaper, Opt. Express, 16 (2008) 17420–17428.
[44] E. Harel, A.F. Fidler, G.S. Engel, B. Alexander Pines, Real-time mapping of electronic structure with single-shot two-dimensional electronic spectroscopy, Proc. Natl. Acad. Sci. USA, 107 (2010) 16444–16447.
[45] R. Augulis, D. Zigmantas, Two-dimensional electronic spectroscopy with double modulation lock-in detection: enhancement of sensitivity and noise resistance, Opt. Express, 19 (2011) 13126–13133.
[46] I.A. Heisler, R. Moca, F.V.A. Camargo, S.R. Meech, Two-dimensional electronic spectroscopy based on conventional optics and fast dual chopper data acquisition, Rev. Sci. Instrum., 85 (2014) 63103.
[47] C. Manzoni, D. Brida, G. Cerullo, Phase-locked pulses for two-dimensional spectroscopy by a birefringent delay line, Opt. Lett., 37 (2012) 3027–3029.
[48] F.D. Fuller, D.E. Wilcox, J.P. Ogilvie, Pulse shaping based two-dimensional electronic spectroscopy in a background free geometry, Opt. Express, 22 (2014) 1018–1027.
[49] D. Milam, M.J. Weber, A.J. Glass, Nonlinear refractive index of fluoride crystals, Appl. Phys. Lett., 31 (1977) 822–825.
[50] F.D. Fuller, J.P. Ogilvie, Experimental implementations of two-dimensional fourier transform electronic spectroscopy, Annu. Rev. Phys. Chem., 66

(2015) 667–90.
[51] V. Perlík, J. Hauer, F. Šanda, Finite pulse effects in single and double quantum spectroscopies, J. Opt. Soc. Am. B, 34 (2017) 430–439.
[52] P.F. Tekavec, J.A. Myers, K.L.M. Lewis, F.D. Fuller, J.P. Ogilvie, Effects of chirp on two-dimensional Fourier transform electronic spectra, Opt. Express, 18 (2010) 11015–11024.
[53] K.W. DeLong, R. Trebino, D.J. Kane, Comparison of ultrashort-pulse frequency-resolved-optical-gating traces for three common beam geometries, J. Opt. Soc. Am. B, 11 (1994) 1595–1608.
[54] W. Dietel, J.J. Fontaine, J.-C. Diels, Intracavity pulse compression with glass: a new method of generating pulses shorter than 60 fsec, Opt. Lett., 8 (1983) 4–6.
[55] R.L. Fork, O.E. Martinez, J.P. Gordon, Negative dispersion using pairs of prisms, Opt. Lett., 9 (1984) 150–152.
[56] D.J. Kane, R. Trebino, Characterization of arbitrary femtosecond pulses using frequency-resolved optical gating, IEEE J. Quant. Electron., 29 (1993) 571–579.
[57] B.M. Cho, M.K. Yetzbacher, K. Kitney, E.R. Smith, D.M. Jonas, Propagation and beam geometry effects on 2D Fourier transform spectra of multi-level systems, J. Phys. Chem. A, 113 (2009) 13287–13299.
[58] D.B. Turner, K.E. Wilk, P.M.G. Curmi, G.D. Scholes, Comparison of electronic and vibrational coherence measured by two-dimensional electronic spectroscopy, J. Phys. Chem. Lett., 2 (2011) 1904–1911.
[59] A. Volpato, L. Bolzonello, E. Meneghin, E. Collini, Global analysis of coherence and population dynamics in 2D electronic spectroscopy, Opt. Express, 23 (2016) 24773–24785.
[60] F.V.A. Camargo, H.L. Anderson, S.R. Meech, I.A. Heisler, Time-resolved twisting dynamics in a porphyrin dimer characterized by two-dimensional electronic spectroscopy, J. Phys. Chem. B, 119 (2015) 14660–1667.
[61] E.E. Ostroumov, R.M. Mulvaney, J.M. Anna, R.J. Cogdell, G.D. Scholes, Energy transfer pathways in light-harvesting complexes of purple bacteria as revealed by global kinetic analysis of two-dimensional transient spectra, J. Phys. Chem. B, 117 (2013) 11349–11362.
[62] K.M. Mullen, I.H.M. van Stokkum, The variable projection algorithm in time-resolved spectroscopy, microscopy and mass spectrometry applications, Numer. Algorithms, 51 (2008) 319–340.
[63] I.H.M. Van Stokkum, D.S. Larsen, R. Van Grondelle, Global and target analysis of time-resolved spectra, Biochim. Biophys. Acta - Bioenerg., 1657 (2004) 82–104.
[64] S.T. Cundiff, Optical three dimensional coherent spectroscopy, Phys. Chem. Chem. Phys., 16 (2014) 8193–200.
[65] F. Milota, V.I. Prokhorenko, T. Mancal, H. Von Berlepsch, O. Bixner, H.F. Kauffmann, J. Hauer, Vibronic and vibrational coherences in two-dimensional electronic spectra of supramolecular J-aggregates, J. Phys. Chem. A, 117 (2013) 6007–6014.
[66] M. Ferretti, V.I. Novoderezhkin, E. Romero, R. Augulis, A. Pandit, D. Zigmantas, R. Van Grondelle, The nature of coherences in the B820

bacteriochlorophyll dimer revealed by two-dimensional electronic spectroscopy, Phys. Chem. Chem. Phys., 16 (2014) 9930–9939.
[67] E. Romero, R. Augulis, V.I. Novoderezhkin, M. Ferretti, J. Thieme, D. Zigmantas, R. van Grondelle, Quantum coherence in photosynthesis for efficient solar-energy conversion, Nat. Phys., 10 (2014) 676–682.
[68] J. Prior, E. Castro, A.W. Chin, J. Almeida, S.F. Huelga, M.B. Plenio, Wavelet analysis of molecular dynamics: efficient extraction of time-frequency information in ultrafast optical processes, J. Chem. Phys., 139 (2013) 224103.
[69] A. Volpato, E. Collini, Time-frequency methods for coherent spectroscopy, Opt. Express, 23 (2015) 20040–20050.
[70] E.E. Ostroumov, R.M. Mulvaney, R.J. Cogdell, G.D. Scholes, Broadband 2D electronic spectroscopy reveals a carotenoid dark state in purple bacteria, Science, 340 (2013) 52–56.
[71] A. Kolli, E.J. O'Reilly, G.D. Scholes, A. Olaya-Castro, The fundamental role of quantized vibrations in coherent light harvesting by cryptophyte algae, J. Chem. Phys., 137 (2012) 174109.
[72] V. Tiwari, W.K. Peters, D.M. Jonas, Electronic resonance with anticorrelated pigment vibrations drives photosynthetic energy transfer outside the adiabatic framework, Proc. Natl. Acad. Sci. U. S. A., 110 (2013) 1203–1208.
[73] R. Dosselli, R. Ruiz-González, F. Moret, V. Agnolon, C. Compagnin, M. Mognato, V. Sella, M. Agut, S. Nonell, M. Gobbo, E. Reddi, Synthesis, spectroscopic, and photophysical characterization and photosensitizing activity toward prokaryotic and eukaryotic cells of porphyrin-magainin and -buforin conjugates, J. Med. Chem., 57 (2014) 1403–1415.
[74] M. Gouterman, Spectra of porphyrins, J. Mol. Spectrosc., 6 (1961) 138–163.
[75] X. Huang, K. Nakanishi, N. Berova, Porphyrins and metalloporphyrins: versatile circular dichroic reporter groups for structural studies, Chirality, 12 (2000) 237–255.
[76] S. Matile, N. Berova, K. Nakanishi, J. Fleischhauer, R.W. Woody, Structural studies by exciton coupled circular dichroism over a large distance: porphyrin derivatives of steroids, dimeric steroids, and brevetoxin B, J. Am. Chem. Soc., 118 (1996) 5198–5206.
[77] V. Butkus, L. Valkunas, D. Abramavicius, Vibronic phenomena and exciton-vibrational interference in two-dimensional spectra of molecular aggregates, J. Chem. Phys., 140 (2014) 34306.
[78] T. Kobayashi, J-aggregates, World Scientific, Singapore, 1996.
[79] L. Bolzonello, F. Fassioli, E. Collini, Correlated fluctuations and intraband dynamics of J-aggregates revealed by combination of 2DES schemes, J. Phys. Chem. Lett., (2016) 4996–5001.
[80] M. Kullmann, A. Hipke, P. Nuernberger, T. Bruhn, D.C.G.G. Götz, M. Sekita, D.M. Guldi, G. Bringmann, T. Brixner, Ultrafast exciton dynamics after Soret- or Q-band excitation of a directly β,β'-linked bisporphyrin, Phys. Chem. Chem. Phys., 14 (2012) 8038–8050.
[81] P. Bouř, K. Záruba, M. Urbanová, V. Setnička, P. Matějka, Z. Fiedler, V. Král, K. Volka, Vibrational circular dichroism of tetraphenylporphyrin in

peptide complexes? A computational study, Chirality, 12 (2000) 191–198.
[82] M. Di Valentin, M. Albertini, E. Zurlo, M. Gobbo, D. Carbonera, Porphyrin triplet state as potential spin label for nanometer distance measurements by PELDOR spectroscopy the porphyrin triplet state as potential spin label for nanometer distance measurements by PELDOR spectroscopy, J. Am. Chem. Soc., 136 (2014) 6582–6585.
[83] H. Wolf, H. Scheer, Stereochemistry and chiroptic properties of pheophorbides and related compounds, Ann. N. Y. Acad. Sci., 206 (1973) 549–567.
[84] C. Houssier, K. Sauer, Circular dichroism and magnetic circular dichroism of the chlorophyll and protochlorophyll pigments, J. Am. Chem. Soc., 92 (1970) 779–791.
[85] T. Mančal, A. Nemeth, F. Milota, V. Lukeš, H.F. Kauffmann, J. Sperling, Vibrational wave packet induced oscillations in two-dimensional electronic spectra II Theory, J. Chem. Phys., 132 (2010) 184515.
[86] E. Collini, C. Ferrante, R. Bozio, Strong enhancement of the two-photon absorption of tetrakis(4-sulfonatophenyl)porphyrin diacid in water upon aggregation, J. Phys. Chem. B, 109 (2005) 2–5.
[87] V. Butkus, D. Zigmantas, L. Valkunas, D. Abramavicius, Vibrational vs electronic coherences in 2D spectrum of molecular systems, Chem. Phys. Lett., 545 (2012) 40–43.
[88] B. Grimm, R.J. Porra, W. Rüdiger, H. Scheer, Chlorophylls and Bacteriochlorophylls (Advances in Photosynthesis and Respiration), Springer, Dordrecht, 2006.
[89] L.O. Björn, G.C. Papageorgiou, R.E. Blankenship, Govindjee, A viewpoint: why chlorophyll a?, Photosynth. Res., 99 (2009) 85–98.
[90] M. Kobayashi, S. Akutsu, D. Fujinuma, Physicochemical properties of chlorophylls in oxygenic photosynthesis - Succession of co-factors from anoxygenic to oxygenic photosynthesis, InTech, Rijeka, 2013.
[91] S.S. Senlik, V.R. Policht, J.P. Ogilvie, Two-color nonlinear spectroscopy for the rapid acquisition of coherent dynamics, J. Phys. Chem. Lett., 6 (2015) 2413–2420.
[92] D. Kosumi, T. Nishiguchi, M. Sugisaki, H. Hashimoto, Ultrafast coherent spectroscopic investigation on photosynthetic pigment chlorophyll a utilizing 20 fs pulses, J. Photochem. Photobiol. A Chem., 313 (2015) 72–78.
[93] R. Moca, S.R. Meech, I.A. Heisler, Two-dimensional electronic spectroscopy of chlorophyll a: solvent dependent spectral evolution, J. Phys. Chem. B, 119 (2015) 8623–8630.
[94] L.L. Shipman, T.M. Cotton, J.R. Norris, J.J. Katz, An analysis of the visible absorption spectrum of chlorophyll a monomer, dimer, and oligomers in solution, J. Am. Chem. Soc., 98 (1976) 8222–8230.
[95] R. Vladkova, Chlorophyll a self-assembly in polar solvent – water mixtures, Photochem. Photobiol., 71 (2000) 71–83.
[96] M. Gouterman, L. Stryer, Fluorescence polarization of some porphyrins, J. Chem. Phys., 37 (1962) 2260.
[97] J.R. Reimers, Z.-L. Cai, R. Kobayashi, M. Rätsep, A. Freiberg, E. Krausz, Assignment of the Q-bands of the chlorophylls: coherence loss via Qx - Qy

mixing, Sci. Rep., 3 (2013) 2761.
[98] M. Umetsu, Z.-Y. Wang, M. Kobayashi, T. Nozawa, Interaction of photosynthetic pigments with various organic solvents, Biochim. Biophys. Acta - Bioenerg., 1410 (1999) 19–31.
[99] M. Rätsep, J. Linnanto, A. Freiberg, Mirror symmetry and vibrational structure in optical spectra of chlorophyll a, J. Chem. Phys., 130 (2009) 1–11.
[100] J. Du, T. Teramoto, K. Nakata, E. Tokunaga, T. Kobayashi, Real-time vibrational dynamics in chlorophyll a studied with a few-cycle pulse laser, Biophys. J., 101 (2011) 995–1003.
[101] C. Zhou, J.R. Diers, D.F. Bocian, Qy-excitation Resonance Raman spectra of chlorophyll a and related complexes Normal mode characteristics of the low-frequency vibrations, J. Phys. Chem. B, 101 (1997) 9635–9644.
[102] K.L. Wells, Z. Zhang, J.R. Rouxel, H.-S. Tan, Measuring the spectral diffusion of chlorophyll a using two-dimensional electronic spectroscopy, J. Phys. Chem. B, 117 (2013) 2294–2299.
[103] F.V.D.A. Camargo, L. Grimmelsmann, L. Anderson, S.R. Meech, I.A. Heisler, Resolving vibrational from electronic coherences in two-dimensional electronic spectroscopy: the role of the laser spectrum, Phys. Rev. Lett., 118 (2017) 33001.
[104] M. Lutz, Resonance Raman spectra of chlorophyll in solution, J. Raman Spectrosc., 2 (1974) 497–516.
[105] A. Telfer, A.A. Pascal, L. Bordes, J. Barber, B. Robert, Fluorescence line narrowing studies on isolated chlorophyll molecules, J. Phys. Chem. B, 114 (2010) 2255–2260.
[106] E.J.G. Peterman, S.-O. Wenk, T. Pullerits, L.-O. Pålsson, R. van Grondelle, J.P. Dekker, M. Rögner, H. van Amerongen, Fluorescence and absorption spectroscopy of the weakly fluorescent chlorophyll a in cytochrome b6f of synechocystis PCC6803, Biophys. J., 75 (1998) 389–398.
[107] K.A. Fransted, J.R. Caram, D. Hayes, G.S. Engel, Two-dimensional electronic spectroscopy of bacteriochlorophyll a in solution: elucidating the coherence dynamics of the Fenna-Matthews-Olson complex using its chromophore as a control, J. Chem. Phys., 137 (2012) 125101.
[108] M. Rätsep, Z.L. Cai, J.R. Reimers, A. Freiberg, Demonstration and interpretation of significant asymmetry in the low-resolution and high-resolution Qy fluorescence and absorption spectra of bacteriochlorophyll a, J. Chem. Phys., 134 (2011) 24506.
[109] E. Bellacchio, K. Sauer, Temperature dependence of optical spectra of bacteriochlorophyll a in solution and in low-temperature glasses, J. Phys. Chem. B, 103 (1999) 2279–2290.
[110] J.R. Caram, G.S. Engel, Extracting dynamics of excitonic coherences in congested spectra of photosynthetic light harvesting antenna complexes, Faraday Discuss., 153 (2011) 93–104.
[111] P.-S. Song, P. Koka, B.B. Prezelin, F.T. Haxo, Molecular topology of the photosynthetic light-harvesting pigment complex, peridinin-chlorophyll a-protein, from marine dinoflagellates, Biochemistry, 15 (1976) 4422–4427.
[112] P. Koka, P.-S. Song, The chromophore topography and binding

environment of peridinin-chlorophyll a-protein complexes from marine dinoflagellate algae, Biochim. Biophys. Acta - Protein Struct., 495 (1977) 220–231.
[113] D. Carbonera, G. Giacometti, U. Segre, E. Hofmann, R.G. Hiller, Structure-based calculations of the optical spectra of the light-harvesting peridinin-chlorophyll-protein complexes from Amphidinium carterae and Heterocapsa pygmaea, J. Phys. Chem. B, 103 (1999) 6349–6356.
[114] J.A. Bautista, R.G. Hiller, F.P. Sharples, D. Gosztola, M. Wasielewski, H.A. Frank, Singlet and triplet transfer in the Peridinin-Chlorophyll a- protein from Amphidinium carterae, J. Phys. Chem. A, 103 (1999) 2267–2273.
[115] D. Zigmantas, T. Polfvka, R.G. Killer, A. Yartsev, V. Sundstrom, Spectroscopic and dynamic properties of the peridinin lowest singlet excited states, J. Phys. Chem. A, 105 (2001) 10296–10306.
[116] B.P. Krueger, S.S. Lampoura, I.H. van Stokkum, E. Papagiannakis, J.M. Salverda, C.C. Gradinaru, D. Rutkauskas, R.G. Hiller, R. van Grondelle, Energy transfer in the peridinin chlorophyll-a protein of Amphidinium carterae studied by polarized transient absorption and target analysis, Biophys. J., 80 (2001) 2843–2855.
[117] D. Zigmantas, R.G. Hiller, V. Sundstrom, T. Polivka, Carotenoid to chlorophyll energy transfer in the peridinin-chlorophyll-a-protein complex involves an intramolecular charge transfer state, Proc. Natl. Acad. Sci. U. S. A., 99 (2002) 16760–16765.
[118] P. a. Linden, J. Zimmermann, T. Brixner, N.E. Holt, H.M. Vaswani, R.G. Hiller, G.R. Fleming, Transient absorption study of peridinin and peridinin−chlorophyll a−protein after two-photon excitation, J. Phys. Chem. B, 108 (2004) 10340–10345.
[119] L. Premvardhan, E. Papagiannakis, R.G. Hiller, R. Van Grondelle, The charge-transfer character of the S0 - S2 transition in the carotenoid peridinin is revealed by stark spectroscopy, J. Phys. Chem. B, 109 (2005) 15589–15597.
[120] N. Christensson, P. Chábera, R.G. Hiller, T. Pullerits, T. Polívka, Four-wave-mixing spectroscopy of peridinin in solution and in the peridinin-chlorophyll-a protein, Chem. Phys., 373 (2010) 15–22.
[121] S. Ghosh, M.M. Bishop, J.D. Roscioli, A.M. LaFountain, H.A. Frank, W.F. Beck, Femtosecond heterodyne transient grating studies of nonradiative deactivation of the S2 (1Bu+) state of peridinin: detection and spectroscopic assignment of an intermediate in the decay pathway, J. Phys. Chem. B, 120 (2016) 3601–3614.
[122] I.H.M. van Stokkum, E. Papagiannakis, M. Vengris, J.M. Salverda, T. Polívka, D. Zigmantas, D.S. Larsen, S.S. Lampoura, R.G. Hiller, R. van Grondelle, Inter-pigment interactions in the peridinin chlorophyll protein studied by global and target analysis of time resolved absorption spectra, Chem. Phys., 357 (2009) 70–78.
[123] A. Damjanović, T. Ritz, K. Schulten, Excitation transfer in the peridinin-chlorophyll-protein of Amphidinium carterae, Biophys. J., 79 (2000) 1695–1705.
[124] W.P. Bricker, C.S. Lo, Excitation energy transfer in the peridinin-chlorophyll a-protein complex modeled using configuration interaction, J.

Phys. Chem. B, 118 (2014) 9141–9154.
[125] J.P. Götze, B. Karasulu, M. Patil, W. Thiel, Vibrational relaxation as the driving force for wavelength conversion in the peridinin-chlorophyll a-protein, Biochim. Biophys. Acta - Bioenerg., 1847 (2015) 1509–1517.
[126] W.P. Bricker, C.S. Lo, Efficient pathways of excitation energy transfer from delocalized S2 excitons in the peridinin-chlorophyl a-protein complex, J. Phys. Chem. B, 119 (2015) 5755–5764.
[127] E. Hofmann, P.M. Wrench, F.P. Sharples, R.G. Hiller, W. Welte, K. Diederichs, Structural basis of light harvesting by carotenoids: peridinin-chlorophyll-protein from Amphidinium carterae, Science, 272 (1996) 1788–1791.
[128] M. Mimuro, U. Nagashima, S. Takaichi, Y. Nishimura, I. Yamazaki, T. Katoh, Molecular structure and optical properties of carotenoids for the in vivo energy transfer function in the algal photosynthetic pigment system, Biochim. Biophys. Acta - Bioenerg., 1098 (1992) 271–274.
[129] H.A. Frank, J.A. Bautista, J. Josue, Z. Pendon, R.G. Hiller, F.P. Sharples, D. Gosztola, M.R. Wasielewski, Effect of the solvent environment on the spectroscopic properties and dynamics of the lowest excited states of carotenoids, J. Phys. Chem. B, 104 (2000) 4569–4577.
[130] H.M. Vaswani, C.P. Hsu, M. Head-Gordon, G.R. Fleming, Quantum chemical evidence for an intramolecular charge-transfer state in the carotenoid peridinin of peridinin-chlorophyll-protein, J. Phys. Chem. B, 107 (2003) 7940–7946.
[131] E. Papagiannakis, D.S. Larsen, I.H.M. Van Stokkum, M. Vengris, R.G. Hiller, R. Van Grondelle, Resolving the excited state equilibrium of peridinin in solution, Biochemistry, 43 (2004) 15303–15309.
[132] C. Bonetti, M.T.A. Alexandre, I.H.M. van Stokkum, R.G. Hiller, M.L. Groot, R. van Grondelle, J.T.M. Kennis, Identification of excited-state energy transfer and relaxation pathways in the peridinin–chlorophyll complex: an ultrafast mid-infrared study, Phys. Chem. Chem. Phys., 12 (2010) 9256–9266.
[133] D. Zigmantas, R.G. Hiller, A. Yartsev, V. Sundstro, Dynamics of excited states of the carotenoid peridinin in polar solvents: dependence on excitation wavelength, viscosity, and temperature, J. Phys. Chem. B, 107 (2003) 5339–5348.
[134] D. Zigmantas, R.G. Hiller, F.P. Sharples, H. a. Frank, V. Sundström, T. Polívka, Effect of a conjugated carbonyl group on the photophysical properties of carotenoids, Phys. Chem. Chem. Phys., 6 (2004) 3009–3016.
[135] R.P. Ilagan, J.F. Koscielecki, R.G. Hiller, F.P. Sharples, G.N. Gibson, R.R. Birge, H.A. Frank, Femtosecond time-resolved absorption spectroscopy of main-form and high-salt peridinin-chlorophyll a-proteins at low temperatures, Biochemistry, 45 (2006) 14052–14063.
[136] S. Ghosh, M.M. Bishop, J.D. Roscioli, J.J. Mueller, N.C. Shepherd, A.M. LaFountain, H.A. Frank, W.F. Beck, Femtosecond heterodyne transient grating studies of nonradiative decay of the S2 (1Bu+) state of β-carotene: contributions from dark intermediates and double quantum coherences, J. Phys. Chem. B, 119 (2015) 14905–14924.

[137] S. Shima, R.P. Ilagan, N. Gillespie, B.J. Sommer, R.G. Hiller, F.P. Sharples, H.A. Frank, R.R. Birge, Two-photon and fluorescence spectroscopy and the effect of environment on the photochemical properties of peridinin in solution and in the peridinin-chlorophyll-protein from amphidinium carterae, J. Phys. Chem. A, 107 (2003) 8052–8066.
[138] N.L. Wagner, J.A. Greco, M.M. Enriquez, H.A. Frank, R.R. Birge, The nature of the intramolecular charge transfer state in peridinin, Biophys. J., 104 (2013) 1314–1325.
[139] J.A. Bautista, R.E. Connors, B.B. Raju, R.G. Hiller, F.P. Sharples, D. Gosztola, M.R. Wasielewski, H.A. Frank, Excited state properties of peridinin: observation of a solvent dependence of the lowest excited singlet state lifetime and spectral behavior unique among carotenoids, J. Phys. Chem. B, 103 (1999) 8751–8758.
[140] T. Polívka, R.G. Hiller, H.A. Frank, Spectroscopy of the peridinin-chlorophyll-a protein: insight into light-harvesting strategy of marine algae, Arch. Biochem. Biophys., 458 (2007) 111–120.
[141] A. Nemeth, F. Milota, T. Mančal, T. Pullerits, J. Sperling, J. Hauer, H.F. Kauffmann, N. Christensson, Double-quantum two-dimensional electronic spectroscopy of a three-level system: experiments and simulations, J. Chem. Phys., 133 (2010) 94505.
[142] T. Schulte, D.M. Niedzwiedzki, R.R. Birge, R.G. Hiller, T. Polívka, E. Hofmann, H.A. Frank, Identification of a single peridinin sensing Chl-a excitation in reconstituted PCP by crystallography and spectroscopy, Proc. Natl. Acad. Sci. U. S. A., 106 (2009) 20764–20769.
[143] S. Ghosh, M.M. Bishop, J.D. Roscioli, A.M. LaFountain, H.A. Frank, W.F. Beck, Excitation energy transfer by coherent and incoherent mechanisms in the peridinin–chlorophyll a-protein, J. Phys. Chem. Lett., 8 (2017) 463–469.
[144] T. Polívka, H.A. Frank, Light harvesting by carotenoids, Acc. Chem. Res., 43 (2010) 1125–1134.
[145] F.P. Sharples, P.M. Wrench, K. Ou, R.G. Hiller, Two distinct forms of the peridinin-chlorophyll a-protein from Amphidinium carterae, Biochim. Biophys. Acta - Bioenerg., 1276 (1996) 117–123.
[146] A. Mezzetti, E. Kish, B. Robert, R. Spezia, Assignment of IR bands of isolated and protein-bound Peridinin in its fundamental and triplet state by static FTIR, time-resolved step-scan FTIR and DFT calculations, J. Mol. Struct., 1090 (2015) 58–64.
[147] E. Kish, M.M. Mendes Pinto, D. Bovi, M. Basire, L. Guidoni, R. Vuilleumier, B. Robert, R. Spezia, A. Mezzetti, Fermi resonance as a tool for probing peridinin environment, J. Phys. Chem. B, 118 (2014) 5873–5881.
[148] H. Kuzmany, Resonance Raman scattering from neutral and doped polyacetylene, Phys. Status Solidi, 97 (1980) 521–531.
[149] S. Saito, M. Tasumi, C.H. Eugster, Resonance Raman spectra (5800-40 cm-1) of all-trans and 15-cis isomers of beta-carotene in the solid state and in solution Measurements with various laser lines from ultraviolet to red, J. Raman Spectrosc., 14 (1983) 299–309.
[150] C. Kolano, J. Helbing, M. Kozinski, W. Sander, P. Hamm, Watching hydrogen-bond dynamics in a beta-turn by transient two-dimensional

infrared spectroscopy, Nature, 444 (2006) 469–472.
[151] C. Kolano, J. Helbing, G. Bucher, W. Sander, P. Hamm, Intramolecular disulfide bridges as a phototrigger to monitor the dynamics of small cyclic peptides, J. Phys. Chem. B, 111 (2007) 11297–11302.
[152] J. Bredenbeck, J. Helbing, P. Hamm, Labeling vibrations by light: ultrafast transient 2D-IR spectroscopy tracks vibrational modes during photoinduced charge transfer, J. Am. Chem. Soc., 126 (2004) 990–991.
[153] C.R. Baiz, M.J. Nee, R. McCanne, K.J. Kubarych, Ultrafast nonequilibrium Fourier-transform two-dimensional infrared spectroscopy, Opt. Lett., 33 (2008) 2533–2535.
[154] H.S. Chung, Z. Ganim, K.C. Jones, A. Tokmakoff, Transient 2D IR spectroscopy of ubiquitin unfolding dynamics, Proc. Natl. Acad. Sci. U. S. A., 104 (2007) 14237–14242.
[155] M. Kullmann, S. Ruetzel, J. Buback, P. Nuernberger, T. Brixner, Reaction dynamics of a molecular switch unveiled by coherent two-dimensional electronic spectroscopy, J. Am. Chem. Soc., 133 (2011) 13074–13080.
[156] M. Gil, J. Waluk, Vibrational gating of double hydrogen tunneling in porphycene, J. Am. Chem. Soc., 129 (2007) 1335–1341.
[157] J.M. Lopez Del Amo, U. Langer, V. Torres, G. Buntkowsky, H.M. Vieth, M. Pérez-Torralba, D. Sanz, R.M. Claramunt, J. Elguero, H.H. Limbach, NMR studies of ultrafast intramolecular proton tautomerism in crystalline and amorphous N,N′-diphenyl-6-aminofulvene-1-aldimine: solid-state, kinetic isotope, and tunneling effects, J. Am. Chem. Soc., 130 (2008) 8620–8632.
[158] E. Vogel, M. Köcher, H. Schmickler, J. Lex, Porphycene - a novel porphin isomer, Angew. Chemie Int. Ed. English, 25 (1986) 257–259.
[159] D. Sánchez-García, J.L. Sessler, Porphycenes: synthesis and derivatives, Chem. Soc. Rev., 37 (2008) 215–232.
[160] J.C. Stockert, M. Cañete, A. Juarranz, A. Villanueva, R.W. Horobin, J.I. Borrell, J. Teixidó, S. Nonell, Porphycenes: facts and prospects in photodynamic therapy of cancer, Curr. Med. Chem., 14 (2007) 997–1026.
[161] S.E. Braslavsky, M. Müller, D.O. Mártire, S. Pörting, S.G. Bertolotti, S. Chakravorti, G. Koç-Weier, B. Knipp, K. Schaffner, Photophysical properties of porphycene derivatives (18π porphyrinoids), J. Photochem. Photobiol. B Biol., 40 (1997) 191–198.
[162] K. Malsch, G. Hohlneicher, P. Chemie, V. Uni, The force field of porphycene: a theoretical and experimental approach, J. Phys. Chem., 5639 (1997) 8409–8416.
[163] P.M. Kozlowski, M.Z. Zgierski, J. Baker, The inner-hydrogen migration and ground-state structure of porphycene, J. Chem. Phys., 109 (1998) 5905–5913.
[164] M.F. Shibl, M. Tachikawa, O. Kühn, The geometric (H/D) isotope effect in porphycene: grid-based Born-Oppenheimer vibrational wavefunctions vs multi-component molecular orbital theory, Phys. Chem. Chem. Phys., 7 (2005) 1368–1373.
[165] H. Cybulski, M. Pecul, T. Helgaker, M. Jaszunski, Theoretical studies of nuclear magnetic resonance parameters for the proton-exchange pathways

in porphyrin and porphycene, J. Phys. Chem. A, 109 (2005) 4162–4171.
[166] T. Udagawa, M. Tachikawa, HD isotope effect on porphine and porphycene molecules with multicomponent hybrid density functional theory, J. Chem. Phys., 125 (2006) 244105.
[167] T. Yoshikawa, S. Sugawara, T. Takayanagi, M. Shiga, M. Tachikawa, Theoretical study on the mechanism of double proton transfer in porphycene by path-integral molecular dynamics simulations, Chem. Phys. Lett., 496 (2010) 14–19.
[168] E.D. Becker, R.B. Bradley, C.J. Watson, Proton magnetic resonance studies of porphyrins, J. Am. Chem. Soc., 83 (1961) 3743–3748.
[169] J. Braun, M. Schlabach, B. Wehrle, M. Kcher, E. Vogel, H. Limbach, NMR study of the tautomerism of porphyrin including the kinetic HH/HD/DD isotope effects in the liquid and the solid state, J. Am. Chem. Soc., 116 (1994) 6593–6604.
[170] J. Braun, H. Limbach, P.G. Williams, H. Morimoto, D.E. Wemmer, Observation of kinetic tritium isotope effects by dynamic NMR The tautomerism of porphyrin, J. Am. Chem. Soc., 118 (1996) 7231–7232.
[171] M. Pietrzak, M.F. Shibl, M. Bröring, O. Kühn, H.H. Limbach, 1H/2H NMR studies of geometric H/D isotope effects on the coupled hydrogen bonds in porphycene derivatives, J. Am. Chem. Soc., 129 (2007) 296–304.
[172] U. Langer, C. Hoelger, B. Wehrle, L. Latanowicz, E. Vogel, H.-H. Limbach, 15N NMR study of proton localization and proton transfer thermodynamics and kinetics in polycrystalline porphycene, J. Phys. Org. Chem., 13 (2000) 23–34.
[173] J. Sepioł, Y. Stepanenko, a Vdovin, a Mordziński, E. Vogel, J. Waluk, Proton tunnelling in porphycene seeded in a supersonic jet, Chem. Phys. Lett., 296 (1998) 549–556.
[174] A. Vdovin, J. Sepioł, N. Urbańska, M. Pietraszkiewicz, A. Mordziński, J. Waluk, Evidence for two forms, double hydrogen tunneling, and proximity of excited states in bridge-substituted porphycenes: supersonic jet studies, J. Am. Chem. Soc., 128 (2006) 2577–2586.
[175] A. Vdovin, J. Waluk, B. Dick, A. Slenczka, Mode-selective promotion and isotope effects of concerted double-hydrogen tunneling in porphycene embedded in superfluid helium nanodroplets, ChemPhysChem, 10 (2009) 761–765.
[176] E.T. Mengesha, J. Sepio, P. Borowicz, J. Waluk, Vibrations of porphycene in the S0 and S1 electronic states: single vibronic level dispersed fluorescence study in a supersonic jet, J. Chem. Phys., 138 (2013) 174201.
[177] P. Ciąćka, P. Fita, A. Listkowski, M. Kijak, S. Nonell, D. Kuzuhara, H. Yamada, C. Radzewicz, J. Waluk, Tautomerism in porphycenes: analysis of rate-affecting factors, J. Phys. Chem. B, 119 (2015) 2292–2301.
[178] J. Waluk, Ground- and excited-state tautomerism in porphycenes, Acc. Chem. Res., 39 (2006) 945–952.
[179] P. Fita, N. Urbanska, C. Radzewicz, J. Waluk, Ground-and excited-state tautomerization rates in porphycenes, Chem. - A Eur. J., 15 (2009) 4851–4856.
[180] C. Schriever, S. Lochbrunner, A.R. Ofial, E. Riedle, The origin of ultrafast

proton transfer: multidimensional wave packet motion vs tunneling, Chem. Phys. Lett., 503 (2011) 61–65.
[181] O. Planas, R. Tejedor-Estrada, S. Nonell, Tautomerism and dual fluorescence in 9-substituted n-propyl- and methoxyethyl-porphycenes, J. Porphyr. Phthalocyanines, 16 (2012) 633–640.
[182] M. Gil, J. Dobkowski, G. Wiosna-Sałyga, N. Urbańska, P. Fita, C. Radzewicz, M. Pietraszkiewicz, P. Borowicz, D. Marks, M. Glasbeek, J. Waluk, Unusual, solvent viscosity-controlled tautomerism and photophysics: meso-alkylated porphycenes, J. Am. Chem. Soc., 132 (2010) 13472–13485.
[183] J. Arnbjerg, A. Jiménez-Banzo, M.J. Paterson, S. Nonell, J.I. Borrell, O. Christiansen, P.R. Ogilby, Two-photon absorption in tetraphenylporphycenes: are porphycenes better candidates than porphyrins for providing optimal optical properties for two-photon photodynamic therapy?, J. Am. Chem. Soc., 129 (2007) 5188–5199.
[184] E.R. Henry, J. Hofrichter, Singular value decomposition: application to analysis of experimental data, Methods Enzymol., 210 (1992) 129–192.
[185] M. Gil, J.A. Organero, J. Waluk, A. Douhal, Ultrafast dynamics of alkyl-substituted porphycenes in solution, Chem. Phys. Lett., 422 (2006) 142–146.